Thermal Management
Of
Solid State Lighting Module

PROEFSCHRIFT

ter verkrijging van de graad van doctor
aan de Technische Universiteit Delft,
op gezag van de Rector Magnificus Prof. ir. K.C.A.M. Luyben,
voorzitter van het College voor Promoties,
in het openbaar te verdedigen

op woensdag 10 september 2014 om 10:00 uur

door

Huaiyu YE

Master of Science in Mechanical Engineering
Technische Universiteit Delft, Nederland
geboren te Guizhou, China

Dit proefschrift is goedgekeurd door de promotor:
Prof. dr. G.Q.Zhang

Samenstelling promotiecommissie:

Rector Magnificus	voorzitter
Prof. dr. G.Q.Zhang	Technische Universiteit Delft, promotor
Prof. dr. E.Suhir	Portland State University, USA
Prof. dr. K.J.Wolter	Technische Universität Dresden, Deutschland
Prof. dr. P.J.French	Technische Universiteit Delft
Prof. dr. J.A.Ferreira	Technische Universiteit Delft
Dr. ir. A.W.J.Gielen	TNO Eindhoven
Dr. ir. J.P.Jacobs	Koninklijke Philips N.V.

This research was carried out under project number E63.9.10397 in the framework of the Research Program of the Materials innovation institute (M2i) in the Netherlands (www.m2i.nl).

Key words: Solid state lighting, Light emitting diode, Thermal management, Electrical thermal luminous chromatic model, Junction temperature, Temperature sensor, MEMS, Two phase cooling, Loop heat pipe, Vertical fin array, Numerical modelling, CFD.

ISBN: 978-94-91909-10-8

Copyright©2014 by Huaiyu Ye

All rights reserved.
No part of this publication may be reproduced, stored in a retrieval system, or transmitted in any form or by any means without the prior written permission of the copyright owner.

Printed by CPI Wöhrmann Print Service, Zutphen, The Netherlands.

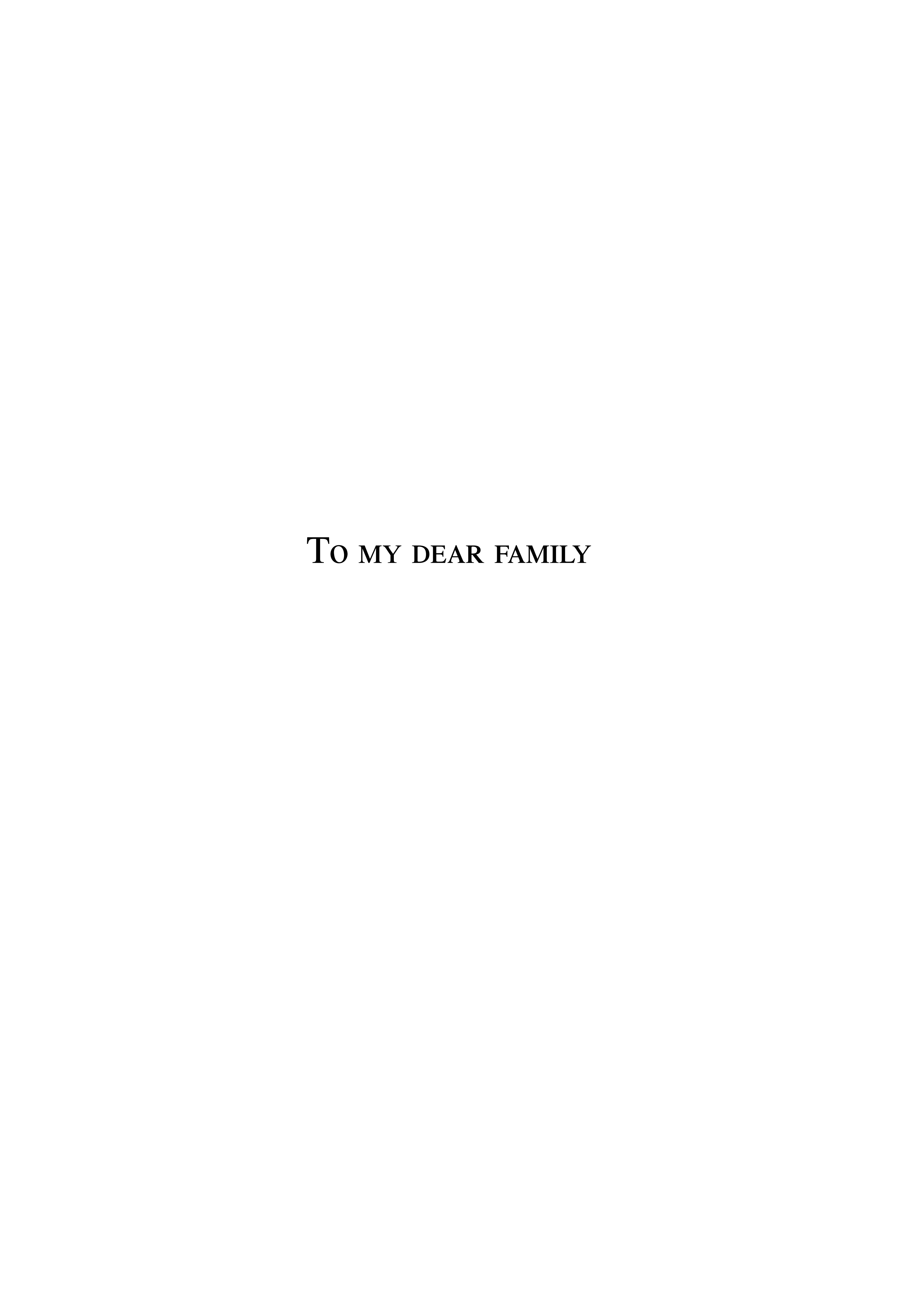

To my dear family

Summary

Solid-State Lighting (SSL), powered by Light-Emitting Diodes (LEDs), is an energy-efficient technology for lighting systems. Blue GaN-based LEDs using InGaN quantum wells combined with a broad spectrum yellow emitting phosphorous materials, such as YAG:Ce^{3+}, are generally used to produce white light. In contrast to incandescent lights which obtain high efficiency at high temperatures, the highest efficiency of LEDs is reached at low temperatures. This introduces a new challenge for both optical designer who need to consider the thermal structure and thermal designer who need to optimize the light performance. The thermal management in LED product is then a key design parameter as the high operation temperature directly affects the maximum light output, quality, reliability and life time.

Currently, the thermal path within a LED package is designed from the die to the heat sink, where the heat is dissipated to environment by convection and radiation. As the electric input power increases, high-power/high-brightness LEDs have higher power density and consequent higher heat dissipation. This results in higher temperatures if no counter-measures are taken. Solutions are sought in optimizing the thermal path, materials with better thermal conductivity and increasing the performance of convection and radiation. However, the apparent dilemma is to optimize light efficiency and effectively designing thermal management. Two questions arise: Firstly, what is the optimum temperature for maximum light performance? Secondly, what temperature leads to thermal management solutions with less weight, energy consumption, and light hindering? The first question can be answered as “the lower temperature the better light”. For the second question, a high temperature gradient will result in high heat fluxes, which can move away large amounts of excess heat and reduce the complexity of cooling solutions. This means that high LED temperatures would be favorable. This gives a contradiction. Therefore, the thermal management of SSL is not just cool down the temperature but to achieve stable and acceptable temperature for optimum light quality, possibly using in situ monitoring, less weight materials, easy fabrication process, less energy consumption cooling solution.

There are two major heat sources in the LED package, the LED die (chip) and the phosphorous layer. The excess heat generated in the die during the conversion from electric energy to blue light and also in the phosphorous layer where blue light is converted into yellow light. The two conversion rates are both temperature

dependent. Thus the temperature is the most important parameter from both thermal and optical point of view. In order to be able to optimize the LED temperature, an electrical-thermal-luminous-chromatic (E-T-L-C) model was developed that takes into account the thermal effect on the energy conversion rate from electric power (E) to primary blue light and from blue light into yellow light as a function of the in-situ temperature (T). As the conversion rates of the die and phosphor differ, the white light performance changes both in flux (L) and spectrum (C). The model was successfully verified using three commercially available LED packages. Furthermore, the model was also used to study the effect of layer thickness and particle density variations of the phosphorous layer on the thermal performance and light quality.

As the temperature is both critical to light performance and thermal management, knowing the temperature in the LED is indispensable. The diode forward voltage method with pulsed currents has been widely used to monitor the junction temperature (T_j) of LEDs. However, this method suffers from a thermal transient effect (TTE) resulting in measurement errors. Using Thermoelectric (TE) physics this phenomena was explained and a group of experiments was used to study the TTE in T_j measurements for high-voltage (HV) LEDs. The measurement uncertainty was more than ± 10 °C which is not acceptable for accurate monitoring. Therefore, an improved Pulse-free Direct Junction Temperature Measurement (DJTM) method was applied to HV LEDs to reduce the errors and to achieve an accurate in situ T_j measurement using DC currents. This also resulted in a simpler setup and a simpler measurement sequence.

Although the T_j is the most relevant temperature to know, the LED package or case temperature is much easier to measure and apply. The case temperature is a very good alternative to the T_j. If the temperature sensors are positioned well, the sensor temperature will be nearly equal to T_j. Besides monitoring the temperature through a sensor, it can be used to control active cooling solutions. A micro-electro-mechanical-system (MEMS) based, temperature triggered, switch was developed as a cost-effective solution for smart cooling control in SSL systems. The switch was embedded in a silicon substrate and fabricated with a single-mask 3D micro-machining process. The device switched on at a designed temperature threshold with a small contact resistance, and switched off when the temperature drops below that limit. Through the embedded MEMS switch, an automatic temperature controller was obtained without adding electrical components to the package. As standard

semiconductor manufacturing processes are used, integration and fabrication in future silicon based SSL systems is expected to be straight forward.

Now that the thermal management design considering heat and light, using in situ temperature sensors, can be correctly applied, there is still a need for novel cooling solutions. Among the cooling solutions, the traditional package-TIM-heatsink (TIM: Thermal Interface Material) structure has already reached its cooling limit because (i) The low heat transfer coefficient by natural convection cannot be improved without extra volume and weight of heat sink, whereas the force convection is not preferred by the extra energy; (ii) Materials with higher thermal conductivity are too expensive; (iii) TIMs suffer from limited reliability; and (iv) the normal thermal conductive materials are opaque which hinder lights and thus limits the area of application in LED products. Apart from the current thermal solutions of SSL system, liquid cooling may enhance thermal management with simple structure, transparency and small weight as it can replace the same volume of traditional metallic heat sinks. Furthermore, liquids can also act as a heat transporter and thus out-class solids in their heat removal capacity. Liquid cooling has already been successfully applied in many (high end) semiconductor microelectronic applications. Therefore it is an ideal candidate to be used in LEDs. In order to exploit the transport capabilities of liquids, a driving force to move the fluid must be installed in the cooling circuit. This “pump” must be cost-effective and small in size. Two types of liquid drivers that are small in volume, which is used for cooling microelectronic devices, are investigated: a pump and heat pipe (HP).

The phase change from liquid to vapor can be used as a driving force to move the fluid in a cooling system. Based on this principle, a cooling solution on MEMS technology was presented. A test vehicle was constructed consisting of a miniaturized evaporator with a fluid channel and an embedded bulk silicon temperature sensor. A commercial HP LED package was mounted on the evaporator, with the goal to achieve maximum light output using a very small coolant flow rate. Results showed that the package obtained high efficiency and correspondingly increased light output by the two-phase cooling. The phase transition of coolant allowed the package temperature to remain below 115 °C with LED power up to 2.8 W, as compared to less than 1.5 W under conventional circumstances. Additionally, via numerical simulation the phase change phenomenon and temperature distribution inside the evaporator was further investigated and optimized water flow rates for specific input powers of the package were calculated.

Micro or micro-wick heat pipes (HPs) have received considerable attraction in the past decades especially for cooling of electronics in a limited volume. Among the HPs, the micro HP (MHP) and loop HP (LHP) with micro wicks are most preferred for their high efficiency, small dimension, and compatible process with semiconductor devices. Especially, the LHP possess all the main advantages of traditional HPs and next to that they can transfer heat over distances up to several meters at any orientation in the gravity field. Although silicon is one the most favorable materials for MHP and LHPs, polymer based MHP and LHPs are very attractive for further investigation. Therefore, a package, using a silicon substrate with temperature sensors and a polymer based LHP was designed, manufactured and assembled. This package was able to provide low and relatively stable temperature, enabling higher optical power, more luminous flux and less color shift.

Whatever cooling configuration is made, a constant element is the heat sink, which eventually dissipates the heat to the ambient environment. Thus, the heat sink design is essential but it needs a case by case approach. Using a thermal design of vertical fin arrays with HPs as passive cooling the design methodology was demonstrated. The HPs may be converted into active/passive liquid cooling as presented previously. As the natural convection and radiation dominate heat transfer in this case, the optimum vertical fin spacing, which is the critical parameter for natural convection, was calculated by the most used empirical correlations. In addition, the fin spacing was further numerical investigated and optimized using Computational Fluid Dynamics (CFD). The design was verified by building a prototype and the experimental and numerical results correlated well. The achieved results show the HPs supply good equivalent thermal conductivity with less weight and volume compared to copper or aluminum base. Furthermore, the HP (liquid cooling) enhanced the natural convection by high thermal conductivity and less obstruction to air flow.

Samenvatting

Solid-State Lighting (SSL), aangedreven door Licht Emitterende Diodes (LED's), is een energie-efficiënte technologie voor de verlichting. Op GaN gebaseerde LED's met blauw licht uitstralende InGaN quantum wells gecombineerd met een breed spectrum geel uitstralende fosfor materiaal, zoals YAG:Ce^{3+}, worden meestal gebruikt om wit licht te produceren. In tegenstelling tot gloeilampen die een hoog rendement bij hoge temperaturen bereiken, wordt het hoogste rendement van LED's bereikt bij lage temperaturen. Dit introduceert een nieuwe uitdaging voor zowel optische ontwerpers die de thermische structuur moet meenemen en de thermische ontwerpers die het licht ontwerp moet meenemen. Daarmee is de warmtehuishouding in LED-producten een belangrijke ontwerp parameter geworden omdat de bedrijfstemperatuur rechtstreeks de maximale lichtopbrengst, kwaliteit, betrouwbaarheid en levensduur beïnvloedt.

Momenteel wordt het thermische pad binnen een LED-product ontworpen vanaf de chip naar het koellichaam, waarna de warmte aan de omgeving wordt afgevoerd door convectie en straling. Daar het elektrische ingangsvermogen wordt verhoogd, stijgt de vermogensdichtheid van high-power/high-brightness LED's met als gevolg een stijgende warmteontwikkeling in de chip. Als geen tegenmaatregelen worden genomen stijgt daarmee de LED temperatuur. Oplossing worden gezocht in optimalisatie van het thermische pad, materialen met betere thermische geleiding en verhoging van de convectie- en stralingsoverdracht. Twee vragen staan daarbij centraal: Ten eerste, welke temperatuur is nodig voor de optimale lichtopbrengst? Ten tweede, welke temperatuur is nodig voor een efficiënte warmtehuishouding met, minimaal materiaal en energie verbruik en welke het lichtbeeld niet verstoord. De eerste vraag kan worden beantwoord met "hoe lager de temperatuur des te hoger de lichtopbrengst". Voor de tweede vraag geldt dat een grote temperatuurgradiënt een grote warmtestroom veroorzaakt die de overtollige warmte kan afvoeren in een eenvoudige constructie. Dit betekent dat een hoge LED temperatuur gunstiger is. Dit is in tegenspraak met de eerste vraag. De warmtehuishouding van SSL gaat dus niet alleen om de LED af te koelen, maar ook om een stabiele en acceptabele temperatuur te bereiken voor een optimale licht kwaliteit, eventueel met inzet van in situ-monitoring, met inzet van minder gewicht, eenvoudige verwerkbaarheid, minder energieverbruik en een betere lichtkwaliteit.

Een LED product bevat twee belangrijke warmtebronnen, namelijk de LED chip en de fosfor laag. De overtollige warmte in de chip komt voort uit de conversie van elektrische energie naar blauw licht en in de fosfor laag door de conversie van blauw licht naar geel licht. De conversie efficiëntie is in beide gevallen afhankelijk van de temperatuur. Daarmee is de temperatuur de belangrijkste parameter zowel thermische en optisch gezien. Om de optimale bedrijfstemperatuur van een LED product te kunnen bepalen is een elektrisch-thermisch-lumen-chromatisch (E-T-L-C) model ontwikkeld welke de licht prestaties bepaald als functie van de in-situ temperatuur (T) als gevolg van de elektrische input (E). Omdat de conversie efficiëntie van de chip en fosfor verschilt, hangt zowel de flux (L) als het spectrum (C) af van de temperatuur. Het model is succesvol gevalideerd aan de hand van drie commercieel verkrijgbare LED producten. Tot slot, is hetzelfde model gebruikt voor het karakteriseren van de effecten van variaties in dikte en deeltjes verdeling van de fosforlaag op de thermische prestatie en licht kwaliteit.

Omdat de temperatuur de bepalende factor is voor zowel de licht prestaties als de warmtehuishouding, is een goede bepaling van de temperatuur essentieel. Daarvoor wordt in het algemeen de diodedoorlaatspanning methode met gepulseerde stromen gebruikt om de diode-junctie temperatuur (T_j) van de LED te bepalen. Helaas bevat deze transiënte thermische effecten (TTE) welke meetfouten kunnen introduceren. Via een thermo-elektrische (TE) beschouwing is dit verschijnsel verklaard. Via een set van experimenten is de TTE tijdens de T_j meting voor hoog-voltage (HV) LED's bepaald. De onzekerheid in de meting was meer dan ±10°C, wat een niet aanvaardbare marge is voor nauwkeurige metingen. Een verbeterde methode is gevonden in een Puls-vrije Directe Junctie Temperatuur Meting (DJTM) welke is toegepast op HV- LEDs. De fouten te zijn verminderd en een nauwkeurige in situ T_j meting via DC stromen is gerealiseerd in een opstelling met een eenvoudigere meet sequens.

Alhoewel de T_j de meest relevante temperatuur is, is de temperatuur van het LED substraat of package veel eenvoudiger te meten en toe te passen. De behuizing temperatuur is een goed alternatief voor de T_j. Als de temperatuursensor goed gepositioneerd is, dan is de sensor temperatuur nagenoeg gelijk aan de T_j. Naast het meten van de temperatuur, kan de sensor ook worden gebruikt om actieve koeling oplossingen te regelen. Een temperatuurgevoelige micro-mechanische schakelaar (MEMS), werd ontwikkeld als een kosteneffectieve oplossing voor slimme koelregelaars in SSL -systemen. De schakelaar werd ingebouwd in een silicium

substraat en gefabriceerd via één-masker 3D micro-mechanisch bewerkingsproces. De schakelaar wordt op de ontworpen temperatuur drempel ingeschakeld met een kleine contactweerstand en weer uitgeschakeld onder die temperatuur grens. Door de geïntegreerde MEMS schakelaar is een automatische temperatuurregelaar gerealiseerd zonder de toevoeging van extra elektronische componenten in de LED package. Het gebruikte halfgeleider fabricageproces is standaard en geeft de mogelijkheid tot integratie in de fabricage van toekomstige silicium gebaseerde SSL systemen.

Nu het ontwerp van de warmtehuishouding met in acht name van warmte en licht, met gebruik van in-situ temperatuursensoren, kan worden toegepast, is het nog steeds nodig om nieuwe koeloplossingen te creëren. Van de koeloplossingen, hebben de traditionele package-TIM-heatsink (TIM: thermische interface materiaal) al hun limiet bereikt omdat (i) de warmteoverdracht via natuurlijke convectie niet kan worden verbeterd zonder het volume of gewicht van de heatsink te vergroten, terwijl de toepassing van geforceerde convectie geen voorkeur heeft vanwege het extra energieverbruik; (ii) materialen met hogere thermische geleiding over het algemeen te duur zijn; (iii) TIM's gepaard gaan met een verminderde betrouwbaarheid; (iv) de meeste thermisch geleidende materialen ondoorzichtig zijn, waardoor ze slechts beperkt ingezet kunnen worden in het volume van het LED product. Naast de conventionele koeloplossingen, kan een op vloeistof gebaseerde koeling de warmtehuishouding verbeteren met een eenvoudige, transparante, lichtgewicht constructie binnen hetzelfde volume als traditionele koeloplossingen. Bovendien kan een vloeistof via stroming van de vloeistof de warmte transporteren en daarmee de vaste stoffen verslaan in de warmte transport capaciteit. Daarnaast is vloeistofkoeling ook al succesvol toegepast in diverse (high end) halfgeleider elektronica. Daarom is het een ideale kandidaat om in combinatie met LED's te worden gebruikt. Om de transport eigenschappen van vloeistoffen te kunnen gebruiken is een drijvende kracht nodig om de vloeistof te bewegen. Deze "pomp" moet kosteneffectief en klein zijn. Twee typen kleine "pompen", die voor de koeling van micro-elektronica worden gebruikt, zijn onderzocht: een pomp en een warmtepijp (HP).

De faseovergang van vloeistof naar damp kan dienen als drijvende kracht om de vloeistof te verplaatsen in een koelsysteem. Een MEMS gebaseerd systeem dat dit principe gebruikt is gepresenteerd. Een testsysteem was samengesteld die bestaat uit een geminiaturiseerde verdamper met een vloeistof kanaal en een ingebouwde bulk silicium temperatuur sensor. Een commerciale HP LED package

is op deze verdamper gemonteerd, met als doel een maximale lichtopbrengst te realiseren met een minieme en kleine vloeistofstroom. De resultaten laten zien dat de constructie een hoge efficiëntie en corresponderende verhoogde lichtoutput heeft bij de twee-fase koeling. De fase overgang van de vloeistof zorgde ervoor dat de temperatuur onder 115 °C bleef bij een vermogen van 2.8 W van de LED, ten opzichte van 1.5 W onder normale omstandigheden. Bovendien, via numerieke simulatie is de faseovergang en temperatuurverdeling in de verdamper onderzocht en is de vloeistofstroom geoptimaliseerd voor specifieke ingangsvermogens van de constructie.

Micro en micro-wick warmtepijpen (HP) hebben de aandacht getrokken in de afgelopen decades voor de koeling van elektronica in beperkte volumes. Van de HP's, hebben de micro warmtepijp (MHP) en gesloten warmtepijp (LHP) met vleugels de voorkeur vanwege de hoge efficiëntie, de kleine afmetingen, en de compatibiliteit met het halfgeleiderfabricage proces. In het bijzonder, verenigt de LHP de voordelen van de gewone HP's met de eigenschap om los van de oriëntatie in de ruimte de warmte over afstanden van meters te kunnen transporteren. Alhoewel silicium het geprefereerde material is voor MHP's en LHP's, zijn polymere MHP en LHP zeer aantrekkelijke alternatieven om te onderzoeken. Daartoe is een LED package op basis van een silicium substraat met ingebouwde temperatuur sensoren en een polymere LHP ontworpen, gefabriceerd en geassembleerd. Dit package was in staat om een lage en relatief stabiele temperatuur te genereren, met een hoger optisch vermogen, een grotere licht flux, en lagere kleurveranderingen.

Los van de koelsysteemconfiguratie, is de heat sink een altijd aanwezig element om uiteindelijk de warmte naar de omgeving af te geven. Het heat sink ontwerp is daarom een essentieel onderdeel, dat moet worden ontworpen op basis van een specifieke case. Op basis van een verticaal vinnen array met warmtepijpen als passief koelsysteem, is de ontwerp methode gedemonstreerd. De warmtepijpen kunnen vervangen worden door actieve of passieve koelontwerpen, zoals eerder is gepresenteerd. Omdat de natuurlijke convectie en straling dominant zijn in dit geval, is de optimale verticale vin plaatsing bepaald op basis van veelgebruikte empirische correlaties, welke de kritische parameter is voor natuurlijke convectie. Bovendien, was de vin plaatsing numeriek onderzocht en geoptimaliseerd doormiddel van Computational Fluid Dynamics (CFD). Het ontwerp was geverifieerd door de bouw van een prototype waarbij de metingen goed correleerden met de experimentele

resultaten. De verkregen resultaten laten zien dan warmtepijpen een goede thermische geleiding leveren met minder gewicht in vergelijking tot koper of aluminium koellichamen. Bovendien, de heatpipe water gebaseerde koeling verbetert de natuurlijke convectie door een hoge thermische geleidbaarheid zonder bijzondere verstoring van de luchtstroom.

Contents

Summary i

Samenvatting v

Contents xi

---

1 Introduction **1**
1.1 Background 2
1.1.1 Light-emitting diodes 2
1.1.2 Design principle of thermal management for SSL 5
1.1.3 Strategic research agenda of thermal management 6
1.2 Thermal management: state of the art 9
1.2.1 Passive thermal management 9
1.2.2 Active thermal management 13
1.2.3 Radiation in thermal management 17
1.3 Liquid cooling for SSL 17
1.3.1 Active liquid cooling 18
1.3.2 Passive liquid cooling 19
1.4 Research objectives 19
1.5 Outline 20

2 Thermal design methodology for white light-emitting diodes **23**
2.1 Introduction 24
2.2 Modeling of phosphor-converted white light-emitting diodes 26
2.2.1 Electrical-thermal model 27

2.2.2 Thermal-luminous-chromatic model 29
2.3 Identification of parameters used in electrical-thermal-luminous-chromatic model 31
2.3.1 Experimental setup 31
2.3.2 Identification of SPD of chip due to current and temperature variation 33
2.3.3 Identification for spectral shift and efficiency drop as temperature rising 35
2.4 Experiment verifications 35
2.4.1 Validation using three common configurations 35
2.4.2 Prediction of color properties by changing the phosphor layer 39
2.5 Discussion 40
2.6 Conclusion 42

3 Thermal transient effect and improved junction temperature measurement 45
3.1 Introduction 46
3.2 Experiment setups and results 48
3.3 Conclusion 51

4 Temperature triggered MEMS switch for cooling control 53
4.1 Introduction 54
4.2 Design and fabrication 55
4.3 Experimental results and validation 58
4.4 Discussion 60
4.4.1 Initial stress of the complex beam 61
4.4.2 Silicon and aluminum thickness 62
4.4.3 Aluminum thickness on side surface 62
4.4.4 Surface protection 64
4.5 Conclusion 64

5 Active two-phase cooling for higher light output and increased efficiency 65
5.1 Introduction 66
5.2 Experimental setups 71
5.3 Measurement results and discussion 71
5.4 Numerical simulation and model validation for two-phase cooling . 74

5.5 Simulation results and discussion 75
5.6 Conclusion 79

6 A polymer based mini LHP with silicon substrate and temperature sensors 81

6.1 Introduction 82
6.2 Design, fabrication and assembly 83
6.2.1 Silicon layer above polymer based miniature loop heat pipe 83
6.2.2 Temperature sensors on silicon substrate 86
6.2.3 Polymer wicks and working fluids 87
6.2.4 Fabrication and assembly 88
6.3 Experimental procedures and measurement 90
6.4 Results and discussion 92
6.4.1 Temperature sensors 92
6.4.2 Performance of the polymer based miniature loop heat pipe 93
6.5 Conclusion 95

7 Design of vertical fin arrays with heat pipes 97

7.1 Introduction 98
7.2 Numerical modeling 100
7.2.1 Governing equations for air 100
7.2.2 Governing equations for solid 101
7.2.3 Solution algorithm 101
7.2.4 Boundary conditions 102
7.2.5 Thermal conductivity of the heat pipe 102
7.3 Results, comparisons and discussion 103
7.3.1 Analytical solutions 103
7.3.2 Thermal conductivity of the heat pipe 104
7.3.3 Numerical results 108
7.3.4 Experiments 110
7.4 Conclusion 112

8 Conclusions and recommendations 113

8.1 Conclusions 114
8.2 Recommendations 117

Appendices 119

A Micro or micro-wick heat pipes for electronics 119

B Numerical modeling of natural convection for SSL 151

Abbreviations 163

Nomenclature 165

Bibliography 169

Acknowledgements 185

Selected publications 189

Curriculum Vitae 191

Chapter 1

Introduction

The increasing electrical currents used to drive the high-brightness light-emitting diodes (LEDs) lead to thermal issues. Thermal management for solid-state lighting (SSL) system is a key design parameter due to the temperature will directly affect the maximum light output, quality, reliability and the lifetime.

1.1 Background

Solid-state lighting (SSL) are recognized as one of the revolutions in the history of lighting. Semiconductor light-emitting diodes (LEDs), organic light-emitting diodes (OLED), or polymer light-emitting diodes (PLED) are used as sources of illumination in SSL rather than electrical filaments, plasma, or gas. Currently, LEDs are the major sources in SSL especially in the area of general illuminations, which are mainly focused in this thesis. LEDs are identified with its high efficiency, tunable chromatic lights and long lifetime. The much improved efficiency from traditional incandescent bulb to SSL drastically decreased the overall heat of light system. However, the traditional incandescent bulbs operate relatively predictably at high temperature since the lamp characteristics and lifetime are not affected by the luminaries' structure nor there is a need for strict operating temperature requirements. Furthermore, heat can be easily dissipated in the form of radiation. In a word, the traditional light are working and relied on the high temperature. This scenario is completely different in LED technology as the operation temperature need to be strictly controlled. Besides, the indispensable electric components in SSL system cannot survive high temperature which further deteriorate the problems. Moreover, higher and higher electrical currents are needed for driving brighter LEDs and this will cause significant heat generation in SSL systems. This will have detrimental effects on the maximum light output, efficiency, quality, reliability and the lifetime. Hence, thermal management is a key design consideration in terms of their cost and performance.

1.1.1 Light-emitting diodes

In 1962, the first practical red LED was invented with a compound semiconductor alloy, gallium arsenide phosphide (GaAsP) [1]. Then the first commercial LED was developed at 0.001 lm/LED. It was exclusively applied as indicator until the mid-1990s [2]. With the development of technologies, Nakamura invented a blue Gallium Nitride (GaN) LED in 1993 [3, 4] and the first commercial white LED was developed using the blue LED in 1997 [5]. Then the SSL has the capability to generate light with very high efficiency [6]. The resulting power conversion efficiency of LED system is dramatically higher than conventional incandescent and fluorescent lamp. White light is more attractive for replacing the current light sources. The human eyes can perceive the white with the combination of blue

light and yellow light. Thus,some of the blue photons are converted into yellow by incorporating phosphor, and the white color are perceived as the converted yellow light plus the rest part of blue light [2]. The GaN-based white LEDs are the main research focus by combining blue-light-emitting Indium Gallium Nitride (InGaN) and a broad-yellow-emitting phosphor, such as YAG:Ce^{3+} [7, 8]. While other methods to generate white light is applied with mixing blue, green and red LEDs [9] or mixing of blue, green and red phosphors within one LED [10]. The white lights for illumination are defined by correlated color temperature (CCT) and the color rendering index (CRI) [2, 11].

LEDs are the evolutional lighting with its high efficiency, tunable chromatic lights and long life time [2, 12]. However, LEDs require relatively low operating temperature and much better thermal structure compared to traditional lightings which are designed to obtain high temperature. Thus, a new challenge emerged to control the temperature without hindering the lights. The internal quantum efficiencies of InGaN green LED system is around 20 - 40% and of blue LED system operating in the 40 - 60% range at typical operating current densities [2]. Yukio et al. made an improvement for blue LED with high external quantum efficiency of 75.5% [13]. The quantum efficiency of the yellow phosphor has achieved around 70% [14, 15]. So the maximum efficiency combining blue light and yellow phosphor may achieve over 50%. But the commercial used white light LED package has much lower power conversion efficiency, normally 20%~30% from electrical energy to light output. Currently, to fulfill the light output requirement which doubles every 18 to 24 month [2], LED is designed with continuously increasing input power. The high power LED is defined with the power range from 500 milliwatts to as much as 10 watts in a single package. High heat fluxes in high power LED are reported already exceeding 70 W/cm^2 currently and will go up to around 100 W/cm^2 by 2018 [16–19]. The heat accumulation in the LED package leads to a degradation of the optical performance and shortens the lifetime. The temperature rise in the chips, driver circuit and package is one of the main causes of failure. The maximum light output, quality, reliability and the lifetime of LEDs are all closely related to the temperature. Thus, thermal management has become a key reliability issue for LED module.

As the LED chip cannot work independently, components are indispensable in product to complete the electric/optical/thermal functions. The SSL system are generally divided into 5 levels as shown in Figure 1.1. Level 1 is the LED chip,

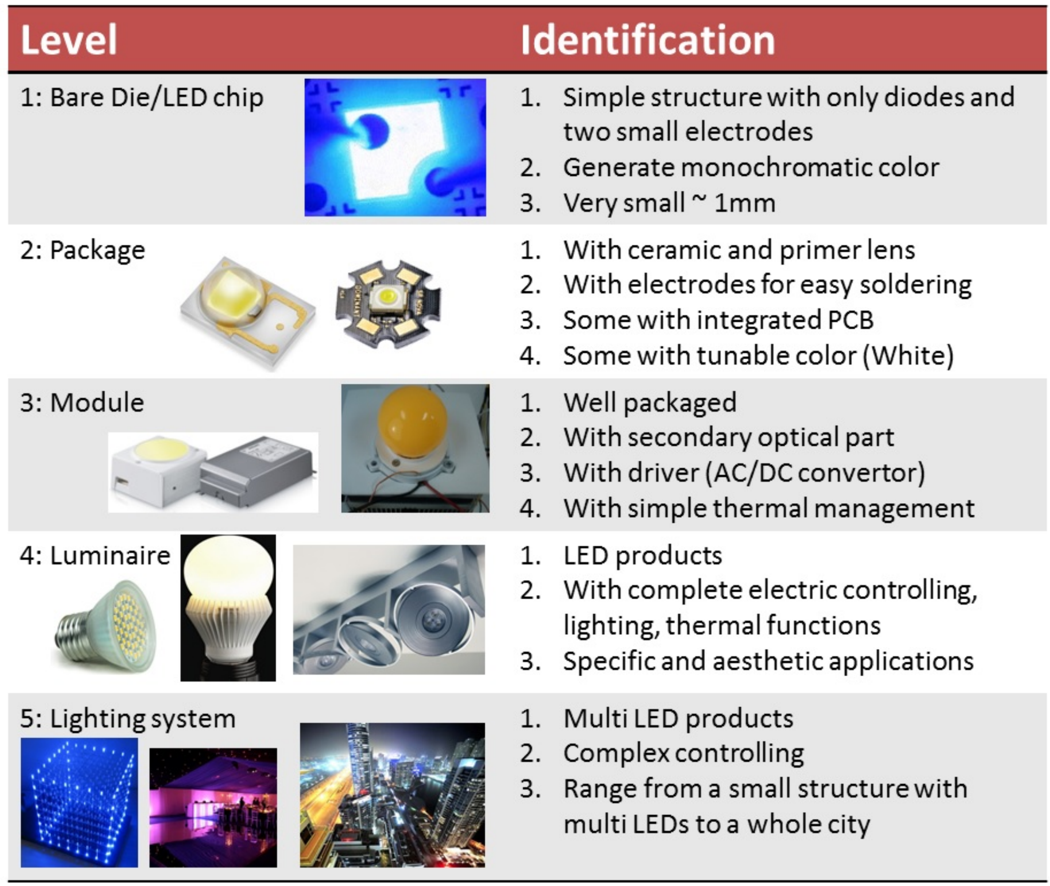

Level	Identification
1: Bare Die/LED chip	1. Simple structure with only diodes and two small electrodes 2. Generate monochromatic color 3. Very small ~ 1mm
2: Package	1. With ceramic and primer lens 2. With electrodes for easy soldering 3. Some with integrated PCB 4. Some with tunable color (White)
3: Module	1. Well packaged 2. With secondary optical part 3. With driver (AC/DC convertor) 4. With simple thermal management
4: Luminaire	1. LED products 2. With complete electric controlling, lighting, thermal functions 3. Specific and aesthetic applications
5: Lighting system	1. Multi LED products 2. Complex controlling 3. Range from a small structure with multi LEDs to a whole city

FIGURE 1.1: The definition from LED chip to SSL system.

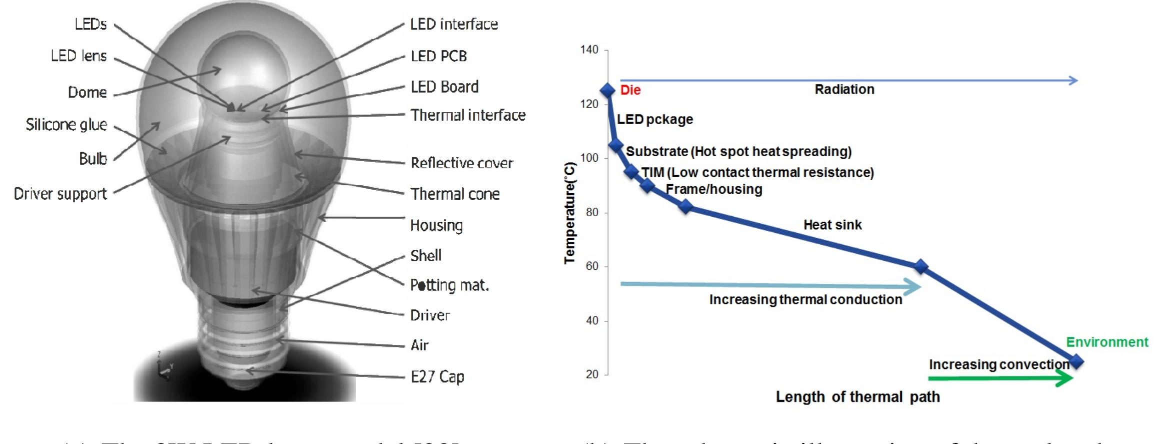

(a) The 8W LED lamp model [20]. (b) The schematic illustration of thermal path.

FIGURE 1.2: Thermal analysis for a SSL system in Level 4.

or bare die, which can only generate mono color with two electrodes for DC input. In Level 2, the chip is packaged with a ceramic protection, a primer lens is added for better light quality, and it is designed for better electric connection by soldering. Phosphors are used in some packages then the light is tunable. In Level 3, the LEDs are well packaged in a module with simple electrical/optical/thermal components

for direct usage. The LED luminaire (Level 4) is defined with complete functions for customization and designed with aesthetics. The more widely applications are considered in Level 5 with multi LED luminaries from a small 3D LED arrays to a whole city. Generally, thermal management of the SSL systems is considered during Level 2 to Level 4.

1.1.2 Design principle of thermal management for SSL

Although the thermal management of SSL systems is considered during Level 2 to Level 4, the boundaries are always ambiguous. Actually, thermal management is considered systematically or wholly in a SSL system rather than by levels. For example, Figure 1.2 shows a thermal analysis for a SSL system. This product (Level 4) which is shown in Figure 1.2(a) includes LED chips(Level 1) which is parts of LED packages (Level 2), a structure with package, driver and heat sink (Level 3). However, thermal management can not divided into those levels. As shown in Figure 1.2(b), heat is generated by LEDs/bare die, conducted by packages and the heat spreader to heat sink and finally dissipated into environment continuously. The horizontal axis is the dimension of the thermal path which also refers to the dimensions of the components. The thermal strategy here is to obtain fast heat spreading on substrate, lower thermal resistance on thermal interface and higher temperature gradient between the surface of heat sink and ambient. And the higher heat sink temperature with larger surface area can then enhance the natural convection. Besides, thermal radiation occurs as the solid surface temperature differs to the environment and is affected by the surface materials and area.

Although the LEDs are kind of semiconductors, thermal management of SSL system is not the same as thermal management of semiconductors. As the light performance is critical, thermal management of SSL systems are defined as follows in this thesis:

- Remove the heat from LED chip to heat spreader/sink by conduction, and then to environment by convection and radiation.
- Find out the best thermal strategy for specific applications with consideration both thermal and optical performance.
- Monitor and control the temperature in situ during designing, testing and applying.

- Utilize maximum surface for convection and radiation as much as possible without hindering the light.
- Achieve stable and acceptable temperature with temperature monitoring, less weight, easy fabrication, less energy consumption and better light quality.

1.1.3 Strategic research agenda of thermal management

1.1.3.1 Advanced Thermal Management of LED Packages

With increased LED wall plug efficiency, the device will definitely be well controlled at low temperatures. White LEDs has quickly matched and overtook the efficacy of standard incandescent lighting systems since 2002. Light output of white light LEDs raised from 20 lm/W to 160 lm/W. Meanwhile, heat generated by the device dropped from 0.97 W/W to 0.76 W/W. The thermal management requires a high efficiency and consequently a low junction temperature.

Currently, the thermal path within a LED package is designed from the die to the heat sink. It is one-dimensional in nature. Therefore, insufficient for heat dissipation for certain application. Hence, three dimensional thermal management architectures are needed. A number of technologies to enable three dimensional flow of heat are available from the semiconductor industry:

- Thermal vias, which dramatically increase the heat transfer rate within FR4 boards.
- Other materials, like ceramics and/or metal core printed circuit boards (MC-PCBs) which have achieved thermal conductivity values of 400 W/mK.
- Monitor and control the temperature in situ during designing, testing and applying.
- The structure, materials and dimension of the thermal management architecture are all critical for efficient heat transfer. But the design also needs to comprise with other important functions such as the optical part, the driver and the reliability performance. Very high thermal conductivity materials may not be the most suitable material.

1.1.3.2 Novel Architectures for SSL Systems

Due to the many levels within SSL systems, a typical product will have many layers or interfaces which could be the bottleneck for thermal reliability. This is due to the mismatch of material properties, such as the coefficient of thermal expansion, within these layers. The mismatch may induce significant thermal stresses which will in turn induce failure of the system. Furthermore, the differences in thermal conductivity values between these layers will also induce thermal hot spots which will also has detrimental effect on the system reliability performance. Although cooling is widely researched, especially for the electronic packaging industry, the efficiency of the current methodologies is currently still insufficient for SSL systems mainly due to:

- The high heat concentration within the LED packages.
- Low effectiveness of heat sink designs since its architecture is often restricted by the maximum allowable dimensions and costs.
- The bottleneck is the heat transfer from heat sinks to environment which reached the limitation by current structure with natural convection.
- Low thermal conductivity of the materials used due to the cost issues.

To solve the above, the lighting industry is in great need for thermal breakthroughs (without compromising the reliability performance) in the area of:

- Cost effective and high conductivity materials for heat sinks (for example thermal plastics).
- Cost effective innovative novel cooling technologies such as micro heat pipes.
- Out-of-the-box thermal architectures that remove excess layers between the LED package and the system.
- Improved thermal efficiencies by minimizing temperature rise through innovative thermal management strategies or perhaps by reducing the thermal sensitivity of the LED package itself.
- Low-cost integrated thermal management techniques to i) protect the LED source but maintain the luminaire efficiency and color quality and ii) to extract heat from the luminaire in a variety of environments and operating conditions.

1.1.3.3 Design for thermal management tools

Thermal analysis with mass, energy, momentum conservation equation are currently developed for LED packages. The results have relative low accuracy and, thus, three dimensional design tools like FEM and CFD are currently used in the design of new SSL systems. These numerical simulations can solve the thermal performance of SSL systems with thermal conductivity, convection and radiation included. The results have high accuracy and a clear visible image for architectural designers. However, such a numerical exercise needs an expert and a quite significant time effort. The challenge is to establish simple but sufficient mathematical models with reasonable assumptions and simplifications that can mimic the temperature distribution in a SSL system.

1.1.3.4 Standardization

Standard LED package measurements use relatively short pulses of current to eliminate thermal effects, keeping the device at 25 °C (or other controlled point). In standard operation, however, the LED is driven under continuous wave conditions. Under these conditions, the device operates at a case temperature typically 100 °C or so higher than room temperature at thermal equilibrium. Calibration is indispensable due to the extra pulsed source which make it tough to integrate a temperature sensor that measures the junction temperature. On a system level, either thermal couples or an IR camera are normally used for temperature measurements. Also here a calibration is required. None of the currently used temperature measurements are accessible in a standard method, although within semiconductor industry the JEDEC organisation has started some activity. Standardization of thermal measurements, be it on the LED package, a sub component such as a driver or on the system level, are crucial for the lighting industry in order to compare apples with apples. Cooperation between thermal, electrical, and optical standards is required to arrive at globally accepted thermal standards to measure junction and system reference temperatures so as to ensure a fair comparison of published performance and reliability data.

1.2 Thermal management: state of the art

1.2.1 Passive thermal management

LEDs generate light and heat by using different mechanisms as compared to the incandescent bulb. With the injection of electrical energy, the electron energy will be partly converted into light and partly into heat. Obviously the research about LED technology is focused on optimizing the light emitting efficiency. Currently, the LEDs in the market have an efficiency of about 20% to 30%. Consequently 70% to 80% of the energy is converted into heat [16, 21]. Hence, the challenge of thermal management is to conduct heat from LED package to the environment with a sufficient heat transfer rate. Figure 1.3 shows a schematic diagram of typical architecture of LED module which includes of a LED package, a thermal solution and a board for electrical and thermal connection. Although each module has a unique structure, generally the LED package consists of a LED chip enclosed in a package of a polymer lens and a plastic carrier holder.

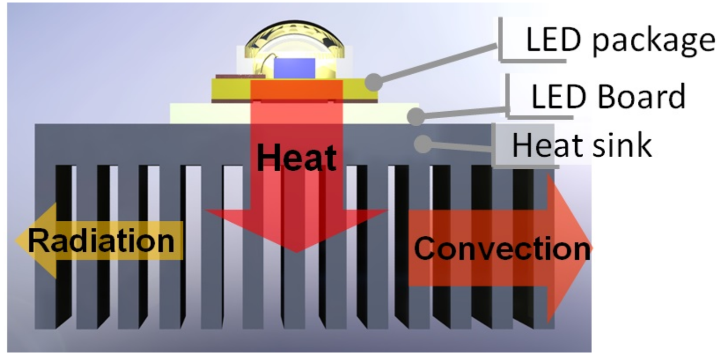

FIGURE 1.3: The schematic diagram of thermal path of LEDs.

Heat is generated by the LED chip inside the package. Although some heat can be dissipated by radiation and natural convection along the package surfaces, most of the heat will be conducted to the heat sink. The major part of heat will be transferred to environment by convection from an optimized designed heat sink. On the other hand, radiation on the surface of heat sink occurs naturally and it cannot be ignored as the average critical temperature of LED module is high [17]. The heat sink could also be replaced by other thermal solutions which include forced air cooling, HP, thermoelectric, synthetic jet flow cooling, liquid system, etc. Compared to active thermal management, passive solutions have advantages of simple structure, easy fabrication, application flexibility and low cost.

1.2.1.1 LED boards

As depicted in Figure 1.3, a LED package is mounted to a substrate. One of the most direct solutions is to use substrate which has sufficient heat conductivity to conduct the heat generated away from the LED package. In industry, printed circuit boards (PCB) are typically used to mechanically support and electrically connect LED package. The most commonly used LED board is FR4. A number of thermal vias for FR4 are essential due to its low thermal conductivity 0.23W/mK since capped or uncapped vias will dramatically increase the heat transfer rate. Meanwhile, an alternative board with high thermal conductivities could be used for better thermal performance. For example, it is very attractive for using ceramic based boards in LED module with aluminum oxide (Al_2O_3 25W/mK), aluminum nitride (ALN 180 W/mK) and the metal core (MC) PCB using copper with 15 W/mK thin dielectric isolation layer [22]. Currently, the MCPCB has the best optimal performance to cost ratio.

1.2.1.2 Passive thermal solutions

A package with a board is the typically current structure of LED module. This structure has to be mounted to a thermal solution for heat dissipating. With the advantages of simple structure and low cost, the passive cooling methods are always preferred. Generally, the passive thermal solutions could be categorized by the mechanisms for removing heat to the environment.

TABLE 1.1: The passive thermal solution for microelectronics devices [23].

Categories	Typical application	Normal load (W)	Cost at 10,000 pieces($)
Heat sink	Plate fin Pin fin	5-50	0.5-10
Phase change recirculation	Heat pipe Vapor chamber	100-150	15-100

*Passive Heat Sink:*It is the basic passive thermal solution which is designed without air flows. The performance of heat sink is relative to various factors under the consideration of natural convection and radiation.

*Phase change recirculation system:*The principle of this system is to conduct heat away from the critical part through phase change at the high temperature region and

reverse phase change at the lower temperature region. The liquid vapor cycle which will be discussed in this study is typically used. Moreover, these phase change systems still need to be connected to heat sinks. Table 1.1 shows the typical range of cost and thermal load for passive solutions of microelectronics which is very similar to LEDs [23]. Currently high-brightness LEDs used 5 to 10 W for small applications and even more than 20 W for larger system designs. Thus, the passive heat sinks should be theoretically sufficient for thermal management of current LED module with low energy consumption less than 50 W. According to the much lower cost compared to HPs, heat sinks are the most widely used type of passive cooling device.

Passive heat sink

In thermal management of LED module, the heat needs to be transferred to the environment, mostly via heat sink, through natural convection and radiation. Natural convection varies from situation to situation depending on the conditions of fluid flow, the structure of heat sink and the mode of fluid flow. Designing methodology of heat sink has been well outlined in many researches. In the design routine, air flow scheme, chimney effects, surface radiation and boundary layer developments need to be taken into consideration.

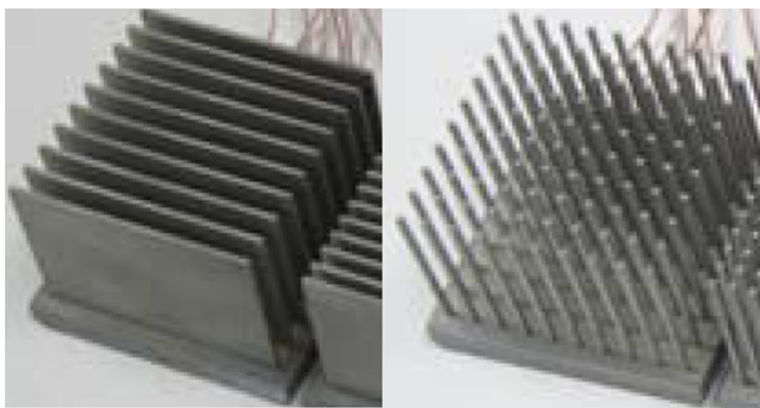

FIGURE 1.4: The plate-fin and pin-fin heat sinks [24].

Figure 1.4 shows the two common types of heat sinks which are widely use in the industry [24]. The parameters need to determine the optimum performance within a set of design constraints which typically include: fin length, fin thickness, fin number, base thickness, material, etc. Iyengar et al. [25] have investigated the optimum parameters for plate and pin fins and their results show that pin-fin type is a superior thermal solution. The design for heat sink is not only depend on the architectures but also the materials. The materials with low cost, low density, high

thermal conductivity and high surface area are very attractive. One example is that Oak Ridge National Laboratory ORNL recently managed to fabrication carbon foam heat sink which has excellent thermal properties at a relatively low cost [26].

Phase change recirculation system

Heat pipe (HP) is one of phase change recirculation systems, which is normally used as interconnect base between the heat sources and fins in passive thermal solution. The pipe dimension, structure and orientation will directly decide their efficiency. Table 1.2 shows the thermal performance of horizontal orientation HP and conventional materials [27]. For a 10W electronics packaging, the HP has advantages of low thermal resistance and intermediate density comparing with the same geometry of aluminum and copper plate. Another major consideration

TABLE 1.2: The thermal performance of heat pipe, aluminum and copper plate for electronics packaging of 10W [27].

	Density (kg/m3)	Thermal conductivity (W/mK)	Thermal resistance (K/W)
Aluminum	2780	240	6
Copper	8330	380	2.3
Heat pipe	4440	25000(effective value for vapor passage)	1.2

in HP is the selection of working liquid as it is directly responsible for the heat transfer capability. Acetone, methanol, ethanol and water are suitable for electronic application at the temperature range from 0 to 100 °C [28]. For improving the heat transfer properties, investigations have shown that nanofluids consisting of nanoparticles exhibit significantly improvement of thermal conductivity in HP [29, 30]. With the high thermal conductivity and relatively low density, HP is quite an efficient passive cooling solution for high power LEDs. Lu et al. [31] implemented the concept of the HP with natural convection for LED module and the results show that the junction temperature can be controlled steadily to less than 100 °C for heat load of 100 W. Kim et al. [32] report the thermal characterization of high power LED arrays with HP as well. Micro HP (MHP) and vapor chamber (VC) have the same principle as HPs. They have already been tested on the semiconductor materials to enhance the thermal performance of silicon and they are found to be very suitable for high-brightness LEDs. One experiment by Berre et al. [33] show a maximum improvement of up to 300% in effective thermal conductivity by the

application of MHP with liquid arteries in silicon. In addition, Wu et al. [34] have studied the VC can significantly improve thermal permeance of heat sinks up to 20% to 40% as compared with the solid copper bases.

1.2.1.3 Thermal interface materials

In order to minimize the thermal resistance, thermal interface materials (TIMs) are essential to apply to connect different components of LED module. Studies show 60% of the thermal resistance of a system is in TIMs [35]. For potential implementation of LED module, Zweben [36] lists serial low or potential to be low cost high thermal conductivity materials with low coefficient of thermal expansion as shown in Figure 1.5.

The boron nitride (BN) is the widely used as TIMs in electronics. Compared to BN, some of other materials are very competitive with their high thermal conductivity and acceptable price. Since thermal management problem is not unique to LEDs and there is a certain similarity between electronic packages and LED packages, materials used in semiconductor industry have a high potential to improve the thermal performance of the LEDs. One potential material in consideration is the carbon nanotubes which have experimentally determined heat conductivities of about 500 - 3000 W/mK for a multi-wall carbon nanotube (MWNT) and about 3500 W/mK for a single wall carbon nanotube (SWNT) [37]. In addition, graphene has the advantages of the ease for silicon integration and extremely high thermal conductivity in the range of 3080 to 5150 W/mK [38], which has high possibility for thermal management in future nanoelectronic circuit and LED applications.

1.2.2 Active thermal management

The passive cooling is the fundamental part of active thermal managements, as the heat spreader and heat sink are also used in active cooling. The active cooling can improve thermal management by mainly enhancing the conduction of heat spreader and convection between air and solid surface. However, more power is consumed and possible less reliable components have to be added. Thus, to identify the situation when active cooling is required are necessary. Lasance [39] has reported the order of magnitude for heat transfer coefficients depending on cooling

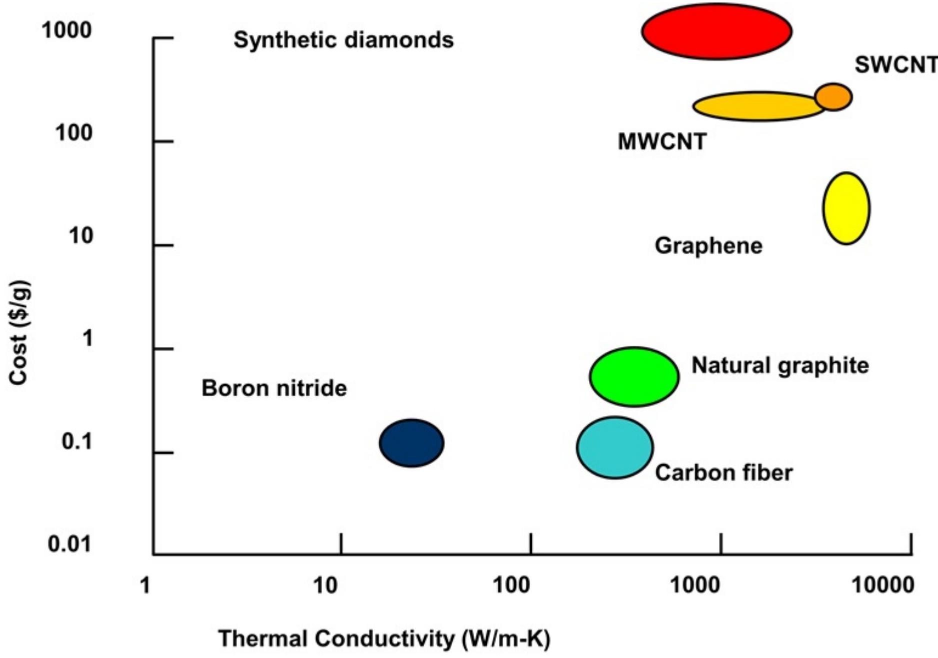

FIGURE 1.5: The cost functions of high thermal conductivity materials [36].

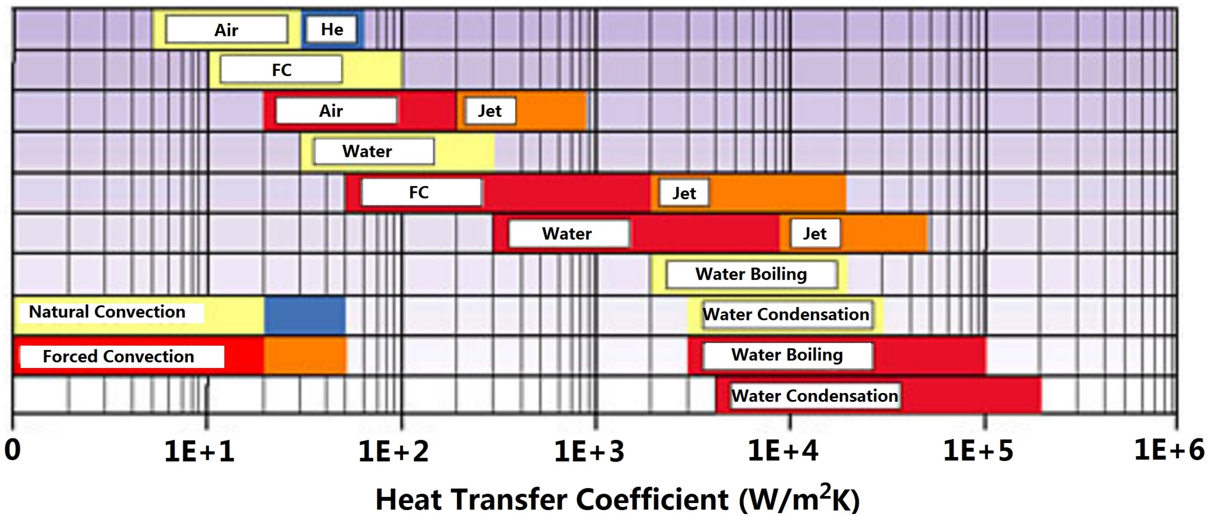

FIGURE 1.6: The order of magnitude for heat transfer coefficients depending on cooling technology [39].

technology as shown in Figure 1.6.The forced air and liquid cooling are always performing better than passive ones.

1.2.2.1 Enhanced thermal conductivity

In thermal management, thermal conductivity is the main path to transfer the heat from small heat source to a larger heat spreader. Then heat from the heat spreader moves to heat sink which is the heat exchanger between solid and environment. Normally, high thermal conductive materials are preferred which is reliable passive cooling solution. However, as the high power density in some devices, the junction temperature become very high then the passive cooling cannot perform well. There are two kinds of materials can enhance the thermal conductivity: solid-state and liquid.

Solid-state materials for enhanced thermal conductivity

As the most known solid-state cooling, thermoelectric effect (TE) was discovered in 1834 by Jean Peltier describing cool of the junction of two different conducting materials when appropriate electric current is applied. One experiment measurement achieves a maximum cooling of 1.2 °C on a $40 \times 40\ \mu m^2$ TE micro cooler [40]. A recent numerical simulation results shows maximum temperature reduction of 3.03 °C for a $70 \times 70\ \mu m^2$ hot spot with 700 W/cm^2 heat flux. The variety of geometric and operating conditions will determine the temperature reduction. Moreover, the conclusion from the results deduces that larger hot spot size and higher hot spot heat flux result in larger temperature reductions [41]. TE is suitable for thermal management of LED package and keeps a steady temperature situation with its small size and fast response time. Chun et al. [42] applied a new thermal management approach of silicon-based TE cooler integrated with high-power LED. The TE cooler directly connects the LED package and heat sink. With a low TE cooler input power of 0.55 W, the junction-to-case thermal resistance can be effectively reduced to zero.

Liquids for enhanced thermal conductivity

Liquid cooling can enhance thermal management with flexible structure, transparency and small weight as it can replace the same volume of traditional metallic heat sinks. Furthermore, liquid can remove the heat rather than conduct it which performs as better ”thermal conductivity” than solid [37, 43]. Liquid can directly connect the LED product from Level 2 (even Level 1) to Level 4 with much less TIMs. Liquid cooling has already been successfully applied in many semiconductor microelectronic applications [44] and would be easily used in LEDs. With exception

of leakage and reliability, the driving force is major obstacle for setting the liquid cooling in the limited volume of LED product. Generally, small volume of liquid can be mainly driven by: micro-pump and HP. The MHP reached an effective thermal conductivity of 600 W/mK for cooling of electronics consisting in a series of 55 parallel triangular shaped channels [33]. With the pumps, the liquids can drastically increase the thermal conductivity. Besides, the refrigeration system can also be applied for SSL system as active liquid cooling.

1.2.2.2 Enhanced convection

Forced air for enhanced convection

As the heat is finally transported into environment by convection, forced air cooling are always better than the passive ones. As the forced air can obtain very fast flow speed, the heat transfer between solid and gas are very fast which is widely used on semiconductor. The heat sink used for forced air cooling can be designed with very small spacing between fins to enlarge the surface area. New materials such as carbon foam are attractive for active air cooling with its low density, high thermal conductivity (between 40 and 180 W/mK) and high surface area. One process for the carbon foam fabrication developed by Oak ridge National Laboratory (ORNL) has excellent thermal properties and relatively low cost [26]. Although the thermal effect of carbon foam in passive cooling system still needs to discuss due to the low fluid velocity in natural convection, this kind of heat sink made by carbon foam dissipates much more heat than the traditional materials with much higher heat transfer coefficients by the forced convection.

Forced liquid for enhanced convection

Liquid has been introduced for enhanced thermal conductivity, which is applied in a closed system without mass loss. Liquid can also be used to enhance the convection between solid and environment and can obtain better convection coefficient than gas. However, there is not always liquid existing in the ambient with exception of man-made environment.

1.2.3 Radiation in thermal management

As the other major thermal path from solid surface to environment, thermal radiation take an importance factor especially in the case of SSL system with natural convection as the operation heat sink with temperature around 60 to 80 °C. The thermal radiation cannot be simply neglected, which typically accounts for 25% of the total heat dissipated by natural convection finned heat sink [45]. However, the designing on thermal radiation is not simple work.

- The large area cannot obtain higher thermal radiation between the fins. Khor et al. [46] concluded the errors induced are more than 30% when thermal radiation is neglected, and exceed 60% when thermal radiation is considered without including view factor.
- The higher surface temperature can dramatically enhance thermal radiation but it depends on the reliability of SSL.
- The emissivity of surface materials is the only simple design factor which varies from 0 to 1.

1.3 Liquid cooling for SSL

Liquid cooling can enhance thermal management with simple structure, transparency and small weight [47] as it can replace the same volume of traditional metallic heat sinks, which is mainly driven by: micro-pump and HP. Several micro-pumps have been introduced by Gravesen et al. [48], but they all require extra electric energy which might deviate from the slogan of ”high efficiency” of LEDs. Therefore, the HP which is driven by the waste heat is more appealing. Especially, the loop HP (LHP) possess all the main advantages of traditional HPs, but obtain special properties to transfer heat for distances up to several meters at any orientation in the gravity field [49, 50]. Polymer can be one of the best materials to achieve easy fabrication, light weight and transparency for thermal management of LEDs. Besides, the normal operation temperature ranges of thermo plastics are quite close to SSL systems. However, poor thermal conductivity limited the applications until the combinations of polymer and liquid cooling were first reported. In 2001, McDaniels and Peterson [51] presented analytical modeling and

estimated the thermal conductivity of a flat, flexible, polymer HP with a grooved wicking structure to be approximately 740 W/mK. A design of MHP channels with polypropylene consists of flexible rectangular or trapezoidal micro channels fabricated with methanol and ethanol as the working fluids was investigated [52]. Then, Oshman et al. [53] fabricated a HP on a flexible liquid crystal polymer substrate using micro-machining techniques compatible with printed circuit board technologies. The device transfers up to 12 W of power with an effective thermal conductivity of up to 830 W/mK.

1.3.1 Active liquid cooling

Active cooling uses pump to drive liquid to channels which enhance the heat transfer between liquid and solid [54–57]. However, active cooling systems cause additional power consumption. In order to obtain less power input, active liquid cooling were improved mainly by two ways: i) smart controls and ii) larger interface between solid and liquid.

Smart controls, e.g. switching on the active cooling only when the temperature exceeds a certain threshold, were applied. Takikawa et al. [58] invented mechanical temperature controlled device with liquid coolant technologies for electronics cooling, and Dinh and Korinsky [59] applied temperature-dependent fan control circuit for personal computer. Such solutions required relatively complex mechanic designs as well as many additional components, including temperature sensor, readout and control circuits (together with its DC power supply). This consequently increased the complexity and cost of the lighting system. It is therefore essential to look for a much simpler and cost-effective alternative solution for smart cooling control.

Recently, micro-structured silicon wafers have been used as substrates for the LED packaging, due to their good thermal conduction and larger contact surface due to the micro process [42, 60–62]. Beside this advantage, silicon substrates are ideal for integration of micro-electro-mechanical systems (MEMS), sensors and actuators. Ye et al. [47] has successfully integrated a temperature sensor and liquid cooling channel on silicon substrate to monitor and to control the temperature of a LED package assembled on the silicon substrate. Therefore, silicon wafers, together with the advanced micro-machining technology, are highly potential solutions in smart system integration for SSL applications.

1.3.2 Passive liquid cooling

Micro or micro-wick HPs have received considerable attention in the past decades especially for cooling of electronics which requires removing the increasing heat from a limited volume to environment. Among the HPs, MHP and LHP with micro wicks are most preferred for their high efficiency, small dimension, and compatible process with semiconductor devices. Silicon is highlighted as one the most favorable materials for MHP as well as LHPs. Moreover, polymer based MHP and LHPs are highly attractive for further development. And the carbon nanotube (CNT) may be the future nano wicks of HPs for their potentially outstanding characteristics. A review on the MHP and LHP including the design, analysis, and fabrication is presented in the Appendix A.

1.4 Research objectives

According to the strategic research agenda, the main objective of this thesis is to achieve optimized light performance by developing advanced cooling technologies with in situ temperature monitoring and controlling. To fulfil the goal, serval objectives need reaching step by step:

- **Designing thermal management with consideration of both heat and light** Develop a model to predict the light performance with thermal management under in-situ temperature. And the model can also answer two questions: what is the difference between the designed and actual light performance at operating temperature? What is the optimum working temperature for thermal management of SSL system with consideration of both light and heat?
- **In situ temperature monitoring and controlling** There are errors to measure the junction temperature (T_j) in traditional pulsed current method. A new T_j measurement method is needed to achieve accurate measurement and reveal the introduced errors by traditional method. Besides, the case temperature is close to T_j just under the chip position and should be sufficient for temperature controlling of LED products.
- **Cooling with enhanced optical performance, less weight, improved natural convection and radiation** A novel thermal management with simple

structure, transparency and small weight is required. Besides, the heat transfer coefficient from solid surface to environment is mainly depended on a well designed heat sink.

1.5 Outline

Thermal management for solid-state lighting (SSL) system is a key design parameter due to the temperature will directly affect the maximum light output, quality, reliability and the life time. But the current method is from the knowledge of traditional lighting or semiconductor devices. As the rapid development of SSL, more investigation and understanding on thermal management is extremely indispensable. The thesis is organized as 5 parts: state of the art, the design methodology, the temperature monitoring, the novel thermal solutions and the conclusions. **Chapter 1** views the recent development of LEDs and the principle of thermal management for SSL. But more importantly, the definition of thermal management is proposed and the strategic research agenda of thermal management is presented. The thermal management is not to cool the device to a temperature as low as possible, but to achieve the best light performance with less materials and energy consumptions.

It is clear that thermal management is important in SSL system. However, the apparent dilemma is to optimize light efficiency and effectively designing thermal management. Two questions arise: Firstly, what is the optimum temperature for maximum light performance? Secondly, what temperature leads to thermal management solutions with less weight, energy consumption, and light hindering? Thus, **Chapter 2** studies the relations between thermal management and the light performance as the light is the wanted product of LEDs. An electrical-thermal-luminous-chromatic (E-T-L-C) model was then developed to predict the light performance with thermal management under in-situ temperature. The proposed dynamic E-T-L-C model definitely benefits the design of future high-brightness LEDs for better light quality.

As the temperature is so important in the methodology, accurate temperature measurement is always required on testing and even applying. **Chapter 3** introduces a new junction temperature measurement for LEDs to reduce the errors in current used measurement. The improved Pulse-free Direct Junction Temperature

Measurement (DJTM) method was conducted for HV LEDs to reduce the errors and to achieve in situ junction temperature measurement with DC currents, simpler setups and a less step sequence. Besides, it revealed that the case temperature is close to junction temperature as the chips have always very small dimensions. That implies, the case temperature is sufficient to monitor temperatures and control the light quality on most of the SSL systems. In **Chapter 4**, a micro-electro-mechanical-system (MEMS) based, temperature triggered, switch was developed as a cost-effective solution for smart cooling control in SSL systems. The switch was embedded in a silicon substrate and fabricated with a single-mask 3D micro-machining process which can monitor and control the case temperature. The device switched on at a designed temperature threshold with a contact resistance, and switched off when the temperature drops below that limit. In this way, this device enhanced the automatic control of a cooling system without any need of additional electronic components.

As the operation temperature is designed and monitored, the thermal solutions are then developed. Liquid cooling can enhance thermal management with flexible structure, transparency and small weight as it can replace the same volume of traditional metallic heat sinks. And the liquid can directly connect the LED product from the LED package to the surface of heat sink with less TIMs. **Chapter 5** presents a cooling solution with phase change phenomenon based on micro-electromechanical (MEMS) technology. Tests were performed on a miniaturized evaporator with a fluid channel and an embedded bulk silicon temperature sensor. The proposed device is quite promising for an integrated water-based thermal management and high-power/high-brightness LED would benefit from the two-phase cooling approach.

Although the active liquid cooling can perform well with several mL/h water flow rates driven by micro pumps, they all require extra electric energy which might deviate from the slogan of ”high efficiency” of LEDs. Therefore, the heat pipe (HP) which is driven by the waste heat is more appealing. Micro or miro-wick HPs which received considerable attraction in the past decades especially for cooling of electronics were reviewed and presented. Among them, the MHP and LHP with micro wicks are most preferred for their high efficiency, small dimension, and compatible process with semiconductor devices. Especially, the LHP possess all the main advantages of traditional HPs, but obtain special properties to transfer heat for the distances up to several meters at any orientation in the gravity field. Silicon is

highlighted as one the most favorable materials for MHP as well as LHPs. Moreover, polymer based MHP and LHPs are highly attractive for further development. The details are presented in **Appendix A**.

Polymer can be one of the best materials to achieve easy fabrication, light weight and transparency for thermal management of LEDs. Besides, the normal operation temperature range of thermo plastics are quite close to SSL systems. However, poor thermal conductivity limited the applications until the combinations of polymer and liquid cooling were first reported. Thus, an innovative thermal management with a package, a silicon substrate with temperature sensors and a polymer based LHP was designed, manufactured and assembled in **Chapter 6**. It supplied a low and relatively stable temperature to maintain higher optical power, more luminous flux and less color shift.

As the liquid can directly connect the hot spot and heat sink surface, the improved "thermal conductivity" can benefit the LEDs. However, from the solid surface to environment, it is still a challenge from designing to application. In **Chapter 7**, a thermal design of vertical fin arrays with HPs as passive cooling was applied. The HPs can supply good thermal conductivity with much less weight and volume compared to copper or aluminum base and consequently less obstruction to air flow with enhanced natural convection. As the natural convection and radiation dominate heat transfer in this case, the optimum vertical fin spacing was calculated by the most used empirical correlations. Then, the design was numerically investigated by Computational Fluid Dynamics (CFD) to obtain best thermal performance. As the fin spacing was both optimized by correlations and modelling, the optimum thermal design was achieved. Finally, we manufactured and tested the design experimentally which consistently approved the thermal design compared to correlations and simulations. As supplementation, **Appendix B** introduces the methodology of natural convection simulation.

Chapter 2

Thermal design methodology for white light-emitting diodes

The drive of increased electrical currents to achieve high luminous output for Phosphor-converted White Light-Emitting Diodes (PW-LED) has led to a series of thermal problems. Spectral shift and consequent color properties change due to the increased temperature during operation were studied by a group of experiments. An electrical-thermal-luminous-chromatic (E-T-L-C) model was then developed to predict the light performance with thermal management under in-situ temperature.

2.1 Introduction

Light Emitting Diodes (LEDs) have gained widely attraction as one of future light systems with the advantages of high efficiency, tunable chromaticity and excellent reliability. The first high-brightness chip with blue light was invented by Nakamura et al. based on InGaN [3, 4]. The phosphor-converted method was developed by Bando et al. [63], and phosphor-converted white LED (PW-LED) packages were then commercialized with combination of two major complementary components: blue light chip(s) and yellow-emitting phosphors. Although LEDs are boasting for its high efficiency to generate light, still approximately 70% to 80% of the electrical energy is converted into heat in commercial packages [47]. In addition, to fulfill the light output requirement which doubles every 18 to 24 month [2], LED is designed with continuously increasing input power. A typical heat flux in high-brightness LED was reported as 100 W/cm^2 [64], and it was predicted in excess of 150 W/cm^2 heat by 2012 [17]. Nowadays, an equivalent light output density archived 300 W/cm^2 by InfiniLED's latest MicroLEDs with consequently several times larger heat fluxes. The high temperature in package will negatively affect the efficiency, light performance and reliability. Therefore, thermal management is a key design parameter for both package and system level of LEDs. Arik et al. reported thermal management concept from chip scale [19] to package and system [17] with resistance network and numerical simulation. And they concluded that a poor thermal design can lead to serious problems for both the optical efficiency and light performance. From then on, more numerical simulations and thermal resistance networks were applied to analyze the thermal performance and to give a guideline for further improved thermal solutions [65–67].

LEDs were designed for desired light and relative researches about the spectral shift due to high temperature were undergoing. As mentioned by Eliseev et al. [68, 69], the spectral shifts of the wavelength peak position of AlGaN/InGaN/GaN single-quantum-well structures were observed with the increasing temperature. Ye et al. [70] reported that blue chip efficiency decreased by 8% with increased case temperature from 30 °C to 120 °C. Besides, the spectral shifts due to phosphor in the package were reported. Zhang et al. [71] studied the well crystalline YAG:Ce^{3+} phosphors in the temperature range from room temperature to 573 K. The increased temperature negatively affected light intensity and changed the chromaticity of the white LED with as-prepared phosphors. Furthermore, works to connect electrical, thermal and light features of LED systems were conducted by Hui and Qin [72].

Their generally theory was used to determine the optimal operating point for an LED system to achieved maximum luminous flux at given thermal design. Huang and Tang [73] derived thermal-electrical-luminous model for polychromatic LED luminaries which can be used to control the lighting with designed feedback system depend on input power and junction temperature. Then, Wang et al. [74] proposed a novel control structure based on former work to regulate the color and luminous output for a RGB LED lighting system. Later, Tao and Hui added a time factor in their photo-electro-thermo-temporal theory to monitor the luminous output drop from the initial operation to the steady-state. Quite recently, Chen and Hui [75] continued to develop a tricolor spectral model with consideration of dynamic electric, thermal and spectral power distribution (SPD) for LEDs with blue die and yellow phosphor, which is declaimed as the first theoretical tool for predicting color properties of PW-LED systems.

As the interests for prediction of color shift continuously increased, the requirement of thermal management will be highly improved accordingly. In order to achieve ”thermal design for light” rather than ”thermal design for heat”, the present paper intends to derive and validate an electrical-thermal-luminous-chromatic (E-T-L-C) model for PW-LEDs differed from the previous works. Firstly, the three dimensional (3D) simulation was applied to obtain the chip and phosphor temperature with consideration of electric power input, electric-optical conversion rate, converted blue light rate and phosphor conversion rate, which is called electrical-thermal (E-T) model. Secondly, an analytic methodology was used to conduct the SPD at high operation temperature derived from the measured SPD at room temperature, which is called thermal-luminous-chromatic (T-L-C) model accordingly. The T-L-C model was established depending on the consumptions: (1) the shift SPD can be divided mathematically into two parts: energy change at each wavelength and peak wavelength shift; (2) the SPD of blue light changes with the chip temperature and the SPD of converted light are mainly affected by phosphor temperature. To identify the parameters used in the E-T-L-C model, a batch of commercial InGaN low voltage chips and several mixture samples of silicone and phosphors were tested under thermal controlled plate in an integrating sphere. In addition, the color properties of three typical commercial LED packages/modules with the InGaN chip and similar phosphors were measured at its working temperature with comparison with the analytical solutions. The comparison showed good similarity and the model was validated for application on prediction of color shift by temperature. Moreover, the color properties changed due to the converted blue light rate, which affected by

the phosphor thickness and particle density, were proved to be estimated by this model too.

2.2 Modeling of phosphor-converted white light-emitting diodes

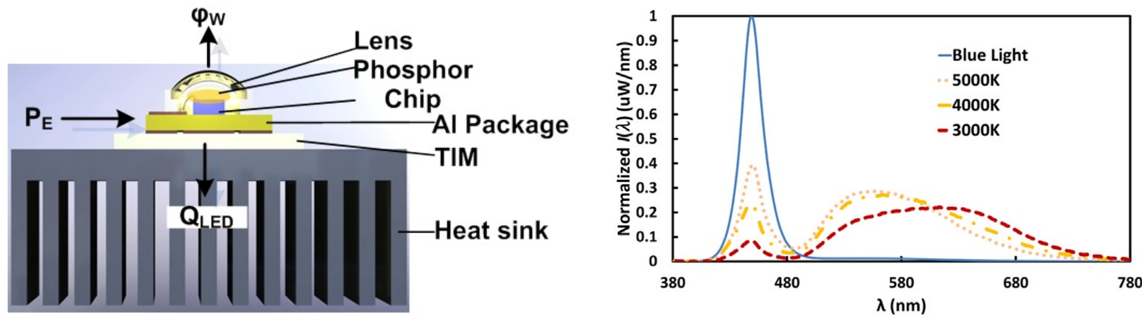

(a) Schematic diagram of high-brightness LED package/ module.

(b) Normalized spectra of blue and white light generated by LEDs and converted by phosphors.

FIGURE 2.1: The light and heat generated in LEDs.

Although heat is undesirable, the electrical energy will be converted partly into light and partly into heat in high-brightness LEDs. The E-T-L-C model thus consists of two parts: E-T model and T-L-C model which are connected by the chip and phosphor temperature as the temperatures are the key parameters. A typical architecture of the LED includes a LED package, a thermal solution and a thermal interface material (TIM) which is shown in Figure 2.1(a). And the LED package normally can be divided into four parts: a chip (generating blue light), a phosphor layer (converting blue light), a lens (distributing light) and a metal/ceramic-based package for electrical and thermal conduction. The electrical-thermal physical relationship can be expressed as:

$$P_E = \varphi_W + Q_{LED} \tag{2.1}$$

Where, P_E is the electrical energy, φ_W is the optical power of white light and Q_{LED} is the total heat generated by the chip and phosphors. Temperature distribution can be obtained by E-T model with 3D simulation from the generated heat and consequently optical power can be calculated. However, optical power cannot be sensed by human's eyes. To measure of the perceived power of light, Commission internationale de l'éclairage (CIE) defined luminous flux, correlated color temperature (CCT) and color rendering index (CRI). With consideration of color, the

brightness is related to the optical power which can be sensed by human was defined by luminous flux. The changes of white light are defined by CCT which is a function of location on the CIE curve [2] and is scaled in Kelvin with the unit symbol K. As shown in Figure 2.1(b), the chip generating blue light owns the wavelength of narrow peak around 450 nm. When phosphors are positioned in front of the chip, blue light can be partly converted and partly penetrate/leak through the phosphor layer. Thus the blue spectra drop but green and red spectra increase. The penetrated blue light mixed with the converted light to generate a kind of spectra that was perceived by human as white light. With changing the portion of blue, green and red spectra, white light LED can be manipulated in various CCTs. For example, CCT over 5,000 K are called cool white (blueish white), while lower CCT (2,700-3,000 K) are called warm white (yellowish white through red). Thus, the higher CCT denotes that more blue light is kept but lower CCT represents that more blue light is converted by phosphors. The color rendering index (CRI) is used to quantitatively measure the ability of light source in comparison with an ideal light source. Several color appearance models have been applied [76, 77], but the general color rendering index is used in this work. Therefore, the T-L-C model can be conducted according to the CIE for light analysis under its operation temperature which is predicted by the E-T model.

2.2.1 Electrical-thermal model

The E-T model is related to the heat generated in chip and phosphors of high-brightness LED from part of electrical energy and transferred to environment by thermal management. The electric-optical conversion rate (ξ_B), the converted blue light rate ($\xi_{B,conv}$) and the phosphor conversion rate ($\xi_{P,conv}$) are the key parameters to define the energy what is changed into optical power. With exception of optical power, the rest part of electrical energy will change into waste heat which is used as input for thermal simulation. However, the values of efficiencies are dynamic with fluctuated chip and phosphor temperature. Thus, iterations are indispensable. As described in Figure 2.2, the electric power and thermal management determine the temperature distribution of a package/module with the specified efficiencies. And the temperature then affects the efficiency correspondingly. After the multi-time calculations, the temperatures are used as the input for the T-L-C model.

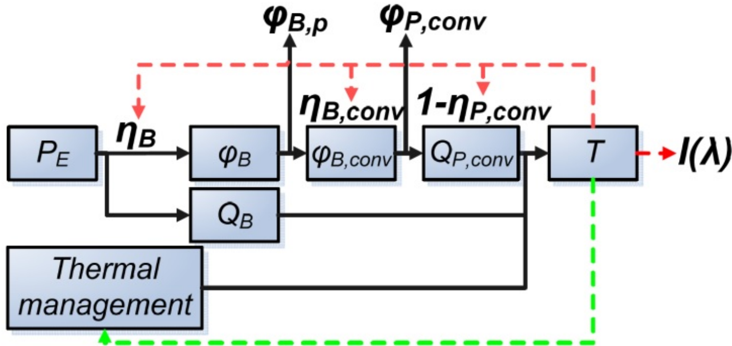

FIGURE 2.2: The block diagram of electrical-thermal (E-T) model of high-brightness LED.

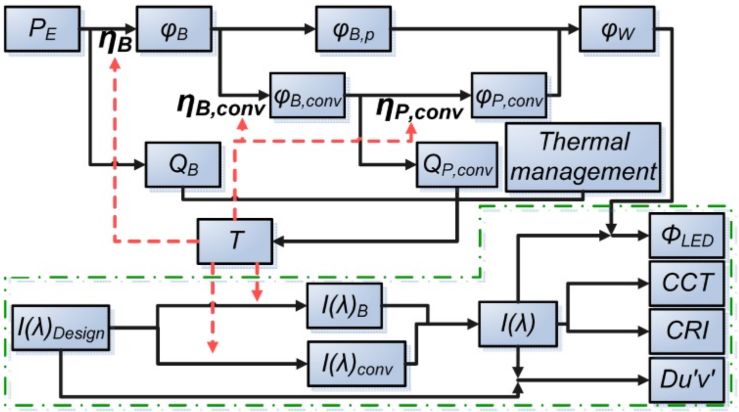

FIGURE 2.3: The block diagram of electrical-thermal-luminous-chromatic (E-T-L-C) model of high-brightness LED and thermal-luminous-chromatic (T-L-C) model (inside the dash line).

φ_B is the optical power of premier blue light, Q_B is the heat generated by the chip, thus electric-optical conversion rate (ξ_B) is defined:

$$\xi_B = \frac{\varphi_B}{P_E} \tag{2.2}$$

The premier blue light will partly penetrate through the phosphor layer and partly converted into green and red light by phosphor particles. Therefore, the converted blue light rate ($\xi_{B,conv}$) is defined as the ratio between the optical power of converted blue light ($\varphi_{B,conv}$) and premier blue light (φ_B):

$$\xi_{B,conv} = \frac{\varphi_{B,conv}}{\varphi_B} \tag{2.3}$$

But only part of converted blue light will be converted into green and red light by the phosphors ($\varphi_{P,conv}$), the rest part is the waste heat ($Q_{P,conv}$) around phosphor particles.

Thus, the phosphor conversion rate ($\xi_{P,conv}$) is defined as:

$$\xi_{P,conv} = \frac{\varphi_{P,conv}}{\varphi_{B,conv}} \tag{2.4}$$

Thus the total heat (Q_{LED}) generated by chip (Q_B) and phosphors ($Q_{P,conv}$) is:

$$Q_{LED} = (1 - \xi_B)P_E + \xi_B \xi_{B,conv}(1 - \xi_{P,conv})P_E \tag{2.5}$$

As the chip, mixed silicone and phosphor samples are selected; all the efficiencies can be identified under specified temperature.

2.2.2 Thermal-luminous-chromatic model

The T-L-C model relates to the spectra, chromaticity, luminous flux, CCT and CRI for specified chips and phosphors which are varying with operation temperature, phosphor particle density and thickness of phosphor layer. The white light consists of penetrated blue light and phosphor converted light. Then the optical power of white light is defined:

$$\varphi_W = (1 - \xi_{B,conv})\varphi_B + \xi_{B,conv}\xi_{P,conv}\varphi_B \tag{2.6}$$

However, the optical power for illuminate is not sufficient due to people's eyes cannot sense the energy. Only those lights with wavelength from 380 nm to 780 nm can be well perceived. The SPD $I(\lambda)$ then are applied according to CIE which is used for calculation of chromaticity coordinates (CIE $xy/u'v'$), luminous flux (Φ_{LED}), CCT and CRI. As the optical power varying with temperature, the SPD is also temperature dependent.

As shown in 2.3, the T-L-C model is shown inside the dash line as a part of the E-T-L-C model. The temperature is calculated by the E-T model and used as input in T-L-C model. The design SPD ($I(\lambda)_{Design}$) is according to the selected chip and phosphors at room temperature. All the characteristics of light can be then conducted according to calculated SPD at its working temperature.

With the CIE luminosity function $V(\lambda)$, the luminous flux is defined as [11]:

$$\Phi_{LED}|_{lm} = 683|_{lm/W} \int_{380}^{780} V(\lambda)I(\lambda)d\lambda \tag{2.7}$$

With the color matching functions $\bar{x}(\lambda)$, $\bar{y}(\lambda)$, and $\bar{z}(\lambda)$ the CIE 1931 xy chromaticity coordinates are expressed as [78]:

$$\begin{aligned} X &= \int_{380}^{780} I(\lambda)\bar{x}(\lambda)d\lambda \\ Y &= \int_{380}^{780} I(\lambda)\bar{y}(\lambda)d\lambda \\ Z &= \int_{380}^{780} I(\lambda)\bar{z}(\lambda)d\lambda \end{aligned} \tag{2.8}$$

$$\begin{aligned} x &= \frac{X}{X+Y+Z} \\ y &= \frac{Y}{X+Y+Z} \\ z &= \frac{Z}{X+Y+Z} \end{aligned} \tag{2.9}$$

Where, X, Y and Z are the three tristimulus values. The expression of CCT is [79]:

$$CCT(xy) = -449n^3 + 3525n^2 - 6823.3n + 5520.33 \tag{2.10}$$

where $n = \frac{x-x_e}{y-y_e}$ is the inverse slope line (x_e=0.3320, y_e=0.1858). Moreover, the calculation of u' and v' are obtained as follows [80]:

$$\begin{aligned} u' &= \frac{4X}{X+15Y+3Z} \\ v' &= \frac{9Y}{X+15Y+3Z} \end{aligned} \tag{2.11}$$

The color shift at any two position (1 and 2) can be calculated using the following formula [80]:

$$Du'v' = \sqrt{(u'_1 - u'_2)^2 + (v'_1 - v'_2)^2} \tag{2.12}$$

The CRI can be 100 for blackbody (incandescent lamps), that is, an illuminant obtains the best effect on color appearance of objects. The general color rendering index (R_a) is most common used which can also be calculated by the SPD with the Euclidean distance (ΔE_i) between the pair of co-ordinates [77]:

$$Ra = \sum \frac{100 - 4.6\Delta E_i}{8} \tag{2.13}$$

To predict SPD at operation temperature, experiments are required to obtain the SPD at room temperature for specified chip and phosphors. If the spectra of PW-LED at position 1 (where $T = T1$) is acquired, the spectra at position 2 (where $T = T2$) can be calculated by Equation (2.13). Based on the assumption that the shift SPD can be divided mathematically into energy change and peak wavelength shift, a thermal-chromatic factor k is introduced for the spectral change with the

temperature, phosphor particle density and thickness of phosphor layer:

$$[I(\lambda)]_{T2}|_{\lambda=380}^{780} = [kI(\lambda)]_{T1}|_{\lambda=380}^{780} \tag{2.14}$$

As the spectra were composite with penetrated and converted light, Equation (2.14) can be redefined as:

$$\begin{aligned} [I(\lambda_1 \rightarrow \lambda_2)]_{T2}|_{\lambda=380}^{485} &= [k_1 I(\lambda_1)]_{T1}|_{\lambda=380}^{485} \\ [I(\lambda_1)]_{T2}|_{\lambda=486}^{780} &= [k_2 I(\lambda_1)]_{T1}|_{\lambda=486}^{780} \end{aligned} \tag{2.15}$$

The thermal-chromatic factor k is divided into k_1 and k_2 to represent the spectral shift of penetrated and converted light. As identified in Figure 2.6(a), the peak wavelength of penetrated blue light moved ($\lambda_1 \rightarrow \lambda_2$) but the wavelength of converted light keeps constant. Equation (2.15) is further rephrased as:

$$\begin{aligned} k_1 &= \alpha \frac{[\xi_B(1-\xi_{B,conv})]_{T2}}{[\xi_B(1-\xi_{B,conv})]_{T1}}\bigg|_{\lambda=380}^{485} \\ k_2 &= \beta \frac{[\xi_B \xi_{B,conv} \xi_{P,conv}]_{T2}}{[\xi_B \xi_{B,conv} \xi_{P,conv}]_{T2}}\bigg|_{\lambda=486}^{780} \end{aligned} \tag{2.16}$$

Where, α and β are the correction factor used with comparison to identification. In this work, α and β are both equal to 1. The converted blue light rate ($\xi_{B,conv}$) is not only depended on the temperature, but also phosphor particle density and thickness of phosphor layer.

2.3 Identification of parameters used in electrical-thermal-luminous-chromatic model

The electric-optical conversion rate (ξ_B), the converted blue light rate ($\xi_{B,conv}$) and the phosphor conversion rate ($\xi_{P,conv}$), thermal-chromatic factor k_1 and k_2, and the designed SPD ($I(\lambda)_{Design}$) at room temperature are all required to be identified experimentally.

2.3.1 Experimental setup

In this work, several commercial chips and phosphor powders were used. Three types of samples were applied: 1) chip/chips with silicone lens; 2) chip/chips with direct phosphors and silicone lens; 3) chip/chips with silicone lens and remote

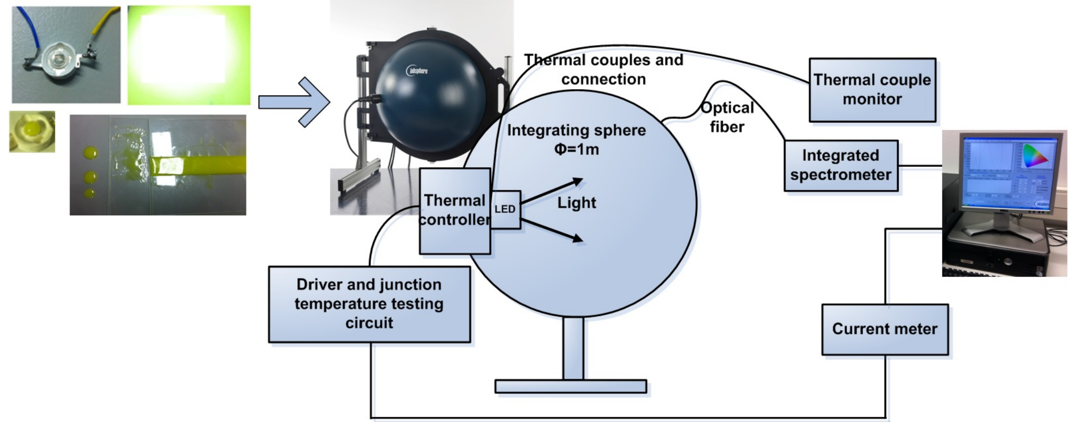

FIGURE 2.4: The schematic diagram of experimental setup for PW-LED samples.

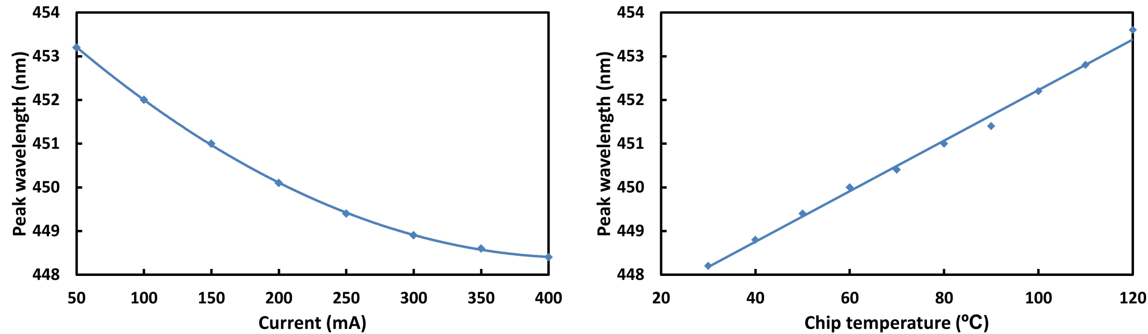

(a) Spectral shift due to current variation for blue light.

(b) Spectral shift due to temperature variation for blue light.

FIGURE 2.5: The spectral shift of LED chips.

phosphors. Single-chip samples were attached on an aluminum-ceramic package with silver paste and positioned on well-controlled thermal plate. And the thermal plate was positioned inside an integrated sphere. The measuring system can provide electrical-thermal-optical measurement simultaneously which is shown in Figure 2.4. The system was integrated by Labsphere Inc. except the external thermal couples. The thermal controller with internal thermal couples set up a constant temperature at the bottom of samples and attached thermal couples were used to validate the controlled temperature and measure the phosphor temperature. The samples were fixed on the thermal controller with thermal paste and screws inside the integrating sphere. All the light measurement was conducted by the sphere, optical fiber, and spectrometer and collected by the computer. Besides, the chip temperature was measured by the junction temperature-forward voltage method

whose relation is almost linear at low current (such as 1mA):

$$T_j = a + bV \tag{2.17}$$

After the determination of the parameter a and b by experiment, the junction temperature which referred as chip temperature in this work can be measured by a current pulse which varies from operation currents to the measuring currents [81, 82].

2.3.2 Identification of SPD of chip due to current and temperature variation

The premier blue light is the fundament in high-brightness LEDs, which will be partly converted and partly penetrate through phosphor layer. Thus, the first step of identification is to obtain the SPD and color shift of the chip. Blue light may be affected by current and temperature. As the current density can directly cause high-power density and consequently high temperature, the spectral shift due to current variation for blue chip was investigated with constant temperature which is controlled by thermal plate in a very short measuring time. As shown in Figure 2.5(a), the peak wavelength of blue light moved towards smaller peak wavelength when optical power rises as well as current increases. However, the peak wavelength had changed from 450 nm of 200 mA to 448.5 nm of 400 mA. It can hardly conduct any spectral shift during application because the LEDs are normally working around 300 mA ± 30 %. Temperature variation can cause much more spectral shift than current change for blue chip. As shown in Figure 2.5(b), the peak of the blue light moved towards longer wavelength when chip temperature increases. The peak wavelength of blue light shifted from 448 nm to 453 nm as chip temperature rising from 30 °C to 120 °C. Normally, LEDs are working from ambient temperature up to more than 100 °C during usage. Compared to 1 nm spectral shift of current variation, temperature variation had stronger effect on spectral shift of blue light and then color shift of LED packages.

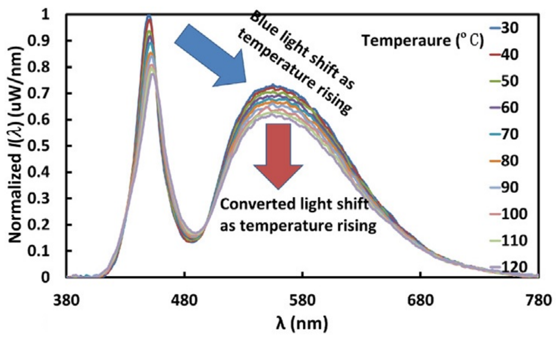

(a) The spectral shift in high-brightness LEDs (5000K) as temperature rising.

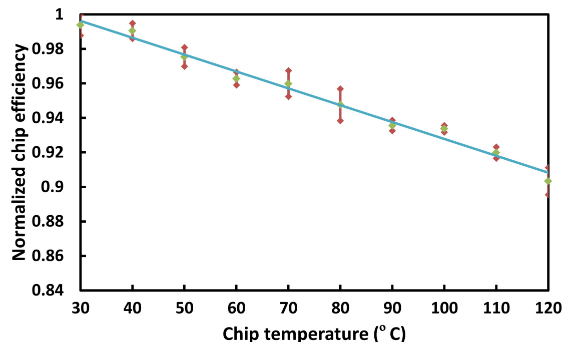

(b) The normalized chip efficiency as temperature rising.

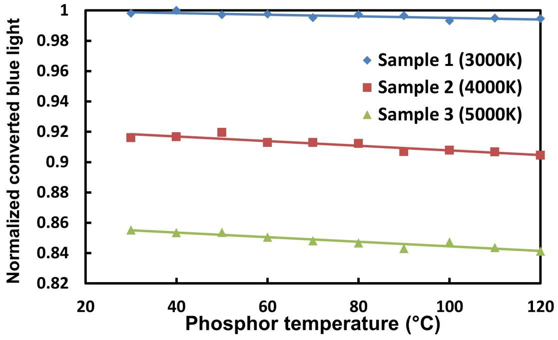

(c) The normalized converted blue light for different samples with variant phosphors which is related to the converted blue light rate ($\xi_{B,conv}$).

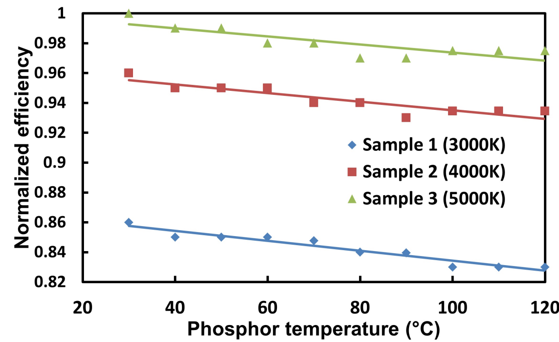

(d) The normalized phosphor efficiency for different samples with variant phosphors which is related to the phosphor conversion rate ($\xi_{P,conv}$).

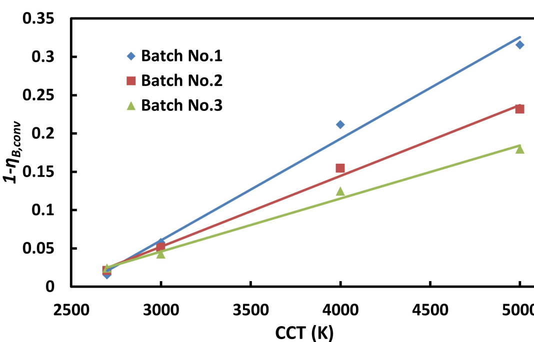

(e) The penetrated blue light rate $(1 - \xi_{B,conv})$ changed with rising CCT (3 batches).

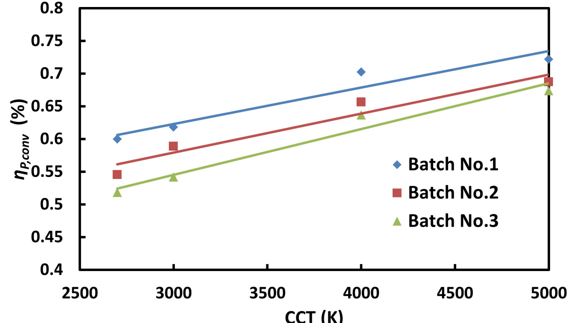

(f) The phosphor conversion efficiency ($\xi_{P,conv}$) changed with rising CCT (3 batches).

FIGURE 2.6: The spectral shift and efficiency drop of high-brightness LEDs as temperature rising.

2.3.3 Identification for spectral shift and efficiency drop as temperature rising

In application, the converted blue light rate ($\xi_{B,conv}$) is around 70% to 99% and the rest part of the blue light will penetrate through the phosphors and then leak to outside. In this situation, identification for blue and converted light are both necessary. Figure 2.6(a) shows the spectral shift in high-brightness LEDs (5000 K) as temperature rising. The leaked blue light obtained peak wavelength shift and SPD dropped with increasing temperature but the phosphor-converted light had only the optical energy drop without peak wavelength shift. Figure 2.6(b) shows the normalized chip efficiency as temperature rising. Although the efficiencies of samples varied a little for several LEDs at the same temperature, we still consider that the efficiency drop linearly for LEDs in one batch as temperature rising from 30 °C to 120 °C. Figure 2.6(c) shows the normalized converted blue light for different samples with variant phosphors which is related to the converted blue light rate ($\xi_{B,conv}$). Just as we described, the higher CCT denotes that more blue light is kept but lower CCT represents that more blue light is converted by phosphors. As the temperature increasing, there were slight converted blue light rate drop. Figure 2.6(d) shows the normalized phosphor efficiency for different samples with variant phosphors which is related to the phosphor conversion rate ($\xi_{P,conv}$). The efficiencies were all decreasing as temperature rising. Figure 2.6(e) shows the penetrated blue light rate ($1 - \xi_{B,conv}$) changed with rising CCT (3 batches). This was a proof of that more blue light penetrated through phosphors as increasing CCT. Figure 2.6(f) shows the phosphor conversion rate ($\xi_{P,conv}$) changed with rising CCT (3 batches). The higher CCT phosphors had better efficiency to change the blue light to yellow. The last two groups of experiments were conducted with several batches, then the phosphor composition, particle density, consolidation time, and phosphor layer thickness varied which gives errors between batches. Therefore, the identification is compulsorily required for each batch in application.

2.4 Experiment verifications

2.4.1 Validation using three common configurations

Nowadays, commercial LED applications are generally divided as three types of configurations: direct phosphor package, multi LEDs package and remote

phosphor product. These configurations are all shown in Figure 2.7. The phosphors are directly coated on the blue chip in direct phosphor package; several blue chips are integrated with phosphors in one pack in the multi LEDs package; and remote phosphor means the phosphors are positioned far away from the blue chips (normally, there are several blue chips with one remote phosphor layer in one application). Three typical samples with phosphors which made in the lab except the remote phosphors were chosen to validate the simulated and calculated results by the E-T-L-C model in this work.

According to the three selected models, simulations were conducted with the boundary conditions: 1) electric power input, 2) initial chip temperature, 3) initial phosphor temperature. Because the efficiencies fluctuated with temperature variation, a multi-step simulation procedure was indispensable. In Figure 2.8, the simulation methodology for thermal simulation is shown. First of all, efficiencies were set when the package working at room temperature. Secondly, temperatures were simulated accordingly. These two steps were considered as a single iteration. If the error is larger than 2 °C in each iteration, then the efficiencies were recalculated by the simulated temperature. Here, only the chip temperature was used for calculation of simulation errors because the phosphor temperature actually varied a lot in the phosphor layer which is a relatively large volume, especially in the multi-LED and remote phosphors.

In order to achieve accurate thermal simulation, 3D modeling with natural convection and radiation were conducted by CFD (Ansys Fluent) using the thermal power input and environment temperature as the boundary conditions. The material properties were chosen empirically and validated by previous work [20, 83]. Chip and phosphor temperature will determine the electric-optical conversion rate (ξ_B), the converted blue light rate ($\xi_{B,conv}$) and the phosphor conversion rate ($\xi_{P,conv}$). But those efficiencies are the parameters of numerical simulation to calculate the temperature. Therefore, iterations were applied and the results were checked after each step. The results of simulated configurations are shown in Figure 2.9. In the direct phosphor package, the highest temperature was in the center where the heat generated by phosphors and chip is accumulated. The multi LEDs package had several separated high temperature points due to the gaps between each chip. In the remote phosphor product, two high temperature areas can be observed. One is in the chip and the other one is in the phosphors. In addition, the simulation results are compared with experiment in Table 2.1. Five samples of three common

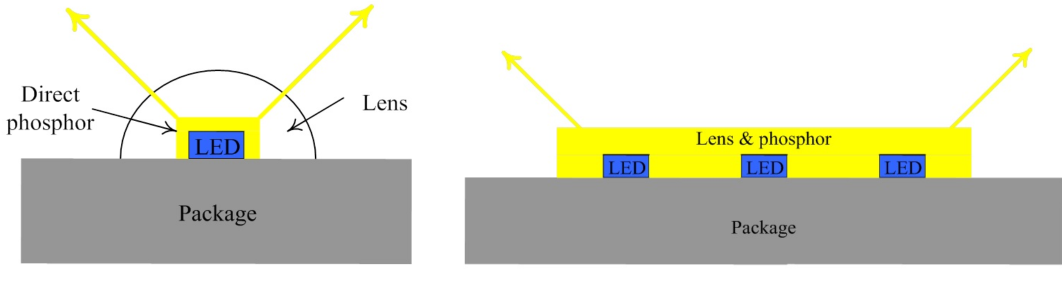

(a) The direct phosphor package. (b) The multi LEDs package.

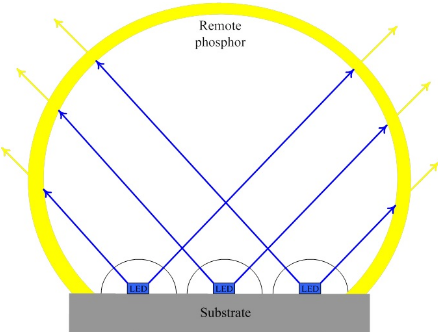

(c) The remote phosphor product.

FIGURE 2.7: The models of three common configurations.

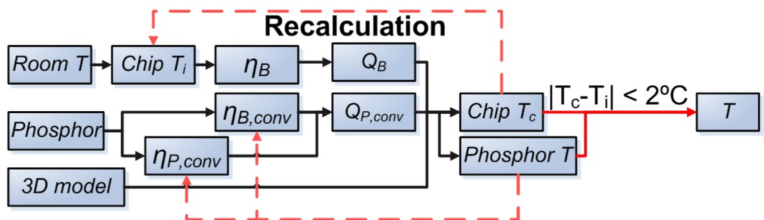

FIGURE 2.8: The methodology for dynamic thermal simulation.

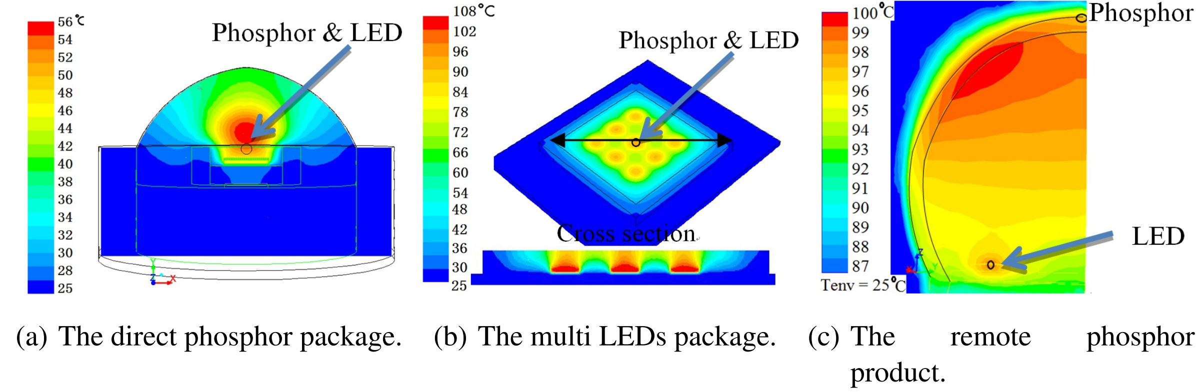

(a) The direct phosphor package. (b) The multi LEDs package. (c) The remote phosphor product.

FIGURE 2.9: The simulated temperature contours of LED packages.

configurations were measured. We chose the chip temperature and top points of those samples for comparison. The errors between measured and simulated

temperature is less than 4 °C. All the samples were simulated and measured in the same condition as the same situation except the remote phosphor. The direct and multi LED samples were directly attached on the thermal controller but the remote one was simulated and tested by a 8W LED Lamp without driver in an environment of 25 °C. With the validated simulation temperature, further calculation of color properties can be continuously conducted.

TABLE 2.1: Comparison of measured temperature of common LED configurations and simulated models.

	Direct (3000K)	Direct (4000K)	Direct (5000K)	Multi (6000K)	Remote (2700K)
Electrical power	1W	1W	1W	8.3W (9 LEDs)	6.8W (6 LEDs)
Case Temp (°C)	25	25	25	25	25 (Environment)
Phosphor eff. ([a]Sim.)	0.58	0.65	0.69	0.69	0.55
Blue chip eff.(Sim.)	0.40	0.40	0.40	0.38	0.38
Chip Temp (Sim.)	53.8	53.1	53.2	107.0	99.5
Top point Temp (Sim.)	37.0	36.8	36.2	91.5	97.9
Chip Temp ([b]Exp.)	50.6	51.0	50.8	108.0	98.0
Top point Temp (Exp.)	36.2	35.0	34.7	95.7	100.2

[a] Sim. represents Simulation results.
[b] Exp. represents Experimental results.

Once the temperature can be obtained by numerical calculation, the changed SPD were conducted according to Equation 2.15 and 2.16. Consequently, all the luminous and chromatic values of light were conducted. According to the block diagram T-L-C model of high-brightness LED in Figure 2.3, the measured color shift of common LED configurations and the analytical solution is compared in Table 2.2. The luminous fluxes decreased from ambient to operation temperature, but the CCT increased as temperature rising. The errors between the measured and calculated results for the direct phosphor packages were acceptable. But the multi chips and remote phosphor model obtained larger errors than measured results. This is because their phosphor layers are much larger than the direct model and result in uneven temperature distribution. Then the T-L-C model can obtain results only by the average phosphor temperature. The color shift ($Du'v'$) of remote phosphor is much lower than multi-LEDs package as expected, even at a high temperature. Although the color shift of analytical solutions and experiment differed in some models, the calculation can indicate how the color shifts. Moreover, the CRI is relatively stable even the temperature rising from ambient to operation value.

Table 2.2: Comparison of measured and calculated color shift of common LED configurations.

	Measured results				Analytical solution			
	[a]$\Delta\Phi_{LED}$ (lm)	[b]ΔCCT (K)	[c]$Du'v'$	[d]Ra	[a]$\Delta\Phi_{LED}$ (lm)	[b]ΔCCT (K)	[c]$Du'v'$	[d]Ra
Direct (3000K)	-4.0	12	0.0012	81	-7.3	9	0.008	81
Direct (4000K)	-4.9	18	0.008	74	-6	30	0.0018	74
Direct (5000K)	-5.4	52	0.0013	72	-10.5	35	0.0007	71
Direct (6000K)	-43.6	216	0.004	72	-57.2	455	0.0081	71
Direct (6000K)	-11.7	13	0.001	81	-21.7	18	0.0016	82

[a] $\Delta\Phi_{LED}$ is the luminous flux increase/decrease from $T1$ (25 °C) to $T2$ (operation temperature).
[b] ΔCCT is the CCT increase/decrease from $T1$ (25 °C) to $T2$ (operation temperature).
[c] $Du'v'$ is the spectral shift from $T1$ (25 °C) to $T2$ (operation temperature).
[d] Ra is the CRI at operation temperature according to Equation (2.13).

2.4.2 Prediction of color properties by changing the phosphor layer

Normally, the chips of LED were selected and the phosphor powders were chosen in the lab for packaging. Then, this model can be used to predict the thermal and chromatic behavior according to the mixture ratio between phosphors and the solvent, and the thickness of phosphor layer. In this model, the change of phosphor layer is mathematically related to the converted blue light rate $\xi_{B,conv}$ or the penetrated blue light rate $1 - \xi_{B,conv}$.

As shown in Figure 2.10(a), the phosphor temperatures were simulated firstly with the changed $\xi_{B,conv}$ from 70% to 99%. Those samples with direct phosphor (direct phosphor and multi LEDs package) obtained relatively constant phosphor temperature because the heat can be directly conducted from the chip to phosphors. The temperature of the sample with remote phosphor almost linearly increased from 70 °C to 99 °C. According to the chip temperature and phosphor temperature, the luminous fluxes were calculated (Figure 2.10(b)). Generally, the luminous flux increased with increasing $\xi_{B,conv}$. That is, more converted light resulted in more luminous flux. CCT were also calculated which is shown in Figure 2.10(c).

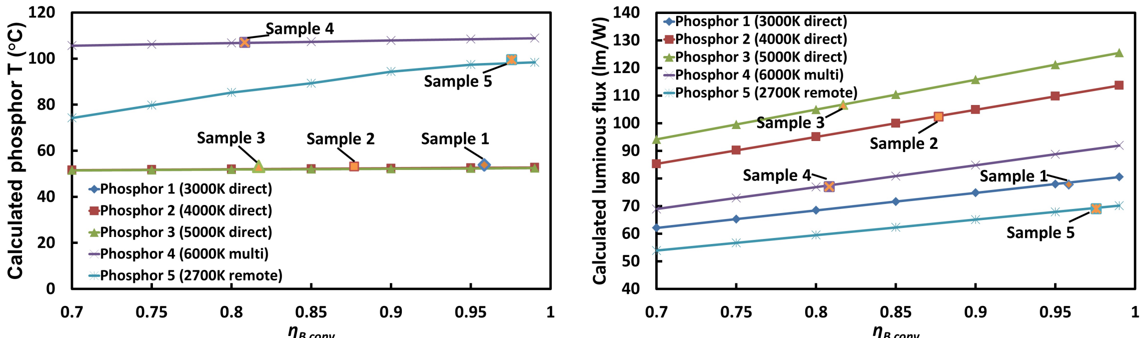

(a) The calculated and measured phosphor temperatures of the samples.

(b) The calculated and measured luminous flux of samples.

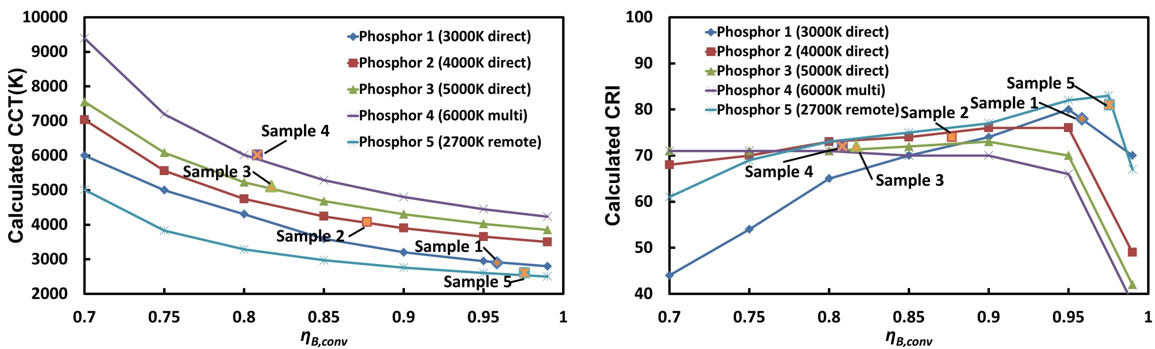

(c) The calculated CCT and measured values of samples.

(d) The calculated CRI and measured values of samples.

FIGURE 2.10: The color properties by changing the phosphor layer.

Oppositely, LED can obtain higher CCT with decreasing $\xi_{B,conv}$. CRI is an important factor for illumination which is shown in Figure 2.10(d). When $\xi_{B,conv}$ is between 0.8 and 0.97, the relatively high CRI can be achieved with the specified phosphors and LED used in this work. Therefore, according to the requirement of final product such as specified CCT, luminous flux, and CRI, the composition of phosphor layer can be decided analytically before experiment.

2.5 Discussion

There are two steps to apply the E-T-L-C model: 1) obtain the chip and phosphor temperatures by 3D simulation; 2) calculate the color properties by equations based on the SPD measured at room temperature. The 3D simulation achieved better accuracy than the analytical calculation [73] to predict the chip and phosphor temperature. After the simulation, an analytical method was used to predict the SPD.

This method was derived from the observation and conclusion from the phosphor-coated GaN based LEDs. In this method, the identifications were the most critical parameter which is varied by different kinds of LEDs. Therefore, comparison with other works is essential in Table 2.3. The spectral shift to long wavelength due to increasing current for blue light was observed in the test which was also supported by the experiment of Peng et al. [84]. And the twice large current can only conduct 4 nm wavelength shifts in the work. The spectral shift to long wavelength due to increasing temperature for blue light was addressed and Chhajed et al. [85] gave similar results, but the sample tested by Chen et al. [75] and Gu et al. [86] showed a first decreasing and then increasing peak wavelength as the temperature rising. In this work, the phosphor efficiency dropped as several literatures [12, 71, 86] but no spectral shift as temperature increasing which was proved by Zhang et al. [71] and Xie et al. [12]. Chen et al. [75] indicated that the penetrated blue light increased with rising temperature, and Shuai et al. [87] tested that the luminous efficiency increase with rising CCT. Admittedly, the parameters used in this method were only available for the tested samples, but it can be widely used for predication most of the phosphor-coated white light LEDs if proper identifications are done.

Table 2.3: Comparison of identification of GaN LEDs.

Identifications	Supported by	Unsupported by
Spectral shift to long wavelength due to increasing current for blue light	Peng et al.[84]	
Spectral shift to long wavelength due to increasing temperature for blue light	Chhajed et al.[85]	Chen et al.[75], Gu et al.[86]
Spectral shift not due to phosphors	Zhang et al.[71], Xie et al.[12]	Chen et al.[75]
Electric-optical efficiency drop with increasing chip/junction temperature	Eliseev et al.[69], Ye et al.[47]	
The penetrated blue light increase with rising temperature	Chen et al.[75]	
Phosphor efficiency drop with increasing temperature	Gu et al.[86], Zhang et al.[71], Xie et al.[12]	
Phosphor efficiency increase with rising CCT	Shuai et al.[87]	

All the properties of color can be predicted by this model, but there are still errors between the measured and calculated results. The three common configurations were applied to check how reliable of the method, which is shown in Figure 2.11. Errors of measured and calculated luminous flux increased as temperature rising with the maximum difference of 5 lm/W. This is acceptable with the accuracy of 5% as the normal LED owns 100 lm/W. And this model obtained low accuracy to predict

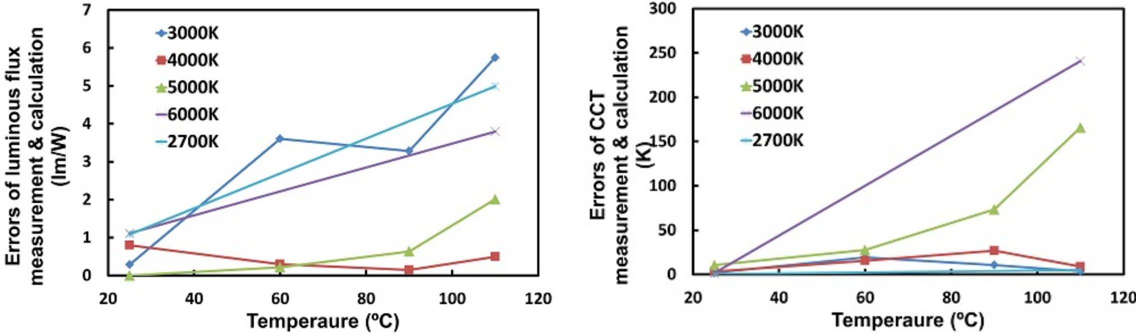

(a) The errors of measured and calculated luminous flux with increasing temperature.

(b) The errors of measured and calculated CCT with increasing temperature.

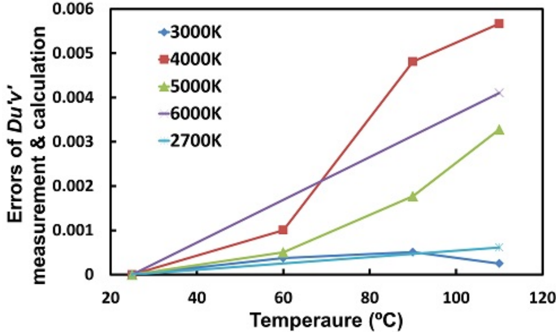

(c) The errors of measured and calculated $Du'v'$ with increasing temperature.

FIGURE 2.11: The errors between measured and calculated results.

the CCT change due to temperature especially for the higher CCT samples. This is because the assumption that the SPD of blue light linearly dropped and moved towards to longer wavelength as temperature rising and the SPD of converted light was assumed linearly drop with increasing temperature. Then the blue light shift obtained higher errors due to the mathematical analysis. If the light is dominated by phosphors, then the model can give better prediction and the high CCT indicate more blue light and less converted light. Further work should be done to improve this method as the work done by Chen et al. [75]. Similarly, the errors of $Du'v'$ between measured and simulated results were high with the higher CCT samples.

2.6 Conclusion

In this work, a model of E-T-L-C includes E-T part and T-L-C part was developed for prediction of color properties under its working temperature according to the

identified LED chip and phosphors. The model was worked depends on two assumptions:
✓ The SPD of light can be divided mathematically into two parts: energy change at each wavelength and peak wavelength shift.
✓ The SPD of blue light changes with the chip temperature and the SPD of converted light are mainly affected by phosphor temperature.
The first assumption was derived from Figure 2.6(a), mathematically concluded by Equations (2.15), (2.16) and the similar shifts were also observed by [12, 71]. In this work, the SPD of blue light linearly dropped and moved towards to longer wavelength as temperature rising and the SPD of converted light was assumed linearly drop with increasing temperature. This consideration gave errors especially for the blue light part and the connection part between blue and converted light. However, the linearity in the equations gives much convenient for analytical simulation and acceptable results. This will conduct some errors which are shown in Figure 2.11. Besides, the second assumption that the wavelength shift mainly due to temperature rather than currents was approved in Figure 2.5.

The E-T model is to calculate the chip and phosphor temperature accurately base on the power input and identified efficiency with 3D simulation requiring follows:
✓ The electric-optical conversion rate change with temperature for blue light
✓ The converted blue light rate with changing temperature
✓ The phosphor conversion rate change due to temperature variation
✓ The phosphor conversion rate variation change with CCT
As the temperature obtained by simulation, the SPD changed from room temperature to working temperature can be calculated with the identified efficiencies and the SPD at room temperature as follows:
✓ SPD of blue light and converted light at room temperature
✓ Spectral shift by current variation for blue light
✓ Spectral shift by temperature fluctuation for blue light
✓ Spectral shift due to temperature changed on phosphors
Then, the model was validated by integrated analyses of common LED packages. Besides, the model can also be used to analyze the thermal performance and light quality due to change of the converted blue light rate which is related to thickness and particle density of phosphor layer. In order to check the reliability for GaN based PW-LEDs, comparison of identification by various literatures was applied. In conclusion, this model is quite efficient to predict the color properties change with temperature and phosphor layer which requires only several experiments

to identify the characteristics. Thus the proposed electrical-thermal-luminous-chromatic model can definitely benefit the design of future high-brightness LEDs for better light performance with thermal management by consideration of electrical-thermal-optical characteristics.

Chapter 3

Thermal transient effect and improved junction temperature measurement

---

The diode forward voltage method with pulsed currents was widely used for monitoring junction temperature (T_j) of Light-Emitting Diodes (LEDs). But a thermal transient effect (TTE) was observed by the pulsed currents and consequent errors were introduced. Thermoelectric (TE) physics was conducted to explain this phenomena and a group of experiments was used to reveal the TTE during T_j measurement for high-voltage (HV) LEDs. Besides, an improved Pulse-free Direct Junction Temperature Measurement (DJTM) method was conducted for HV LEDs to reduce the errors and to achieve in situ T_j measurement with DC currents, simpler setups and a less step sequence.

3.1 Introduction

Light-emitting diodes (LEDs) composed of InGaN and yellow phosphors have undergone a very rapid development over the last decades with the high efficiency, tunable chromaticity, excellent reliability and environmental benefit [3, 88]. Although LEDs boast very high energy conversion efficiency, they are suffering many problems due to the high junction temperature (T_j) [47]. Among the T_j measurement methods, the conventional diode forward voltage method or Pulsed Junction Temperature Measurement (PJTM) is the most attractive one [81, 89]. However, few researchers paid attention to the measurement errors resulting from the pulsed currents. Cain et al. [90] reported the errors introduced by the pulsed currents used for T_j measurement of an RF power transistor. Recently, beside the traditional materials, III-Nitride alloys have shown promising thermoelectric (TE) figures of merit [91–94]. Blue LEDs which are made of InGaN may perform similarly. Therefore, the TE physics can be used to explain the thermal transient effect (TTE) due to pulsed currents on LEDs [95]: the Peltier effect occurred locally confined to the junction and the Joule heating occurred volumetrically. We observed that: a suddenly decreasing temperature with a step-up current and rising temperature with a step-down current. By coincidence, the measured lowest/highest temperature appeared around 100us after the current step which was also calculated by Thonhauser et.al [96] and Miner et.al [97]. A roughly estimation of the TTE in 500 μs according to the equation [97] is:

$$\Delta T = \frac{t}{\beta+1}\left[\left(\frac{(M-1)I_0 S T_{min,dc}}{lwdc_m} - \frac{(M^2-1)I_0^2\rho_m}{l^2w^2c_m}\right) - \frac{(M^2-1)I_0^2\rho}{d^2w^2c}\beta\right]$$
$$with \quad \beta = \frac{\sqrt{kct}}{lc_m} \tag{3.1}$$

However, the maximum height of the transient current pulse used in Equation (3.1) is 11.7 times higher than the steady-state current while it is 150 times in our experiment. Then, a very low temperature may achieve in the response time less than 100us according to Landecker and Findlay [98]. Nevertheless, the TTE introduced lots of uncertainty (can be ±12 °C from Equation (3.1) of T_j measurement with the PJTM for diodes with TE properties. In this work, a group of experiments was conducted to approve the proposed theory and reveal the introduced errors in Tj measurement of high-voltage (HV) LEDs. An improved Pulse-free Direct Junction Temperature Measurement (DJTM) derived from the diode forward voltage method was then reported. Besides, this method also achieved fast and in situ

T_j measurement for HV LEDs with DC currents, simple setups and a two-step sequence. Moreover, it was approved to be able to apply for single or multi HV LEDs in series with two-point calibration.

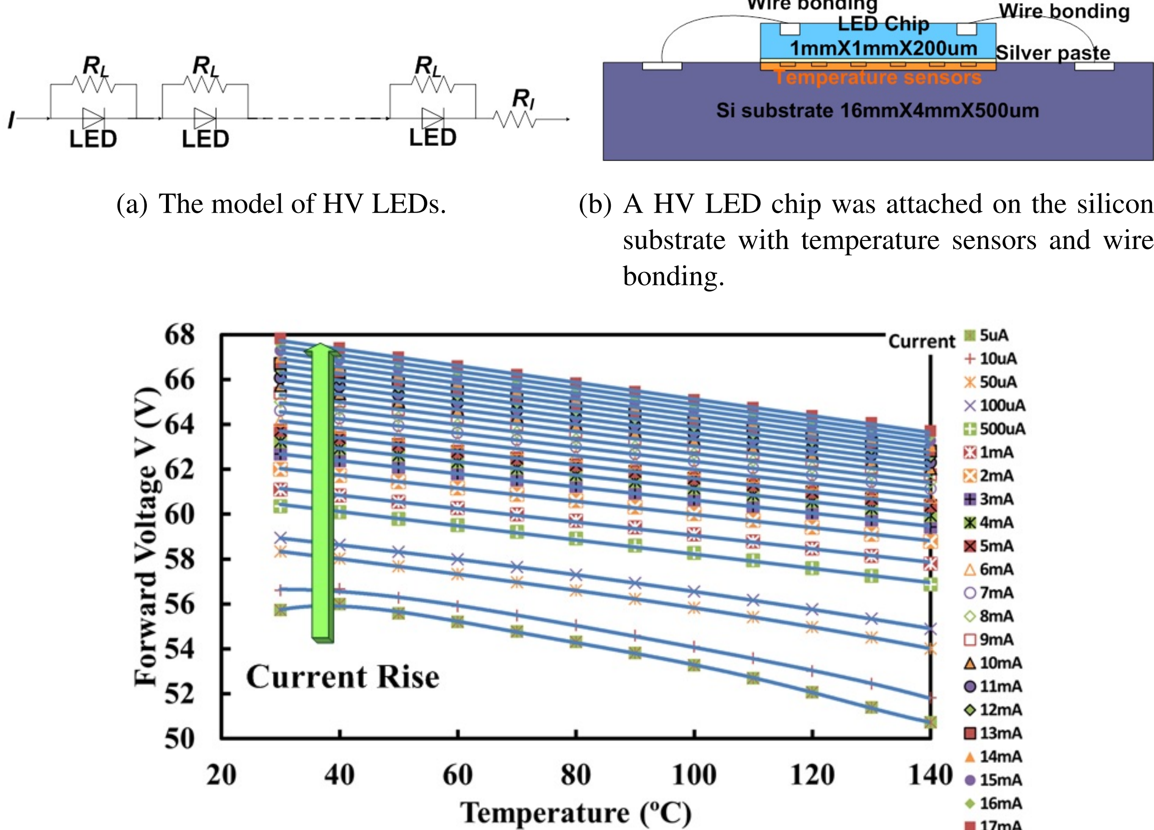

(a) The model of HV LEDs.

(b) A HV LED chip was attached on the silicon substrate with temperature sensors and wire bonding.

(c) The experimental forward voltage vs sensor temperature for different DC currents.

FIGURE 3.1: The set-ups and calibrations of T_j measurement for HV LED.

As reported by Lau and Makino [99], the increasing currents led to diverse reduction in dV/dI of different long wavelength quantum-well laser diodes. Relatively low/moderate currents were reported as a preferred measurement approach. Xi et al and Keppens et al. [81, 89] approved that the T_j measurement of low-voltage (LV) LED was conducted with the moderate currents between 100 μA to 10mA in which the tested samples can be considered as ideal p-n junctions. HV LEDs are driven by a turn-on voltage greater than 20 V with operation currents typically 10 mA to 20 mA which benefited AC/DC converter for high efficiency in application. This indicates a Pulse-free Direct Junction Temperature Measurement (DJTM) due to their working currents are in the range of moderate currents. As shown in Figure 3.1(a), it is assumed that a HV LED chip is composed of elements which include a series of p-n diodes (R_{pn}), leakage resistances (R_{lere}) and an integrated internal

resistance (R_{inre}). In the measurement, the T_j is determined by monitoring the diode forward voltage (V_f). However, it is only possible to measure the total forward voltage on all the components. With the forward current I, R_{inre}, sum of diode resistances and leakage resistances $nR_{lere//pn}$, V_f can be defined as:

$$V_f = I(nR_{lere//pn} + R_{inre}) \tag{3.2}$$

As the resistance of diode changing with the forward current, the value of $R_{pn}$is very high at low currents and very low at high currents. If R_{lere} and R_{inre} keep constant, then V_f is dominated by R_{lere} in low currents ($R_{pn} >> R_{lere}$), by R_{pn} in moderate currents ($R_{lere} >> R_{pn} >> R_{inre}$), and by R_{inre} in high currents ($R_{lere} >> R_{pn}, R_{inre} >> R_{pn}$). Although, the effect by R_{lere} and R_{inre} cannot be eliminated totally, the V_f can be obtained more accurately at the moderate currents.

3.2 Experiment setups and results

We established the testing setups to validate the model which is shown in Figure 3.1(b). A HV LED chip was directly attached on silicon substrate with thin thermal interface material (TIM). The temperature sensors were fabricated using standard silicon processing technologies which were calibrated ranging from 30 °C to 150 °C. The thickness of the chip and TIM were 153 μm and 59 μm. Thus the sensors were very close to the p-n junction. The silicon substrate was positioned and vacuumed on a cumbersome thermal plate with accurate temperature controller in an enclosure.

In order to avoid the self-heating/fast cooling as the currents changing, the measurement should be done as soon as possible, but TTE will occur if time is too short. Therefore, we applied step-up currents and measured the characteristics between temperature and V_f after 100 ms (this time is conducted from calculation and experiment in Figure 3.2). Figure 3.1(c) shows the IV curves under DC currents at various temperatures monitored by the temperature sensors. If the current is lower than 100 μA, the dV_f/dT was not linear which indicates the measured V_f is dominated by R_{lere}. Unlike the LV LEDs, the dV_f/dT of HV LEDs still kept constant even with its operation currents from 10 mA to 20 mA. The linearity shows that they are able to achieve nearly ideal p-n voltage-temperature characteristics at its working currents. Thus the DJTM method can be used by only a two-step sequence: firstly conducting two-point calibration at working state and subsequent T_j measurement with stable DC currents. Consequently, this method can achieve

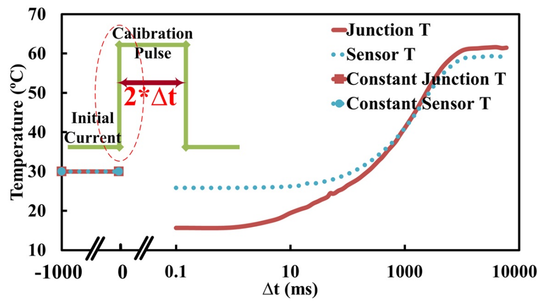

(a) The temperature measured by DJTM and sensor with a step-up current from 100 μA to 15 mA.

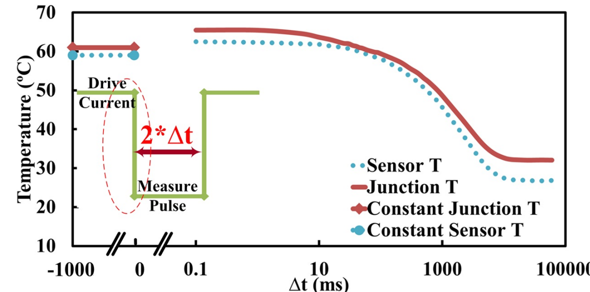

(b) The temperature measured by DJTM and sensor with a step-down current drop from 15 mA to 100 μA.

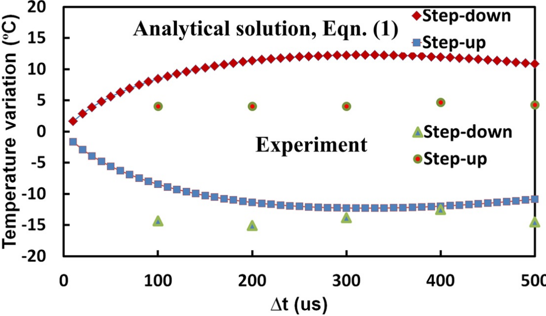

(c) The analytical solutions compared to experimental temperature variation due to a step-up current from 100 μA to 15 mA and a step-down current from 15 mA to 100 μA in 500 μs.

FIGURE 3.2: The temperature measured by DJTM and sensor with a step-up/step-down current for HV LED.

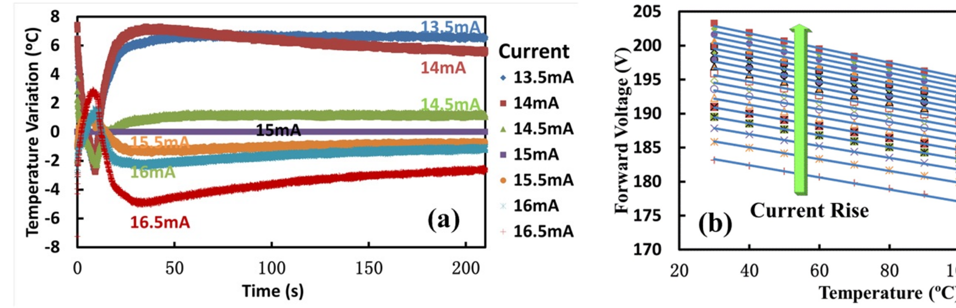

(a) The errors introduced by current variation when DJTM method is applied.

(b) The forward voltage linearity of three HV LEDs in series.

FIGURE 3.3: The error analysis by using DJTM measurement for HV LED.

fast and in situ measurement for HV LEDs with DC currents, simple setups and a less-step sequence. Moreover, the errors introduced by the pulsed currents can be

reduced. The results obtained by the DJTM method are sensitive and its accuracy is estimated to be ±1 °C for each HV LED.

Most of researches declaimed that the temperature should keep constant in a moment. However, the TTE on III-Nitride alloys was theoretically approved and the temperature would instantaneously change innegligibly. DJTM method was applied to monitor the effect introduced by the pulsed currents in HV LEDs which can hardly be inspected in PJTM. There are two kinds of pulses: 1) step-up pulses for calibration; 2) step-down pulses during measurement. We monitored the temperature on the rising/dropping current during a time slot Δt (the pulse width is $2\Delta t$ but measuring time is Δt). As shown in Figure 3.2(a), a suddenly temperature dropped when a step-up current (15 mA) was applied. After around 100 ms, the measured T_j will return to 30 °C and the sensors monitored the similar temperature trend. Figure 3.2(b) shows the temperature measured with the current from 15 mA to 100 μA. The chip was powered firstly and it was stable at T_j of 61.4 °C and sensor temperature of 59.2 °C. In opposite to the step-up current, the T_j rapidly rose by 4 °C and the sensor temperature increased by 2 °C when the current dropped. After around 100 ms, the measured junction and sensor temperature returned to the initial temperature. Figure 3.2(c) compares the analytical temperature changed for a step-up current from 100 μA to 15 mA and a step-down current from 15 mA to 100 μA in 500 μs according to Equation (3.1).The calculation shows that the temperature changed ±12 °C with a step-down current and -12 °C with a step-up current around 300 μs. But the measured values were +4 °C and -15 °C in this short time correspondingly. During application, the LEDs are normally connected in series and the power supply may be unstable which affected by the main. Therefore, we tested the DJTM method under current variation and with HV LEDs in series. The results in Figure 3.3(a) approved that this method can be used in specific applications without stable currents. When the chip was calibrated at 15 mA, the measuring errors can be still acceptable as the currents fluctuate less than ±10%. Its uncertainty is only around 6 °C while the normal working situation of LED chips is around 100 °C [47]. And Figure 3.3(b) shows the linearity of forward voltage with three chips from the same batch in series. It approved that the DJTM can be still available for multi-HV LEDs in series. In this work, the errors for T_j measurement were no more than 3 °C.

3.3 Conclusion

In conclusion, TTE due to pulsed currents was conducted by TE physics and observed during T_j measurement of HV LEDs. This effect will result in considerable errors in a short-time pulse and can hardly be monitored in the conventional diode forward voltage method or PJTM. To reveal and reduce the errors, an improved DJTM method was applied for monitoring T_j. Besides, this method can obtain accurate, fast and pulse-free measurement with two-point calibration and be applied on single or multi-HV LEDs. Moreover, the measuring errors can be still acceptable with currents fluctuating of $\pm 10\%$.

Chapter 4

Temperature triggered MEMS switch for cooling control

As the power of Solid State Lighting (SSL) system continuously rising and consequently high temperature occurred in the light source, active cooling solutions with controlling were widely used and smart controlling was indispensable for less energy consuming. A micro-electro-mechanical-system (MEMS) based, temperature triggered, switch was developed as a cost-effective solution for smart cooling control in SSL systems.

4.1 Introduction

In order to control SSL temperature, thermal management is compulsory. Currently, LEDs are mounted on heat sinks, which are used to transfer heat to the environment by natural or forced convection. With the continuously increasing driver power of LEDs, natural convection is about to reach its limit for compact heat sink. In such cases, active cooling solutions [54–57] are required. However, active cooling systems cause additional power consumption. To reduce that, smart controls, e.g. switching on the active cooling only when the temperature exceeds a certain threshold, were applied. Takikawa et al. [58] invented mechanical temperature controlled device with liquid coolant technologies for electronics cooling, and Dinh and Korinsky [59] applied temperature-dependent fan control circuit for personal computer. Such solutions required relatively complex mechanic designs as well as many additional components, including temperature sensor, readout and control circuits (together with its DC power supply). This consequently increased the complexity and cost of the lighting system. It is therefore essential to look for a much simpler and cost-effective alternative solution for smart cooling control.

Recently, micro-structured silicon wafers have been used as substrates for the LED packaging, due to their good thermal conduction [42, 60–62]. Beside this advantage, silicon substrates are ideal for integration of micro-electro-mechanical systems (MEMS), sensors and actuators. Ye et al. [47] has successfully integrated a temperature sensor and liquid cooling channel on silicon substrate to monitor and to control the temperature of a LED package assembled on the silicon substrate. Therefore, silicon wafers, together with the advanced micro-machining technology, are highly potential solutions in smart system integration for SSL applications.

In this paper, a temperature-triggered switch (TTS) integrated in silicon substrate is proposed as a cost-effective solution to achieve an automatic regulation of the active cooling. As the concept and numeric analysis were presented firstly, a single-mask fabrication process was developed. The fabricated switch was then characterized and experimental results were discussed in detail.

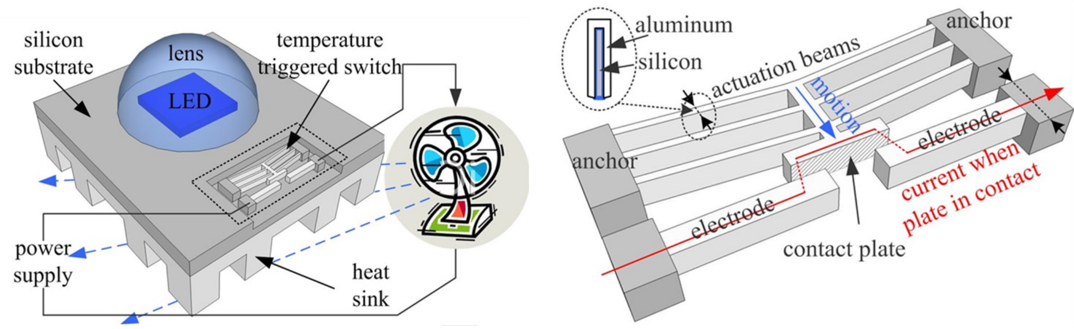

(a) The schematic drawing of the proposed cooling system for LED.

(b) The schematic drawing of the TTS, illustrating the structure and the working principle.

FIGURE 4.1: The TTS is embedded to detect the temperature of the substrate. It switches on the active cooling component, i.e. a fan, when the temperature exceeds a designed threshold.

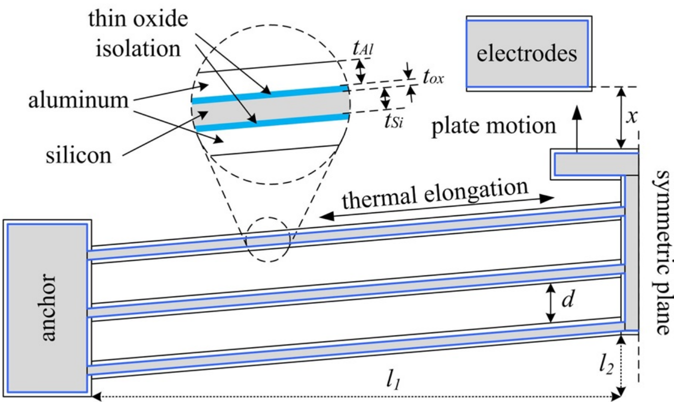

FIGURE 4.2: The layout and size of the V-shape actuation beam used for the analysis and fabrication of the TTS.

4.2 Design and fabrication

In Figure 4.1(a), to accurately detect the temperature of the LED chip and to switch on a cooling unit, the TTS is integrated in the same silicon substrate with the LED chip. As shown in Figure 4.1(b), the device consists of a V-shape thermal actuator, a suspended contact plate and two counter-electrodes. When temperature rises, the suspended beams of the V-shape actuator expand due to the thermal expansion. The contact plate will be pushed against the two electrodes to create an electrical connection, thus switching on the cooling unit. When temperature drops, the device switches back to the off-state. This device allows an automatic control of the cooling system without any need of additional, costly electronic components.

The integrated thermal actuator is different from traditional MEMS V-shape thermal actuators made from silicon beams [100]. In the traditional silicon V-shape thermal actuators, the actuation beams and the substrate are made of same material, and thus have the same coefficient of thermal expansion (CTE). Therefore, the actuation is generated by the temperature difference between the actuator and its substrate. This usually requires local heaters embedded in the actuator beams. However, the dimension of LED package is typically within millimeter scale and obtains uniform high temperature around the chips [21]. Besides, the package temperatures become more uniform with changing the package materials to silicon, which have much higher thermal conductivity than traditional ceramic package [47]. For these reasons, the traditional silicon thermal actuator concept cannot be applied.

TABLE 4.1: The geometrical parameters of the TTS.

Symbol	Description	Size
l_1	Size of beam in x-axis	500 μm
t_{Si}	Thickness of silicon in beam	2.0 μm
l_2	Size of beam in y-axis	10 μm
t_{ox}	Thickness of oxide on each side of beam	0.2 μm
h	Height of beam and contact plate	35 μm
t_{Al}	Thickness of aluminum on each side of beam	1.0 μm
d	Distance between adjacent beams	15 μm
x	Initial distance between moving plate and electrodes	10-15 μm

TABLE 4.2: Material properties used in the FEA simulation.

Material	Young's Modulus (GPa)	Coefficient of Thermal Expansion (1/°C)	Poisson Ratio
Silicon (beam and substrate)	180 [101]	6.73e-6 [102]	0.20 [101]
silicon oxide	70 [101]	2.30e-6 [102]	0.17 [101]
aluminum	69 [103]	22.2e-6	0.334

For the proposed TTS, the CTE of the actuation beams needs to be designed higher than the silicon substrate, so that an effective motion can be generated, when the temperature rises uniformly. The generated motion is a function of the absolute temperature increase of the substrate. To achieve large motions at a low switching temperature (100~150 °C) as required for SSL applications, complex actuator beams with large CTE are used. The beams are made of narrow silicon beams coated on the two side surfaces with a large CTE material, such as metals.

In this paper, aluminum is used due to its easy deposition process. A thin layer of silicon oxide is inserted between the silicon and aluminum layer for a good electrical isolation. The effective CTE of the complex beam in the longitude direction α_{eff} can be roughly estimated with equation:

$$\alpha_{eff} = \frac{\alpha_{Si}E_{Si}t_{Si} + 2\alpha_{ox}E_{ox}t_{ox} + 2\alpha_{Al}E_{Al}t_{Al}}{E_{Si}t_{Si} + 2E_{ox}t_{ox} + 2E_{Al}t_{Al}} \tag{4.1}$$

where α, E and t with different subscript are the CTE, Young's modulus and thickness of each beam material respectively. Figure 4.2 gives a detailed drawing of the V-shape actuator. The geometrical parameters of the TTS and their designed values are listed in Table 4.1. The values are chosen to validate the proposed concept, and can be changed to satisfy the different needs of potential applications.

To illustrate the behavior of the TTS device, the motion of the contact plate depended on the thickness of the materials was simulated firstly with finite element analysis (FEA). In the simulation, a uniform temperature was set on the whole structure and symmetric boundary conditions were applied on the symmetric plane. As the beams are repeatedly designed to enhance the strength of the structure, we considered that the number of beams is not relevant to the simulation. But the material properties were critical to the numerical results. The thin film of silicon and silicon dioxide differed to the bulky ones [102]. The material properties used in the analysis are listed in Table 4.2. And the motion of the V-shape actuator for a 130 °C temperature raise with the design parameters illustrates in Figure 4.3. As the calculated movement will reach to 12 μm, the designed distance between moving plate and electrodes was set as 6 numbers from 10-15 μm with consideration of the uncertainty introduced by manufacturing process.

A fabrication process was developed to integrate the proposed TTS on a silicon substrate. In order to keep the process low-cost, only one photolithography step was involved. As shown in Figure 4.4, the process is similar to the single crystal reactive etching and metallization (SCREAM) [104] process. First, a deep reactive-ion etching (DRIE) step is performed to define the 2D geometry and the height of the TTS beams. Then a silicon isotropic etching step is used to release the silicon beams to form free-standing structures. A thermal oxidation is carried out to create a thin oxide layer (200 nm) on all the exposed surfaces of the silicon structure for electrical isolation. An aluminum layer on both the top and side surfaces of the silicone structure is deposited using a sputtering process. The aluminum not only servers as a conductive layer to carry the electrical current when the TTS is switched on, but

also forms complex actuation beams with large effective CTE. The aluminum layer is immediately covered by a thin titanium nitride (TiN) layer to prevent oxidation of the aluminum surface for a better electrical contact. The width of each silicon beam is designed to be 2.0 μm. Due to the nature of the sputtering process, the thickness of the aluminum layer on the top and side surface is not identical. The aluminum layer is 4 μm thick at the top surface of wafer, and is expected to be approximately 1 μm on the side surfaces.

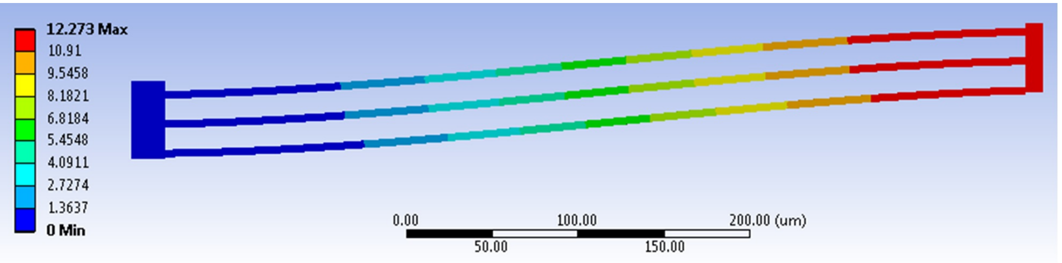

FIGURE 4.3: The motion of the contact plate.

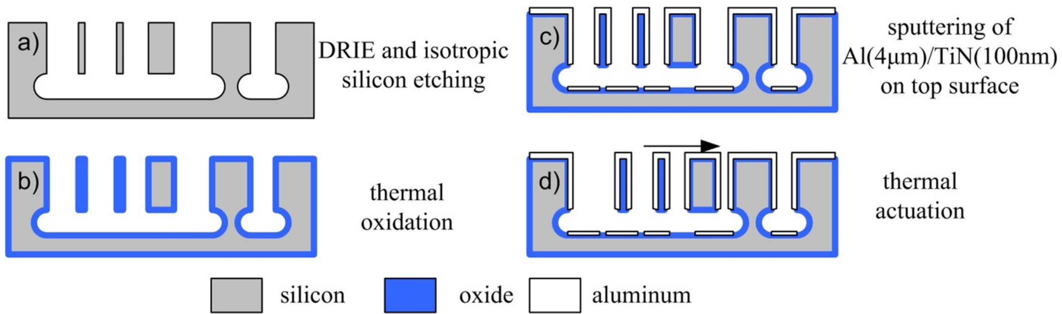

FIGURE 4.4: The schematic drawing of the single-mask fabrication process.

4.3 Experimental results and validation

A fabricated device is shown in Figure 4.5. There are in total 20 complex beams (10 on each side), forming the V-shape actuator. The device is 1.04 $\times$ 0.4 mm^2 in size, and the height of the switch structure is 35 μm. The other geometrical parameters of the TTS can be found in Table 4.1. Slight deviations of the thickness in each layer of the complex beam are observed by scanning electron microscope (SEM) measurement. The silicon core and oxide thickness are 1.9 μm and 0.24 μm, respectively, and the thickness of the sputtered aluminum layer is a variable, which will be discussed in the next section of this paper.

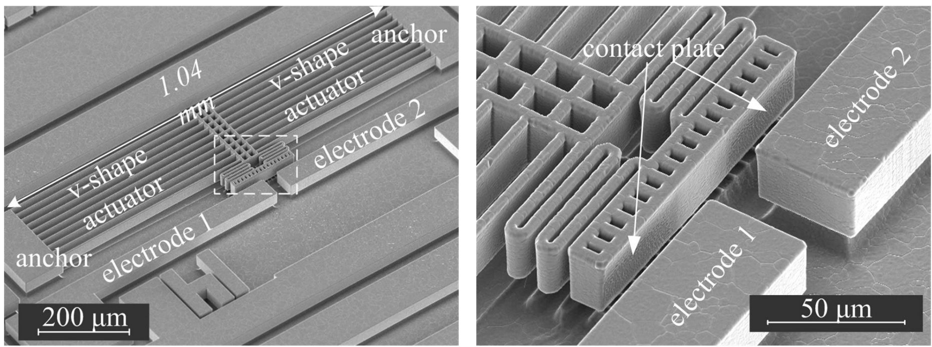

(a) The fabricated temperature triggered switch.

(b) A close-up photo of the contact plate.

FIGURE 4.5: The SEM photo of the temperature triggered switch.

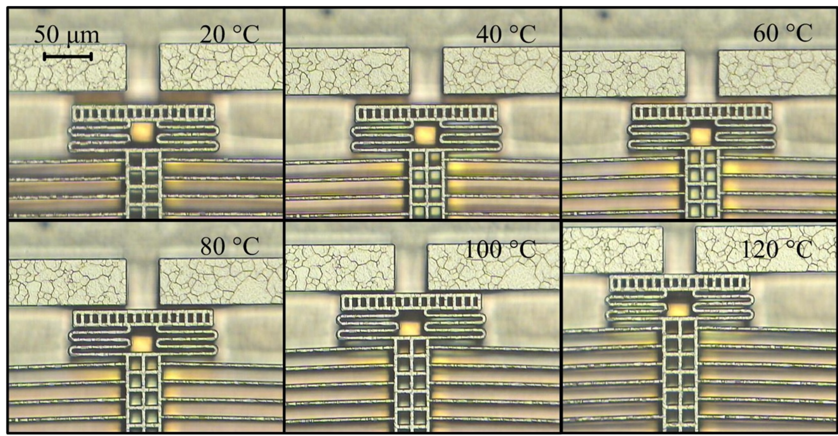

FIGURE 4.6: The microscope images of the temperature triggered switch at different temperatures. A solid contact is achieved at 130 °C. The contact resistance is < 2 Ω.

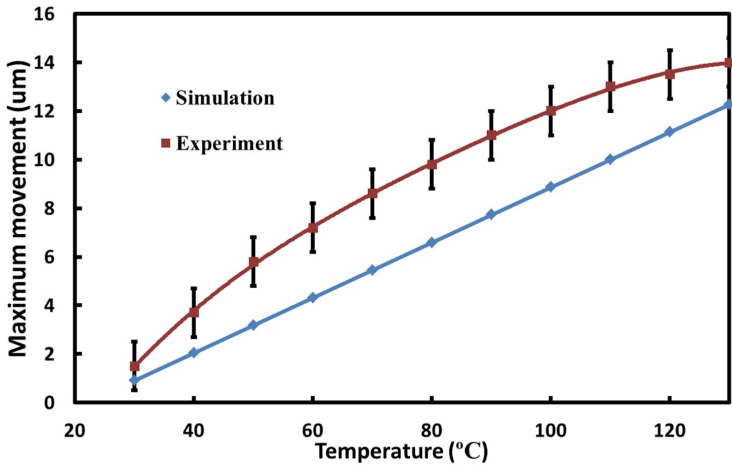

FIGURE 4.7: The motion of the contact plate as a function of substrate temperature.

To measure the switching temperature of the TTS, the device was placed on a probe-station equipped with a built-in heater for temperature control. A microscope was used to examine the motion of the contact plate as a function of the substrate temperature, as depicted in Figure 4.6. For the fabricated TTS, a solid contact was achieved at around 130 °C, which is around the working temperature of the LED chip. As the switching temperature can be modified by choosing a different geometry, it is possible to adjust the design to meet the requirements for different LED cooling control. The I-V measurements show that the contact resistance through the electrodes is less than 2 Ω (including the contact resistance between probes and connection pads).

Figure 4.7 shows the motion of the contact plate as a function of substrate temperature by the measurement and simulation. The experiment movements were higher than the simulation results and the movement was not linear. The error bars indicate the resolution of the microscope ($\sim 1\ \mu$m). The movement of the contact plate by the temperature in the experiments was observed and divided by several periods. (1) At low temperature, the initial movement obtained a high gradient which indicated that the plate had fast movement. (2) When the temperature increases, the lower gradient shows the slower movement of the plate. (3) In the end, the movement gradient became lowest when temperature rose up. The reason is that the thermal expansion coefficient is not linear but a function of temperature [105]. In the simulation, we achieved similar gradient of the middle temperature period, but the movement at low and high temperature differed with the experiment due to the used constant material properties [102]. Nevertheless, the simulation results obtained good prediction for such a device in designing.

4.4 Discussion

The measurements have validated the proposed concept of the TTS. However, to further understand its behavior, a few aspects in the design and fabrication of the device are discussed in more details.

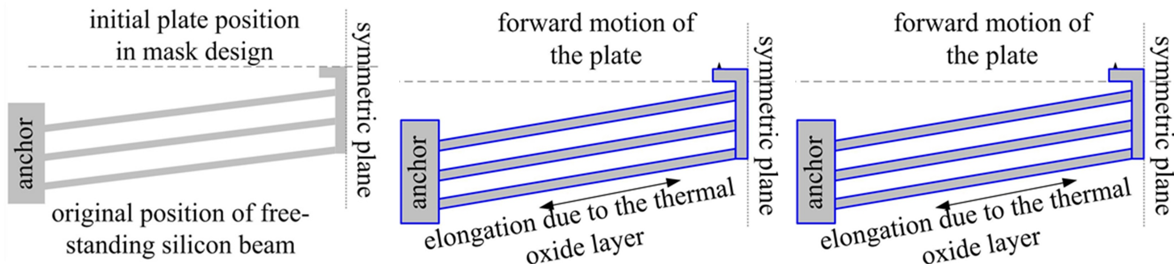

(a) The position of the silicone beam after DRIE process.

(b) The forward motion of the structure due to the compressive stress induced by the thermal oxidation.

(c) The retraction of the structure due to the tensile stress of the sputtered aluminum layer.

FIGURE 4.8: The influence of the process on the initial motion of the free-standing structure.

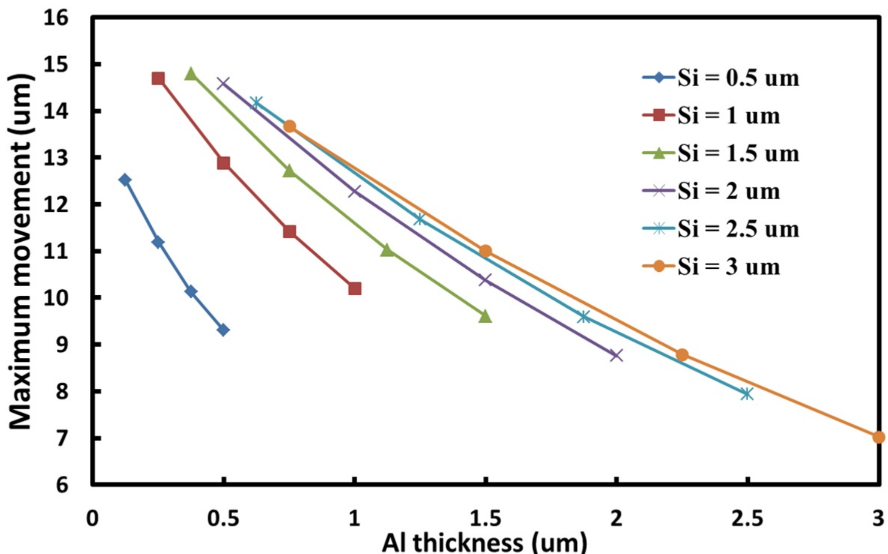

FIGURE 4.9: The motion of the contact plate as a function of the silicon and aluminum thickness at 130 °C by simulation.

4.4.1 Initial stress of the complex beam

Initial stress in the free-standing structure introduced during the fabrication process, has an influence on the initial distance between the contact plate and the electrodes. As illustrated in Figure 4.8, the isolation layer made by thermal oxidation induces a compressive stress on the complex beam, pushing the contact plate closer to the electrodes. On the contrary, the sputtered aluminum layer introduces a tensile stress on the complex beam, and therefore pulls the contact plate away from the electrodes. As the switching temperature is function of the initial distance, it is important to select a good thickness and stress combination of

the deposited material, so to control this initial distance. Furthermore, the designed initial distance between the plate and electrodes has to be larger than the forward motion caused by the compressive stress. Otherwise, the contact plate will touch the electrodes after the thermal oxidation step, and consequently be fixed with the electrodes by the sputtered aluminum in the next step, resulting in a defective device. For the realized device described in this paper, the thermal oxidation step causes a ~10 μm forward motion of the plate, which is smaller than the initial distance in the design. The tensile stress introduced by the sputtered aluminum layer almost cancels the compressive stress, and the final initial distance is about 14~15 μm at room temperature (20 °C). For the above reasons, the process parameters and the device layout need to be carefully considered during the design phase.

4.4.2 Silicon and aluminum thickness

As the trigger temperature selected, the distance between the contact plate touches the electrodes is determined with specified silicon and aluminum thickness of the beam. In this work, 2 μm silicon and 1 μm aluminum layers were applied according to the simulation and validated by experiment. In order to achieve better design, the simulated motion of the contact plate as a function of the silicon and aluminum thickness is shown in Figure 4.9. We kept the $2t_{Al}/t_{Si}$ ratio as 0.5, 1, 1.5, 2 and trigger temperature was 130 °C during the simulation. In conclusion, silicon thickness was optimized from 1 to 2 μC and the aluminum thickness was preferred thinner to achieve the maximum movement. However, the designed movement can be always tuned as required. Besides, the trigger temperature can be designed to satisfy requirements related to different applications, by modifying the geometry of the device, e.g. the length and the layer thickness of the beams, as well as the initial distance between the plate and the electrodes.

4.4.3 Aluminum thickness on side surface

As the expansion of the complex beams are mainly generated by the aluminum layer on the side surface, the thickness of the aluminum layer on the side surface is a key parameter for the TTS performance. Although the aluminum thickness deposited on the top surface of the wafer has be chosen to the 4 μm, the actual thickness of the aluminum layer on the side surface formed in the sputtering process

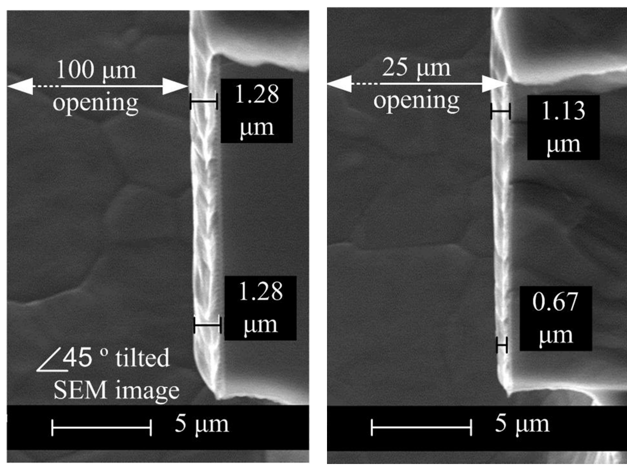

(a) The opening size is 100 μm, and the aluminum can easily deposit at the bottom part of the side surface.

(b) The opening size is 25 μm, and the aluminum deposited at the bottom part of the side surface is limited.

FIGURE 4.10: The cross-section SEM image showing the thickness of the aluminum layer sputtered on the side surface, with different opening size of the cavity.

is not optimized. This thickness is usually only 20-30% of the thickness on the top surface. Furthermore, the uniformity of the deposition on the sidewall is significantly influenced by the 2D geometry of the DRIE etched structure. For example, FIG. 10 shows the cross-section of the aluminum layer deposited on two different side surfaces. In FIG. 10 (a), the side surface had a wide opening (100 μm) on the top of the cavity, and thus gave a large incoming angle (a large possibility in another word) for the aluminum particles to reach the side surface during sputtering. Consequently, the aluminum layer thickness along the side surfaces was almost identical from the top to the bottom. On the contrary, FIG. 10 (b) shows a situation with a narrow opening (25 μm). Due to the limited incoming angle at the deeper part of the side surface, the thickness of the deposited aluminum layer was significantly reduced, when compared with the thickness measured at the top part of the side surface. As the effective CTE is very sensitive to the thickness of the aluminum layer, the above mentioned phenomenon needs to be considered in the layout design, so that an accurate trigger temperature can be achieved.

4.4.4 Surface protection

To ensure a good ohmic contact when the TTS is switched on, the side surfaces of the plate and both electrodes need to have good electrical properties. Aluminum is easily oxidized on its surface, thus degrading its electrical performance. It is therefore necessary to have a conductive layer, such as the thin TiN layer used in this work, coated on the aluminum surface to protect it from oxidation. The TTS without TiN coating has never achieved good electrical contact, even when the temperature is much higher than the switching temperature, giving the movable plate a strong push against the electrodes. The TTS with TiN coating can achieve a good contact resistance when a solid mechanical contact is made. To further improve the contact quality, a better metallic layer, such as Au, might be chemically plated on the aluminum surface for better electrical performance and durability.

4.5 Conclusion

A temperature triggered MEMS switch is proposed for cooling control in SSL applications. The device switched on when the substrate temperature exceeds the designed value, and switched off when the temperature drops under the designed temperature. The device was fabricated with a single-mask 3D micro-machining process. A switching temperature threshold of 130 °C has been achieved with a contact resistance of $< 2\ \Omega$. The device allows an automatic control of the cooling system without any need of additional, costly electronic components. The same concept can be applied to other smart systems where a temperature triggering is necessary.

Chapter 5

Active two-phase cooling for higher light output and increased efficiency

---

High power LED obtained around 70% of the input power to heat. To solve the thermal problem, a cooling solution with phase change phenomenon based on microelectromechanical (MEMS) technology was presented and the proposed device is quite promising for an integrated water-based thermal management.

5.1 Introduction

LED is one of high efficient illuminations which can replace the incandescent lamp and compete with the fluorescent tube in the recent years. Since the high brightness InGaN-based blue light LED is commercialized in 1993 [3, 4, 88, 106], the luminous efficiency and light output have been dramatically improved. Based on the blue emitting InGaN as the primary light source, white light LED could be fabricated mainly by combining a broad-yellow-emitting phosphor, such as YAG:Ce^{3+} [8]. It can provide energy saving and environmental benefit in a large number of applications. However, approximately most of the electrical energy is converted into heat during usage.

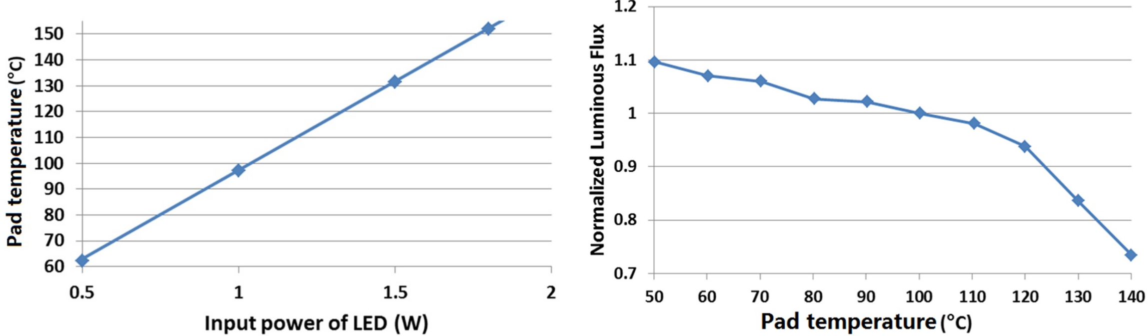

(a) The increased input power of LED results in high pad temperature (the thermal pad is in the bottom of a commercial LED package with dimension of 0.1 cm^2).

(b) The consequently declined light output for the LED package.

FIGURE 5.1: The increased input power of LED results in high pad temperature but low luminous flux.

Figure 5.1 shows that the effect of increasing input power to package temperature (dimension of the LED package is 0.1cm^2 and temperature of the thermal pad in the bottom of the package is identified as the package temperature) and the rising temperate would affect light output of the commercial package. The pad temperature increased linearly with rising input power without any thermal management. Consequently, the luminous flux declined linearly around 8% as the pad temperature rising from 100 °C to 120 °C. However, light output suddenly dropped rapidly when the pad temperature exceeded 120 °C. Only 80% light was retained as the temperature increasing from 120 °C to 140 °C. Therefore, reduction of the temperature is important to maintain the optical performance. Besides, thermal management is the strategy of controlling temperature rather than just cooling the package to a very

low temperature. With consideration of LED working temperature (limitation of 150 °C), cooling efficiency and energy consumption, the best working temperature for high-power LED with two-phase cooling should be between 80 °C and 120 °C.

Although advanced thermal materials and novel thermal solutions are already successfully applied on high-power LED [36, 107, 108], the heat sink is still indispensable to dissipate heat to environment. However, the heat sink required for sufficient heat transfer is bulky and heavy usually with the metals. This results in unattractive LED product with cumbersome and ugly metal bulk. Nowadays, the products weigh more than 200 g. Around 80% of mass and volume are contributed by those components used for thermal management [36]. Besides, the product may own several thermal interfaces (TIMs) with small or large contact surfaces, and all the TIMs are suffering lots of troubles [109]. The liquid cooling is boasting its advantages of much less TIMs, simple structure and small weight. Especially, two-phase cooling could reach the smallest volume and weight for a compact thermal management. Thus, the miniaturized liquid cooling solution has attracted substantial concern in thermal management. And liquid cooling has already been successfully applied on semiconductor microelectronic packages which have high potential to be used in high-power LED. Embedded micro fluid channels on silicon substrates with good thermal characteristics were suggested as a cost-saving cooling solution with MEMS processing. Extensive work was performed on improving/optimizing liquid cooling approach [110–114]. Shakouri demonstrated an improvement of up to 300% (compared to thermal conductivity of silicon) of micro fluid channel in silicon as evaluated by both experiment and thermal modeling [37]. In addition, fluids with nanoparticles in micro fluid channel were expected to display significantly enhanced thermal conductivities [43]. Recently, Mihailovic et al. [115] introduced an all-silicon micro-evaporator heat sink device fabricated using MEMS technology with an embedded silicon heater to mimic an external heat source. The design could achieve two-phase cooling of up to $40W/cm^2$ heat by liquid flow rate of 5 mL/h. Moreover, the phase change phenomenon was simulated by Zhang et al. [116] which can clearly show the heat exchange inside the fluid channel.

The liquid cooling method generally removes heat by either 1) absorption by liquid or 2) dissipation as latent heat when the liquid evaporates in phase transition. Figure 5.2 shows the principle of two-phase cooling for heat dissipation in three stages. In the first stage where all the heat are absorbed by coolant in liquid phase (liquid fraction remained as 1), the coolant absorbs heat and its temperature

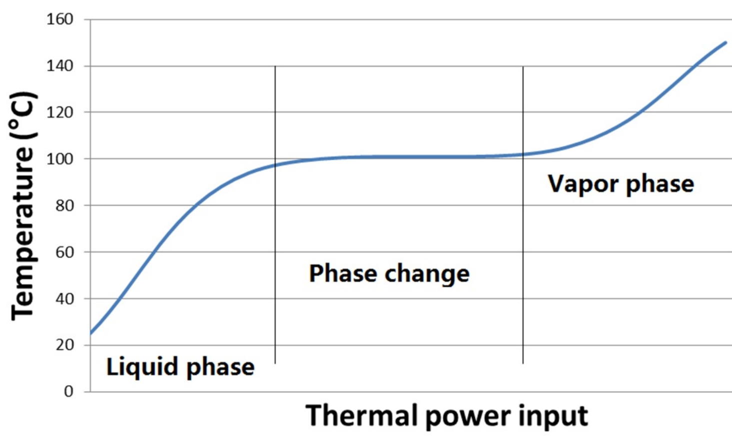

FIGURE 5.2: The principle of two-phase cooling.

consequently goes up. The amount of heat removed depends on the specific heat of coolant. In the second stage, the liquid fraction changes accordingly during the evaporation. This enables additional heat absorption due to the latent heat whereas the package temperature remains constant. While all the coolant evaporates in the third stage, the package temperature has a dramatic increase. The cooling in the last stage is no longer effective because it is gas cooling rather than liquid cooling.

The high-power LED package with high input power generally generates more heat and requires higher water flow rate for cooling. However, high flow rate does not mean cost-efficient cooling as it requires more amount of liquid and pumping power. In one hand, too high flow rate causes too much coolant flow, the coolant leaves the channel without absorbing enough amount of heat for vaporization (output liquid fraction =1), no phase change occurs. On the other hand, LED package will reach an unacceptable high temperature with too slow flow rate. To fully utilize the pumping energy, optimization of the coolant flow rate needs to be considered. Thus exception of temperature, the output liquid fraction is an important indicator for the flow rate optimization in the two-phase cooling because it should be kept in the range between 0 and 1.

The effectiveness of two-phase cooling depends on: 1) The amount of heat needs to be dissipated which is shown in equation (5.1). The total heat of LED is represented as Q_LED, which will be removed by convection (Q_c), radiation (Q_r) and fluid cooling (Q_f). A certain part of heat can be removed by the natural convection and radiation. But the fluid flow is indispensable for extra cooling if more heat is generated by LED.

$$Q_{LED} = Q_c + Q_r + Q_f \tag{5.1}$$

2) The heat dissipated by fluid cooling is determined by specific heat, latent heat and flow rate of the coolant. As shown in the following equation (5.2), Q_f is the heat removed by fluid (both liquid cooling and two-phase cooling), c_p represents specific heat of coolant, $\dot{m}_l$ denotes the liquid flow rate, T_b is boiling point of liquid, T_0 is ambient temperature, the latent heat of liquid and flow rate of vapor are L_H and $\dot{m}_v$ respectively.

$$Q_f = \frac{c_p \rho_l \dot{m}_l (T_b - T_0) + \rho_v \dot{m}_v L_H}{3600000} \tag{5.2}$$

According to the Equation (5.2), Table 5.1 demonstrates the effectiveness of cooling capacity of water from 25 °C to 100 °C, with/without phase transition. The two-phase cooling is quite efficient with 8 times less flow rate than pure liquid cooling to keep the temperature around the boiling point. Besides water, other liquids are also acceptable for the two-phase cooling. And Table 5.2 illustrates several liquid properties as coolant for the target temperature between 80 °C and 120 °C. However, water has the highest latent heat which directly leads to lowest flow rate around the best working temperature for a high-power LED package.

TABLE 5.1: The cooling capacity of water from 25 °C to 100 °C.

Q_f (W)	Specific heat (kJ/kgK)	Liquid cooling $\dot{m}_l$ (mL/h)	Latent heat (KJ/kg)	Two-phase cooling $\dot{m}_l + \dot{m}_v$ (mL/h)
0.5	4.2	5.7	2270	0.7
1	4.2	11.4	2270	1.4
1.5	4.2	17.1	2270	2.1

TABLE 5.2: The liquid properties as coolant.

Substance	Latent heat of evaporation (kJ/kg)	Boiling point (°C)
Alcohol, ethyl	855	78.3
Water	2260	100
Toluene	351	110.6

Here, we applied a miniaturized evaporator device equipped with a fluid channel to study the two-phase cooling for high-power LED packages with demineralized water as coolant (boiling point around 100 °C @ 1bar). Commercialized package with 0-2.8 W powers was cooled by the evaporator with the coolant of 0-2 mL/h flow rates inside the fluid channel. Since the latent heat of a coolant taken for phase transition is always higher than specific heat of the coolant at liquid phase,

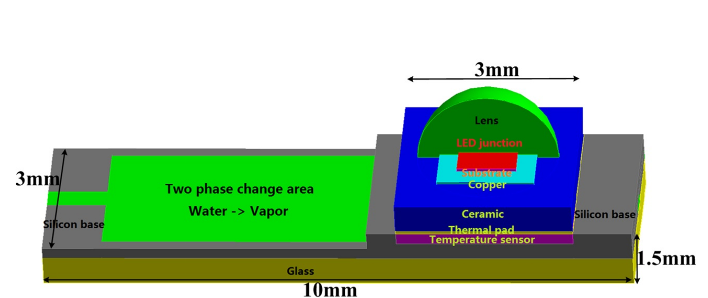

(a) The schematic illustration of a high-power LED package attached on a miniaturized evaporator.

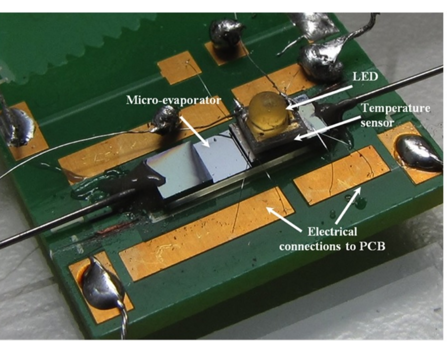

(b) The temperature measurement setup of the LED package attached to the evaporator for the two-phase cooling.

FIGURE 5.3: The experimental set-ups for a LED package with two-phase cooling.

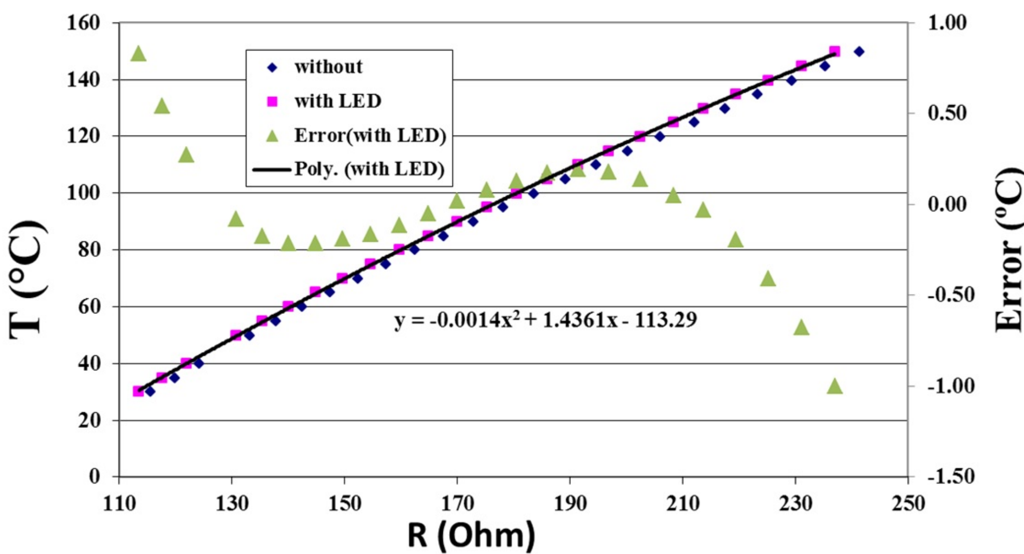

FIGURE 5.4: Calibration of temperature sensor and its accuracy.

maximizes the amount of coolant in the phase change stage would be the most efficient way for cooling. The pad temperature of the LED package was monitored to evaluate the cooling performance. Base on the experiment, 3D thermal simulation was adopted to deduce the temperature distribution and the liquid fraction. Finally, the optimized coolant flow rate for two-phase cooling could be calculated from the simulation.

5.2 Experimental setups

Figure 5.3 shows the measurement setup of a LED package attached to the miniaturized evaporator on a PCB. The evaporator is consisted of a fluid channel and a silicon substrate with a temperature sensor in the top. The fluid channel is fabricated by wet etching and wafer bonding with silicon and glass. The package is a chip on board type with a ceramic substrate and a thermal pad in the bottom for heat dissipation. To direct monitor the pad temperature of the package, the bulk silicon sensor in silicon substrate is secured with the package by good thermal glue. Calibration of the sensor was done by measured the resistance change of the resistor upon temperature change inside a well-controlled oven. As shown in Figure 5.4, the bulk temperature sensor obtained the measuring accuracy of 1 °C. And the accuracy could even achieve less than 0.5 °C when the temperature is around water boiling point (80 °C to 120 °C).

The experiment was performed by powering the LED package from 0 to 2.8 W. And the resistance of the bulk silicon sensor was measured by a source measurement unit Keithley 2601. The coolant flow was generated by a syringe with the flow rate controlled by a programmable syringe pump KDS200. The pump has the accuracy of 1% and reproducibility of 1%. And the light output was measured by the ATP LX-1308 light meter which was positioned 10 cm away from the package in a photographic laboratory. The light meter has the resolution of 1 Lux with the accuracy of ±5% ±10 Lux below 10,000 Lux.

5.3 Measurement results and discussion

Light output should be measured in order to evaluate the cooling performance for the LED package. Figure 5.5(a) shows the normalized luminous flux as a function of input powers and cooling flow rates. This figure tells that more light can be obtained from the LED as the cooling flow rate increasing. In addition, the package could be powered more than its nominal usage (around 1 W) with the two-phase cooling. However, light output declined with the high-power input (more than 1.5 W) because of the unrecoverable damage by the high currents. Thus Figure 5.5(b) shows the normalized luminous flux for power input from 0.8 to 1.3 W. It clearly shows that the increasing water flow rate can definitely benefit more light output.

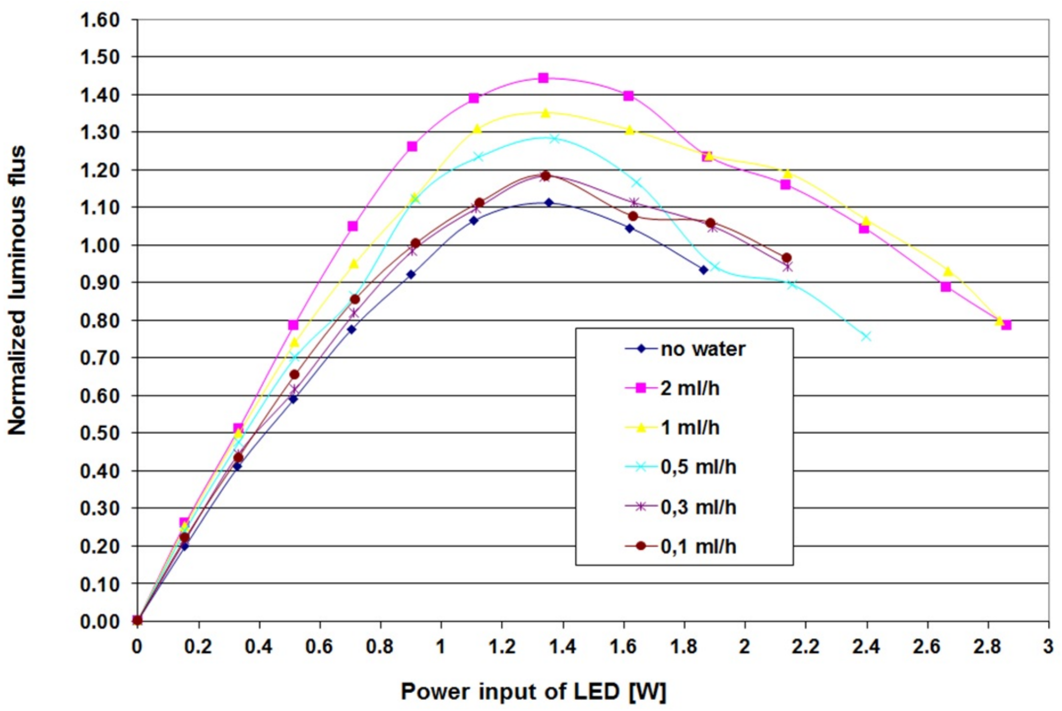

(a) The normalized luminous flux at different coolant flow rates for the LED package with various powers.

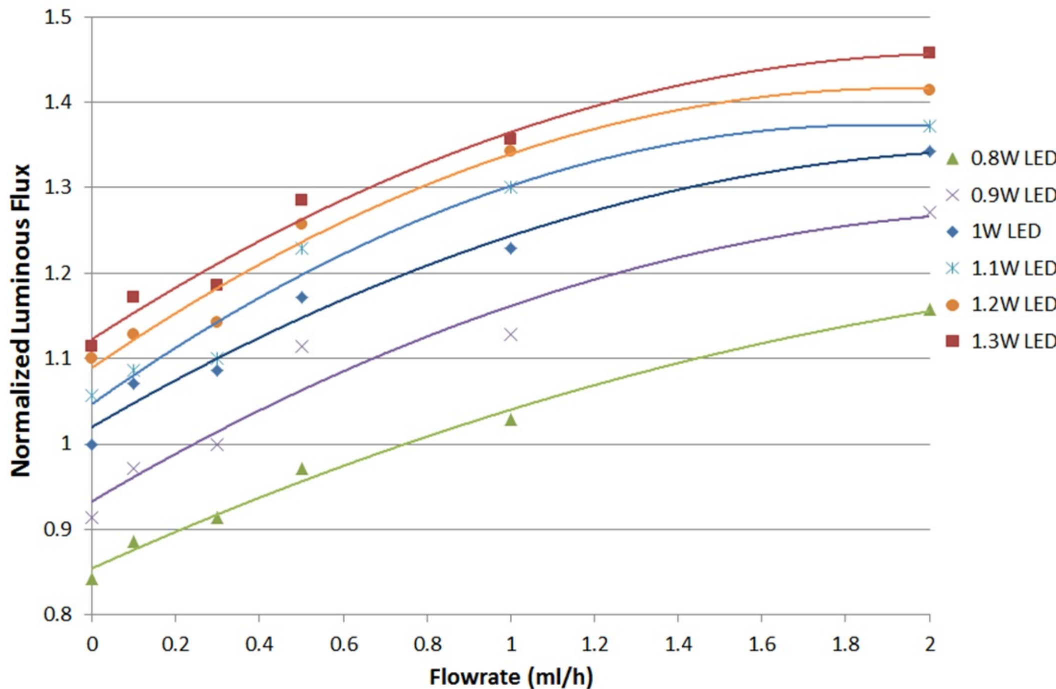

(b) The normalized luminous flux for power input of LED from 0.8 to 1.3W.

FIGURE 5.5: The improved light performance of LEDs with two-phase cooling.

For example, at least 30% more light was generated with 2 mL/h water cooling compared to the package without any cooling solution.

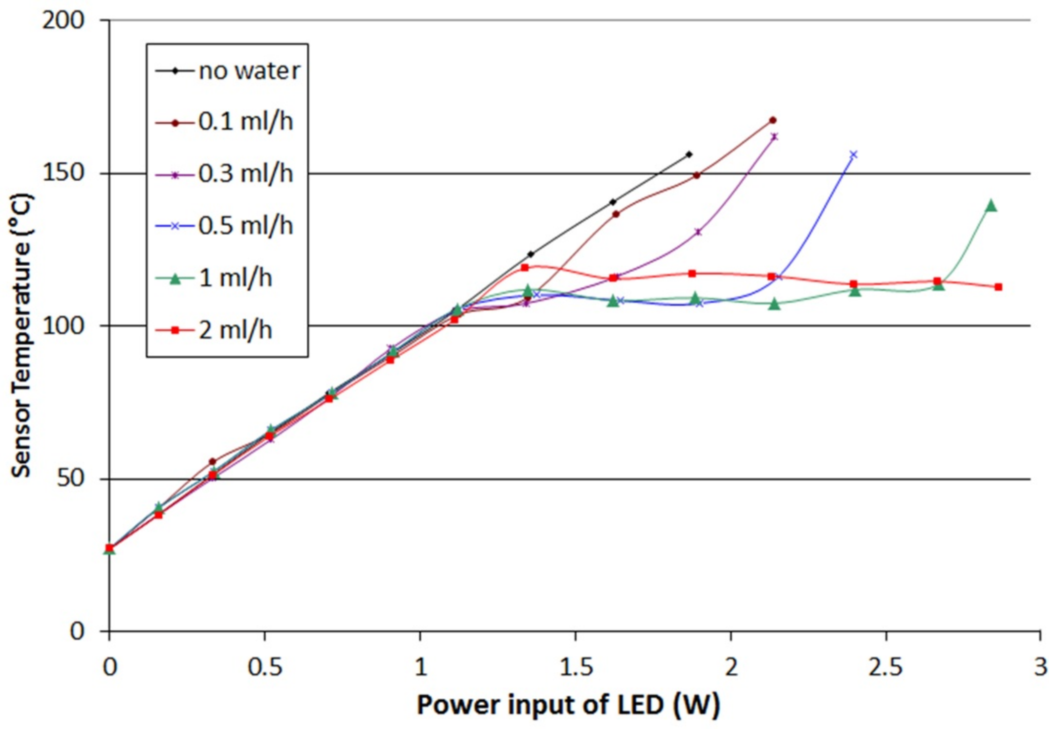

FIGURE 5.6: The temperature of a LED package at different input powers under various coolant flow rates.

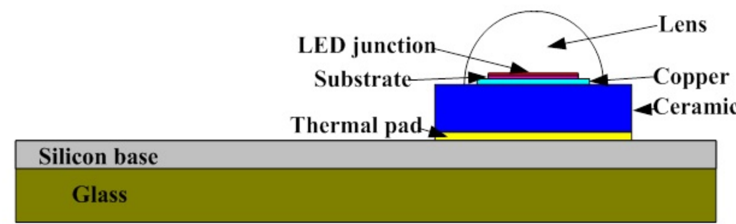

FIGURE 5.7: The schematic illustration of simulation model.

The significance of two-phase cooling was demonstrated by the 0.1 cm^2 package with the miniaturized evaporator. As a rule of thumb, the LED package has a restricted temperature limitation because the temperature above 150 °C will cause unrecoverable degradation. Thus, all the experiments were controlled within the temperature range. Figure 5.6 shows the temperature of the package monitored by the bulk silicon sensor. Without coolant supply (0 mL/h), the package temperature rose linearly. When powered by 1.8 W, the package temperature reached the limitation of 150 °C. When cooling water was supplied, the package temperature would maintain below 100 °C regardless of flow rates if the input power is lower

than 1.2 W. However, as the input power rose above 1.2 W, the cooling performance by latent heat appeared. Due to the uneven evaporation in the fluid channel, the flattened temperature varied a bit according to the coolant flow rate. For example, in the case of 2 mL/h flow rate, the package temperature remained constant lower than 115 °C when LED was powered from 1.2 W up to 2.8 W. While the package temperature kept around 110 °C in the case of 0.5 mL/h flow rate. In conclusion, if it is powered below 1.2 W, the package temperature will be lower than the boiling point of water which is cooled by liquid rather than two-phase cooling. When it is powered with more than 1.2 W, the liquid in the channel starts to evaporate. Due to the large number of latent heat, package temperature will be controlled around the boiling point. Obviously, more liquid performs better thermal management, but suffers increasing flow rate which requires more reservoir volume and pumping energy. Obviously, the experiment shows that the two-phase cooling is able to keep the package temperature below 115 °C. This temperature is therefore being set as the best working temperature for two-phase cooling of high-brightness LED.

5.4 Numerical simulation and model validation for two-phase cooling

Numerical simulation is advantageous over experimental methods in design and optimization in less time consumption, little restricted input and readily analysis data. So phase change simulation can be used to check the heat exchange in a LED package by two-phase cooling. Physical quantities, such as temperature distribution, pressure change, velocity and liquid fraction can be easily deduced then. In this work, a three dimension model was developed for the two-phase cooling for high-brightness LED.

Table 5.3 summarizes material properties for the LED package and the silicon-glass evaporator. And Figure 5.7 presents the schematic illustration of the simulation model. Besides, it is assumed that the input powers of the LED are ranging from 0 W to 2.8 W. A constant percent of heat has been transferred from input power to heat in all the cases. In this work, 30% of total energy would be converted into light according to experimental measurement. Consequently, 70% of input energy was considered as the waste heat.

TABLE 5.3: The substantial properties.

Component	Material	Thermal conductivity (W/mK)	Specific heat (J/kgK)
Lens	Silicone	0.22	1460
LED junction	GaN	130	490
Substrate	Al_2O_3	30	105
Copper	Cu	400	385
Ceramic	Ceramic	20	1500
Thermal pad	Cu	400	385
Silicon	Si	130	700
Glass	SiO_2	1.1	840

As mentioned before, the package temperature was measured by a sensor contact with the bottom pad in the experiment. In order to validate simulation results, the tested and simulated pad temperature were compared in Table 5.4 and Table 5.5. In these two tables, the maximum error between modeling and measurement was no more than 1% without cooling and no more than 4% with cooling.

TABLE 5.4: The substantial properties.

LED power (W)	0.5	1	1.5
Measured Pad temperature (°C)	62.9	97.5	132.1
Simulated Pad temperature (°C)	62.1	97.0	132.9

TABLE 5.5: The substantial properties.

LED power (W)	1	1.5	2
Input flow rate (mL/h)	0.1	0.3	1
Measured Pad temperature (°C)	94.2	112.0	109.1
Simulated Pad temperature(°C)	95.0	116.8	113.1

5.5 Simulation results and discussion

Figure 5.8 shows the simulated temperature distribution from top view of the LED package on the miniaturized evaporator. Temperature contours are shown for the package with input power of 2 W and input water ranging from 0.3 mL/h to 1 mL/h.

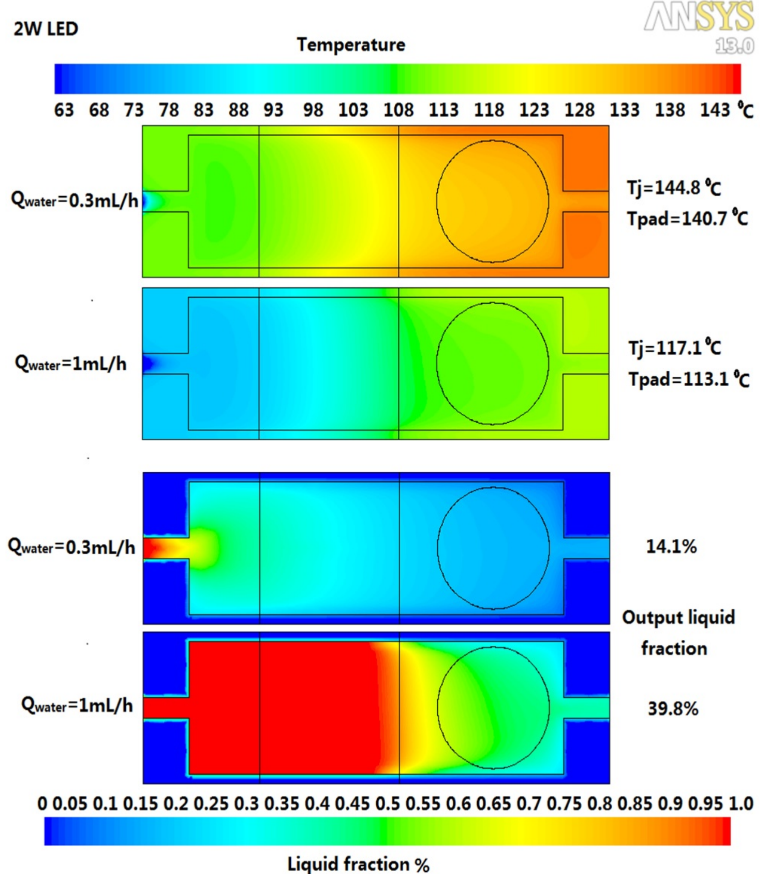

FIGURE 5.8: The simulated temperature and liquid fraction distribution: Powered LED with 2W and liquid was pumped into evaporator range from 0.3 ml/h to 1 ml/h; the contours are shown from top view.

The non-uniform temperature distribution is mainly due to the non-uniform liquid fraction. For 2 W LED, 0.3 mL/h water flow started to evaporate at the entrance due to the small flow rate. Then there was only 30% liquid in the middle position of the channel. However, the package was located on the top of evaporator close to the exit. So, there was no sufficient coolant just under LED for cooling. But if the input water flow is pumped in as 1 mL/h, liquid fraction would still keep as 1 before reaching the position of LED package. And then water evaporated just under the heat source which results in directly cooling for the package. In the end, 60% of water evaporated due to the heat, and sill 40% kept as liquid.

Table 5.6 is the summarized simulation results for two-phase cooling of the LED package. Without liquid cooling for 1 W LED, package temperature kept 97 °C. When 0.3 mL/h water cooling was applied, pad temperature of the package reduced by 5 °C. As water flow rate increasing to 1 mL/h, the package was cooled down to 87 °C. There is no phase change phenomenon because the heat generated by

TABLE 5.6: The simulated temperature with water flow.

Input power of LED (W)	Coolant flow rate (mL/h)	Junction temperature (°C)	Pad temperature (°C)	ΔT (°C)
1	0	100.9	97.0	3.9
1	0.3	94.9	92.8	2.1
1	1	89.2	87.0	2.2
2	0	171.1	166.0	5.1
2	0.3	144.8	140.7	4.1
2	1	117.1	113.1	4.0
3	0	240.0	234.0	6.0
3	0.3	207.8	201.2	6.6
3	1	172.0	165.5	6.5
3	2	120.0	113.4	6.6

1W LED could not boil water yet. When LED was powered above 1 W, package temperature would go up significantly. For 2 W LED, pad temperature was already 166 °C if no any thermal management. When 0.3 mL/h water flow was pumped into the evaporator, pad temperature would drop accordingly. Although it is still relatively high, package temperature is already lower than the limitation of 150 °C. As liquid flow rate increased to 1 mL/h, the pad temperature of package could be cooled down to less than 115 °C. For 3 W LED, the pad temperature increased to 234 °C without cooling. Thus, more liquid is required. When 2 mL/h water was applied, the pad temperate could be cooled down to 113.4 °C with junction temperature of 120 °C. Because junction temperature is hard to measure, pad temperature is chosen for evaluate the cooling performance in this work. Besides, the junction temperature is only slightly higher than pad temperature in all the simulation cases. So we can definitely deign thermal management for LED package with its pad temperature.

As mentioned before, higher flow rate results in better cooling performance with phase transition. But, more water flow requires more pumping power. The experiment shows that the two-phase cooling has the best efficiency (balance between low pumping power and suitable cooling performance) when keep the pad temperature below 115 °C. Thus, Figure 5.9 shows the optimization procedure of flow rate for specified LED input powers. Firstly of all, water flow rate according to the LED power was chosen empirically before simulation. Then the liquid fraction (should be between 0 and 1) need be checked after the first simulation. If output liquid fraction is equal to 1, the coolant has no phase change. So less coolant is required. Otherwise, if output liquid fraction is equal to 0, all the coolant evaporates which could not achieve sufficient cooling. Thus, more coolant needs to be pumped in. Moreover, the simulated pad temperature is calculated and compared with target

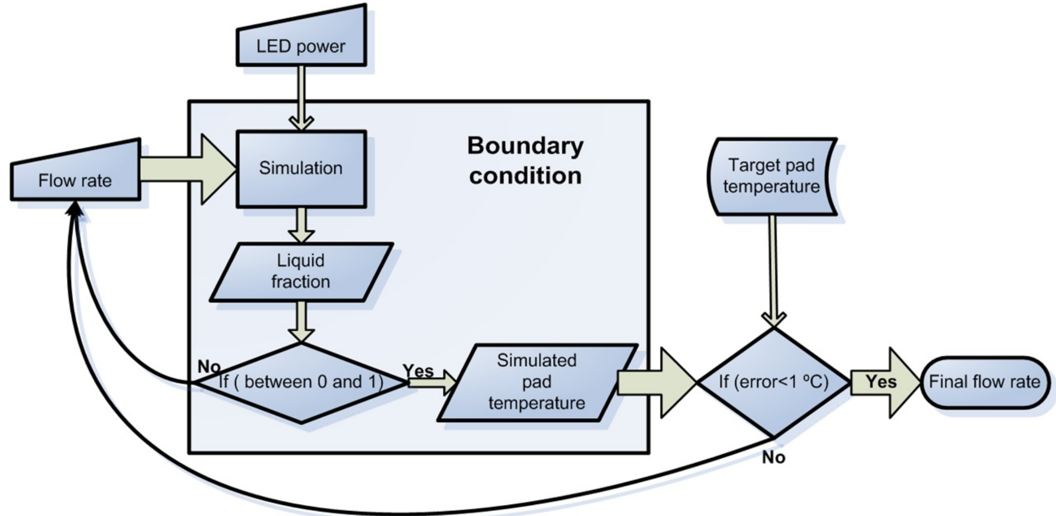

FIGURE 5.9: Optimization of flow rate for specified input power of LED.

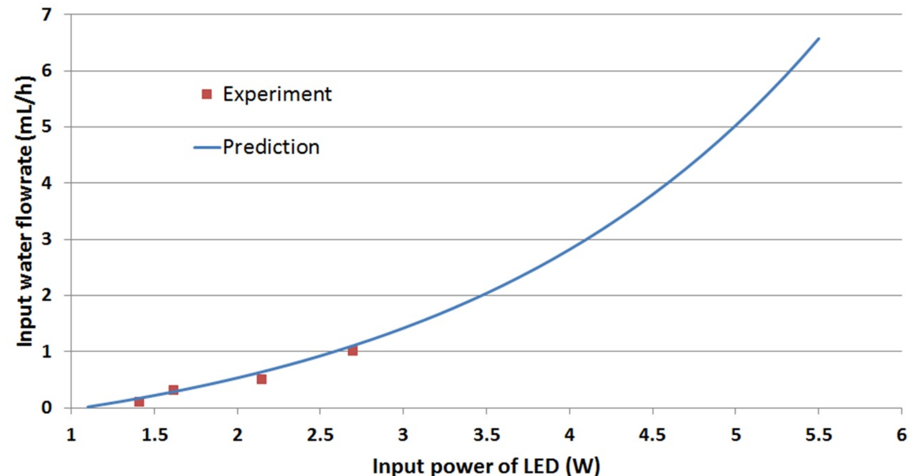

FIGURE 5.10: The results of optimized flow rate for specified input power of LED.

pad temperature (115 °C). If the error is less than 1 °C, the preset flow rate has met the design requirement. Else, more iterations are compulsory to search the optimized flow rate. Finally, the optimized coolant flow rate for efficient cooling could be calculated for the high-power LED with specific powers. In this work, the relation of optimized flow rate and input power is shown in Figure 5.10. For the silicon-glass miniaturized evaporator, the optimized flow rate almost linearly raised with increased input power ranging up to 3 W. But when the input power is much higher, it would require exponentially increased water flow rate.

5.6 Conclusion

This work presents a MEMS-based thermal management of high-power LED package. And the miniaturized silicon-glass evaporator was manufactured by wet etching and wafer bonding. Tests were performed with water flow rates in the range of 0-2 mL/h. The generated heat by LED would be removed by the two-phase cooling of water flow in the evaporator. The phase transition of coolant allowed the package temperature to remain below 115 °C with LED power up to 2.8 W, as compared to less than 1.5 W of its nominal usage. Additionally, light output was measured in a customized setup to investigate light performance with the two-phase cooling. Since the used LED is optimized for operation of around 1W, we tested the power range from 0.8 W to 1.3 W. There was a clear increase of light output at constant driving power when it was cooled by phase transition. Moreover, the simulation of two-phase cooling was applied to investigate temperature distribution and output liquid fraction. The simulation results were validated by the experiments, and the best working temperature for two-phase cooling of LED was determined. Then according to this temperature, optimization of water flow rate for the package with various powers was achieved. In addition, the coolant flow rate should be strictly controlled, in order to cool LED with the phase change phenomenon. In this work, both the experiment and simulation results confirm that the proposed cooling principle is quite promising for an integrated water-based cooling system and will definitely benefit the high-power LED.

Chapter 6

A polymer based mini LHP with silicon substrate and temperature sensors

---

An innovative thermal management with a package, a silicon substrate with temperature sensors and a polymer based loop heat pipe (LHP) was designed, manufactured and assembled. It can supply a low and relatively stable temperature to maintain higher optical power, more luminous flux and less color shift.

6.1 Introduction

As the elevated LED temperature directly affects the maximum light output, efficiency, quality, reliability and the lifetime of the SSL systems, thermal management is a key design aspect for LED products in terms of cost and performance [107]. The drive to obtain more light output is increasing, and consequently more heat needs to be dissipated from the LEDs. Current materials and novel thermal solutions all require heat sinks which are indispensable to dissipate heat to the environment. However, the bottleneck is always the low convection efficiency from solid surface to air [83]. Thus, more area is needed for better convection. To achieve more surface area with a solid, generally larger volume is required, resulting in bulky and heavy heat sinks, leading to unattractive LED products with cumbersome metal bulk. Besides, most highly thermally conductive materials are opaque and the heat sinks then completely prevent light transmission through them.

Liquid cooling can enhance thermal management with simple structure, transparency and small weight [47] as it can replace the same volume of traditional metallic heat sinks. Furthermore, liquid can remove the heat rather than conduct it which performs as better ”thermal conductivity” than solid [37, 43]. Liquid cooling has already been successfully applied in many semiconductor microelectronic applications [44] and will be easily used in LEDs. With exception of leakage and reliability, the driving force is major obstacle for setting the liquid cooling in the limited volume of LED product. Generally, small volume of liquid can be mainly driven by: micro-pump and HP. The HP which is driven by the waste heat is more appealing. Especially, the LHP possess all the main advantages of traditional HPs, but obtain special properties to transfer heat for distances up to several meters at any orientation in the gravity field [49, 50]. Polymer can be one of the best materials to archive easy fabrication, light weight and transparency for thermal management of LEDs.

In addition, LEDs also offer controllability of their spectral, spatial distribution, color temperature, etc. To control such ”smart” light sources, ”smart” thermal management is required. It is necessary to monitor and control the temperature of LED chip because the light performance is sensitive to temperature variation. Temperature can introduce color shift and consequently undesirable light quality [21, 75]. To achieve the controlled thermal management, integrated temperature

sensors on silicon can be a better choice [117] compared to the more complicated junction temperature measurement [81, 82].

In this work, a novel polymer based LHP with ethanol as working fluid was designed, fabricated and assembled in order to cool LEDs to lower temperature and obtain better light performance. The polymer material demonstrated light weight and transparency; and the LHP highly improved the thermal conductivity of polymer. The boiling point can also supply a relatively stable working temperature to improve the LED performance. Besides, The LED chip was directly attached on silicon substrate with thin thermal interface material. A group of sensors can provide the accurate temperature measurement. The semiconductor diodes and resistors were calibrated for temperature sensing at the ranges from 30 °C to 150 °C. The monitored temperature can be used to control the active cooling for LED products in further work.

6.2 Design, fabrication and assembly

6.2.1 Silicon layer above polymer based miniature loop heat pipe

The polymer based miniature LHP was designed and manufactured with acrylic polymer. And a commercial LED package was chosen to position above the two-phase region with a polymer cover. However, the dimension of the package is too small and the polymer has very poor thermal conductivity as heat spreader. So a heat spreader made from silicon is inserted between the package and the polymer layer, which is shown in Figure 6.1. And the LED package has the junction, lens, copper layer, ceramic part and thermal pad. In order to estimate the performance of the silicon substrate, a group of simulations was carried out first.

The LED package was considered as the heat source, and two simulations were conducted: one with the package directly attached on the polymer layer and the other one with the silicon heat spreader sandwiched between the LED package and polymer layer. The boundary conditions were: (i) a constant temperature at the bottom of polymer where it contacted with the two-phase region, (ii) natural convection and radiation at the surfaces except the bottom of polymer layer. In order to achieve accurate thermal simulation, 3D modeling with natural convection and radiation were conducted by Computational Fluid Dynamics in Ansys Fluent using

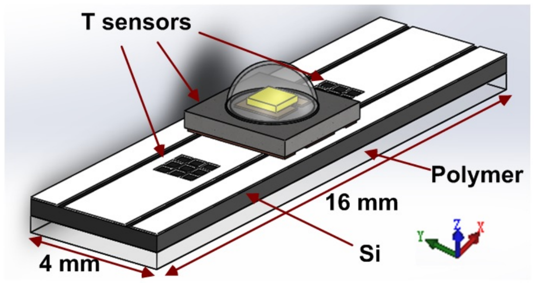

(a) Illustration of silicon-polymer layer under a LED package; temperature sensors can be arranged under/beside the package on the silicon substrate; the polymer layer is above the two-phase region which is considered as constant temperature on the boiling point of working fluid during designing.

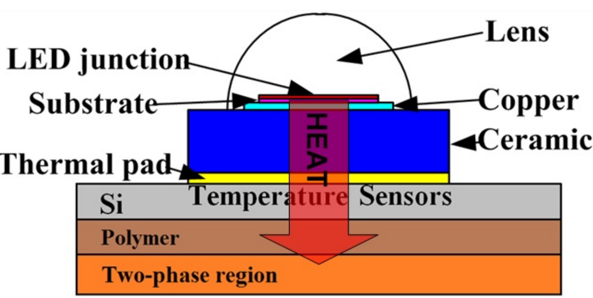

(b) The schematic drawing of the cross section along the YZ plate; the heat generated from the LED junction and mostly through the package to the silicon substrate and removed by working fluid by its latent heat.

FIGURE 6.1: The model of the silicon substrate with a polymer layer under a LED package.

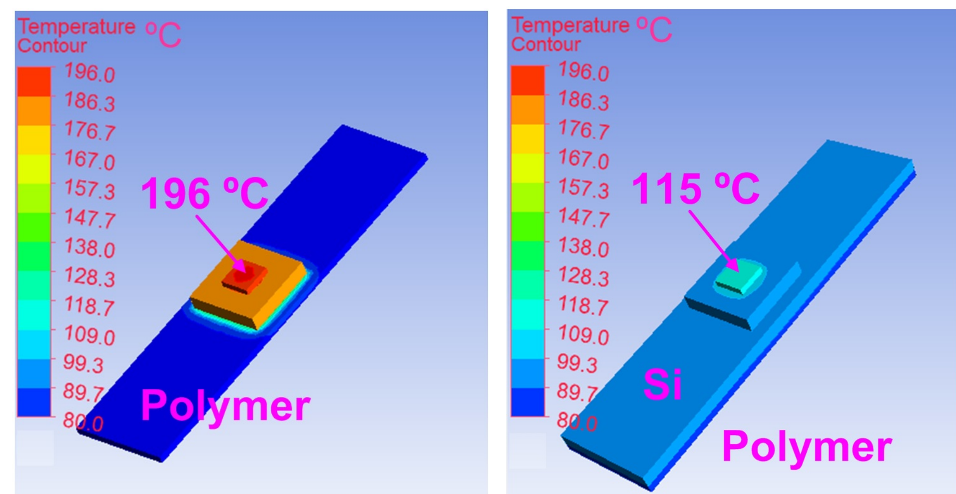

(a) 1W heat generated by LED and the simulated junction temperature reached to 196 °C without silicon substrate; polymer thickness is 0.3mm, and the temperature at bottom was assumed at 80 °C.

(b) 1W heat generated by LED and the simulated junction temperature was cooled to 115 °C with silicon substrate of 0.5mm; polymer thickness is 0.3mm, and the temperature at bottom was assumed at 80 °C.

FIGURE 6.2: The simulation results for silicon substrate design.

25 °C as ambient temperature. The material properties were chosen empirically and validated by previous work [20, 47, 83]. As shown in Figure 6.2(a), the package contained a high temperature hot spot whereas the polymer layer was hardly heated.

So the polymer cannot conduct heat from the small volume of hot spot to the two-phase region efficiently. A 0.5 mm thick silicon substrate demonstrated much better performance as a heat spreader in Figure 6.2(b). Besides, the simulated junction temperature was significantly reduced from 196 °C to 115 °C with ethanol keeping the bottom temperature constant at 80 °C.

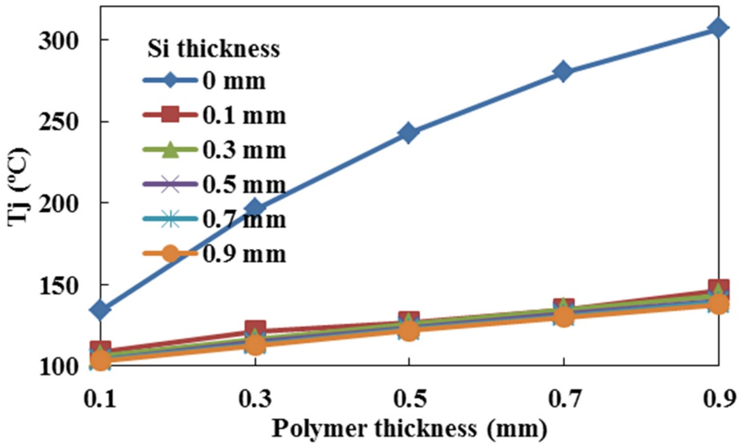

FIGURE 6.3: The simulated junction temperature versus polymer-silicon heat spreader thickness in polymer based miniature loop heat pipe.

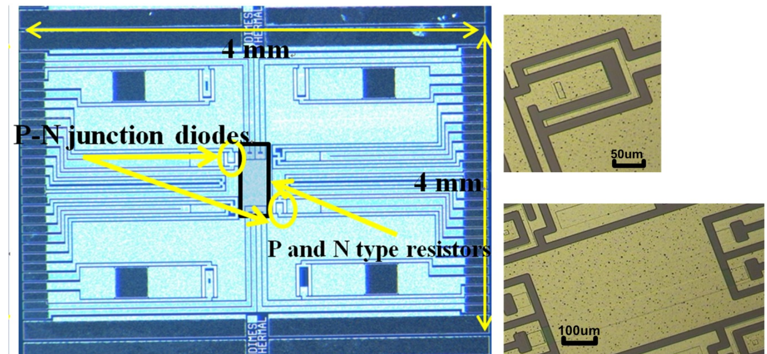

FIGURE 6.4: The temperature sensors under LED package on silicon substrate. Top right: P-N junction diode as temperature sensor. Bottom right: P and N type resistors as temperature sensors.

In Figure 6.3, a group of simulation about simulated junction temperature versus the heat spreader thickness was conducted to optimize the thickness of the polymer-silicon layer. Firstly, if only the polymer is used as the heat spreader without silicon substrate, the junction temperature was very high which can permanently damage the LED and acrylic polymer. With increasing polymer thickness, the thermal performance became worse and worse. Secondly, even a very thin, 0.1 mm, silicon substrate can dramatically reduce the junction temperature. Thirdly, a thicker

silicon layer led to lower junction temperature, but no significant improvements were observed. Therefore, as a very important component for polymer based miniature LHP, silicon substrate is indispensable as heat spreader. Besides, the required thickness of polymer layer between silicon and the two-phase region is always recommended to be as thin as possible. In this work, a 0.5 mm thick silicon layer was chosen, which is the standard thickness for a 4 inch wafer, and a 0.3 mm thick layer of polymer was designed with considerations of mechanical strength and durability.

6.2.2 Temperature sensors on silicon substrate

As the spectral and spatial distribution as well as color temperature of LEDs is affected by temperature, temperature sensors are required to monitor and even to control active cooling. However, the junction temperature measurement required several time calibrations and is relatively complex. The temperature sensors can be other option to monitor the temperature just under the LEDs which differs only slightly from junction temperature [82]. These temperature sensors can be simply integrated on silicon substrate shown in Figure 6.4. Several sensors were developed with conventional silicon processing. Two p-n junction diodes, one P type and one N type resistor were designed just under the LED chip. And the aluminum layer can supply electric connection and work as reflection. The diode sensor is a common temperature sensor used in electronic equipment due to the advantage that it can be included in a silicon integrated circuit at very low cost. The p-n junction diode which is fabricated in silicon substrate by doping with As^+ and B^+ ions. From diode equation, a linear relation between forward voltage V_f and absolute temperature T at fixed diode current I is shown as Equation (6.1):

$$\begin{gathered} T_{p-n,sensor} = a + bV_f|_I \\ b = \frac{T_1 - T_2}{V_{f1} - V_{f2}} \\ a = T_1 - V_{f1} b \end{gathered} \tag{6.1}$$

Resistor thermometer is also common temperature sensor with wide usage. In this work, we integrated the P-type doping and N-type doping resistors as temperature sensors in silicon substrate . The resistor sensors should keep linear variation of

resistivity ρ_{ele} with increasing temperature in Equation (6.2):

$$\begin{aligned} T_{ohm,sensor} &= a + b\rho_{ele} \\ a &= T_1 - b\rho_{ele,1} \\ b &= \frac{T_1 - T_2}{\rho_{ele,1} - \rho_{ele,2}} \end{aligned} \tag{6.2}$$

6.2.3 Polymer wicks and working fluids

In the polymer based miniature LHP, the driving force is from the capillary pressure gained across the liquid/vapor interface in the pores of the wick which is given by the Young-Laplace equation [50, 118]: [50, 118, 119]:

$$\Delta P_{cap} = \frac{2\sigma_l}{r_{wick}} \cos\theta \approx \frac{2\sigma_l}{r_{wick}} \tag{6.3}$$

where σ_l is the surface tension of the working fluid, r_{wick} is the wick pore radius and θ is the contact angle of the meniscus. For hydrophilic solids and wetting liquids, the contact angle can be assumed to be zero. As shown in Figure 6.5(a), the wicks were positioned in a polymer chamber with LED package above. And the chamber was divided into two parts: evaporator and compensation chamber in traditional LHP [49]. The compensation chamber was made to two purposes: (i) to accommodate excess liquid in the loop during normal operation, and (ii) to supply the capillary pump wick with liquid at all times. According to the Equation (6.4), the smaller pores can produce more capillary force. Thus we designed the pore radius as 0.3 mm, which are shown in Figure 6.5(b). And ethanol was chosen as the working fluid which is wetting liquid for polymer, obtaining suitable latent heat and working temperature with liquid density ρ_l of 789 kg/m^3, boiling point T_b of 352 K, latent heat L_H of 850 kJ/kg, and surface tension σ_l of 22.3 mN/m. As the LHP performance is far less sensitive to gravity compared to a HP, the produced device can suffer the problem as LEDs tilting. The adverse elevation of normal LHP [49], when the compensation chamber is blew the evaporator, is not favorable, but can still work with the secondary wicks. In this work, the LHP was designed specially with very long wicks extrude to the middle of the compensation chamber. Thus, it can work even at adverse elevation if the liquid inside the compensation chamber is more than half filled.

6.2.4 Fabrication and assembly

In the polymer based miniature LHP, the driving force is from the capillary pressure gained across the liquid/vapor interface in the pores of the wick which is given by the Young-Laplace equation [50, 118]: [50, 118, 119]:

$$\Delta P_{cap} = \frac{2\sigma_l}{r_{wick}} \cos\theta \approx \frac{2\sigma_l}{r_{wick}} \tag{6.4}$$

where σ_l is the surface tension of the working fluid, r_{wick} is the wick pore radius and θ is the contact angle of the meniscus. For hydrophilic solids and wetting liquids, the contact angle can be assumed to be zero. As shown in Figure 6.5(a), the wicks were positioned in a polymer chamber with LED package above. And the chamber was divided into two parts: evaporator and compensation chamber in traditional LHP [49]. The compensation chamber was made to two purposes: (i) to accommodate excess liquid in the loop during normal operation, and (ii) to supply the capillary pump wick with liquid at all times. According to the Equation (6.4), the smaller pores can produce more capillary force. Thus we designed the pore radius as 0.3 mm, which are shown in Figure 6.5(b). And ethanol was chosen as the working fluid which is wetting liquid for polymer, obtaining suitable latent heat and working temperature with liquid density ρ_l of 789 kg/m^3, boiling point T_b of 352 K, latent heat L_H of 850 kJ/kg, and surface tension σ_l of 22.3 mN/m. As the LHP performance is far less sensitive to gravity compared to a HP, the produced device can suffer the problem as LEDs tilting. The adverse elevation of normal LHP [49], when the compensation chamber is blew the evaporator, is not favorable, but can still work with the secondary wicks. In this work, the LHP was designed specially with very long wicks extrude to the middle of the compensation chamber. Thus, it can work even at adverse elevation if the liquid inside the compensation chamber is more than half filled.

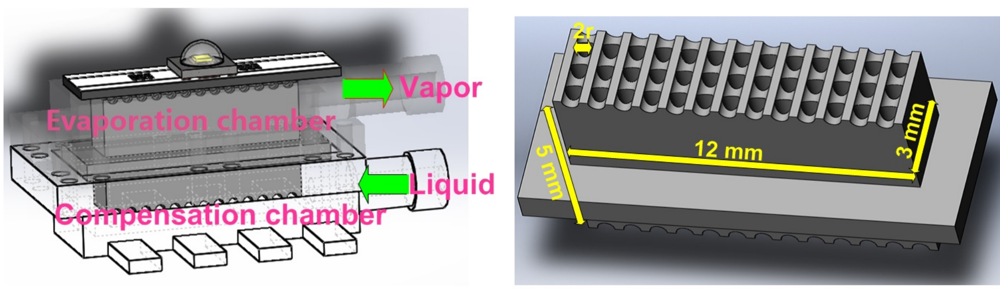

(a) The polymer wicks are positioned between the evaporation and compensation chamber.

(b) The dimensions of polymer wicks.

FIGURE 6.5: The schismatical model of the evaporator of polymer loop heat pipe.

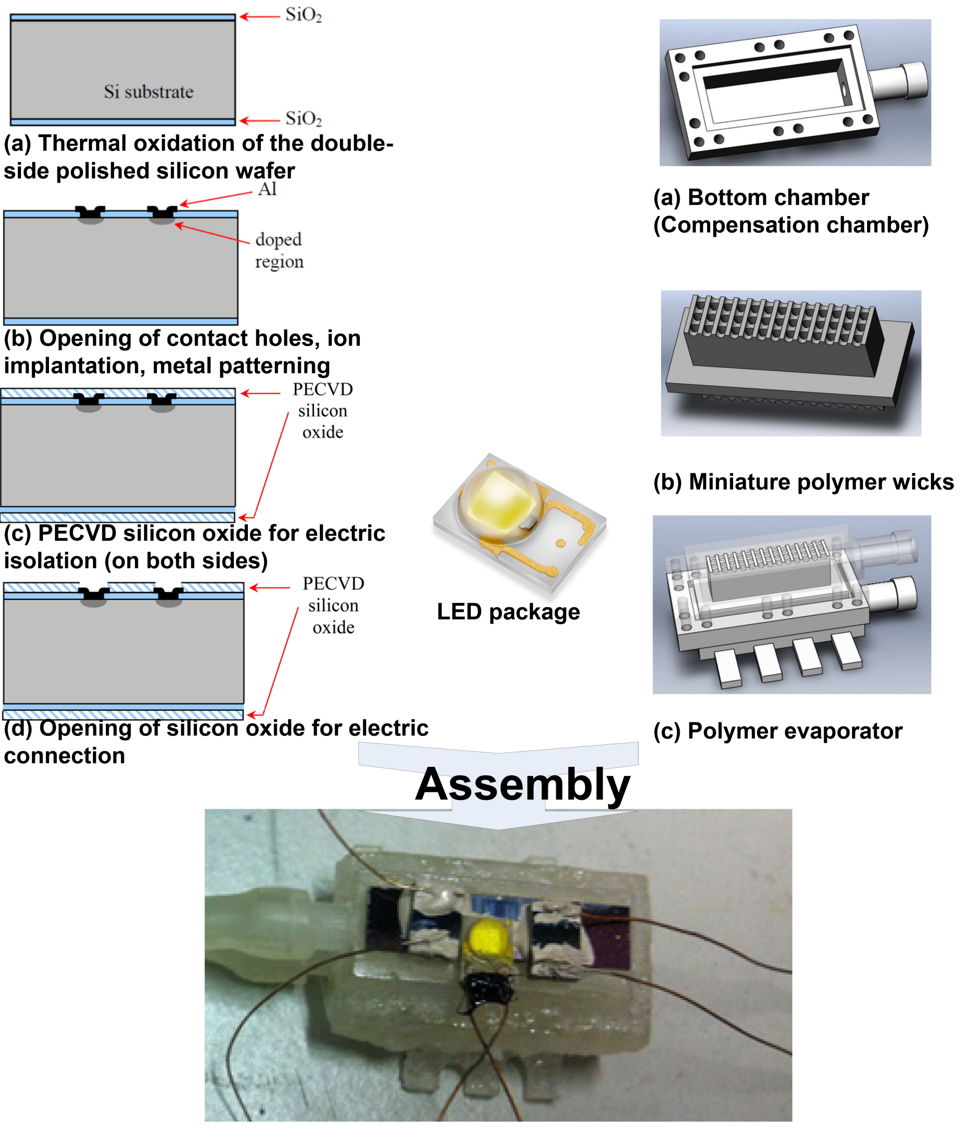

FIGURE 6.6: The manufacturing flowchart of polymer loop heat pipe: LED package, Si substrate and evaporator.

To fabricate the silicon substrate and temperature sensors, several p-type 1-0-0 wafers with thickness of 525±15 μm, and diameter of 100.0±0.2 mm were used. Firstly, a 20-22 nm thick silicon oxide layer was thermally grown by dry oxidation at 800 °C. Secondly, arsenic implantations with dose of 5.0×10^{15} ions/cm^2 under 40.0 keV, and boron implantation with dose of 5.0×10^{15} ions/cm^2 under 20.0 keV were applied to form the P-N junction diode, P and N type resistors. Then, a thickness of 100 nm silicon dioxide was formed on undoped areas by annealing. Thereafter, a layer of 400 nm aluminum was sputtered and patterned after window etching on the annealed oxide layer. Then, a 600 nm oxide layer was deposited by PECVD at 400 °C. Finally, this oxide layer was partly opened for electrical connection of the sensors. And the aluminum layer also worked as reflection. The polymer wicks and the container were both fabricated from acrylic polymer. As the wicks are in the middle, the compensation chamber and evaporator were directly separated. A commercial LED package was chosen and positioned above the silicon substrate and sensors. Then, the silicon substrate working as a heat spreader was firmly attached on the polymer LHP as shown in Figure 6.6. Two silicone tubes were used to conduct the liquid from outside tank which works as a condenser.

6.3 Experimental procedures and measurement

The calibration of the sensors was conducted by a well-controlled thermal plate in an enclosure. And junction temperature can be measured by the junction temperature-forward voltage method whose relation is almost linear at low current (such as 1 mA):

$$T_j = a + bV \tag{6.5}$$

After the determination of the parameter a and b by experiment using a thermal plate, the junction temperature can be measured by a current pulse which varies from operation currents to the measuring currents [81, 82].

In the experiment, the calibration of junction temperature and sensors were done first. The LHP with LED package worked in a liquid gas system as shown in Figure 6.7. The two syringe pumps worked oppositely to generate vacuum first and fill the ethanol. And the reservoir actually worked as complementary liquid supply and condenser in this system. As described by the limitation of LHP, the capillary force

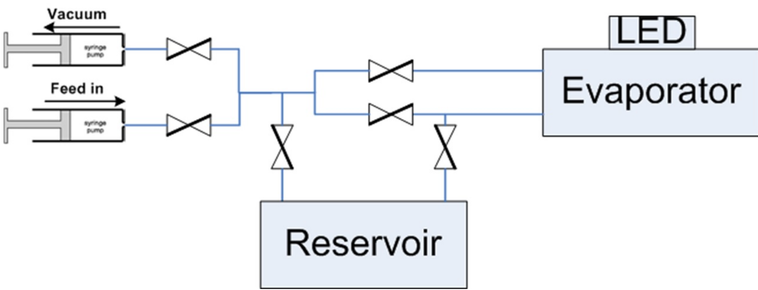

FIGURE 6.7: The schematic of the experimental setup for polymer loop heat pipe degassing, filling and test.

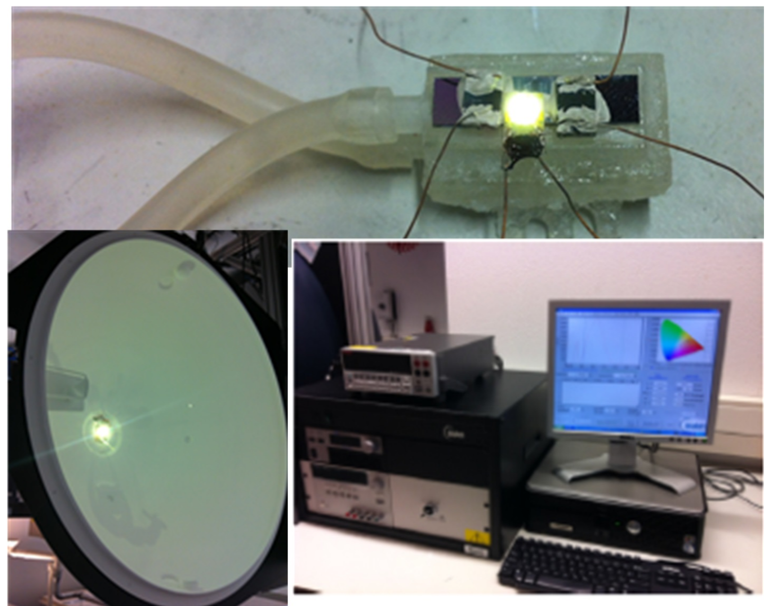

FIGURE 6.8: The test device for electric and light measurement.

should overcome the gravity which is $\Delta P_{cap} < \rho gh$ and further Equation (6.6) was conducted:

$$h < \frac{2\sigma_l}{\rho g r_{wick}} \tag{6.6}$$

Then in the measurement, the vertical height from the wick to the lowest part of the system should be no more than 19 mm according to the 0.6 mm wick pore. A system which was integrated in the lab by both optical (integrating sphere of Labsphere Inc.) and electric measurement device was used (Figure 6.8). The junction temperature, silicon temperature and light performance can be measured simultaneously after the calibration of the temperature sensors and the junction temperature-forward voltage characteristics.

6.4 Results and discussion

6.4.1 Temperature sensors

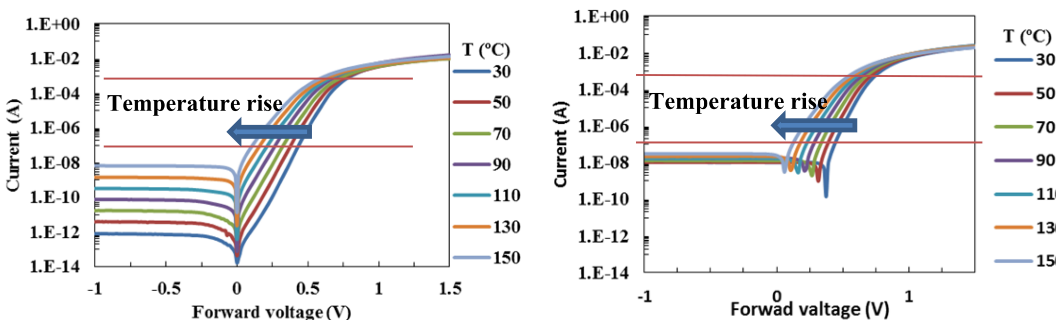

(a) The I-V curves of P-N junction diode at measured temperatures (light off).

(b) The I-V curves of P-N junction diode at measured temperatures (light on).

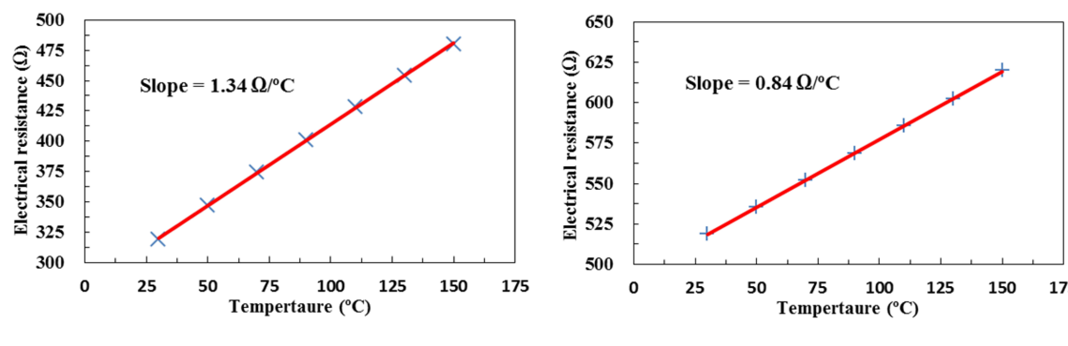

(c) The R-T curves of P-type resistor.

(d) The R-T curves of N-type resistor.

FIGURE 6.9: Calibrations of the temperature sensors.

Figure 6.9(a) shows the I-V curves of P-N junction diode at measured temperatures. In this measurement, the sensor was kept in a dark chamber without any visible light. When the current was between 10^{-8} A and 10^{-4} A, the forward voltages kept linear decrease as temperature rose from 30 °C to 150 °C. But LEDs are designed to generate light, so unexpected light response was discovered during measurement. Figure 6.9(b) shows I-V curves of the P-N junction diode at measured temperatures when an incandescent light was powered on. The forward voltage shift was obvious and the reverse current rose. However, calibration would not be affected. When the current was between 10^{-8} A and 10^{-4} A, the forward voltages kept almost the same as in the darkness. But in the end, we chose the current between 10^{-7} A and 10^{-4} A in order to avoid the ambiguous forward voltage values under the current around 10^{-8} A. During the test, the error remained very small which were all under 0.7 °C.

Meanwhile, the R-T curves of P-type resistor are illustrated in Figure 6.9(c). The P-type resistor sensor obtained high electric resistance in the same range of temperature from 30 °C to 150 °C. Figure 6.9(d) shows the R-T curves of N-type resistor. When the forward voltage is lower than 0.02 V, the error will be very large during our testing. So voltage larger than 0.02 V was used because the larger voltage between 0.02 V to 0.1 V gave better accuracy as temperature sensor whose errors are less than 1 °C with voltage larger than 0.08 V.

6.4.2 Performance of the polymer based miniature loop heat pipe

The assembled LED package and polymer LHP was measured in the test device which is shown in 6.8. The comparison was conducted by using the polymer chamber with/without working fluid. Firstly, junction temperature was calibrated and measured according to Equation (6.4). As shown in Figure 6.10(a), the junction temperature achieved 113.5 °C when 1 W electric power is input and dramatically increased to 157.9 °C in very short time as the power up to 1.72 W. And the ethanol directly cooled the junction temperate to 77 °C at 1 W electric power to 140 °C at 1.9W. Figure 6.10(b) shows the silicon temperature measured by the manufactured sensors which indicates the same rising trends as the junction temperature. As the temperature directly affects the voltage at the same current, the power difference with currents was investigated as in Figure 6.10(c). Obviously, relatively higher voltage and consequent higher power achieved with cooling by the polymer LHP. However, similar electric power still contributed lots of differences for optical power due to the temperature variation.

As the current increased, optical power raised under cooling. But a drop in optical power was observed without cooling after the current reached 400 mA, as shown in Figure 6.10(d). The diversity emerged as the electrical power increased up to about 1.35 W. This is because the junction temperature reached 133 °C at 400 mA which is the possible critical temperature for the LED. This demonstrated that a better cooling solution enhanced the optical power of the same LED up to 1.9 W.

The light quality is the most important indicator for LED performance. Then investigations of color properties when using the polymer LHP were carried out. As defined by Commission internationale de l'eclairage (CIE), the brightness is related to the optical power which can be sensed by human's eyes was defined by luminous flux;

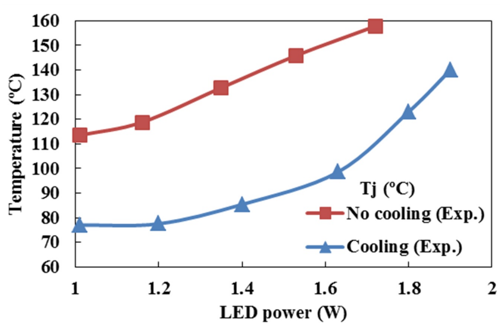

(a) The measured junction temperature differed with/ without working fluid.

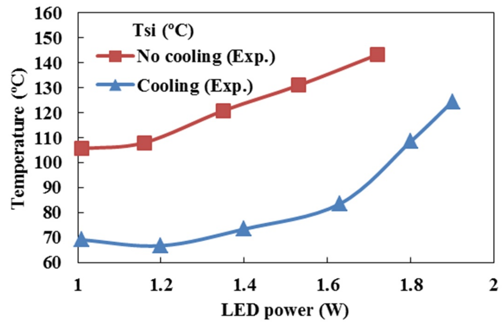

(b) The measured temperature on the silicon substrate differed with/ without working fluid.

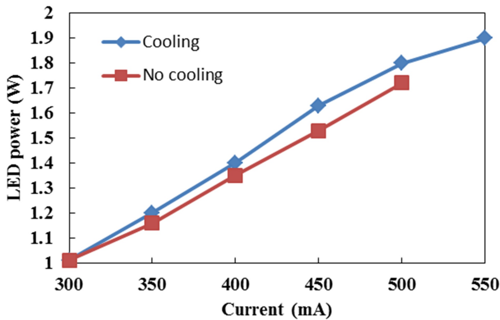

(c) The measured electric power consumed by LEDs differed with/ without cooling.

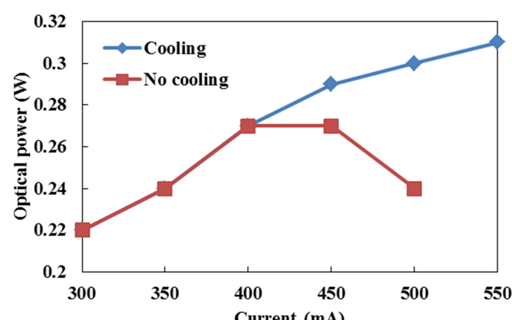

(d) The measured optical power differed with/ without cooling.

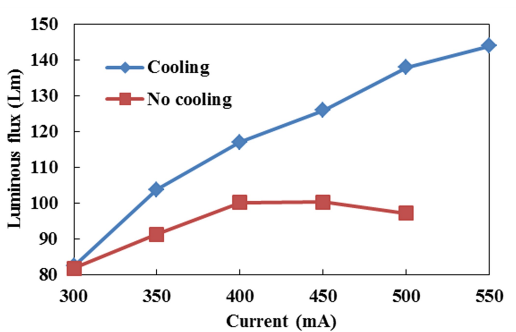

(e) The measured luminous flux differed with/ without cooling.

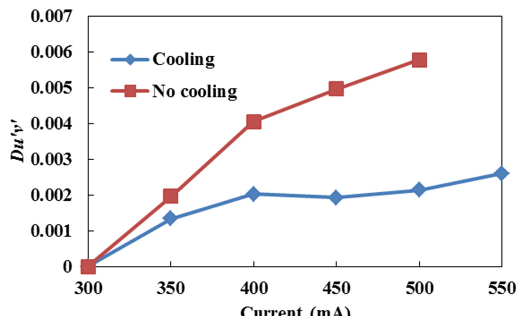

(f) The measured color shift differed with/ without cooling.

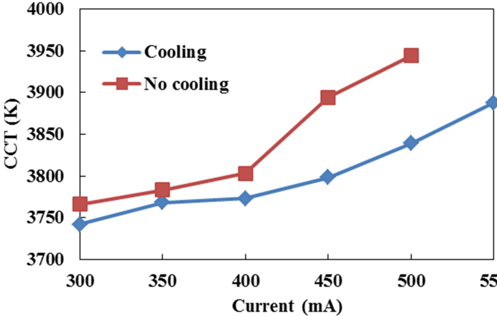

(g) The measured CCT differed with/ without cooling.

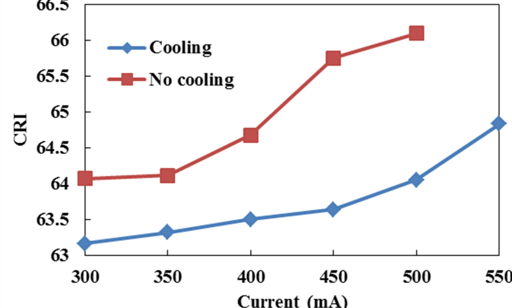

(h) The measured CRI differed with/ without cooling.

FIGURE 6.10: The measured light performance with the polymer loop heat pipe.

the changes of white light are defined by correlated color temperature (CCT) which is a function of location on the CIE curve and is measured in Kelvins with the unit symbol K; the color rendering index (CRI) is used to quantitatively measure the ability of light source to reproduce object colors in comparison with a reference light source; and the color shift at any two situations can be calculated by $Du'v'$. As shown in Figure 6.10(e), the luminous flux exhibited the same trends as the optical power and more light output was gained with the cooling solution. Oppositely, the lower temperature contributed to lower color shifts in Figure 6.10(f). As the LED products require stable color properties, the reduced color shifts, CCT change and CRI variation benefited the light performance. Therefore, this polymer LHP obtained less CCT and CRI change benefited the LED a lot in this work, which are shown in Figure 6.10(g) and Figure 6.10(h) respectively.

6.5 Conclusion

In general, a lower and stable temperature definitely enhanced the light performance of LED. However, the lower operating temperature requires very good thermal conductive materials, a complex structure for passive cooling and less efficient energy consumption for active cooling. In a word, thermal management of LEDs is not a concept to just cool but is the strategy to achieve stable temperature as low as possible with simple structure, common materials, and reliable configurations. Hence, a relatively lower but stable temperature can be the best compromise when applying thermal management for a SSL system.

The polymer based LHP can be one of the best candidates for future LEDs with its reduced weight, transparency, and better ”thermal conductivity” with less gravity affect. And silicon substrate is indispensable as heat spreader between the small package and relatively large two-phase area. Meanwhile, the silicon substrates enable the integration of semiconductor devices, such as the temperature sensors. Then, a novel polymer based LHP with silicon substrate and commercial LED package was designed, manufactured and tested in this work. All the sensors on silicon were made based on standard semiconductor processing and LED chip can be attached by pick-and-place. The temperature sensors reached accuracy within 1 °C with calibration on a well-controlled thermal plate which gives a relatively simple method to estimate the performance of cooling solutions. The junction temperatures were also measured by the junction temperature-forward voltage method. Besides,

the aluminum layer can work as light reflection layer. The two-phase cooling then was proved that it can contribute to a relatively low and stable temperature without extra power consumption for higher luminous flux, more stable CCT and CRI. In a word, the novel LED package with temperature sensors and polymer LHP can lead to the best thermal management for LEDs which achieves stable and acceptable temperature with temperature monitoring, less weight, easy fabrication, less energy consumption and better light quality.

Chapter 7

Design of vertical fin arrays with heat pipes

A thermal design of vertical fin arrays with heat pipes (HPs) as passive cooling was applied. The HPs can supply good equivalent thermal conductivity with much less weight and volume compared to copper or aluminum base and consequently less obstruction to air flow with enhanced natural convection. As the natural convection and radiation dominate heat transfer in this case, the optimum vertical fin spacing was calculated by the most used empirical correlations. Then, the design was numerical investigated by Computational Fluid Dynamics (CFD) to obtain best thermal performance.

7.1 Introduction

In order to maintain the characteristic of high efficiency and reliability to LED system, passive cooling solutions are preferred [107]. Although high heat fluxes in LED systems exceeded 100 W/cm^2 in recent years [16, 17], the generated heat in normal applications was still lower than compact and micro-sized electronic components. Therefore, thermal management under natural convection with fin arrays is attractive as they are relative more reliable, noise free and economical.

Former researchers mainly focused on the traditional heat sink with vertical or horizontal fins on vertical or horizontal base. Compared to a bare plate, fins dramatically increased the heat transfer interface between heat sink and environment, and consequently achieved highest heat dissipation to volume ratio. However, the performance of heat sinks with natural convection is highly dependent on the geometry parameters. In limited volume, the vertical fin length, fin inclination and spacing are critical to optimize the performance of heat sinks. Elenbaas [120] firstly measured the heat dissipation of two plates of h × h cm^2 as function of distance. They found that the natural convection coefficient between two plates rose until a certain distance around 1 cm. Bar-Cohen and Rohsenow [121] gave theoretical analysis aimed at establishing an analytical solution for optimization of vertical arrays with natural convection. Starner and McManus [122] presented natural convection heat transfer performance data for four large rectangular fin arrays oriented vertically, 45 °C and horizontally. Form their conclusion, the vertically based orientation is the most favorable system for application of the base and fin type heat sink. Welling and Woolbridge [123] reported there existed an optimum values of the ratio of fin height to spacing for rectangular vertical fins. From then on, many researchers experimentally studied vertical and horizontal fin arrays with natural convection and some simplified correlation were reported [124–127]. Recently, Yazicioğlu and Yüncü [128] reported the convective heat transfer rate from fin arrays obtained a maximum value as a function of fin spacing and height for a given base-to-ambient temperature difference. Their experiments were conducted by fin length of 250 and 300 mm, aluminum fin thickness of 3 mm, fin height varied from 5 to 25 mm and fin spacing differed from 5.75 to 85.5 mm. Besides, three-dimensional numerical studied on this subject were carried out which obtained good agreement with experimental results [129, 130]. And the numerical method can predict Nusselt numbers with correlations based on the effects of various fin geometries and spacing [131, 132]. More recently, Tari and Mehrtash [133] generated a set of dimensionless

correlations for the convective heat transfer rate from steady-state simulation. Their results have a practical use in electronics cooling applications due to the investigated ranges of parameters are suitable for electronics device cooling. In addition, thermal radiation which typically accounts for 25% of the total heat dissipated by natural convection finned heat sink cannot be simply neglected [45]. Rammohan Rao and Venkateshan [134] calculated natural convection and radiation contributions independently and then adding them to obtain the total heat loss from the fin arrays. Khor et al. [46] concluded that the errors induced are more than 30% when thermal radiation is neglected, and exceed 60% when thermal radiation is considered without including view factor.

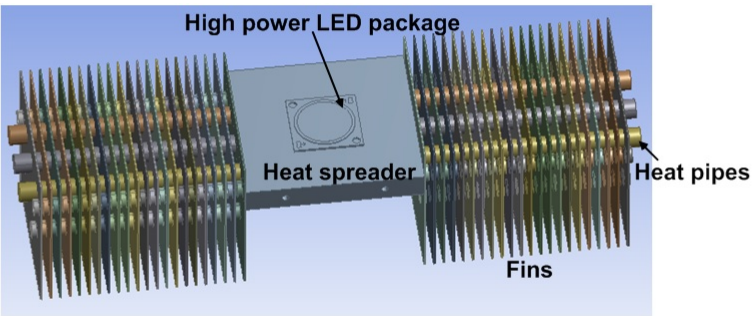

FIGURE 7.1: Designed structure with heat pipes for air cooling of a high power LED package.

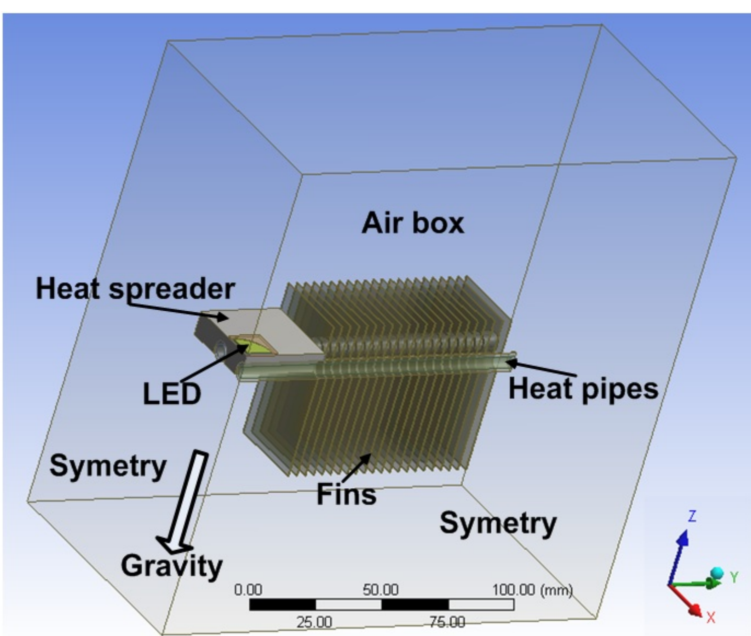

FIGURE 7.2: The schematic view of the model for simulation.

In this work, we designed a heat sink with heat pipes and parallel vertical fins to control the case temperature of a 80 W LED under 70 °C, as about 75% of

electric power was estimated as heat [21, 47]. The used HPs can replace the base which significantly reduced the total weight. Beside, as the base especially on the top position will dramatically decrease the fin efficiency [83, 133], the HPs can achieve sufficient conduction with less volume and consequently less obstruction for vertical air flow of natural convection. Compared to previous work, both empirical correlations and numerical simulations were conducted for designing the heat sink with consideration of natural convection and thermal radiation. As shown in Figure 7.1, the high-power LED package was positioned on the top of aluminum heat spreader with three HPs underneath. The designed aluminum fins connected to the three HPs at right-hand and left-hand side. Due to the application, there was limitation of 85 mm total width for fins at each side. As the fins dominate the convective and radiative heat transfer from heat sink to environment, the analytical solutions were conducted firstly to decide the fin spacing. Then, a set of testing with steady-state natural convection and radiation is numerically investigated according to the parameters of analytical solutions in order to obtain accurate prediction of thermal performance and achieve the optimum thermal design. Finally, the experiment tests were applied to validate the design.

7.2 Numerical modeling

The computational domain can be reduced to a quarter model which significantly decreased the calculation time. As shown in Figure 7.2, a simplified LED package with a short cylinder heat source and a thin rectangle substrate was positioned on the aluminum heat spreader, and aluminum fins thermally connected to the three HPs. Then heat can be conducted from heat source to fins through the heat spreader and the HPs. All the solid components were simulated in the air box where heat finally should be transferred to air by natural convection and thermal radiation. The dimension of aluminum heat spreader was designed as $72 \times 68 \times 10$ mm^3 and aluminum fin dimension was designed as $1 \times 68 \times 62$ mm^3 on xyz directions.

7.2.1 Governing equations for air

The physical phenomenon can be expressed by a set of partial differential equations which represent the conservation of mass, momentum and energy and

these equations were solved using a commercial solver with adequate boundary conditions.

Conservation of mass:

$$\frac{\partial(\rho u)}{\partial x} + \frac{\partial(\rho v)}{\partial y} + \frac{\partial(\rho w)}{\partial z} = 0 \tag{7.1}$$

Conservation of momentum:

$$\frac{\partial(\rho u^2)}{\partial x} + \frac{\partial(\rho uv)}{\partial y} + \frac{\partial(\rho uw)}{\partial z} = -\frac{\partial P}{\partial x} + \mu(\frac{\partial^2 u}{\partial x^2} + \frac{\partial^2 u}{\partial y^2} + \frac{\partial^2 u}{\partial z^2}) \tag{7.2}$$

$$\frac{\partial(\rho uv)}{\partial x} + \frac{\partial(\rho v^2)}{\partial y} + \frac{\partial(\rho vw)}{\partial z} = -\frac{\partial P}{\partial y} + \mu(\frac{\partial^2 v}{\partial x^2} + \frac{\partial^2 v}{\partial y^2} + \frac{\partial^2 v}{\partial z^2}) \tag{7.3}$$

$$\frac{\partial(\rho uw)}{\partial x} + \frac{\partial(\rho vw)}{\partial y} + \frac{\partial(\rho w^2)}{\partial z} = -\frac{\partial P}{\partial z} + \mu(\frac{\partial^2 w}{\partial x^2} + \frac{\partial^2 w}{\partial y^2} + \frac{\partial^2 w}{\partial z^2}) + g(\rho - \rho_0) \tag{7.4}$$

Where β is the thermal expansion coefficient, the density was simplified by Boussinesq Model:

$$(\rho - \rho_0)g = -\rho_0\beta(T - T_0)g \tag{7.5}$$

Conservation of energy:

$$\frac{\partial(\rho uT)}{\partial x} + \frac{\partial(\rho vT)}{\partial y} + \frac{\partial(\rho wT)}{\partial z} = \frac{k}{c_p}(\frac{\partial^2 T}{\partial x^2} + \frac{\partial^2 T}{\partial y^2} + \frac{\partial^2 T}{\partial z^2}) \tag{7.6}$$

7.2.2 Governing equations for solid

Fourier's heat conduction equations were used to calculate the temperature distribution for a solid part, such as heat spreader and fins.

$$\frac{\partial^2 T}{\partial x^2} + \frac{\partial^2 T}{\partial y^2} + \frac{\partial^2 T}{\partial z^2} = 0 \tag{7.7}$$

7.2.3 Solution algorithm

The numerical model was based on finite volume formulation which was solved by the widely used commercial Computational Fluid Dynamics (CFD) solver

ANSYS Fluent. These equations were solved by employed SIMPLE algorithm [132]. The surface-to-surface radiation model was used to handle the radiative heat transfer due to the view factor was critical [133].

7.2.4 Boundary conditions

Only one quarter of the total structure and air box were simulated, and symmetry conditions were then applied. The air box walls were set as constant temperature 23 °C and for radiation emissivity $\varepsilon = 0.8$ was used for all the aluminum surfaces. As the too small air box dimension negatively affect the accuracy of simulation [83], the dimension of $400 \times 200 \times 200$ mm3 on *xyz* directions was chosen.

7.2.5 Thermal conductivity of the heat pipe

Three HPs with length about 250 mm and diameter of 8 mm were applied. The heat pipe is shown in Figure 7.3, with the four points for thermal couples. As the convection and radiation dominate the overall thermal performance of the heat sink, the HPs were considered as solid rod with equivalent thermal conductivity (ETC) for simplification in simulation. As shown in Figure 7.4, the ETC tests for heat pipes were conducted by measuring the temperature difference with specified powers supplied. Our setups for one heat pipe in Figure 7.4(a) are similar to the previous testing as reported by Legierski [135], but a heat source rather than the hot water container was used and there was only air around the adiabatic sector without specified insulation layer. Four thermal couples were put on the heat pipe with one at evaporator, two at condenser and one at the adiabatic section. After measurements, the ETC of the heat pipe under thermal power 13.65 to 21 W was varied from 13487 to 20230 W/mK when it is in horizontal configuration, as shown in Table 7.1. The measured values of ETC when the heat pipe is horizontal are close to the reference [135]. However, the heat pipes obviously did not work in such conditions with ideal cooling. Thus, a testing setup based on application configurations was establish to measure the real ETC of heat pipes, which is shown in Figure 7.4(b). Similar to the designed structure for LED application, the heat source was set in the middle of heat pipes with air cooling by ten fins at each side. The ETC of heat pipes derived on application configurations is much lower than the value with water cooling, which is only around 2500 W/mK in Table 7.1. Even though the real ETC is much lower

than the prediction, the heat pipes already archives much better thermal properties than normal materials.

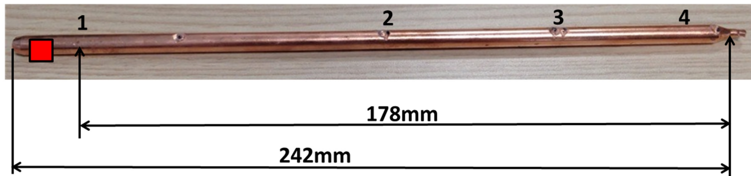

FIGURE 7.3: The heat pipe with 4 points for thermal couples.

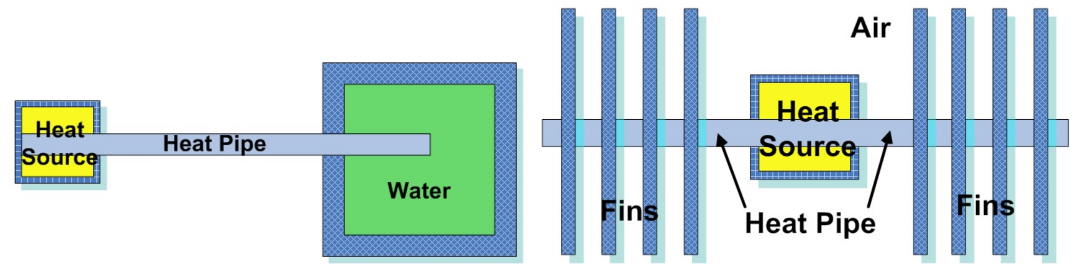

(a) The normal testing setup for one heat pipe. (b) The testing setup for heat pipes derived on application configurations.

FIGURE 7.4: The ETC testing for the heat pipes:

TABLE 7.1: The equivalent thermal conductivity of the heat pipe.

Configuration	Test	Average ΔT (°C)	Power (W)	Average ETC (W/mK)
single heat pipe with water cooling (Horizontal)	Test 1	24.63	13.6	13487
	Test 2	26.53	15.15	21355
	Test 3	34.47	21	20230
Heat Pipes with air cooling (Horizontal)	Test 1	7.21	30.86	2472
	Test 2	9.72	42.94	2543
	Test 3	11.93	61.17	2940

7.3 Results, comparisons and discussion

7.3.1 Analytical solutions

Analytical solutions can directly supply quick estimation at the beginning of design for vertical fin arrays. Although the most used correlations were mainly focused on the base and fin type heat sinks, the convective and radiative heat transfer were mainly dominated by fins. Therefore, the analytical solutions based

on correlations derived from vertical fin arrays on vertical base still can give good prediction as our design requires optimum fin spacing.

7.3.2 Thermal conductivity of the heat pipe

As shown in Figure 7.5, a simplified model without base and HPs was establish to analytically calculate the total heat transfer by radiation and natural convection in order to optimize fin spacing. As we designed, the fin vertical length L is 62 mm, the fin horizontal length H is 68 mm, and the aluminum fin thickness t is 1 mm. The total fin width W is decided as 2×85 mm. Thus, the fin number n and fin spacing s can be tuned to optimize the thermal performances in this design.

Bar-Cohen and Rohsenow [121] reported their work on natural convection by theoretical analysis without consideration of base. Their results showed the rate of heat transfer from each plate decreased as plate spacing was reduced. The natural convection heat transfer rate was concluded as:

$$Q_c = (s+t)^{-1} s^{-1} \left(\frac{576}{G^2 s^8} + \frac{2.873}{G^{0.5} s^2}\right)^{-0.5} (2LHW \triangle Tk) \tag{7.8}$$

Where, k is the thermal conductivity of the fins, ΔT is the temperature difference between fin and air, and G is an intermediate parameter with specific heat c_p, air density ρ, volumetric thermal expansion coefficient β, dynamic viscosity μ, and gravity g.

$$G = \frac{c_p \rho^2 g \beta \Delta T}{\mu k L} \tag{7.9}$$

From Equation (7.8), the optimized spacing is calculated between 4.5 mm to 7 mm as shown in Figure 7.6(a). When the temperature difference between fin and air is 50 °C, maximum 39 W heat can be removed by natural convection of the vertical fin arrays.

Yazicioğlu and Yüncü [128] experimentally investigated the steady-state natural convection heat transfer from aluminum vertical rectangular fins extending perpendicularly from vertical rectangular base. They determined the order of magnitude of fin spacing for the maximum convection heat transfer rate from the fins, with consideration of two extreme conditions: (1) Limiting cases of very small value of s (small-s limit). (2) Opposing limiting cases in which the ?n spacing s is large (large-s limit). The first limit is represented by $Q_c^{(1)}$ in Equation (7.10) and the second limit

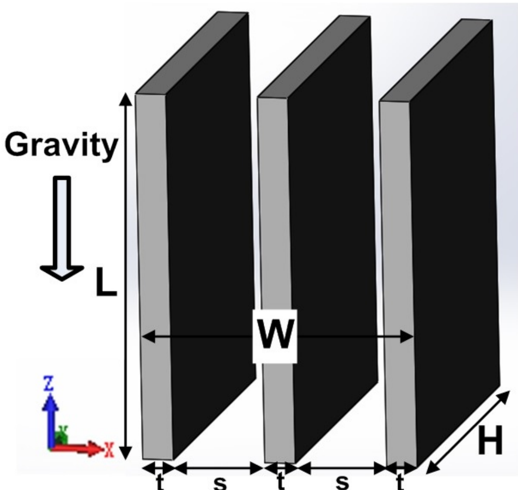

FIGURE 7.5: The schematic drawing of analytical model.

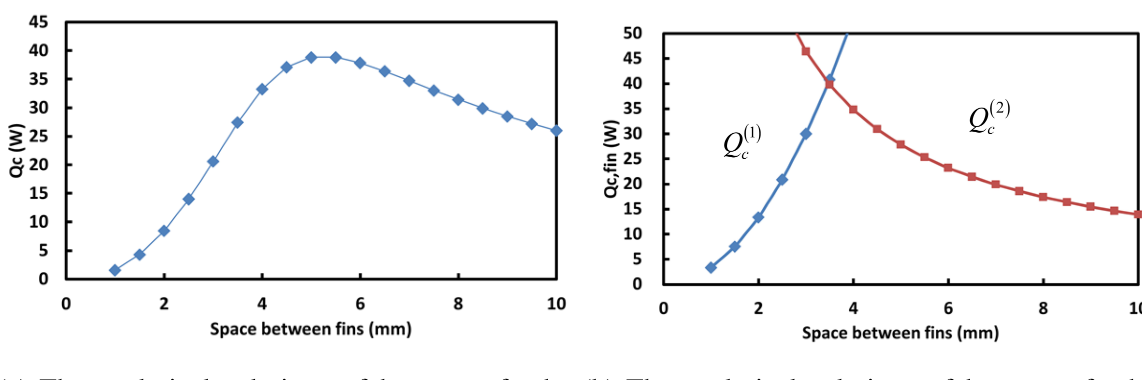

(a) The analytical solutions of heat transfer by natural conviction (Bar-Cohen and Rohsenow [121]).

(b) The analytical solutions of heat transfer by natural convection (Yazicioğlu and Yüncü [128]).

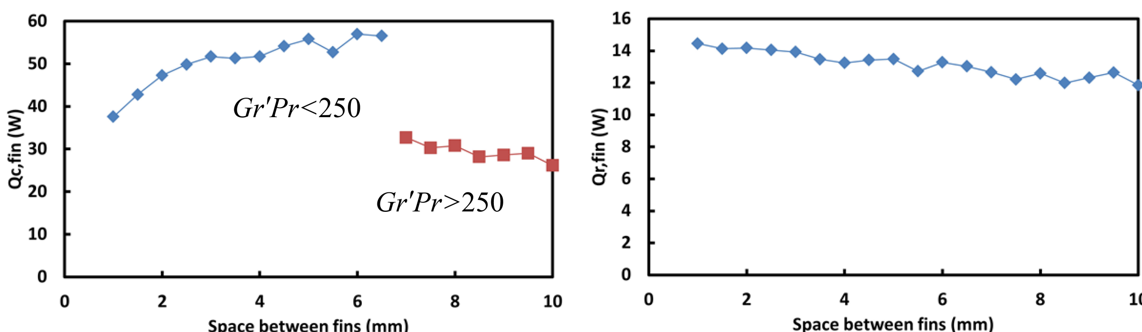

(c) The analytical solutions of heat transfer by natural convection (Tari and Mehrtash [133]).

(d) The analytical solutions of heat transfer by radiation (Khor et al. [46]).

FIGURE 7.6: The analytical solutions between fin spacing and heat transfer rate by natural conviction .

is defined as $Q_c^{(2)}$ in Equation (7.11).

$$Q_c^{(1)} \approx \frac{g\beta s^3(T_f - T_a)}{\upsilon\alpha} Hk(T_f - T_a)\frac{W}{s} \tag{7.10}$$

$$Q_c^{(2)} \approx [\frac{\rho g \beta L^3 (T_f - T_a)}{\upsilon \alpha}]^{\frac{1}{4}} Hk(T_f - T_a)\frac{W}{s} \tag{7.11}$$

Where, ρ is air density, β denotes the volumetric thermal expansion coefficient, k is the thermal conductivity of the fins, $(T_f - T_a)$ is the temperature difference between fin and air, and υ represents the kinematic viscosity, α is thermal diffusivity and g is the gravity. As shown in 7.6(b), the optimum fin spacing is the value of the intersection of small-s limit and large-s limit. The optimized fin spacing calculated in this work is from 3 to 5.5 mm for dissipation of maximum 40 W heat with temperature difference of 50 °C.

Tari and Mehrtash [133] numerably investigated the steady-state natural convection from heat sinks with parallel arrangement of rectangular cross section vertical plate fins on a vertical base and obtained a validated model which can also predict the optimum fin spacing. They conducted their correlations from a modified Grashof number suggested by Leung and Probert [136]:

$$Gr' = \frac{g\beta(T_f - T_a)s^4}{\upsilon^2 (HL)^{\frac{1}{2}}} \tag{7.12}$$

Then their suggested correlations [133] for Nusselt number are:

$$Nu = 0.0929(Gr'Pr)^{\frac{1}{2}} \quad Gr'Pr < 250 \tag{7.13}$$

$$Nu = 0.2413(Gr'Pr)^{\frac{1}{3}} \quad 250 < Gr'Pr < 10^6 \tag{7.14}$$

The average natural convection coefficient can consequently be generated by the definition of Nusselt number as Equation (7.15).

$$Nu = \frac{h_c L}{k} \tag{7.15}$$

As the total natural convection heat transfer rate is defined by $Q_c = h_c A(T_f - T_a)$, the relation between heat transfer rate and fin spacing is shown in Figure 7.6(c). According to the correlations 7.13 and 7.14, the optimized fin spacing is from 3 to 6 mm at temperature difference of 50 °C and the corresponding heat transfer rate differs slightly. The discontinuity occurs at fin spacing of 6.5 mm where $Gr'Pr$ is just equal to 250.

As radiation account for more than 20% heat transfer on heat sinks by natural convection, Khor et al. [46] suggested that the view factor is critical to avoid

errors when considering radiation. The grey body view factor of the channel formed between adjacent fin walls is given as:

$$\hat{F} = \frac{1}{\frac{1-\varepsilon}{\varepsilon} + \frac{1}{F_c}} \tag{7.16}$$

where F_c is the channel view factor, characterizing the total view factor between the base (or heat pipes) and the fin walls and its surrounding medium. With $\bar{H} = \frac{H}{s}$, $\bar{L} = \frac{L}{s}$ and correlations for F_{1-4}, F_{1-5}, F_{2-4}, F_{2-5} [46]:

$$F_c = \frac{F_{1-4} + 2F_{1-5} + 2\bar{H}(F_{2-4} + 2F_{2-5})}{1 + 2\bar{H}} \tag{7.17}$$

With consideration of the fin heat sink as a diffuse and a grey body, and taking the effect of the view factors, the total radiation heat transfer rate by radiation Q_r from the heat sink is computed as:

$$Q_r = [\hat{F}(n-1)2HL + \varepsilon[2nt(H+L) + 2HL]]\sigma(T_f^4 - T_a^4) \tag{7.18}$$

Differed from the original equation, the effect between the base and fins was neglected in Equation 7.18. The calculated heat transfer by radiation is shown in Figure 7.6(d) as we consider the emissivity of fin is equal to 0.8 and temperature difference is 50 °C. As the fin spacing decreasing, the heat radiative heat transfer rate drops slightly. However, the 1 W difference only take account for 8% of radiative heat transfer and 1.7% of total heat transfer. Therefore, we do think that the changing of fin spacing hardly has effect on radiation.

As the fin spacing hardly change the radiative heat transfer rate, the optimization of vertical fin arrays conducted by calculation of fin spacing according to natural convection firstly. Then, the maximum heat transfer rate is the conducted by adding the radiation effect at optimum fin spacing under natural convection. In our design, the Q_r keeps constant during fin spacing from 3 mm to 7 mm as 13 W, the maximum heat transfer by natural convection and radiation can be calculated during the optimum fin spacing range as:

$$Q = Q_c + Q_r \tag{7.19}$$

7.3.3 Numerical results

In simulation, the input heat of 60 W were applied and dissipated by convective and radiative heat transfer with air temperature 23 °C. Figure 7.7 shows the temperature distribution of the thermal design for LED with fin spacing of 3 mm. The highest temperature is in the heat source with simulated junction temperature of 123 °C. Under the LED package, the solder temperature is 78.8 °C. And the $\frac{1}{2}$ HP with 125mm obtains 13 °C difference from the heat spreader to the end which is about 56.7 °C. The ETC of the heat pipe used by simulation is 2940 W/mK.

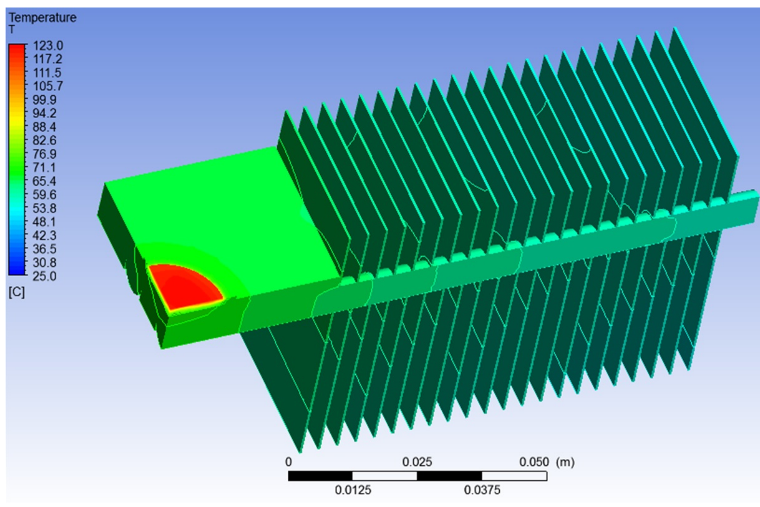

FIGURE 7.7: The temperature distribution of thermal design for LED with fin spacing of 3 mm.

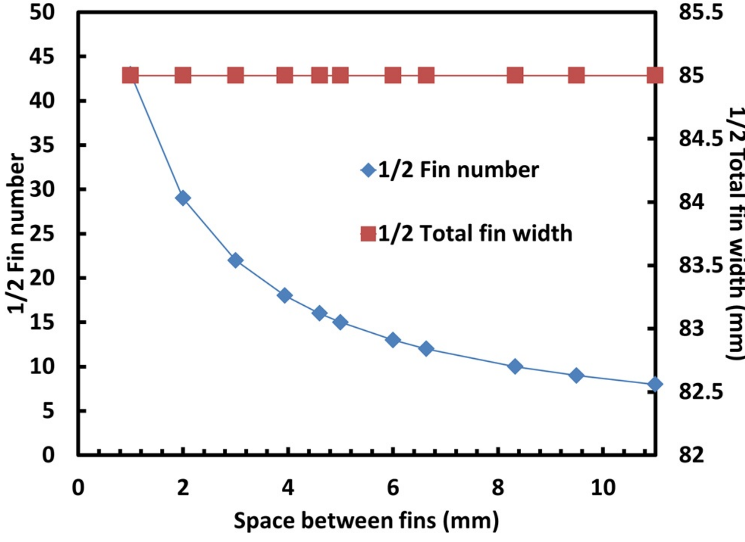

FIGURE 7.8: The fin spacing and total fin width.

As the total fin width W is decided by the application. The following equation is used to calculate the fin number n and fin spacing s:

$$W = nt + (n - 1)s \tag{7.20}$$

As shown in Figure 7.8, the total fin width is fixed as 2 × 85 mm, then the fin number decreases with increasing spacing. According to the analytical calculations, the optimum fin spacing exists in the range from 3 mm to 7 mm. Therefore, the corresponding combination between fin number and spacing were chosen for numerical solutions: 22 fins, 3 mm spacing; 16 fins, 4.6 mm spacing; 13 fins, 6 mm spacing; 12 fins, 6.6 mm spacing.

According to the decided fin number and spacing, simulations were conducted with natural convection and radiation under heat of 60 W and the temperature distribution of all fins and the average temperature of heat spreader were used for optimization of fin spacing. Figure 7.9(a) shows the average heat spreader temperature and temperature of aluminum fin middles close to the HPs. Although HPs obtained very good thermal conductivity, the temperature differs around 8 °C from first fin to the last fin. On the aluminum fin edges at the bottom, the temperature is lower than fin part close to HPs in Figure 7.9(c). When we compared with the aluminum fin middle and edge temperature, the temperature differs around 4 °C as shown in Figure 7.9(e). As the fin spacing of 3 mm, 4.6mm, 6mm and 6.6 mm were compared, we concluded that the aluminum fin spacing of 6 mm obtained best cooling performance. At this spacing, the distance between fins is not small to obstruct the flow and not too large to reduce the total surface in this design. And the fin spacing of 3 mm performed worst due to the too narrow distance to pass the air flow. As the aluminum fins have certain temperature difference, copper fins can obtain lower temperature variation due to the higher thermal conductivity as shown in Figure 7.9(f). The average value of Δt drops from 4 °C to 2 °C with copper replaced aluminum as fin material. Then higher edge temperatures in Figure 7.9(d) and lower fin middle temperature in Figure 7.9(b) are shown. The optimum copper fin spacing is changed to 4.6 mm which is less the optimum aluminum fin spacing. The reason may be that the higher temperature at the bottom can enhance the air flow faster and the flow boundary condition change. Thus, more heat transfer surface (more fins) is required since narrow fin spacing can work well. However, as the copper fins only achieved 1.5 °C better average spreader temperature, we still recommend to apply aluminum with its small weight, low cost and easy fabrication.

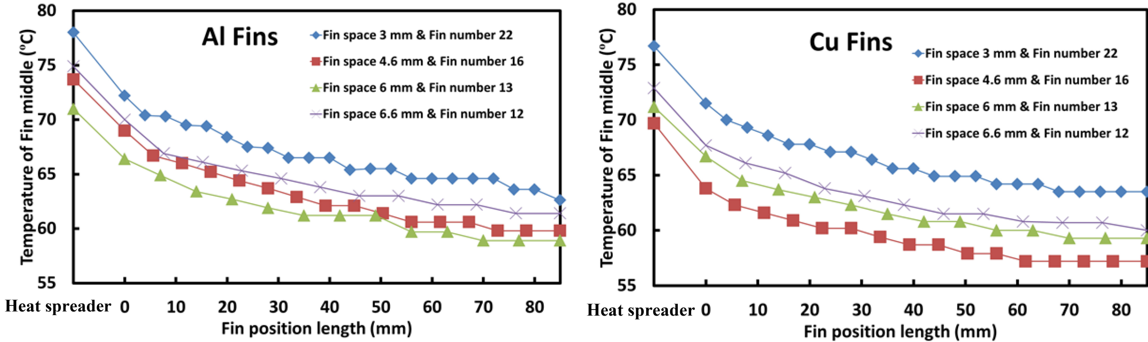

(a) The temperature of aluminum fin middles close to the heat pipes.

(b) The temperature of copper fin middles close to the heat pipes.

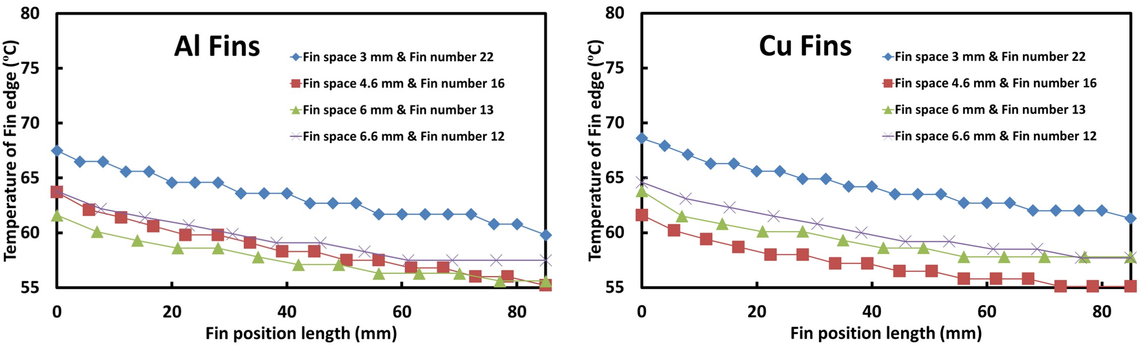

(c) The temperature of aluminum fin edges at the bottom.

(d) The temperature of copper fin edges at the bottom.

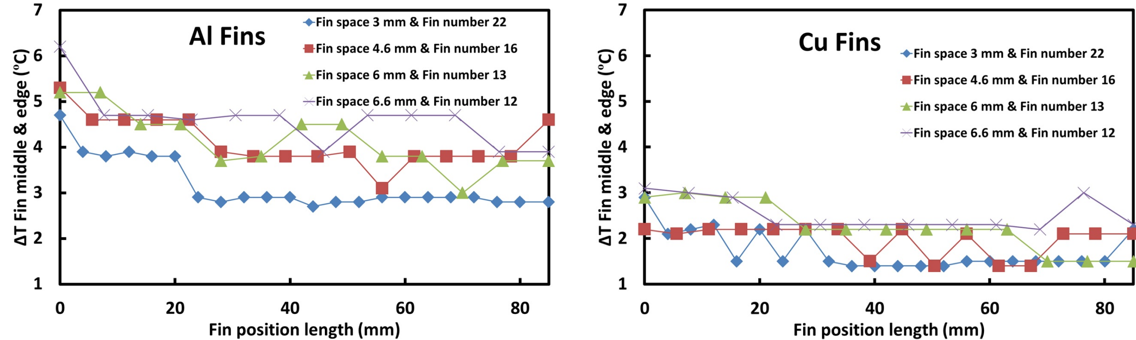

(e) The temperature difference on aluminum fins from middle to edge.

(f) The temperature difference on copper fins from middle to edge.

FIGURE 7.9: The temperature distribution on aluminum/copper fins on heat pipes.

7.3.4 Experiments

Three samples with aluminum heat sink and fins were manufactured as the designed parameters. As shown in Figure 7.10, the high-power LED package was fixed on the top of the heat spreader with good thermal conductive paste and the

electric connection was set through holes of the heat spreader. The three HPs were buried inside the heat spreader and connected to aluminum fins. Form top and bottom view, it is obvious that the HPs can hardly obstruct the vertical air flow between fins. And we measured the heat spreader temperature at the red point between fins to evaluate the performance of the designs.

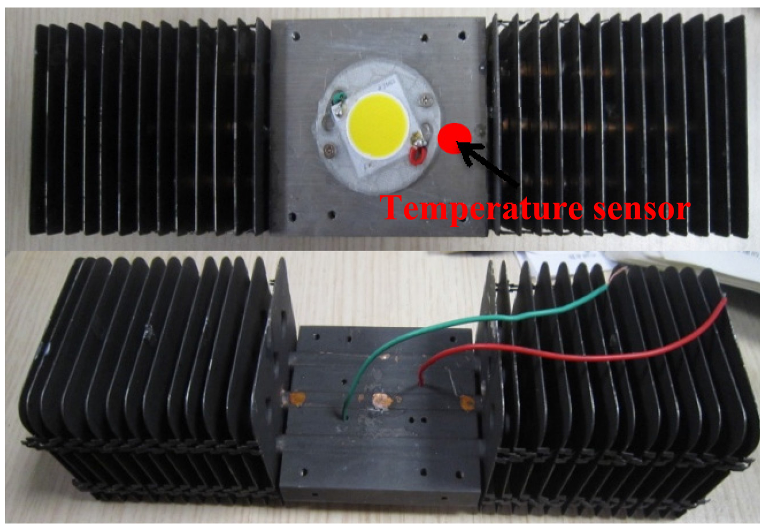

FIGURE 7.10: The tested sample of vertical aluminum fins with heat pipes.

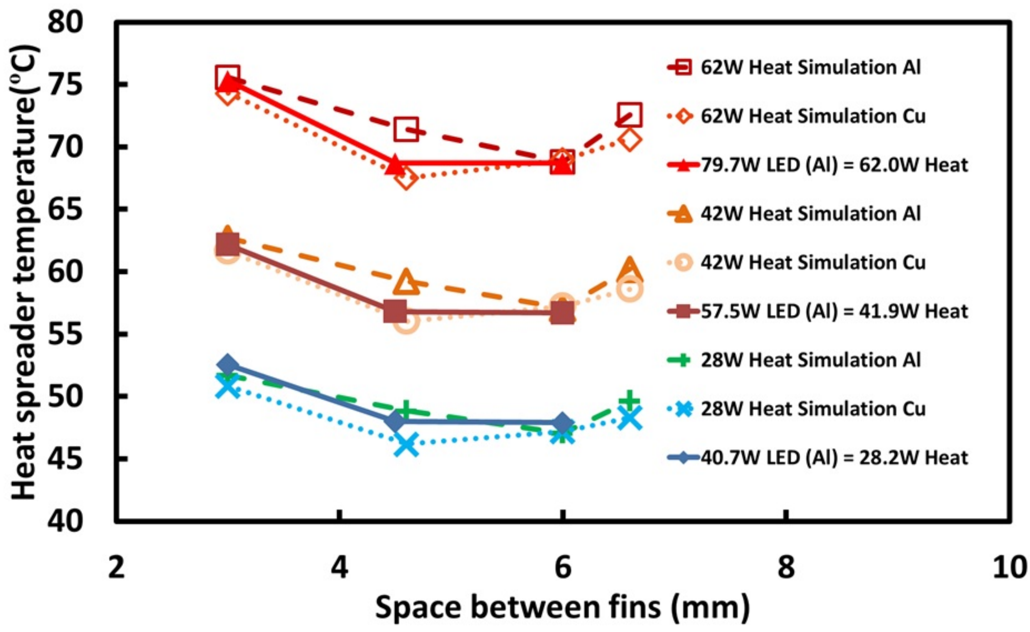

FIGURE 7.11: The measured temperature of heat spreader.

When powered the LED package with different currents, the heat spreader temperature is measured under different thermal powers. The measured efficiencies of LED package were 22.2%, 27.2%, 30.8% as electric power input of 79.7, 57.5 and 40.7 W correspondingly and the rest part of power changed into heat. The measured

temperature of heat spreader is shown in Figure 7.11, there is a clear temperature drop about 7 °C when powered the LED with 80W if the fin spacing increased from 3 to 4.5 mm, which is consistent with numerical calculation. However, the temperature drop as the fin spacing from 4.5 to 6 mm is not significant. 6 mm of fin spacing is the optimized value from the modeling results which can obtain only 0.1 °C less the case with 4.5 mm fin spacing in experiment. However, 6 mm fin spacing can significant contribute to less fins and consequently less materials and weight which benefit the design for applications. When the LED was powered with 57 W and 40 W, the optimized fin spacing is also 6 mm which is consistence with the simulations.

7.4 Conclusion

A thermal solution with Hps as passive cooling for Light-Emitting Diodes (LEDs) are designed, manufactured and tested. As the natural convection and radiation dominate heat transfer, the optimum vertical fin spacing was calculated by the most used empirical correlations. Then, the design was numerical investigated according to the analytical solutions to obtain more accurate prediction in order to optimize the thermal performance. As the fin spacing was both optimized by correlations and modelling, the optimum thermal design achieved. Finally, we manufactured and tested the design experimentally which consistently approved the performance compared to correlations and modelling.

Chapter 8

Conclusions and recommendations

Thermal management for SSL system requires a systematic consideration from designing, manufacturing and testing. The light performance which is the most important output should be considered before the designing. Accurate temperature monitoring is always indispensable. The liquid cooling with optimized structure and well manufacture will be the future fancy thermal management with better thermal performance, less weight and novel transparent appearance.

8.1 Conclusions

The high-brightness LEDs have begun to be designed for illumination application. The increased electrical currents used to drive LEDs lead to thermal issues. Thermal management for LED module is a key design parameter as high operation temperature directly affects their maximum light output, quality, reliability and life time. The definition of thermal management was proposed and the strategic research agenda of thermal management was presented. In a word, thermal management is not to cool the device to a temperature as low as possible, but to achieve the best light performance with thermal solutions of less volume, weight, materials, and energy consumption.

Designing thermal management with consideration of both heat and light

Thermal design methodology for white Light-Emitting Diodes As the drive of increased electrical currents to achieve high luminous output for Phosphor-converted White Light-Emitting Diodes (PW-LED) has led to a series of thermal problems. There are two major heat sources in the LED package, the LED die (chip) and the phosphorous layer. The excess heat generated in the die during the conversion from electric energy to blue light and also in the phosphorous layer where blue light is converted into yellow light. The two conversion rates are both temperature dependent. Thus the temperature is most important parameter from both thermal and optical point of view. Spectral shift and consequent color properties change due to the increased temperature during operation were studied by a group of experiments. An electrical-thermal-luminous-chromatic (E-T-L-C) model was then developed to predict the light performance with thermal management under in-situ temperature. The major purpose of this model is to solve the contradiction with consideration of compromise between light and heat, and bridge the optical and thermal designing with the key parameter - temperature. It was then validated by integrated analyses of common LED packages. Besides, the model was also used to analyze the thermal performance and light quality due to thickness and particle density variation of phosphors. The proposed dynamic E-T-L-C model definitely benefits the design of future high-brightness LEDs for better light quality.

In situ temperature monitoring and controlling

Thermal transient effect and improved junction temperature measurement The diode forward voltage method with pulsed currents was widely used for monitoring junction temperature (T_j) of Light-Emitting Diodes (LEDs). But a thermal transient effect (TTE) was observed by the pulsed currents and consequent errors were introduced. Thermoelectric (TE) physics was conducted to explain this phenomena and a group of experiments was used to reveal the TTE during T_j measurement for high-voltage (HV) LEDs. The uncertainty was measured more than ± 10 °C which is not acceptable for accurate monitoring. Besides, an improved Pulse-free Direct Junction Temperature Measurement (DJTM) method was conducted for HV LEDs to reduce the errors and to achieve in situ Tj measurement with DC currents, simpler setups and a less step sequence.

Temperature triggered MEMS switch for cooling control As the power of Solid State Lighting (SSL) system continuously rising and consequent high temperature in the light source, active cooling solutions with controlling were widely used. A micro-electro-mechanical-system (MEMS) based, temperature triggered, switch was developed as a cost-effective solution for smart cooling control in SSL systems. The switch (1.0×0.4 mm^2) was embedded in a silicon substrate and fabricated with a single-mask 3D micro-machining process. The device switched on at a designed temperature threshold with a contact resistance, and switched off when the temperature drops below that limit. In this way, this device enhanced the automatic control of a cooling system without any need of additional electronic components and the used standard semiconductor manufacturing process gave highly possibility for integration and fabrication for future silicon based SSL systems.

Cooling with enhanced optical performance, less weight, improved natural convection and radiation

Active two-phase cooling for higher light output and increased efficiency To solve the thermal problem of SSL systems, this work presents a cooling solution with phase change phenomenon based on microelectromechanical (MEMS) technology. Tests were performed on a miniaturized evaporator with a fluid channel and an embedded bulk silicon temperature sensor. A commercial high-power LED package was mounted on the evaporator with power ranging from 0 to 2.8W, aiming to achieve maximum light output and possibly very small coolant flow rate. Results showed the package obtained high efficiency and correspondingly increased light output by the two-phase cooling. The proposed device is quite promising for an

integrated water-based thermal management and high-power LED would benefit from the two-phase cooling approach. Additionally, numerical simulation was applied to understand the phase change phenomenon and temperature distribution inside the evaporator. Moreover, optimized water flow rates for specific input powers of the package were calculated.

A polymer based mini loop heat pipe with silicon substrate and temperature sensors Micro or miro-wick heat pipes (HPs) have received considerable attraction in the past decades especially for cooling of electronics which requires removing the increasing heat from a limited volume to environment. Especially, the LHP possess all the main advantages of traditional HPs, but obtain special properties to transfer heat for the distances up to several meters at any orientation in the gravity field. Silicon is highlighted as one the most favorable materials for MHP as well as LHPs. Moreover, polymer based MHP and LHPs are highly attractive for further development. An innovative thermal management with a package, a silicon substrate with temperature sensors and a polymer based loop heat pipe (LHP) was then designed, manufactured and assembled. The polymer LHP supplied a low and relatively stable temperature to maintain higher optical power, more luminous flux and less color shift. The novel design provided LEDs with the efficient thermal management and temperature monitoring with reduced weight, easy fabrication, less energy consumption and better light quality.

Design of vertical fin arrays with heat pipes Although liquid cooling can enhance the equivalent thermal conductivity by removing the heat and improve convection by increasing temperature gradient between surface to ambient, the heat sink, specified for liquid cooling, is still needed to design. A thermal design of vertical fin arrays with heat pipes as passive cooling was applied. The heat pipes supplied good equivalent thermal conductivity with much less weight and volume compared to copper or aluminum base and consequently less obstruction to air flow with enhanced natural convection. As the natural convection and radiation dominate heat transfer in this case, the optimum vertical fin spacing was calculated by the most used empirical correlations. Then, the design was numerical investigated by Computational Fluid Dynamics (CFD) to obtain best thermal performance. As the fin spacing was both optimized by correlations and modelling, the optimum thermal design achieved. Finally, the design was experimentally manufactured and tested, which consistently approved the designing methodology according to the correlations and modelling.

In conclusion, thermal management for SSL system requires a systematic consideration from designing, manufacturing and testing. From the beginning, the light performance which is the most important output should be considered firstly. Accurate temperature monitoring is always indispensable. The liquid cooling with optimized structure and well manufacture will be the future fancy thermal management with better thermal performance, less weight and novel transparent appearance. The electrical-thermal-luminous-chromatic (E-T-L-C) model can be used to predict the light performance at the start of designing, and the methods such as Finite Element Analysis (FEM) and Computational Fluid Dynamics (CFD) can help designer to decide materials and structures.

8.2 Recommendations

Integrated thermal designing As thermal management for LED module is a key design parameter as high operation temperature directly affects their maximum light output, quality, reliability and lifetime, then a designing methodology is necessary with consideration of all the performances. The model in this work is the commencement but it is still far away to establish applicable method for the LED industry. More investigations and identifications among electric, thermal, optical, and reliability parameters are required.

Temperature monitor and controlling Smart system to control the temperature of SSL system are already available, but most of them are complex and relative high cost. In recent future, integrated temperatures sensors can help LEDs achieve stable temperature in order to getting reliable lights. Besides, the temperature is currently mainly controlled by tuning the fans. Other ways to control temperature need investigating; such as, "variable power input" can reduce the power if the working temperature is too high; "smart environment" can tune the light lower if the LED in the corner of the room where has less efficient convection; "communications" can inform the LED there is no people need the light in the room; and etc.

Liquid cooling Liquid cooling boasts its flexible structure, transparency and small weight as it can replace the same volume of traditional metallic heat sinks. And liquid can remove the heat rather than conduct it which performs as better "thermal conductivity" than solid. With liquid cooling, some poor thermal

conductive materials can obtain dramatic improved performance if a thin wall tube can be made, such as polymer. Currently, the HPs are limit by the rigid materials which obtain less leakage and reliability problems. Actually, the HPs do not need the heavy metal because any kinds of materials can be used with careful consideration of processing and leakage. Thin-wall HPs made by transparent, flexible, high-strength, low weight and fancy appearance are the best future of thermal management for SSL systems.

Multi functioning The thermal management is not only to cool the SSL system, but also the heat can be used. Although the waste heat is not feasible for generating power as the very low efficiency of energy conversion, there are still lots of chances for consideration multi functions with thermal management. For example, heat can be used to defrost and de-icing because the light will be affected in the cold seasons; heat can supply a good temperature controlled environment for a small green house; or for some precision instruments around LEDs need to work at certain temperature, etc.

Appendix A

Micro or micro-wick heat pipes for electronics

Micro or miro-wick HPs have received considerable attraction in the past decades especially for cooling of electronics which requires removing the increasing heat from a limited volume to environment. Among the HPs, the MHP and LHP with micro wicks are most preferred for their high efficiency, small dimension, and compatible process with semiconductor devices. Silicon is highlighted as one the most favorable materials for MHP as well as LHPs. Moreover, polymer based MHP and LHPs are highly attractive for further development. And the carbon nanotube (CNT) may be the future nano wicks of HPs for their potentially outstanding characteristics.

A.1 Introduction

During the past decades, more and more power dissipation and consequent more heat were introduced in electronic systems due to decreasing chip size, increasing device density and faster circuit speeds. Moreover, emerging developed semiconductor devices such as Radio Frequency (RF) systems, high-power Light-Emitting Diodes (LEDs), solar cells and solid-state laser light sources were all suffering large on-chip temperature gradient due to localized high heat flux resulting from the substantial non-uniformity in power dissipation [32, 137–141]. To solve the hot problems including, but not limited to, electronic systems, Marcinichen et al. [142, 143] suggested primarily four competing technologies for the cooling of chips: microchannel single-phase flow, porous media flow, jet impingement cooling, and microchannel two-phase flow. Those technologies could also be divided into two types: passive and active cooling. The passive solutions are always preferred with its advantages of waste energy recovery. A HP is a simple device working with cooling fluid and energy recovery unit using the waste heat generated by electronics to drive the cooling fluids. Meanwhile, HPs can also be defined as passive cooling with two-phase flow which can obtain self-drive without external power input. The use of HPs has been conducted for a long period with its very high thermal conductivity, high efficiency without extra electric energy consumption, and suitable working temperature for electric devices. As the technology progressing, two-phase loops including LHP and CPL were invented and attracted more and more interests for their special properties to transfer heat for the distances up to several meters at any orientation in the gravity field. Moreover, the trend toward miniaturization is more and more obvious for HPs, in order to approach the heat source as close as possible, obtain higher contact surface and enhance capillary force. Mini- and micro- HPs with micro-wicks or microgrooves were booming which requires micro-fabrication and new materials. Silicon was then highlighted as the most favorable materials to replace the metals for its fabricability and compatibility with semiconductor devices. But other materials were still very attractive for variant applications. Especially, the carbon nanotube (CNT) may be the future nano wicks for their potentially outstanding characteristic to miniaturize the wicks of HPs from micro to nano scale. Besides, traditionally metals were still under investigation to make micro wicks with continuous improving process. And polymer based HPs were very attractive for its flexibility and low cost, especially for LHPs.

The application on electronics is normally limited by the compact structure and dimension. Therefore, those HPs used for cooling of electronics are mostly defined as micro or mini HPs according to the definitions using hydraulic diameter Dh by Mehendale et al. [144] and Kandlikar [145]. In generally, a size classification is defined as follows [114, 146]: the micro-channels (50 to 600 μm), mini-channels (600 μm to 3 mm) and conventional channels (D_h > 3 mm). However, the D_h of wicks may be a more suitable criterion for micro and mini channels. The equivalent D_h of wicks in HPs using the tips of triangle/rectangle can be also calculated accordingly. Therefore, this review focuses on two types of HPs with micro wicks: the MHP and LHP with microgrooves (or wicks). Vapor chambers (VCs) were also mentioned as flat HPs with micro grooves and CPL is very similar to LHP which was introduced as well. And an overview of the rapid progress of HPs on small hot devices especially electronics with design, analysis and fabrication was supplied. Besides, as new exciting materials, the polymer HPs and nano-wick VCs for cooling of electronics were introduced and highlighted. Furthermore, the prospects of the scientific and technological challenges would be addressed.

A.2 Development of heat pipes for electronics

A.2.1 Heat pipes and loop heat pipes

A HP is a device for heat transfer with phase change and no moving parts [147–149]. It is composed of three sections: the evaporator section, the condenser section and the adiabatic section in between [150, 151]. A HP can transport large quantities of heat efficiently from evaporator to condenser but it is still not a complete cooling system without combination of natural or force air cooling [152]. Its capability results from the latent heat of working fluid and the capillary force through the wick. In this work, the HPs are either the generally name for all the two-phase capillary thermal control devices or the specific name for the traditional HP invented in 1892 [49, 153] excluding LHP, CPL and VC, etc. Besides, the micro LHP/CPL (MLHP/MCPL) and mini LHP/CPL (mLHP/mCPL) are mentioned which also refers to micro-wick with micro/mini tubes.

Figure A.1 shows the typical micro-wick HPs used on electronics: (a) Metallic tubular HP with microgrooves (the equivalent D_h calculated from the U shape wick). (b) Silicon triangle MHP (the equivalent D_h calculated from the tips of triangle).

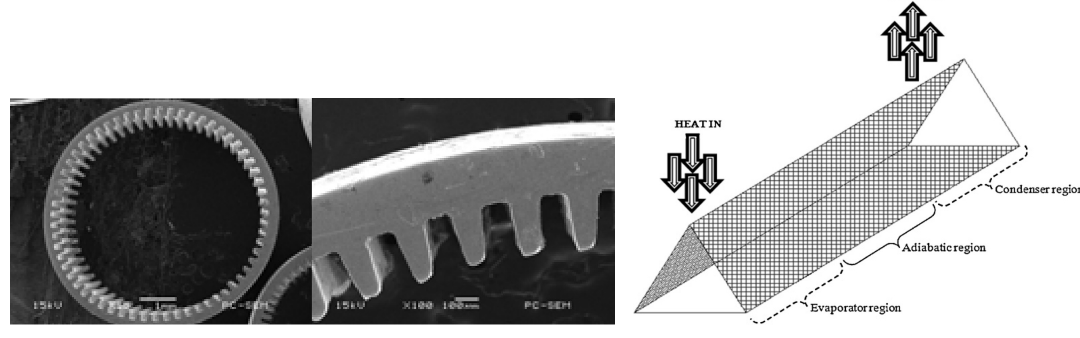

(a) The metallic tubular micro heat pipe [154]. (b) The silicon triangle micro heat pipe [150].

FIGURE A.1: The typical micro heat pipes.

Unlike the conventional HPs, the wicks in silicon produced MHP could be replaced by the tip of the triangle, rectangle or pentagram [155]. In addition, the flat HP, which is also called VC, was widely applied with its excellent heat dissipation ability due to its uniform temperature distribution and large condensation area [156–160]. Although the VC is normally used as mini or even larger size, the micro wicks are always required which supply capillary force [156, 157, 161].

The two-phase loops including LHP and CPL are the ones of the most promising technologies for cooling of electronics. The first feasibility study for CPL was done by Stenger in 1966 [162] and the LHP was developed and tested in 1972 in the former Soviet Union [163]. Compared to HPs, the two-phase loops offer many advantages in terms of operation against gravity, maximum heat transport capability, smooth walled flexible transport lines, and fast diode action [49]. A LHP is very similar to a CPL, except that the LHP has a compensation chamber (CC) to instead the remote reservoir [164, 165]. As shown in Figure A.2, the basic distinction between CPL and LHP is obviously the position of the CC. This results in a large impact on the design and operation of capillary loop [49]. The CC is directly connected to the evaporation chamber (EC) (the CC and EC consist of the evaporator in LHP/CPL) which simplified the LHP start-up and the LHP operation vapor-tolerant. However, the CC in CPL is separated by the connection tube which required the preconditions. The comparison between LHP and CPL is listed in Table A.1. Launay et al. [49] concluded that the CC can simplify the LHP start-up and make the LHP operation vapor-tolerant, which contribute to the robustness under various condition. However, the LHP is more complex system with strong coupled thermal and hydrodynamic characteristics between the CC and

EC. Currently, researchers show intensive interest in the development of LHP/CPL to solve the hot problems in electronics or other small devices. Moreover, the liquid/gas channels are becoming smaller and smaller to penetrated into the local hot spot for better cooling performance.

TABLE A.1: Comparison between LHP and CPL.

	CPL	LHP
Compensation chamber (CC) connected to evaporation part	In direct	Direct
Preconditions needed for Start-up	Yes	No
Primer wicks needed	Yes	No
Secondary wicks needed	No	Yes
Complexity due to thermal and hydrodynamic couples	No	Yes
Temperature and pressure dynamic stabilities	Poor	Good

A.2.2 From macro to micro

As we discussed, the application of HPs on electronics device is limited by the compact structure and dimension. Thus mini- and micro- HPs are more favorable for those relatively small structures. Li et al. [166] made a great progress to the traditional HP technology for high heat-flux electronic products. As shown in Figure A.3, the micro grooves with depth of 0.2-0.3 mm and top-width-to-depth ratio of 1.2-1.5 were fabricated along the metallic MHP. Besides, they built capillary limit models for MHP with dovetail-groove, rectangular-groove, trapezoidal-groove and V-groove wick structures respectively for theoretical analyses.

In order to direct cool the device of semiconductor, researchers were using silicon to manufacture the MHPs [168–171]. As shown in Figure A.4, Berre et al. [33] developed an effective thermal conductivity of 600 W/mK MHP for cooling of electronics consisting in a series of 55 parallel triangular shaped channels. The working fluids were ethanol and methanol for cooling of the poly silicon heater. The temperature difference between the evaporator and the condenser finally reached 4.7 °C and it was only 1.6 °C when the HP array is empty. But the MHPs cannot work properly without heat sink. McGlen et al. [172] have developed the system uses MHP and loop thermosyphon technology to maintain chip operational temperatures of <70 °C at an ambient air temperature of 55 °C. The prototype combined micro

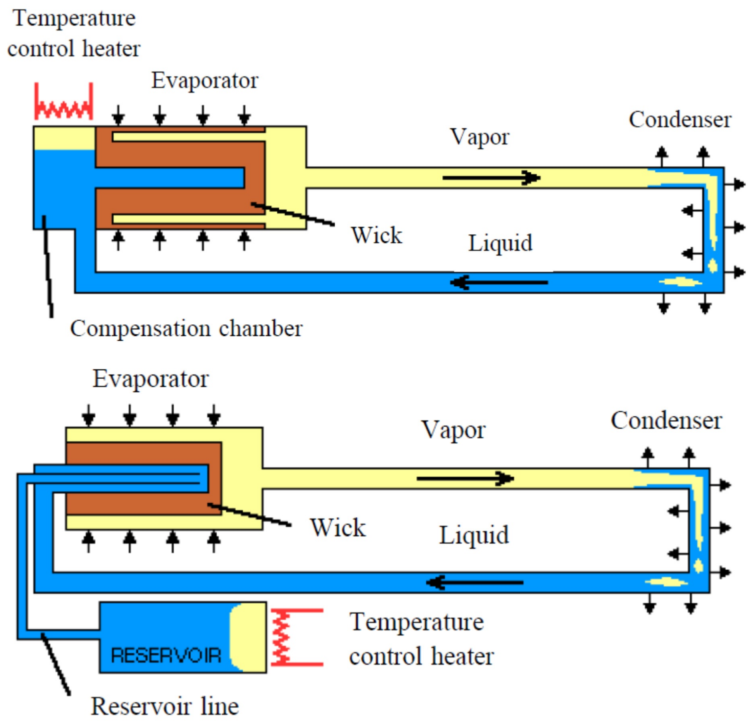

FIGURE A.2: The loop heat pipe and capillary pumped loop [167].

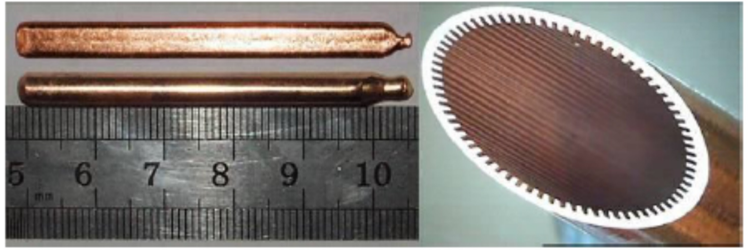

FIGURE A.3: The micro-grooved heat pipe and its grooves [166].

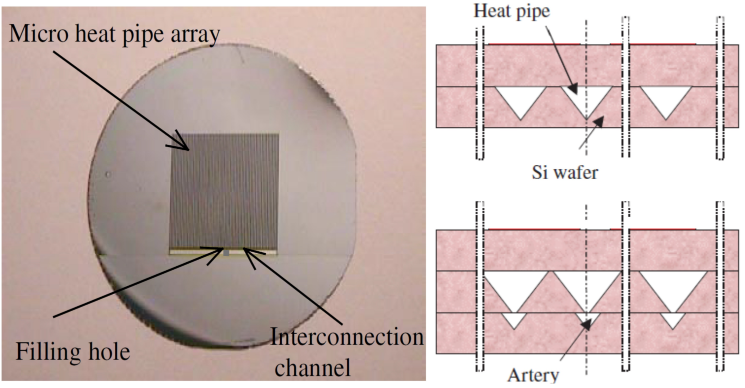

FIGURE A.4: The layout of the MHP array with 55 ”V” grooves micromachined in a silicon wafer [33] with triangle and artery channels.

and mini HP with force convection cooling is to increase the total manageable power of each unit to 230 W, which gives a total rack power of approximately 8 kW.

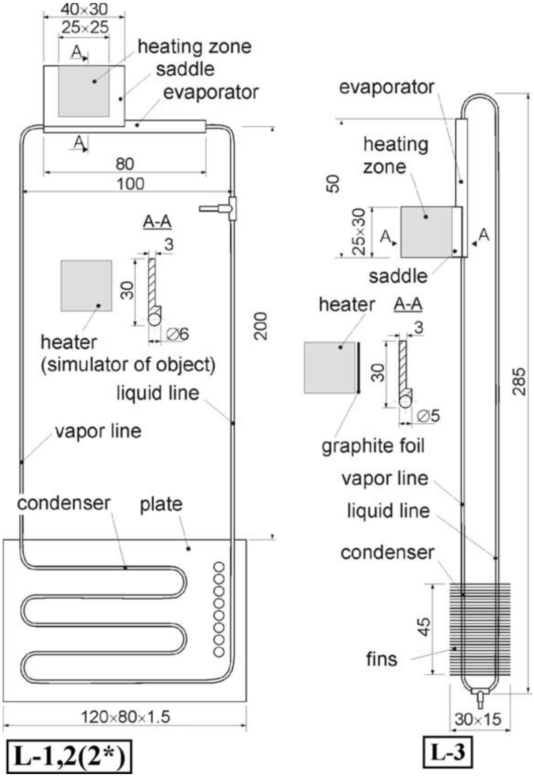

Figure A.5: The schemes of mLHPs of ”L” type [173].

LHPs can obtain better connection between the hot spot to heat sink due to the relatively flexible loop [174, 175]. As shown in Figure A.5, Pastukhov et al. [173] developed of mLHP for remote heat exchanger (RHE) systems. This ”L” loop is with an effective length of about 250 mm and evaporators 5 and 6 mm in diameter. The working fluids ammonia and acetone ensured sufficient heat-transfer efficiency in the temperature range from 50 to 100 °C. Chen et al. [176] reported the mLHP can be used for an evaporator heat load up to 70 W with a cylindrical evaporator of 5 mm outer diameter and 29 mm length at 75 °C. Maydanik et al. [177] tested the mLHP with capable of heat loads of 100 W to 200 W for distances up to 300 mm in the temperature range 50 to 100 °C with ammonia and water as working fluids. Singh et al. [178] demonstrated that the mLHP with a flat disk shaped evaporator for thermal control of computer was capable of transferring a heat load of 70 W through a distance up to 150 mm using 2 mm diameter transport lines.

In order to achieve higher heat transfer coefficient and heat transfer surface area per unit flow volume, MLHP and MCPL were conducted with smaller hydraulic diameter [169] and the ”micro” normally means the micro wicks. Dhillon et

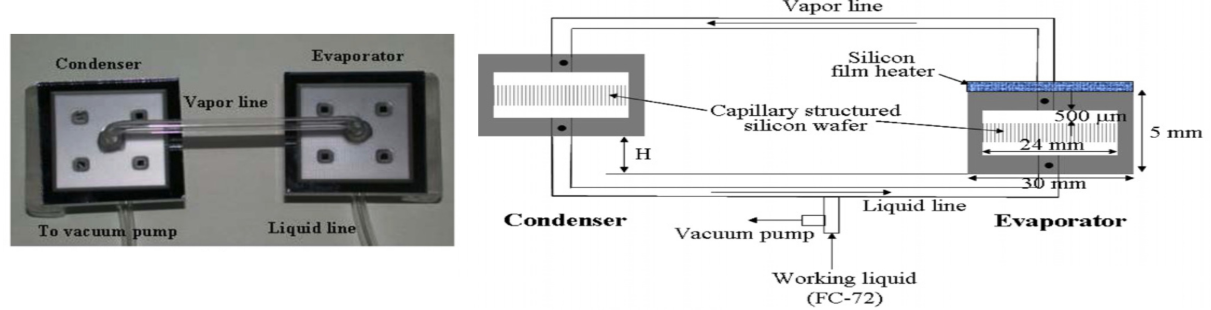

FIGURE A.6: A capillary-pumped loop (CPL) with microcone-shaped capillary structure [112].

al. [119] have recently built and tested MLHP to demonstrate the feasibility of two phase cooling at the micro scale. Hamdan [167] reported in his thesis about the performance of a MLHP (100 W/cm^2) utilized coherent porous silicon wick with 5 μm effective pore diameter and porosity of 50% or higher. MCPL were demonstrated with micro fabrication by Jung et al. [112]. Their CPL can handle a heat flux of about 6.22 W/cm^2 for the air-cooled condenser. Kirshberg et al. [179] reported that the MCPL resulted in a backside cooling effect of at least 7 °C when a laser delivering 7.5 W with a spot-size diameter of 1.0 mm. Wang et al. [180] tested MCPL which can be executed by yielding input heat fluxes of 185.2 W/cm^2 at an evaporator temperature of 165 °C. A typical MEMS-based integrated CPL with micro-cone-shaped capillary structure [112] is shown in Figure A.6. It was developed consisting of an evaporator and condenser both with the same size of 30 × 30 × 5.15 mm^3 which were fabricated using two layers of glass wafer and one layer of silicon wafer. An array of 56 × 56 cone-shaped micro-holes that generates the capillary forces was fabricated and inserted above the CC for liquid transportation as micro wicks. The same cone-shaped microstructure was used in the condenser to create a stable interface between the liquid and vapor phases. With an allowable temperature of 110 °C on the evaporator surfaces, the CPL can handle a heat flux of about 6.22 W/cm^2 for the air-cooled condenser.

A.2.3 From micro to nano: nano carbontube wicks

As the nano technology, especially nano carbontube (CNT), booming in this century, the behavior of fluid flowing through nanoscale channels was investigated [181]. The practical applications based on nanofluidic technologies in medicine and process engineering have been produced recently [181, 184]. Majumder et

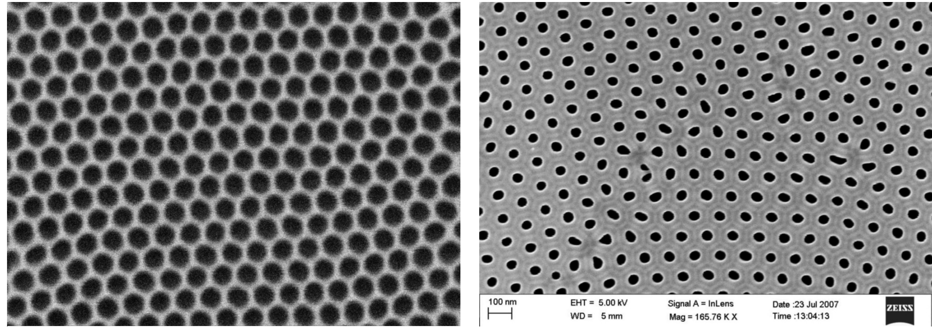

(a) The surface of porous alumina template prior to CVD treatment.

(b) The template after CVD now covered in a layer of amorphous carbon which has reduced the diameter of the pores.

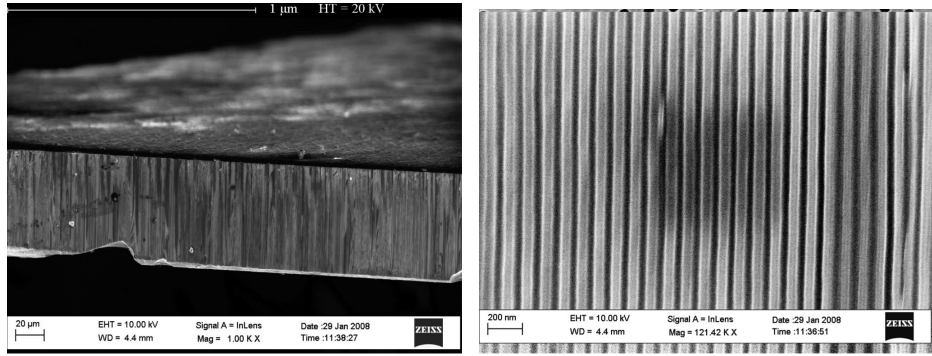

(c) The cross section through snapped membrane.

(d) The higher magnification view of cross section revealing the well-aligned and highly regular carbon nanopipe array.

FIGURE A.7: The SEM images showing the CNT pipe [181, 182].

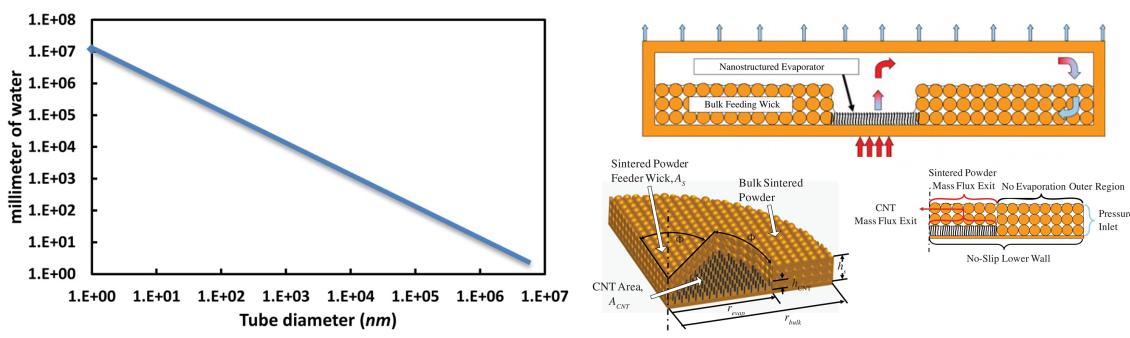

(a) The millimeter of water increases with decreasing tube diameter.

(b) The design of integrated nanostructured wicks for high-performance vapor chambers [183].

FIGURE A.8: The capillary force used in nanostructured wicks.

al. [185] reported and average velocity through 7 nm pores in an aligned sealed array of multiwalled CNT(MWNT) more than 60 000 times for water flowing,

~32 000 times for ethanol and ~4000 times for decane greater than predicted using conventional fluid flow theory. And Holt et al. [186] reported minimum flow enhancements in the range 560 to 8400 for water though even smaller 1-2 nm diameter pores in an aligned array of double-walled CNT sealed in a silicon nitride matrix. Their experiment indicated that a very strong capillary force existed in the nanostructure. As calculated by Young-Laplace equation [50, 118, 179], Figure A.8(a) shows the millimeter of water increased dramatically with decreasing tube diameter. However, the conventional theory may not predict the microfluidic performance at nanostructure. A recent theoretical investigation was prompted [187–189] which included a molecular dynamics (MD) study of fast water transport in CNT. The force to drive liquid through the nano tube may be much stronger than prediction. Ranjan et al. [190, 191] developed a model to calculate evaporating liquid meniscus in wick microstructures under saturated vapor conditions. For a very wire small diameter (10 μm), the percentage thin-film area of the meniscus is very high (>80%) and hence the base heat flux is highest at the smallest diameter.

The nano wicks made of CNT was firstly applied on the VC as the nano-tech improving [181–183]. As shown in Figure A.8(b), Weibel et al. [183] had designed integrated nanostructured wicks for high-performance VCs. He reported that using interspersed nanostructured wicking surfaces, the evaporator thermal resistance may be reduced significantly when adequately sized feeder wicks are utilized and the relative micro to nano wick area is optimized. And he proposed the process of combined micro and nano scale surface structuring for enhancement of both evaporation and boiling heat transfer from porous wick structures [192]. The CNT coating was shown to reduce the surface superheat temperature by as much as 72% by initiating boiling at low heat fluxes and avoiding the boiling incipience temperature overshoot observed for uncoated samples. Besides, lots of researches and fabrication are undergoing with the CNT tube for fluids. Melechko et al. [193] reported a general method for creating patterned arrays of silica nanopipes precisely positioned over pores in a silicon nitride membrane on a silicon substrate. Bau et al. [194] described another method for constructing a nanofluidic device comprising a single carbon nanopipe (diameter 250 nm) connecting two fluid reservoirs. Flashbart et al. [195] described the fabrication using contact printing of a microfluidic array with nanochannel interconnects to ensure their device to take advantage of nanocapillary effects. Han et al. [196] had used surface micromachining on silicon nitride, silica and polysilicon in combination

with micromoulded polydimethylsiloxane to fabricate flexible nanofluidic device architectures.

A.3 Thermodynamic analysis on micro heat pipe

A.3.1 Overall analysis

MHPs are small scale devices that are used to cool microelectronic chips and their hydraulic diameter is on the order of 10 to 500 μm [168]. Smaller channels application is desirable because of two reasons: (1) higher heat transfer coefficient, and (2) higher heat transfer surface area per unit flow volume. Actually new cooling techniques of MHPs are being attempted to dissipate heat fluxes in electronic components in order of 100 up to 1000 W/cm^2 [197]. As shown in Figure A.9, heat added to the evaporator region of the HP results in vaporization of the working fluid and consequently the high temperature and associated high pressure induces vapor flow to the condenser region where it is condensed, releasing the latent heat of the working fluid. Liquid can be transported through the sharp angled corner regions by the capillary pressure. Babin et al. [198] did the first theoretical analysis and experiment on MHP. Moreover, Khrustalev and Faghri [199] proposed a numerical model of the heat and mass transfer occurring in a MHP including the effects of shear stresses at the liquid-vapor interface. These and several other models have been summarized in detail and the results compared by Peterson et al. [171, 200]. Besides, the approximate analytical approach of Cotter [201] has been reevaluated with currently available experimental data in order to modify it to better predict the actual operating conditions and maximum heat transport capacity. Wang et al. [202] reported that this new model better approximates the physical behavior of the liquid-vapor interface in the dryout region. 3D numerical model was later developed to simulate the MHP. Mallik et al. [170] got the results which indicate that significant reductions in the maximum chip temperature, thermal gradients and localized heat fluxes can be obtained through the incorporation of arrays of MHP. Rahmat and Hubert [203] applied a two-phase model of a single MHP and a 3D network of micro-channels were simulated using the finite element method. Besides, wire-bonded MHP arrays were analyzed by Wang et al. and Launay et al. [204–206]. Metallic MHPs were conducted by li et al. [207, 208] and Kang et al. [209, 210]. They developed their design base on the over analysis with analytical solution or

simulation results. The VC is a special type of HP, which is very good heat spreader for electronics.

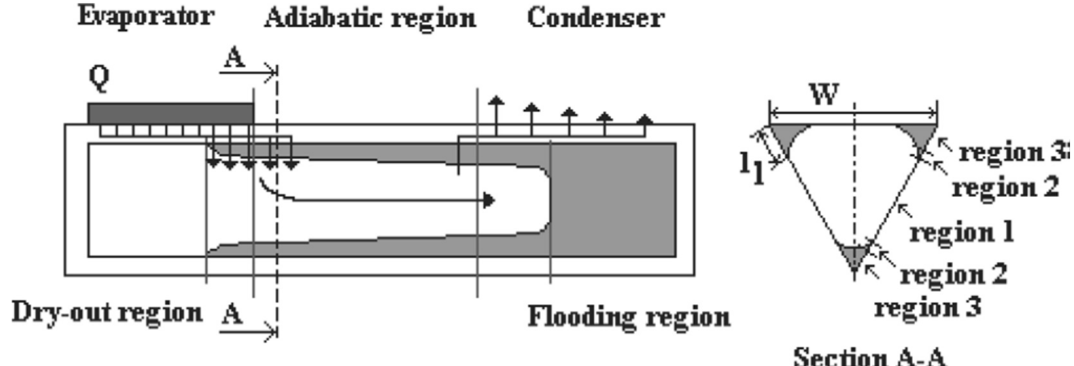

FIGURE A.9: Micro heat pipe with triangular capillary microchannels [169, 197].

The design of VC is similar to the HPs as well. Reyes et al. [211] presented the overall analysis including an experimental and theoretical/numerical study on a vertically placed VC based heat spreader intended for avionics applications. They considered the boiling inside, heat spreading and natural convection at once. The experimental results were also used to calibrate a theoretical and numerical model of the heat spreader behavior. And according to the calibrated mode, an optimization process was carried out to find the minimum weight heat spreader compatible with a series of design requirements. Koito et al. [212] studied the velocity, pressure and temperature distributions inside the vapor chamber by solving the equations of continuity, momentum and energy numerically. From the numerical results, the capillary pressure head necessary to circulate the working fluid is estimated and the temperature drop inside the vapor chamber is determined. More recently, Hassan and Harmand [213] presented 3D transient model for VC and the effect of nanofluids on its performance. The return of liquid from wick region adjacent to condenser wall to the wick region adjacent to evaporator wall was considered in the numerical model coupled with a transient hydrodynamic model.

A.3.2 Wicks

As discussed, the conventional metallic MHPs are still using the micro grooves as the wicks as shown in Figure A.1(a). In general, the gravity and capillarity are the most important parameter in tubular MHP as the drive force. They are fully driven by the capillary force which is mainly depended on the wicks but negatively

affected by the gravity. Li et al. [207] reported that metallic MHP with 6mm of diameter (trapezium-grooved wick with teeth number of 60) can achieve 100 times heat conduction coefficient than that of copper. Li et al. [166] recommended that MHP with the grooved wick of a small-angle dove-tailed structure or a rectangular or a small-angle trapezoidal structure be employed so as to obtain better heat transfer performances. Besides, a MHP with compound structure of a sintered wick on trapezium-grooved substrate has been analysis [154], its capillary limit decreases with particle size of copper powders and how to reduce backflow resistance of working fluid is crucial to increasing capillary limits. A report about the collapse in flattening a micro grooved HP was conducted by Li et al. [208], clearance between the tube and plates occurs at room temperature. As the temperature increases, the incidence of wall collapse decreases and finally disappears and the critical temperature is approximately 130 °C for various heights of flattened HPs. Murer et al. [214] have developed experimental and numerical analysis of the transient response of a mHP. The analytic model was validated by the tested samples which are copper-water flat HPs with a rectangular cross section (10×2.1 mm^2) and cylindrical HPs (diameters 2, 3 and 4 mm). The angle was defined positive if the condenser is below the evaporator in the test and the HP cannot work with the angle larger than +45°.

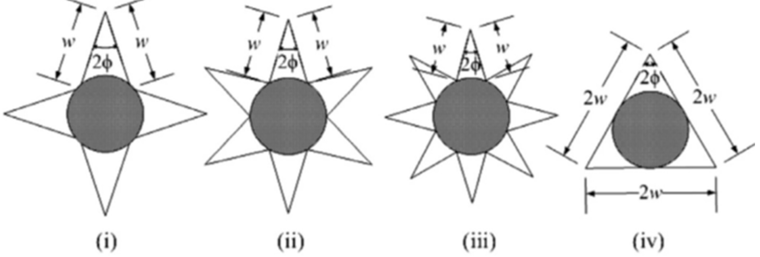

FIGURE A.10: The geometries of different cross-sectional shape of micro-heat pipes [215].

As the interest for silicon HPs increases, Hung et al. [215] reported the work on the effects of geometric design on the thermal performance of star-groove MHPs. Comparisons between the star-groove and regular polygonal MHPs were conducted and the factors contributing to the enhancement of heat transport due to the variations of geometrical parameters were identified and discussed. Ha and peterson [216] and Sartre et al. [217] also studied triangular MHP with an aluminum/ammonia. Beside Launay et al. [168] has used MHP arrays etched by silicon wafers have been investigated for electronic cooling purposes. The results shown the effective thermal conductivity of the silicon wafer with the artery MHP

array is significantly improved compared to massive silicon. Peterson and Ma [218] developed a detailed mathematical model for predicting the heat transport capability and temperature gradients that contribute to the overall axial temperature drop as a function of heat transfer in a MHP.

A.4 Thermodynamic analysis on loop heat pipe

A.4.1 Overall analysis

The operation of a LHP is based on the same physical processes as those of conventional HPs [49, 163, 219–221]. The LHP consists of a capillary pump (also called wicks), a EC (also called evaporator), a CC (also called reservoir), a condenser, and vapor and liquid transport lines (Figure A.11); and the capillary pump, EC and CC are also called as evaporator. Only the evaporator contains wicks; the rest of the loop can be made in smooth tubing which differed with the traditional HPs. The liquid is vaporized as a heat input Q_{evap} supplied to the EC which is indicted as point 1 in the P-T diagram of Figure A.11. The liquid is pumped by the capillary forces of vapor evaporator wicks from the CC. The vapor becomes superheated and its temperature becomes higher especially the region contacted with the heated EC wall but the pressure drop at the exit of the grooves (point 2). Then the vapor moves to the vapor line with constant temperature due to the almost thermal isolated tube, but the pressure drops along the vapor line until it reaches the entrance of condenser (point 3). The vapor is condensed as the temperature decreasing to boiling point. During the condensation, the vapor is cooled with decreasing temperature and pressure (point 4 to point 5). At the end of the condensation (point 5), all the vapor is condensed into liquid. After the condensation, the liquid is continuously cooling and stars to be subcooled inside until it reaches the end of the condenser (point 6). The heat dissipated by the condenser from point 3 to point 6 is Q_{cond}. The subcooled liquid flows in the liquid line, but its temperature may increase or decrease which is depending on whether the liquid loses or gains heat from the ambient. As the liquid reaches the CC inlet (point 7), the working fluid is heated up by the heat conducted from EC to the end of the CC (point 8) which is connected to the wick. The evolution from point 8 to 9 corresponds to the liquid flow through the wick into the evaporation zone. On this way, the liquid may be

superheated, but boiling does not take place because it remains in such a state for a too short time.

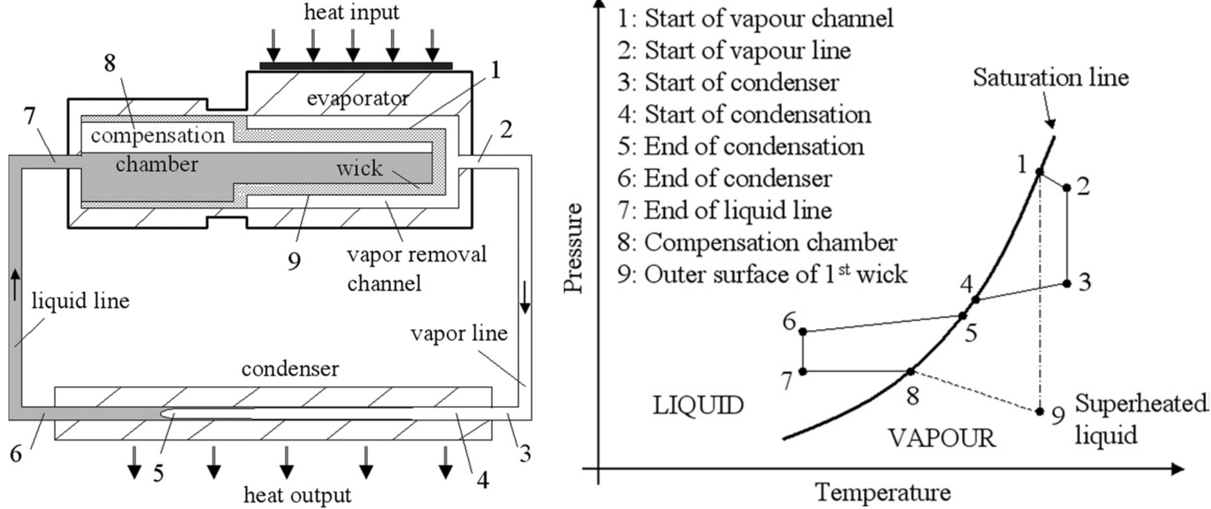

FIGURE A.11: Geometry of a LHP and T diagram for LHP steady-state operation (capillary controlled mode) [49, 163, 219, 222].

The CC is the largest component (by volume) of the loop and is often an integral part of the pump. It has two mains functions [49]: (1) to accommodate excess liquid in the loop during normal operation, and (2) to supply the capillary pump wick with liquid at all times. The primary wick which is in the evaporator is make of fine pores for a high capillary pressure, but the secondary wick is the connection between the evaporator to the reservoir in order to supply the primary wick with liquid, particularly when the reservoir is below the evaporator or in microgravity conditions. Both the liquid and vapor lines are made of small-diameter tubes which can easily be arranged around the hot devices. The operating principle of the LHP is as follows. Under steady state conditions, liquid is vaporized and the menisci formed due to the capillary forces at the liquid/vapor interface in the evaporator wick for a heat input Q_e supplied. As the vapor temperature and pressure is higher in the evaporator zone (vapor grooves) than in CC. The wick in this case serves as a "thermal lock" [49, 163]. At the same time, hotter vapor cannot penetrate into the CC through the saturated wick due to the capillary forces which formed the interface. Thus, another function of the wick is that of a "hydraulic lock" [49, 163]. The arising pressure difference causes the displacement of the working fluid around the loop. Therefore, three two phase interfaces may exist in the LHP simultaneously: in the EC, in the condenser and in the CC. As the heat load changed, these interfaces may move depending except in the EC, and the excess of liquid is stored into the CC. For the overview analysis, the total pressure drop in the system is the sum of

frictional pressure drops in the evaporator grooves ΔP_{groove}, the vapor line ΔP_{vapl}, the condenser ΔP_{cond}, the liquid line ΔP_{liql}, and the evaporator wicks ΔP_{wick}, plus any static pressure drop due to gravity ΔP_{grav} [49, 163]:

$$\Delta P_{tot} = \Delta P_{groove} + \Delta P_{vapl} + \Delta P_{cond} + \Delta P_{liql} + \Delta P_{wick} + \Delta P_{grav} \tag{A.1}$$

As the capillary force is the only driven force in LHP, the condition that pump pressure due to wicks overwhelm the frictional pressure drop must be satisfied all the time:

$$\Delta P_{tot} < \Delta P_{cap} \tag{A.2}$$

A.4.2 Wicks

As the liquid will evaporate in the evaporator with heat input, the wick works as "thermal lock" and "hydraulic lock". Figure A.12(a) shows a schematic of the evaporator section when the system reaches the quasi-steady state condition, where the liquid injected from the CC is vaporized. The temperature of the working fluid is increased as the heat is applied until the liquid begins to vaporize. And all the liquid in the vaporization chamber will change gradually and finally into vapor. The liquid-vapor interface is formed as the menisci which are supported by the capillary force. The interface in the vapor line is then moved to the loop side as the vapor pressure is increased. This movement is continuing as the vapor is cooled in the condenser. Therefore, it pumps the working fluid without any external pump.

The wick is the most important part to drive the liquid with heat input. Meyer et al. [164] fabricated a SiC MCPL using high density interconnect processing techniques with etched trapezoidal grooves etched. Jung et al. [112] developed an array of 56 $\times$ 56 cone-shaped microholes 55 μm in diameter at the liquid side and 250 μm in diameter at the vapor side fabricated in the middle of a 24 $\times$ 24 mm62 silicon wafer with a pitch of 430 μm is shown in Figure A.12(b). And Holke [223] produced the wicks from coherent porous silicon (CPS) in silicon wafers with pore diameters ranging from 1 to 8 μm and center-to-center distances ranging from 4 to 10 μm as shown in Figure A.12(c). By Dhillon et al. [119], the columnated wick can be fabricated out the primary wick using standard dry etching techniques in Figure A.12(d). The secondary wicks for LHP/CPL is indispensable [50, 119, 224]. As shown in Figure A.12(e), Cytrynowicz et al. [50] used the quartz fiber as a secondary

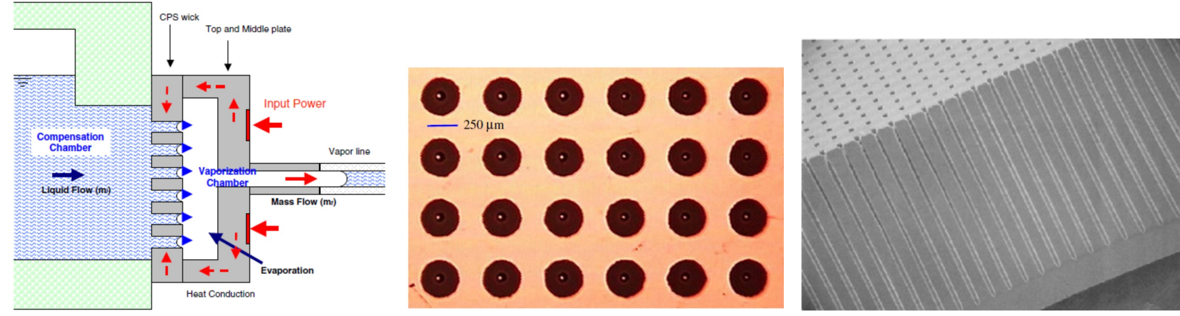

(a) The wicks between the vaporization chamber and condensation chamber in a MEMS bubble pump [55].

(b) The capillary array on microcapillary-structured silicon wafer in CPL [112].

(c) The coherent porous silicon (CPS) wick [223].

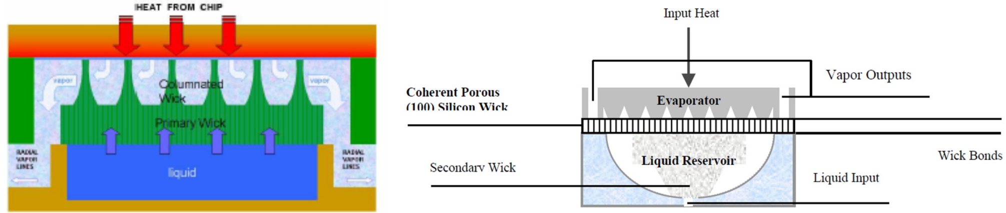

(d) The micro-columnated CPS wicking structure [119].

(e) The silicon wicks and components of micro loop heat pipe [50].

FIGURE A.12: The micro wicks in LHP and CPL.

wick to conduct the liquid to the primary wick which provide the necessary capillary pressure to deliver water to the primary wick while maintaining a low pressure drop.

The capillary pressure gain across the liquid/vapor interface in the circular pores of the wick is given by the Young-Laplace equation [50, 118, 119]:

$$\Delta P_{cap} = \frac{2\sigma_l}{r_{wick}} \cos\theta \approx \frac{2\sigma_l}{r_{wick}} \tag{A.3}$$

where σ_l is the surface tension of the working fluid, r_{wick} is the wick pore radius and θ is the contact angle of the meniscus. For hydrophilic solids and wetting liquids, the contact angle can be assumed to be zero. Using the Clasius-Clapeyron equation, one may obtain the pressure drop due to the temperature difference between vapor and liquid in the wafer where the cone-shaped holes are fabricated. That is pressure loss due to the wick [112]:

$$\Delta P_{wick} = \frac{h_{lv} P_v \Delta T_{wick}}{R_{gas} T_v^2} \tag{A.4}$$

where P_v,T_v, ΔT_{wick}, h_{lv} and R_{gas} are the vapor pressure, the vapor temperature, the temperature difference of the wicks, the enthalpy of evaporation and gas constant of the vapor, respectively.

A.4.3 Evaporation and compensation chamber

For CPL the EC and CC are connected directly, while the CC in CPL is separated by the connection tube. We consider them as one equation in this work. The heat will be transferred to liquid in the EC Q_{EC} and CC Q_{CC} [49, 163]:

$$Q_{evap} = Q_{EC} + Q_{CC} \tag{A.5}$$

The heat in the evaporator will be removed mainly by the latent heat. With the latent heat L_H of liquid and flowrate m_p:

$$Q_{EC} = m_p L_H \tag{A.6}$$

A part of heat will be transferred to the CC. With the temperature difference ($T_E C - T_C C$) and the thermal conductance from the evaporator and the CC:

$$Q_{CC} = k_{EC,CC}(T_{EC} - T_{CC}) \tag{A.7}$$

The subcooled liquid flow region will appear before the condenser outlet and heated by energy leak in the CC [49]:

$$Q_{EC} = c_p m_p (T_{CC} - T_{in,CC}) \tag{A.8}$$

To evaluate the appropriate quantity of the working fluid in the loop, two conditions have been proposed to be considered in the evaluation of the proper fluid inventory: cold base and hot base [49, 219, 225]. The cold base is when no heat is applied to the loop and everywhere is flooded by liquid except for the CC:

$$M_{cold} = \rho_{l,cold} V_{tot} + \rho_{l,cold} V_{CC} \beta + \rho_{l,cold} V_{CC}(1 - \beta) \tag{A.9}$$

where $\beta = \frac{V_{l,CC}}{V_{CC}}$ in the cold base and V_{tot} is the total volume of the loop cavity excluding the CC. The hot base is when the maximum tolerable heat is applied to the loop and vapor occupies every section of the loop except CC which contains

mostly liquid:

$$M_{hot} = \rho_{v,hot}(V_{tot} - Vvap) + \rho_{l,hot}V_{vap} + \rho_{l,hot}V_{CC}(1-\alpha) + \rho_{v,hot}V_{CC}\alpha \quad \text{(A.10)}$$

and $\alpha = \frac{V_{l,CC}}{V_{CC}}$ in the hot base. Therefore, the arranged space(M) in the CC should be adequate to [219]:

$$M \leq \rho_{l,max}(V_{tot} + V_{CC}) \quad \text{(A.11)}$$

A.4.4 Vapor line and liquid line

The vapor line and liquid line are smooth walled tubes that transport the fluid between the evaporator and the condenser. If assuming laminar flow, the pressure drop in the vapor line is given by [112]:

$$\Delta P_v = f_v \frac{\rho_v u_v L_{vapl}}{2D_{vapl}^{0.25}} \quad \text{(A.12)}$$

where ρ_v, u_v, L_{vapl} and D_{vapl} are density, velocity and length and diameter of the vapor line, respectively. In the above equation, the Blasius friction factor f_v is given by:

$$f_v = \frac{0.3164}{Re_v} \quad \text{(A.13)}$$

where Re is the Reynolds number. The pressure in the liquid line may be obtained by the following equation [112]:

$$\Delta P_{liql} = f_l \frac{\rho_l u_l L_{liql}}{2D_{liql}^{0.25}} \quad \text{(A.14)}$$

where the friction factor for laminar flow is given by:

$$f_l = \frac{64}{Re_l} \quad \text{(A.15)}$$

Ghajar et al. [225] observed that the heat removal capability of the device decreases as increasing grooves' length, the distance between two adjacent grooves, and vapor line's length. But the maximum possible heat removal increases as increasing the evaporator's width, vapor line's width and liquid line's width. Jung et al. [112] estimated the pressure drop of vapor line is from 0.00185 to 0.00333 Pa, and pressure drop of liquid line is from 10.752 to 12.855 Pa for heat input from 2.05

to 6.22 W/cm^2. Meyer et al. [164] designed his device with vapor line (150 μm $\times$ 460 μm $\times$ 19.9 to 33.8 mm) and liquid line (150 μm $\times$ 160 μm $\times$ 33.4 to 47.3 mm). The tested maximum power decreased with increasing line length. Hamdan [167] concluded that the length of vapor line and liquid line should be designed as short as possible to remove more heat power, but the cross-section requires more area to enhance the heat and mass transfer. Besides, if the thermodynamics and hydrodynamics changed in the tube due to the imbalance heat, the surface tension-driven effects in wickless tubes may be introduced [226–232]. Chen et al. [146] tested the flow pattern in four circular tubes with internal diameters of 1.10, 2.01, 2.88 and 4.26 mm with vertical upward two-phase flow using R134a as the working fluid. They observed that the smaller diameter tubes (1.10 and 2.01 mm) exhibit strong ”small tube characteristics” but the larger tubes not.

A.4.5 Condenser

The condenser of MLHP for electronics is the structure to remove the heat to next loop of cooling or environment. As shown in Figure A.11, the condenser should ensure all the vapor will be cooled and condensed to liquid.

$$Q_{cond} = m_p L_H + h_{cond} A_{cond} (T_{b,cond} - T_0) \tag{A.16}$$

The Q_{cond} is the total heat removed by the condenser, m_p is the vapor flow in, L_H is the latent heat of the vapor , h_{cond} is the total heat transfer coefficient from condenser to environment, and $T_{b,cond}$ is the boiling point of coolant. As shown in Figure A.5, Pastukhov et al. [173] developed the traditional heat sink for LHP. As shown in Figure 6, Jung et al. [112] and Muraoka et al. [233] had a new type of CPL with a porous wick element in the condenser instead of the conventional tube condenser, which reduced or eliminated the start-up problem and the occurrence of pressure oscillation during operation. And Ghajar et al. [225] had integrated the condenser, evaporator, vapor and liquid line in one process to obtain a compact MLHP.

A.5 Configurations and micro-fabrication

A.5.1 Materials

In generally, traditional HPs are made from metals, and so do the MHPs. As shown in Figure A.13(a), a series of tests was done on miniature copper-water HPs copper with diameters 2, 3 and 4 mm by Murer et al. [214]. MHP with curved rectangular type and curved triangular type with 1-2 mm of the equivalent diameter was fabricated by Moon et al. (Figure A.13(b)) [155]. The copper was used to fabricate even smaller MHP on the central circle with a 14 mm diameter. Seventy-two rectangular grooves each narrowed to 200 μm in width and 5.5 mm in length are positioned in this circle which is shown in Figure A.13(c).

As the MHP as was first described by Cotter [201], silicon was introduced to fabricate the MHP due to the dimension is with a hydraulic diameter of 10 to 500 μm. Many researchers investigated on the MHP [33, 150, 234] as shown in Figure A.1(b) and Figure A.4. Actual view of the shape of vapor phase, liquid phase and central interface of MHP after etching is as shown in Figure A.14 which is similar to the copper-screen-styled MHP. The width at inner end of groove is 350 μm and the width at outer end of groove is 700 μm and the etching depth is 162.5 μm. The silicon process can definitely applied on the LHP/CPL as shown in Figure A.6 and Figure A.12.

The metallic structure of HPs exhibit relatively high physical rigidity, and so does the silicon HPs. The concept of a flexible HP initially appeared in a paper published in 1970 [235]. It had the advantage of application in multiple possible configurations where the heat sink may be out of plane with the heat source and would allow heat removal from oscillating heat sources. Schweickart and Buchko [236] use the flexible HPs contain ammonia as the working fluid and a rolled screen mesh wick for CCD Cooling on the advanced camera with flexible stainless steel of external tubing. But in generally, the HP with a flexible adiabatic section was developed with wickless metal tube. In 2001, McDaniels and Peterson [51] presented analytical modeling and estimated the thermal conductivity of a flat, flexible, polymer HP with a grooved wicking structure to be approximately 740 W/mK. A design of MHP channels, currently being investigated, consists of flexible rectangular or trapezoidal micro channels fabricated in a polymer material with methanol and ethanol as the working fluids in Figure A.15(a) [52]. The material is polypropylene

and has an internal dimension of the individual MHPs of 200 μm with 26-μm-wide capillary grooves. More recently, Oshman et al. [53] fabricated a HP on a flexible liquid crystal polymer substrate using micro-machining techniques compatible with printed circuit board technologies. The device transferred up to 12 W of power with an effective thermal conductivity of up to 830 W/mK. As shown in Figure A.15(b), Oshman et al. [237] developed a flat, flexible, lightweight, polymer HPs with the overall geometry of $130 \times 70 \times 1.31$ mm^3. It was made from commercially available low-cost film composed of laminated sheets of low-density polyethylene terephthalate, aluminum and polyethylene layers.

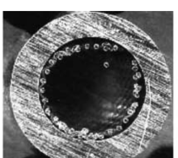
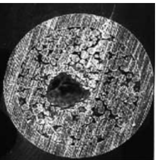

(a) The traditional HPs with micro wicks [214].

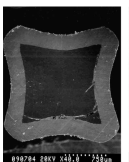

(b) The curved rectangular type and curved triangular type [155].

(c) The diagram about the structure of each layer of a copper-screen-styled micro heat pipe heat spreader. Left: gas phase; central: partition panel; right: liquid phase [209].

Figure A.13: The cross-section of micro-heat pipes.

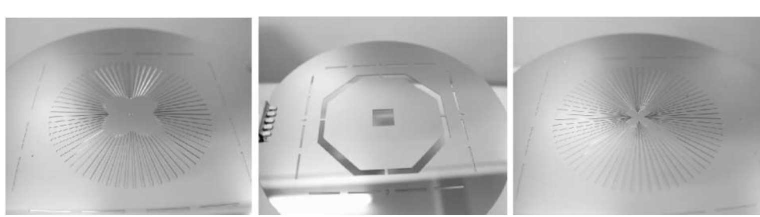

Figure A.14: Fabrication and test of radial grooved micro heat pipes [210].

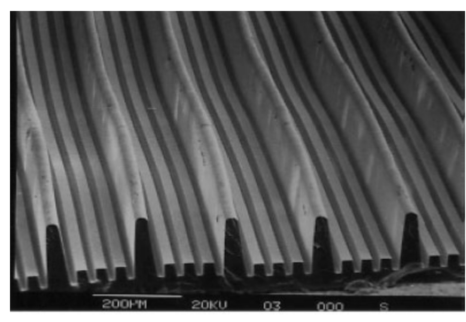

(a) The flexible polymer micro heat pipes with rectangular [52, 230].

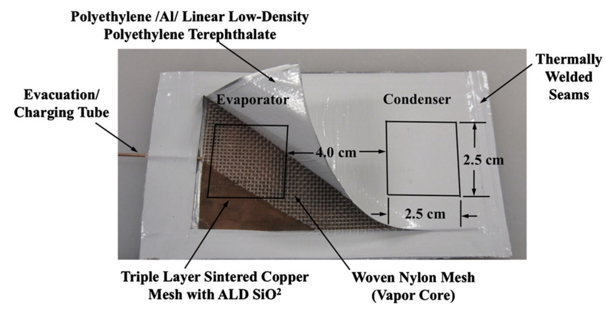

(b) The flat flexible polymer heat pipes [237].

Figure A.15: The flexible polymer micro heat pipes.

A.5.2 Structure, fabrication and process

The traditional HPs were made from metal, and MHP with the diameter smaller than 2 mm can also be made from metallic structure. Li et al. [207] (Figure A.1(a)) made MHP with trapezium grooved wick was digitally described, mathematical modeled and finally tested which had different groove structures manufactured by high speed spinning. Their analysis results shown that better heat transfer performances can be obtained in MHP with small-angle dovetail, rectangular and small-angle trapezoidal grooved wick structures when groove depth is 0.2-0.3 mm and top-width-to-depth ratio is 1.2-1.5 [166]. Besides, the collapse of thinwalled microgrooved HPs was analyzed [208]. MHP with curved rectangular type and curved triangular type with 1-2 mm of the equivalent diameter was fabricated by Moon et al. (Figure A.13(b)) [155]. Kim et al. [238] reported the experiments performed on microporous coated surfaces on flat and cylindrical heaters with micron-size aluminum particles as the microporous structures on the heated surfaces.

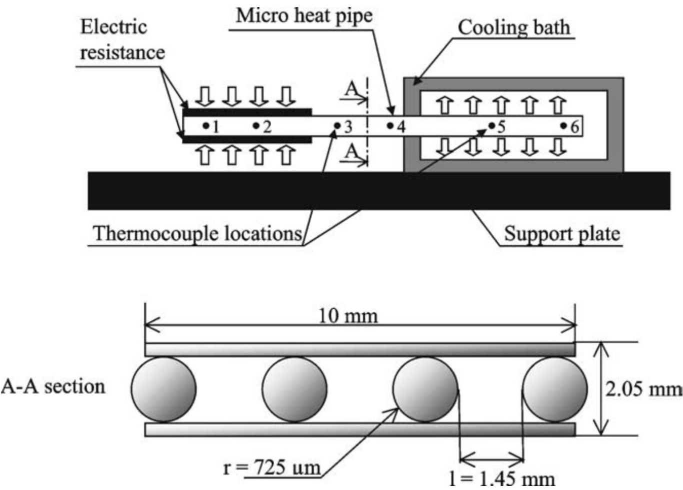

FIGURE A.16: The schematic view of the wire plate MHP array and thermocouple Locations [77].

A copper/water wire plate MHP was investigated by Launay et al. [205] as shown in Figure 16. The experimental results shown that its effective thermal conductivity is improved by a factor 1.3 as compared to the empty MHP array. Basically, the process of wire plate MHP is similar to flat HP [239], but more process required to manufacture. Wang and Peterson [204] developed the flat MHP utilizing arrays of parallel metal wires sandwiched between two thin metal sheets.

A MHP is typically a wickless, noncircular channel with a channel radius approximately the same as the characteristic radius of the liquid meniscus [198]. Silicon is preferred to generate the MHP as small as possible. Launay et al. [168] developed the MHP of triangular cross-section and with liquid arteries were fabricated by wet anisotropic etching with a KOH solution. Peterson et al. [234] and Ha et al. [239] fabricated the MHP in silicon wafers with an anisotropic etching process to produce triangular channels. And Hung and Tio [240] did the thermal analysis of a water-filled MHP with the triangular channels. Besides, lots of researches on the silicon MHP were done based on the etching and bonding technology [33, 115, 203, 210, 215, 241–245]. As shown in Figure A.17(a), the process of wick in vaporization chamber was fabricated on silicon wafer: Oxidation and backside oxide etch; Phosphorus diffusion; Oxide strip, LPCVD nitride deposition or re-oxidation; Photolithography; Open windows in masking layer by RIE; Etch pit initiation in silicon with KOH; Photoelectrochemical coherent porous silicon wick etch; Backside mechanical lapping; and the plates were bonded together with VACSEAL to protect against leakage and baked in an oven for 1 hour at 260 °C. And in Figure A.17(b), the process is similar but to fabricate radial grooved MHPs.

A.5.3 Working fluids

The working fluids of HPs are the essential components which decide the thermal performance. In generally, the water should be the best one for cooling of electronics with the largest latent heat and suitable boiling point. However, other fluid should be considered seriously. Table 2 listed the typical physical properties of common liquids which can be considered as working fluids for HPs. Among the liquid density ρ (kg/m^3), boiling point T_b (K), latent heat of evaporation L_H (kJ/kg), specific heat capacity c_p (J/kgK) thermal conductivity k (W/mK), surface tension σ_l (mN/m), and dynamic viscosity η (Pa·s), latent heat and surface tension are the most essential parameter for design HPs. Therefore, Acetone, Diethyl ether, Ethanol, Methanol, and water are the most favorable. Besides, The perfluorocarbons (FCs) and hydro-fluoro-ethers (HFEs) made by the 3M Corporation provide this mix of properties, along with very low wetting angles on most engineering surfaces and relatively low critical pressures, thermal conductivities, and specific heats, but air solubilities approaching 50% by volume, some 25 times higher than in water [246–248].

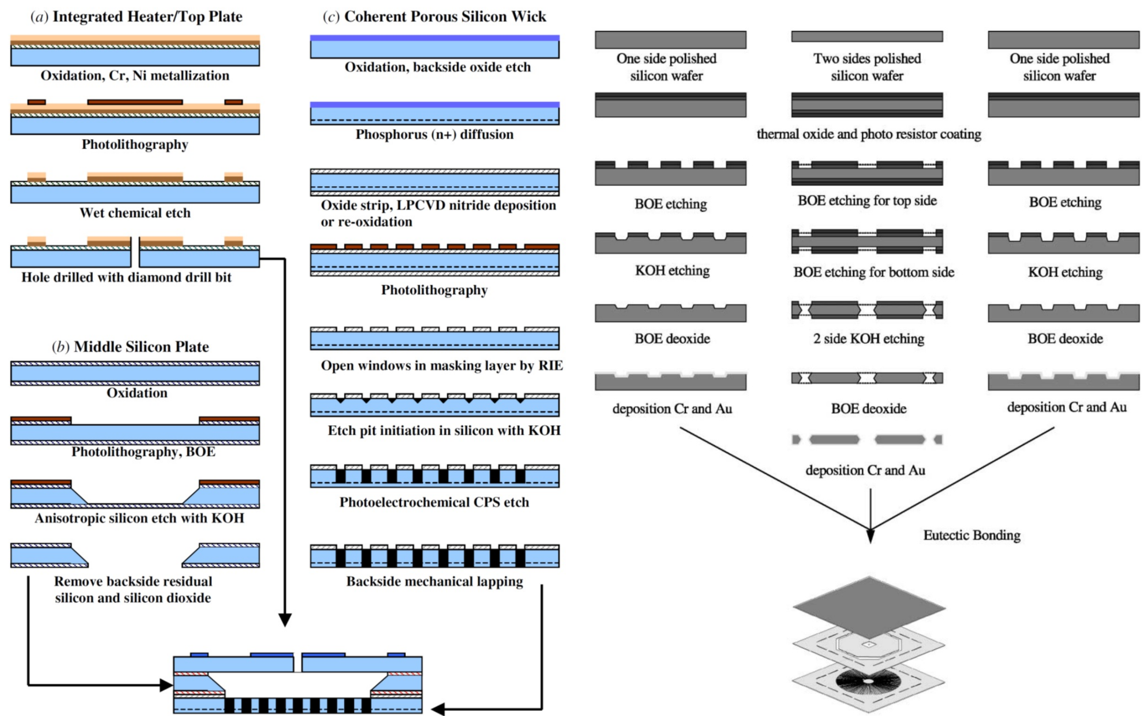

(a) The processing sequence: vaporization chamber component fabrication [55].

(b) The manufacturing flowchart of micro radial grooved heat pipe [210].

FIGURE A.17: The manufacturing of micro silicon heat pipes.

Qu et al. [229] tested a silicon-based micro-pulsating HP with trapezoidal microchannels with a hydraulic diameter of 352 μm. FC-72 with latent heat of $<$ 88 kJ/kg and average surface tension $<$ 100 N/m and R113 with latent heat of 139.4 kJ/kg and average surface tension 130.7 N/m were used as working fluids. Although the values of dynamic viscosity, latent heat, and surface tension for FC-72 were less than that of R113, which is favorable for the heat transfer of a MHP [249], R-113 with a higher value of (dP/dT)sat could lower the evaporator temperature. Charoensawan et al. [228] have investigated on the closed loop pulsating HPs with the influence characterization for the variation of working fluid of water, ethanol and R-123. They concluded that since the thermal performance is a complex combination of the above noted it is certainly difficult to prescribe or proscribe a certain working fluid unless all the boundary conditions are exactly known and individual effects have been explicitly isolated and quantified. Besides, Savino et al. [227] tested the ordinary liquid (such as water) with the surface tension decreasing with temperature in which the slug moves in the direction of the temperature gradient (towards the warmer side), and a self-rewetting fluid (the long-chain Alcohols) with surface tension increasing with temperature in which the slug

TABLE A.2: The proprieties of possible working fluids for HPs to cool electronics .

No.	Name	ρ	T_b	L_H	c_p	k	σ_l	η
1	Acetic acid ($C_2H_40_2$)	1049	391	390	1960	0.180	27.6	1.219×10^{-3}
2	Acetone (C_3H_60)	780	330	520	2210	0.161	23.7	0.324×10^{-3}
3	Benzene (C_6H_6)	879	353	400	1700	0.140	28.9	0.647×10^{-3}
4	Bromine (Br)	3100	332	183	460		41.5	0.993×10^{-3}
5	Carbon disulphide(CS_2)	1293	319	360	1000	0.144	32.3	0.375×10^{-3}
6	Carbon tetrachloride	1632	350	190	840	0.103	26.8	0.972×10^{-3}
7	Chloroform ($CHCl_3$)	1490	334	250	960	0.121	27.1	0.569×10^{-3}
8	Ether, diethyl($C_4H_{10}O$)	714	308	350	2300	0.127	17	0.242×10^{-3}
9	Ethyl alcohol (C_2H_60)	789	352	850	2500	0.177	22.3	1.197×10^{-3}
10	Methyl alcohol (CH_40)	791	337	1120	2500	0.201	22.6	0.594×10^{-3}
11	Toluene (C_7H_8)	867	384	350	1670	0.134	28.4	0.585×10^{-3}
12	Turpentine	870	429	290	1760	0.136	27	1.49×10^{-3}
13	Water (H_2O)	958	373	2257	4217	0.68	58.9	0.279×10^{-3}
14	Ammonia	681	240	1369	1463.9			
15	R134		246	215			91.2	
16	FC-40	1870	429	711.6			16	3.54×10^{-3}
17	FC-72	1623	329	85.0	1098		8.4	0.457×10^{-3}
18	HFE-7100	1500	334	125.6	1180		14	0.61×10^{-3}
19	HFE-7200	1430	349	122.6	1210		14	0.61×10^{-3}

is expected to move from the warmer to the cooler side. In addition, mixture of liquid can tune the liquid characteristics. Savino et al. [227] mixed the Water, Butanol, Heptanol, Ammonia and Ethylene Glycol to obtain the self-rewetting fluid. And Troniewski and Ulbrich [250] changed the liquid viscosity with varied a sugarwater solution. Moreover, Miner et al. [251] reported cooling of high-power-density micro devices with pump using liquid metal coolants such as Hg, $Ga_{68}In_{20}Sn_{12}$, $Na_{27}K_{78}$, and SnPbInBi. The thermophysical properties of liquid metals make them attractive coolants given that the high thermal conductivity allows for efficient heat transfer, and that the high electrical conductivity allows for these coolants to be pumped efficiently. Yu et al. [252] used the alkali metals as working fluids in MHP which had better evaporating characteristics for the high-temperature HP than normal working fluids.

Recently, advances in nanofabrication and processes have permitted the manufacturing of solid particles down to the nanometre scale, which has conducted to the creation of a new and rather special class of fluids, which is termed 'nanofluids' [253]. They were successfully applied on single-phase and two-phase heat transfer device for better heat transfer. Nguyen et al. [254] enhanced using Al_2O_3-water nanofluid for an electronic liquid cooling system. They reported that for a particular

nanofluid with 6.8% particle volume concentration, heat transfer coefficient has been found to increase as much as 40% compared to that of the base fluid and an increase of particle concentration has produced a clear decrease of the heated component temperature. And Lee and Mudawar [255] studied the effectiveness of nanofluids for single-phase and two-phase heat transfer in micro-channels with water-based nanofluids containing small concentrations of Al_2O_3. In addition, Hassan et al. [213] analyzed the effect of Cu, CuO and Al_2O_3 nanofluids on the vapor chamber for different wick porosities. At volume fraction 9% of Cu nanoparticles which is better than CuO and Al_2O_3, the maximum temperature gradient of vapor chamber decreases by about 19.5% for wick porosity 0.75% and 15.7% for wick porosity 0.35. Titanium nanofluids were tested by Naphon et al. [137, 138] and silver-water nanofluids were reported by Asirvatham et al. [256] for increasing the efficiency of HPs. Yang et al. [257] carried out an experiment to study the heat transfer performance of a horizontal microgrooved HP using 0.5 wt% to 2.0 wt% 50 nm CuO nanofluid as the working fluid. In addition, Liu et al. [258] recently reported an experimental study on the heat transfer performance of a miniature thermosyphon using water-based CNT (with an average diameter of 15 nm and a length range of 5-15 μm) suspensions as the working fluid. Similar experiments were done for an axially microgrooved HP using water-based CNT suspensions as the working fluid [259].

A.5.4 Limitations

Although large quantities of heat can be removed with a small volume of coolant, a catastrophic temperature increase occurs if power source is over the limitations to heat transport. The work was presented firstly by the researches on conventional HPs [153, 260–262]. The type of limitation that restricts the operation of the HP is determined by the one, which has the lowest value of heat transfer rate at a specific HP working temperature (Figure A.18). (1) Viscous Limit - At low temperatures, the vapor from the evaporator doesn't move to the condenser and the thermodynamic cycle doesn't occur because the vapor pressure difference between the condenser and the evaporator may not be enough to overcome viscous forces. (2) Sonic limit - As the temperature increasing, the vapor velocity continuously raise but limited to sonic speed which usually occurs during startup of HP. (3) Capillary limit - The capillary pressure may be too low to provide enough liquid to the evaporator from the condenser which leads to dryout in the evaporator. Dryout prevents the

thermodynamic cycle from continuing and the HP no longer functions properly. (4) Entrainment Limit - at high vapor velocities, droplets of liquid in the wick are torn from the wick and sent into the vapor which results in dryout. (5) Boiling Limit - the dryout occurs when the radial heat flux into the HP causes the liquid in the wick to boil and evaporate.

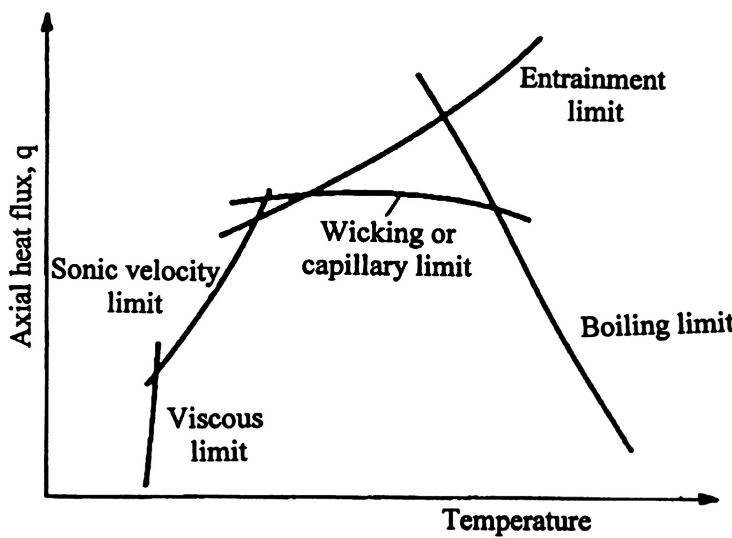

FIGURE A.18: Limitations to heat transport in the heat pipe, By Noie-Baghban and Majideian [260].

The boiling limitation also can be expressed by Critical heat flux (CHF) or burnout which is a limiting operating heat flux for the safe operation of heat dissipation applications and refers to the replacement of liquid being in contact with the heated surface with a vapor blanket (Revellin and Thome [263]). The CHF is an important consideration in the design of most flow boiling systems rather than only HPs. The researches on microchannels under saturated flow boiling conditions have been investigated which is coupled with an extensive database covering a wide range of fluids, channel configurations, and operating conditions. One example is that the CHF in parallel microchannels would be higher if the flow is stabilized by an orifice at the entrance of each channel. The nature of CHF in microchannels is thus different than anticipated, but recent advances in microelectronic fabrication may make it possible to realize the higher power levels(Bergles and Kandlikar [264]).

A.6 Summary and discussion

The design of HPs used for cooling of electronics are complex, ranging from structure, materials, working fluids, gravity, wicks. Development of MHP or LHP that enable very fast cooling for hot spot could have significant impact for all the electronic devices. Generally, the principle of design is shown in Figure A.19. The dimensions can be the first parameter to be considered: 1) the heat source dimension; 2) the heat sink dimension. For instance, if the device has allowed using a large heat sink then HP is unnecessary. Besides, the dimension of total system will decide the volume to set up the HP. VC or flat HP requires relatively large contact surface; the traditional tubular HPs and variable conductance HP need relatively large space for setup; or the semiconductor chips are too tiny for normal HP. Secondly, the effect of wicks and gravity are emerging together. Thermal diodes and pulsating LHP cannot work without gravity and gravity has negative affect on tubular HP. But the MHP and LHP can obtain special properties to transfer heat for the distances up to several meters at any orientation in the gravity field. However, the ability of MHP and LHP is based on the wick position, dimension, material, structure. Therefore, the type of HP can be decided accordingly. Depends on the application, the material, wick (microgroove), structure and process will be considered thirdly. For semiconductor device, silicon could be favorable with its matched CTE and standard process. For those device requires flexibility, polymer HP maybe the candidate for its fast fabrication and easily application. However, the design also requires calculation to deicide the wick porosity, the pipe diameter, the condenser and the evaporator. The last but not the least, although the calculation or simulation can give results to indicate the performance, the experimental tests are essentially compulsory.

As MHPs or LHPs are selected to apply, the design process is still continuing. Although, calculation or simulation can give qualitative analysis, design of HPs is the work mainly depended on the experiment. Sobhan et al. [230] reported that the experiments differed with cross-sectional shape, operating temperature, heat input, cross-sectional area of a channel, heat transfer coefficient, temperature drop, dimension and thermal resistance undertaken in the past two decades. The discussions and data presented in the paper were expected to act as guidelines in designing MHPs and in introducing innovative designs for various applications. And Bai et al. [265] presented the design flowchart for the LHP models. This work was based on steady-state mathematical modeling. To improve the solution accuracy, the liquid and vapor lines are divided into several nodes, each of which represents

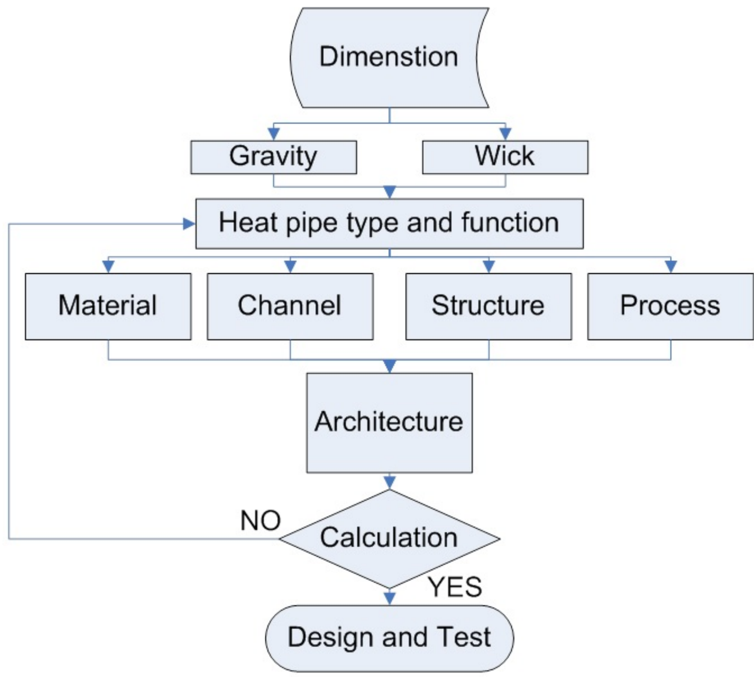

FIGURE A.19: Principle to design and fabricate HP for cooling of electronics.

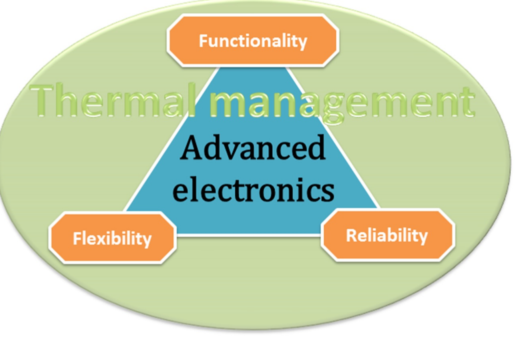

FIGURE A.20: Thermal management/cooling for advanced electronics.

a certain control volume, and the calculations are conducted on every node. And Zhang et al. [266] had demonstrated the design, fabricate and test with LHP applied on the specific application (a solar photovoltaic/loop-heat-pipe (PV/LHP) heat pump system). Dedicated thermo-fluid and energy balance analyses were done by computer model to calculate the operational parameters, optimize the geometrical configurations and sizes, and recommend the appropriate operational condition, and then experimental verification and modification were applied accordingly.

A.7 Conclusion

The combined need for digital and non-digital functionalities in an integrated system is translated as a dual trend in the International Technology Roadmap for Semiconductors: miniaturization of the digital functions (”More Moore”) and functional diversification (”More-than-Moore”) [267, 268], which is called advanced electronics in this work. However, the more functions requires more power generally as well as more miniaturization leads to more concentrated power. The waste heat then gives a very high temperature hot spot accordingly. The thermal management will be one of most important issues for electronics. However, cooling devices are indispensable but always not desirable as they usually introduced problems of large volume, overweight, hinder, and reliability. As shown in Figure A.20, the advanced electronics are defined to the device with three criterions: functionality, flexibility and reliability. (1) Functionality - more functions requires more power or power density due to more devices added to 1 cm^3. (2) Flexibility - It requires that all the functionally devices can be flexibly arranged to anywhere the designer needed. (3) Reliability - Products should be stable, environment friendly and with long enough life time. Accordingly, the thermal management is requiring supplying sufficient supports for the criterions.

MHPs are highly efficient heat-transfer devices for cooling of electronics especially with the silicon compatible process but lack of flexibility, which are one of the best thermal management for advanced electronics. Especially, LHP can be used to create ramified, reversible, controllable systems for heat-transfer possessing mechanical flexibility and high adaptability to various operating conditions. The process of LHP can be derived from conventional metallic HPs, silicon MHP or polymers. As the new materials booming in the century, CNT as one of next candidate for nano wicks with their outstanding characteristic of nanofluidics. With the systematically design based on the application, a new generation of MHP or LHP can be developed to solve the cooling problem of electronics and obtain energy recovery in recent future.

Appendix B

Numerical modeling of natural convection for SSL

The thermal performance of two geometrically different passive heat sink designs for consumer SSL applications with radiation were numerically simulated. With passive cooling, the natural convection plays an important role, and results show that if free ambient air flow is blocked by the heat sink design and the performance reduces considerably. Furthermore, the volume of free air in the luminaire is expected to have significant impact to the heat sink performance.

B.1 Introduction

Compared to active thermal management solutions, passive solutions have advantages of simple structure, easy fabrication, application flexibility and low cost. Air cooling is an important thermal control scheme for passive thermal solution of SSL by combined conductive spreading, natural convection and radiation. Designing methodology of architecture for heat sinks was well outlined in many researches [269]. However, there is little work on the influence of natural convection and radiation of SSL. Arik et al. [17, 19] developed sophisticated numerical models to analyze the effects of different heat sink configurations with a plate. From that work the thermal performance of natural convection on the surface of different heat sink configurations can be derived. Most work on natural convection of SSL assumes that the natural convection coefficient is constant. However, the natural convection coefficient varies widely in real applications. Yu and Joshi [270] studied the natural convection heat transfer coefficients with a heat source on substrate in a partially open compact enclosure. To calculate fluid and air movement, in particular natural convection, finite volume method (FVM) is used in many computational fluid dynamics (CFD) packages. Furthermore, many CFD software packages have solvers to determine the radiation effect in transparent/semitransparent materials. Adams [271] shows the simulation and experiment results of an compact electronic system in still air. This work provides guidance for thermal management of electronic system with natural convection cooling. In this study, two heat sink designs with natural convection are investigated. Meanwhile, a theoretical model of radiation is considered since the effect cannot be simply neglected. Currently, LED packages are commonly enclosed in a bulb or luminaires which has various shapes and spaces. The volume available is essentially important to facilitate natural convection. And to address the influence of natural convection cooling, this work established a series of FVM models with SSL in several dimensions of enclosed space. The FVM models are simulated using CFD software.

B.2 Heat sink designs with considering natural convection

Nowadays, air cooling of electronic components continues to be very important for SSL system. The designs of heat sink with considering conductive spreading, natural connection and radiation cause different thermal performances. While, the

conductive spreading mainly depends on the thermal conductivity of materials and specific technologies (heat pipe, thermal electric, etc.). Many researches are applied to investigate the effects of thermal conduction. However, the consumer used SSL is mainly designed to dissipate heat in still air which fully depends on the natural convection and radiation. Hence, more work for natural convection and radiation is needed when designing heat sink, especially for consumer low cost SSL.

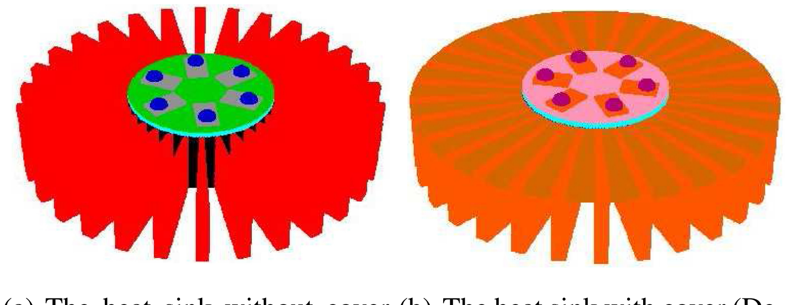

(a) The heat sink without cover (Design I). (b) The heat sink with cover (Design II).

FIGURE B.1: The heat sink design with/without cover.

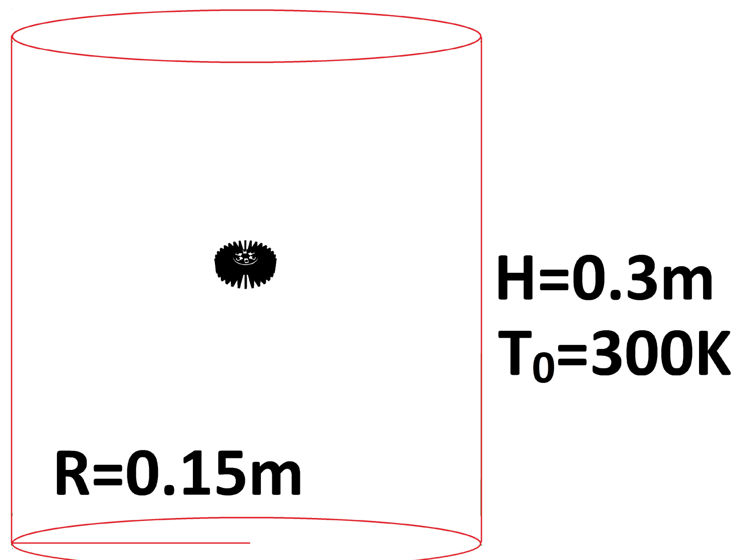

FIGURE B.2: The geometry and dimensions of the simulation enclosure.

Figure B.1(a) and B.1(b) show two heat sink designs for SSL (Design I and Design II) with axial symmetrical fins. These designs are basically derived from current available retrofit LED bulbs. Six LEDs have been arranged on a PCB board axial symmetrically and connected with the aluminum heat sink by silicone glue on a inner aluminum, which is used as heat spreader to conduct heat from LEDs to fins. The two designs are similar but have only one difference; in design II, a cover

is used on the fins which can help heat spread from LEDs to fins and enlarge the heat sink surface. The cover has the same materials as fins. Table B.1 illustrates the dimensions of the two designs.

TABLE B.1: The dimensions of the heat sink designs.

	Design I	Design II
Inner cylinder		
Inner cylinder radius(mm)	10	10
Inner cylinder height(mm)	10	10
Fin		
Fin number	30	30
Fin length(mm)	15	15
Inner cylinder height(mm)	10	9
Cover		
Cover radius(mm)	0	25
Cover height(mm)	0	1

The inclination angle is also important for natural convection [108]. For commercial used LED bulb, two orientations are basically applied. One is called LED up orientation which is shown in B.1(a) and B.1(b). The other one is called LED down orientation which means Design I and Design II are turned over to make the heat sink at the top and the LEDs at the bottom. Thus, four configurations will be simulated in this study (see Table B.2). Besides the configuration, the model

TABLE B.2: The simulation configurations.

	LED up orientation	LED down orientation
Design I	Configuration I	Configuration II
Design II	Configuration III	Configuration IV

boundary conditions needs to be set. In this simulation, the boundary conditions are chosen based on the JEDEC standard [272]. Although this standard is designed for a compact electronic device, standard boundary conditions allows the compassion of different model methodologies form different research groups and model evaluation by experiments. Figure B.2 depicts the geometry and dimensions, SSL is made by semiconductor which is very similar. The LEDs and heat sink are simulated in the center of an enclosed cylinder with the dimension of 0.15 m radius and 0.3 m height. This cylinder is totally adiabatic and the wall temperature keeps constant at 300 K.

B.3 Comparison of two heat sink designs

Convection involves the heat transfer by actual mass motion of a fluid. The heated fluid is caused to move away from the heat source with carrying energy with it. If the motion is only caused by density variations resulting from temperature differences within the fluid, the term natural convection is used. Above a hot surface, air expands, becomes less dense and then rises due to the transportation of heat from heat sink surface to air. Therefore, the heat produced by LEDs can be transferred from heat sink to cooling air.

It is more difficult to analyze the heat convection compared to heat conduction because no single property of the heat transfer medium can be defined to describe the mechanism. Convection varies from situation to situation depended on the fluid flow conditions and coupled with the mode of fluid flow. In practice, analysis of convection is treated empirically with the factors that affect the stagnant film thickness: fluid velocity, fluid viscosity, heat flux, surface roughness (materials), type of flow (single-phase/two-phase, gas/liquid).

Normally, the heat transfer coefficient of natural convection is 5-25 W/m^2K. However, a constant heat transfer coefficient has less accuracy for calculation of natural convection. In CFD, the natural convection can be termed as buoyancy-driven flows due to the gravity acting on the fluid density which varies with temperature [273]. In pure natural convection, the strength of the buoyancy-induced flow is measured by the Rayleigh number:

$$R_a = \frac{g\beta\Delta T L^3\rho}{\mu\alpha_T} \tag{B.1}$$

Where, β is the thermal expansion coefficient, α_T denotes the thermal diffusivity, g is the gravity acceleration, ΔT represents the temperature difference between the surface and the environment temperature, μ is the dynamic viscosity and L is the characteristic length of the geometry. If the Rayleigh numbers less than 10^8, the laminar flow is indicated for buoyancy flow. In this work,the simulation is laminar flow according to estimated calculation.

The Boussinesq Equation (B.2) is applied for a steady state calculation. The density is treated as constant value in all solved equations except for the buoyancy

term in momentum equation.

$$(\rho - \rho_0)g \approx -\rho_0\beta(T - T_0)g \tag{B.2}$$

With the constant density of flow ρ_0 , the operation temperature T_0, and the thermal expansion coefficient β, the approximation is accurate as long as changes in actual density are small.

$$\rho = \rho_0(1 - \beta\Delta T) \tag{B.3}$$

For natural convection in SSL, air is only used fluid as coolant.Thus, the boussinesq in CFD model is applied with the thermal expansion of air. Based on the equations and air properties, accurate prediction of SSL junction temperature and overall system temperature is necessary to allow for analysis of designs.

In order to assess the importance of natural convection around the heat sinks, simulations run for the four configurations which are listed in Table B.2. Based on experimental measurement, the value of 1 W heat dissipation to heat sink for each LED is implemented. The radiation is also considered in this work, which has very significant effect.

Due to the asymmetry of the SSL system and the enclosure, simulations show only half of the cross section of flow and temperature distribution. A comparison of configuration I and III demonstrates the heat sink cover will disturb and block the flow through the heat sink. The maximum air velocities are much different in these two configurations. In this study, air surrounding heat sink removes heat by conduction and natural convection, where air flow passes through the surface and removes the heat. Due to the poor thermal conductivity of air, the natural convection is the key factor for the thermal performance of heat sink. For natural convection, good circulation is one of the most important issues to heat transfer from the surface of solid to cooling air. As shown in the Figure B.3(a), the air temperature remains close to ambient with the exception of the thermal flow in the center of enclosure in both of Configuration I and III. However, due to heat sink cover, the warm air spread wider in Configuration III. And the most important difference is the thermal performance of heat sinks in these two configurations. In the figures, the various colors represent the temperature. In Configuration III, It is obviously that the temperature differs larger from heat sink to air (from yellow to aqua) than former case without cover (from green to aqua). In average, the heat sink with cover has 38 K temperature difference between air and solid heat sink, while the former one

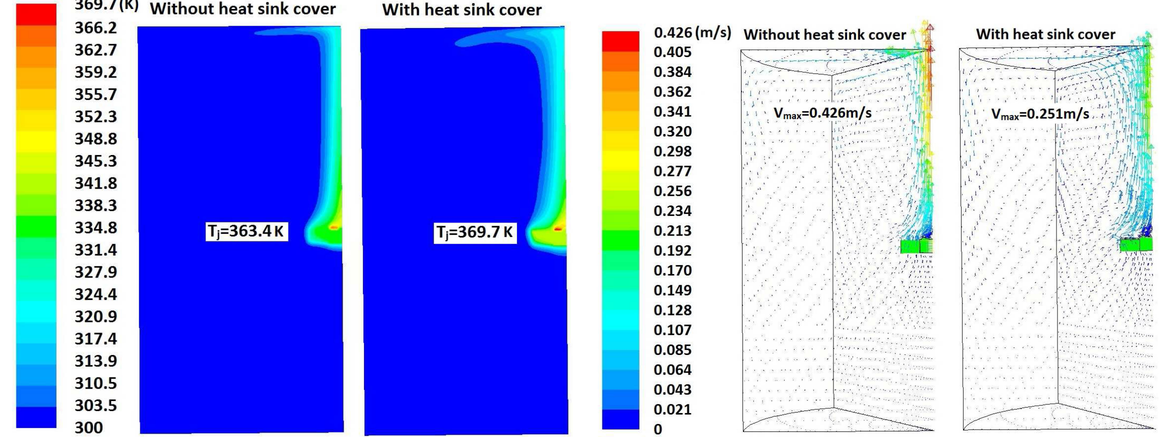

(a) The junction temperature and temperature distribution in closure with two heat sink designs.

(b) The velocity vectors of air in closure with two heat designs.

FIGURE B.3: The simulation results of Configuration I and III.

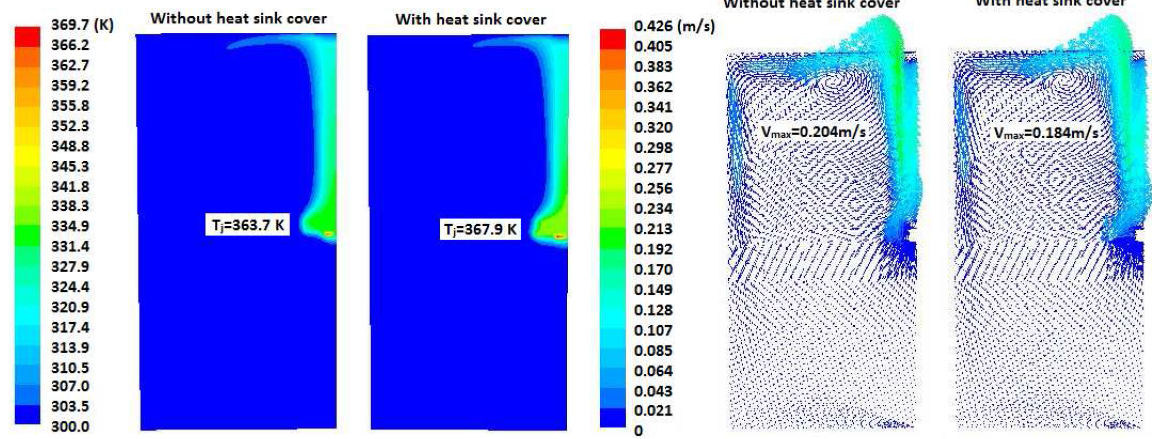

(a) The junction temperature and temperature distribution in closure with two heat sink designs.

(b) The velocity vectors of air in closure with two heat designs.

FIGURE B.4: The simulation results of Configuration II and IV.

has only 32 K temperature difference. Consequently, the junction temperature (T_j) differs from 369.7 K to 363.4 K in the two configurations. Thus, the design I has better geometry for natural convection because there is better air circulation on the surface of heat sink inside the closure. It can be approved by Figure B.3(b) that the maximum velocity of air flow in Configuration I is twice larger than in Configuration III. The cooling air velocity is one of the most important factors for convection. That is the reason that the forced air cooling has much better thermal performance than

natural convection. Therefore, the larger air velocity in Configuration I has definitely positive impact to the thermal performance of heat sink.

To validate the simulation and check the effect of incline angle of heat sink, simulations run for the LED down Configuration II and IV (see Figure B.4(a) and B.4(b)). The temperature differences between the LED up and LED down orientations are not significant. But the air velocities in LED down orientation are much less compared to LED up configurations. The reason is that the hottest part in SSL system is the LEDs. And when the LEDs have been put at the bottom, the air will be heated at the bottom first and rise due to the density changes. But the heated air will be blocked by the inner cylinder and heat sink (or heat sink cover). Therefore, air in the LED down configurations has less velocity. However, the air velocity in Configuration II is still larger than the later one due to the heat sink cover which obstructs the air flow. Thus, the junction temperatures are 363.7 K and 367.9 K respectively.

The junction temperature of LED will directly affect light output, reliability of the solid state lighting and the life time. According to Che Cheung et.al [274], for 5 K deference, lumen output of blue light LEDs will decrease 4% and lifetime drops from 60,000 down to 50,000 hours. Thus, the effect for LEDs cannot be ignored due to the temperature changes around 363 K. From the simulation results, it is found that the effect of the heat sink cover is significant. To compare the results, the thermal resistance of junction to environment R_{j-env} is defined as:

$$R_{j-env} = \frac{T_j - T_0}{Q} \tag{B.4}$$

Where, T_j is the junction temperature, T_0 indicates the environment temperature and Q represents the generated heat by LEDs. From Table B.3, the thermal resistances calculated by Equation (B.4) vary mainly due to the heat sink cover which causes 1 K/W difference with or without it. But the effect of orientations of SSL system is not significant in this study.

TABLE B.3: The thermal resistance of various configurations.

	LED up orientation	LED down orientation
Design I	10.6 (K/W)	10.6 (K/W)
Design II	11.6 (K/W)	11.3 (K/W)

B.4 Natural convection in enclosed spaces

In this work, air will be heat up and allow natural circulation carry the heat around the space containing the heat source. Warm air rises in the natural circulation and gradually heating the entire space. Therefore, the space is very important for the natural circulation and then for better thermal performance of heat sinks.

Currently, SSL luminaires have been applied and existed in commercial market. Most of these systems spread the heat from LED junction to environment depending on nature convection heat sinks. However, little LED luminaires has been well designed with considering nature convection. A high temperature needed as much as possible for the incandescent light, but low temperature for LEDs. Thus all the SSL systems may have different structures comparing with traditional light. For nature convection, the volume of space is very essential due to larger space leads to high air velocity. To investigate the relations between space and the natural convection around SSL systems, simulations with various dimensions of enclosures run for a general methodology of designing.

Using the model of Configuration I, the 6 LEDs on an aluminum heat sink without cover is applied in various volumes of spaces. All the enclosures have the same boundary conditions with environment temperature 300 K. The simulation results show the temperature distribution in enclosures (see Figure B.5(a)). The enclosures dimensions vary from R 0.3 m $\times$ H 0.3 m to R 0.04 m $\times$ H 0.08 m. The most obvious difference of temperature distribution in various dimensions is consistent with the air flow in the enclosures. In the largest enclosure, most of the air remains the same temperature as the environment with exception of the area close to heat sink and on the top of LEDs. However, with gradual reduction of space, air temperature in enclosure rises. In the smallest enclosure, most of air on the top of heat sink is already heated to relative high temperature. That is, the natural convection has less heat transfer efficiency in small space, due to the low air velocity.The air velocities are shown in Figure B.5(b). As expected, larger space results in fast movement of air flow. If the space is very limited, air velocity can be almost neglected due to it is very low. In that condition, the heat transfer due to natural convection drops significant. Thus, when designing a luminaire for SSL system, it is necessary to consider the space with avoiding stagnation of air.

With applying the Equation (B.4), thermal resistances of junction to environment are carried out which are shown in Figure B.6. The air velocity gradually increases

with the increasing space of enclosure. However, the trend of the thermal resistance curve is totally opposite comparing to the air velocity curve. It dramatically decline at first where the enclosure space is limited. But when the space has the dimension larger than R 0.05 m × H 0.1 m, the thermal resistance drops slightly.Although more study needed, the gradient of thermal resistance indicates a turning point at R 0.05 m for the heat sink design Configuration I. Therefore, the natural convection due to volume of space should be well considered, when designing the LED luminaires. Because the volume will directly affect the natural convection efficiency of heat sink in still air.

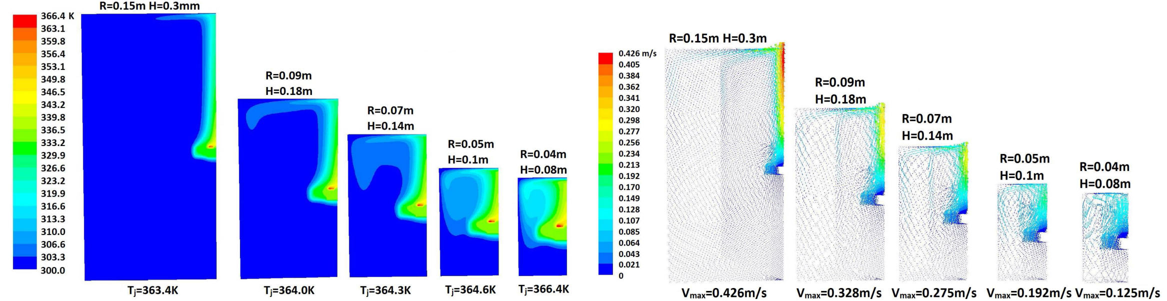

(a) The junction temperature and temperature distribution in various enclosures with natural convection on heat sink.

(b) The velocity vectors of air in various enclosures with natural convection on heat sink.

FIGURE B.5: The simulation results of Configuration I tested in various enclosures.

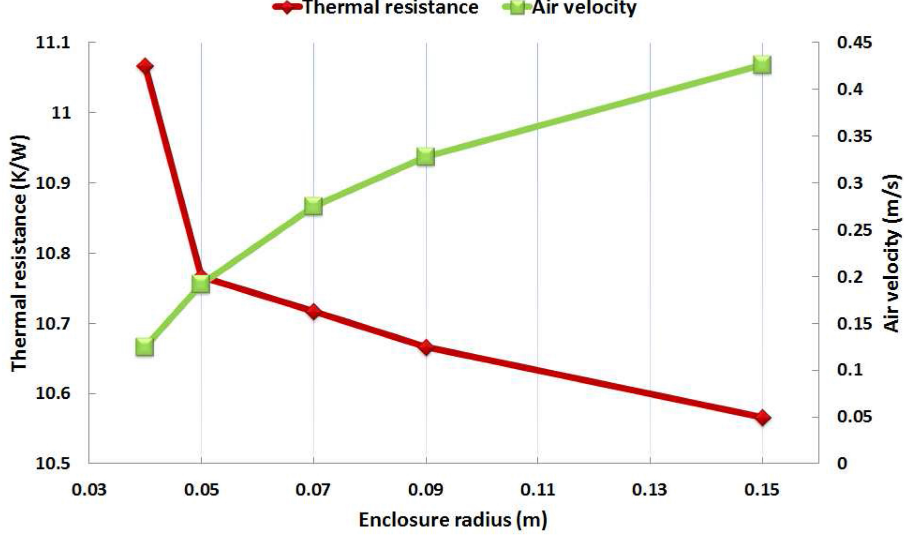

FIGURE B.6: The thermal resistance and air velocities in various enclosures with natural convection on heat sink (Configuration I).

B.5 Conclusion

Based on a commercial available SSL system, two simplified models and four configurations are simulated to validate the effect of thermal performance with natural convection heat sinks. Meanwhile, the radiation effect is considered. The models are applied in CFD to simulate the natural convection performance in a test closure. A straightforward method is used to calculate the thermal resistance of the LED junction to ambient in order to compare the results. Temperature and air velocity distribution gives results that the effect of heat sink geometry is significant when applying natural convection cooling for SSL systems. In addition, the space for LEDs in the luminaire is also discussed. The enclosures differ from various dimensions, where the simplified SSL system is put in the center. The temperature distribution is the most obvious difference in various spaces and the air velocities in the enclosures change a lot. With increasing luminaire volume, the thermal resistances of the LED junction to environment declines dramatically particularly for an enclosure radius below 0.06 m. Trend of the thermal resistance curve is totally opposite comparing to the air velocity curve. In addition, the gradient of thermal resistance indicates a turning point which is a balance for the luminaire volume and natural convection cooling effect. According to the work done in this study, the luminaire volume for SSL system should be essentially considered when applying a natural convection heat sink.

Abbreviations

LED	**L**ight **E**mitting **D**iode
SSL	**S**olid **S**tate **L**ighting
HP	**H**eat **P**ipe
MHP	**M**icro **H**eat **P**ipe
LHP	**L**oop **H**eat **P**ipe
CPL	**C**apillary **P**umped **L**oop
CC	**C**ompensation **C**hamber
EC	**E**vaporation **C**hamber
VC	**V**apor **C**hamber
CIE	**C**ommission **I**nternationale de l'**É**clairage
SPD	**S**pectral **P**ower **D**istribution
CRI	**C**olor **R**endering **I**ndex
CCT	**C**orrelated **C**olor **T**emperature
TIM	**T**hermal **I**nterface **M**aterial
MEMS	**M**icro**e**lectro**m**echanical **S**ystem
CTE	**C**oefficient of **T**hermal **E**xpansion

Nomenclature

A	The area [m^2]
c_p	The specific heat [kJ/kgK]
D_h	The hydraulic diameter [m]
E	The Young's modulus of materials in the MEMS beam [GPa]
ΔE_i	The Euclidean distance to calculate CRI
Gr	The Grashof number
h	The heat transfer coefficient [W/m^2K]
h_{lv}	The enthalpy of evaporation [kJ/kg]
I	The electric current [A]
$I(\lambda)$	The spectral power distribution [μW/nm]
k	The thermal conductivity [W/mK]
L_H	The latent heat of liquid [kJ/kg]
T_0	The ambient temperature [°C]
$\dot{m}$	The volume flow rate [mL/h]
Nu	The Nusselt number
P	The pressure [Pa]
P_E	The electrical energy [W]
Q	The generated heat [W]
R	The electric resistance [Ω]

Ra The color rendering index

Re The Reynolds number

r The pore radius [mm]

T The temperature [°C]

T_j The junction temperature of LED chip [°C]

t The time [s]

t The thickness of materials (with subscripts) in the MEMS beam [μm]

V The volume [m^3]

$V(\lambda)$ The CIE luminosity function

V_f The diode forward voltage [V]

u The velocity on x direction [m/s]

v The velocity on y direction [m/s]

w The velocity on z direction [m/s]

u' The $(u'v')$ chromaticity

v' The $(u'v')$ chromaticity

X The tristimulus value

Y The tristimulus value

Z The tristimulus value

$\bar{x}(\lambda)$ The CIE's color matching function

$\bar{y}(\lambda)$ The CIE's color matching function

$\bar{z}(\lambda)$ The CIE's color matching function

x The xyz coordinates or (xy) chromaticity

y The xyz coordinates or (xy) chromaticity

z The xyz coordinates

Subscripts

$_{Al}$	The aluminum in the MEMS beam
$_{B}$	The chip which generating premier blue light
$_{b}$	The boiling point of liquid
$_{c}$	The heat generated by LED removed by convection
$_{cap}$	The capillary force due to the evaporator wicks in loop heat pipe
$_{CC}$	The condensation chamber (CC) of evaporator in loop heat pipe
$_{evap}$	The evaporator in loop heat pipe
$_{cond}$	The condenser in loop heat pipe
$_{conv}$	The converted blue light which will become white light
$_{EC}$	The evaporation chamber (EC) of evaporator in loop heat pipe
$_{eff}$	The effective coefficient of thermal expansion in the MEMS beam
$_{ele}$	The electric
$_{evap}$	The evaporator in loop heat pipe
$_{f}$	The heat generated by LED removed by fluid (both liquid cooling and two-phase cooling)
$_{grav}$	The gravity
$_{groove}$	The evaporator grooves in loop heat pipe
$_{inre}$	The internal electrical resistance of one p-n in LED chip
$_{a}$	The air
$_{l}$	The liquid
$_{LED}$	The LED with blue light chip and yellow phosphors
$_{lere}$	The leakage electrical resistances of one p-n in LED chip
$_{liql}$	The liquid line in loop heat pipe
$_{ox}$	The silicon oxide in the MEMS beam

$_P$ The phosphors used to convert white light to blue light

$_{pn}$ The electrical resistance of one p-n in LED chip

$_r$ The heat generated by LED removed by radiation

$_{Si}$ The silicon in the MEMS beam

$_{tot}$ The total frictional pressure drops in loop heat pipe

$_v$ The vapor

$_{vapl}$ The vapor line in loop heat pipe

$_W$ The white light of LED which is converted from blue light by phosphors

$_{wick}$ The evaporator wicks in loop heat pipe

Greek symbols

α The coefficient of thermal expansion [1/°C]

ε The radiation emissivity

η The dynamic viscosity [Pa·s]

ξ The electric-blue light/blue-to-white light conversion rate [%]

λ The light wavelength [nm]

ρ The density [g/mL]

σ_l The surface tension of the working fluid [N/m]

υ The kinetic viscosity [m^2/s]

Φ The luminous flux [lm]

φ The optical power [W]

Bibliography

[1] N. Jr. and S.F.Bevaqua, Coherent(visible) light emission from GaAs(1-x)Px junctions *Applied physics letters*, vol. 1, pp. 82–83, 1962.

[2] D. A. Steigerwald, J. C. Bhat, D. Collins, R. M. Fletcher, M. O. Holcomb, M. J. Ludowise, P. S. Martin, and S. L. Rudaz, Illumination with solid state lighting technology *Selected Topics in Quantum Electronics, IEEE Journal of*, vol. 8, no. 2, pp. 310–320, 2002.

[3] S. Nakamura, T. Mukai, M. Senoh, S.-i. Nagahama, and N. Iwasa, Inx Ga (1-x)N / Iny Ga(1-y)N superlattices grown on GaN films *Journal of applied physics*, vol. 74, no. 6, pp. 3911–3915, 1993.

[4] S. Nakamura, M. Senoh, and T. Mukai, P-GaN/N-InGaN/N-GaN double-heterostructure blue-light-emitting diodes *Japanese Journal of Applied Physics Part 2 Letters*, vol. 32, pp. L8–L8, 1993.

[5] S. Nakamura, S. Pearton, and G. Fasol, *The blue laser diode: the complete story*. Springer, 2000.

[6] N. Holonyak Jr, Is the light emitting diode (LED) an ultimate lamp? *American Journal of Physics*, vol. 68, p. 864, 2000.

[7] S. Lee and S. Y. Seo, Optimization of yttrium aluminum garnet: Ce3+ phosphors for white light-emitting diodes by combinatorial chemistry method *Journal of The Electrochemical Society*, vol. 149, no. 11, pp. J85–J88, 2002.

[8] J.-h. Yum, S.-Y. Seo, S. Lee, and Y.-E. Sung, Y3Al5O12: Ce0.05 Phosphor Coatings on Gallium Nitride for White Light Emitting Diodes *Journal of The Electrochemical Society*, vol. 150, no. 2, pp. H47–H52, 2003.

[9] S. Muthu, F. J. Schuurmans, and M. D. Pashley, Red, green, and blue LED based white light generation: issues and control in *Industry Applications Conference, 2002. 37th IAS Annual Meeting. Conference Record of the*, vol. 1, pp. 327–333, IEEE, 2002.

[10] J.-K. Sheu, S.-J. Chang, C. Kuo, Y.-K. Su, L. Wu, Y. Lin, W. Lai, J. Tsai, G.-C. Chi, and R. Wu, White-light emission from near UV InGaN-GaN LED chip precoated with blue/green/red phosphors *Photonics Technology Letters, IEEE*, vol. 15, no. 1, pp. 18–20, 2003.

[11] G. Wyszecki, V. Stiles, and K. L. Kelly, Color Science: Concepts and Methods, Quantitative Data and Formulas *Physics Today*, vol. 21, no. 6, pp. 83–84, 1968.

[12] R.-J. Xie, N. Hirosaki, M. Mitomo, K. Sakuma, and N. Kimura, Wavelength-tunable and thermally stable Li-α-sialon: Eu 2+ oxynitride phosphors for white light-emitting diodes *Applied physics letters*, vol. 89, no. 24, pp. 241103–241103, 2006.

[13] Y. Narukawa, M. Sano, M. Ichikawa, S. Minato, T. Sakamoto, T. Yamada, and T. Mukai, Improvement of luminous efficiency in white light emitting diodes by reducing a forward-bias voltage *Japanese Journal of Applied Physics*, vol. 46, pp. L963–L965, 2007.

[14] P. Schlotter, J. Baur, C. Hielscher, M. Kunzer, H. Obloh, R. Schmidt, and J. Schneider, Fabrication and characterization of GaN/InGaN/AlGaN double heterostructure LEDs and their application in luminescence conversion LEDs *Materials Science and Engineering: B*, vol. 59, no. 1, pp. 390–394, 1999.

[15] J. K. Park, C. H. Kim, S. H. Park, H. D. Park, and S. Y. Choi, Application of strontium silicate

yellow phosphor for white light-emitting diodes *Applied physics letters*, vol. 84, no. 10, pp. 1647–1649, 2004.

[16] J. Petroski, Thermal challenges facing new-generation light-emitting diodes (LEDs) for lighting applications in *International Symposium on Optical Science and Technology*, pp. 215–222, International Society for Optics and Photonics, 2002.

[17] M. Arik, C. A. Becker, S. E. Weaver, and J. Petroski, Thermal management of LEDs: package to system in *Optical Science and Technology, SPIE's 48th Annual Meeting*, pp. 64–75, International Society for Optics and Photonics, 2004.

[18] C. Che and H. Kim, Thermal management: comparison of passive and active cooliing effectiveness *LED professional review*, vol. 5, 2009.

[19] M. Arik and S. Weaver, Chip-scale thermal management of high-brightness LED packages in *Optical Science and Technology, the SPIE 49th Annual Meeting*, pp. 214–223, International Society for Optics and Photonics, 2004.

[20] J. Jakovenko, R. Werkhoven, J. Formanek, J. Kunen, P. Bolt, and P. Kulha, Thermal simulation and validation of 8W LED Lamp in *Thermal, Mechanical and Multi-Physics Simulation and Experiments in Microelectronics and Microsystems (12th EuroSimE)*, pp. 1–4, IEEE, 2011.

[21] H. Ye, S. W. Koh, C. Yuan, H. van Zeijl, A. W. Gielen, S.-W. R. Lee, and G. Zhang, Electrical–thermal–luminous–chromatic model of phosphor-converted white light-emitting diodes *Applied Thermal Engineering*, vol. 63, no. 2, pp. 588–597, 2014.

[22] O. Kuckmann, High power LED arrays special requirements on packaging technology in *Proc. SPIE*, vol. 6134, p. 613404, 2006.

[23] S. Lee, Optimum design and selection of heat sinks in *Semiconductor Thermal Measurement and Management Symposium, 1995. SEMI-THERM XI., Eleventh Annual IEEE*, pp. 48–54, IEEE, 1995.

[24] D.-K. Kim, S. J. Kim, and J.-K. Bae, Comparison of thermal performances of plate-fin and pin-fin heat sinks subject to an impinging flow *International Journal of Heat and Mass Transfer*, vol. 52, no. 15, pp. 3510–3517, 2009.

[25] M. Iyengar and A. Bar-Cohen, Least-material optimization of vertical pin-fin, plate-fin, and triangular-fin heat sinks in natural convective heat transfer in *Thermal and Thermomechanical Phenomena in Electronic Systems, 1998. ITHERM'98. The Sixth Intersociety Conference on*, pp. 295–302, IEEE, 1998.

[26] N. C. Gallego and J. W. Klett, Carbon foams for thermal management *Carbon*, vol. 41, no. 7, pp. 1461–1466, 2003.

[27] M. Ivanova, Y. Avenas, C. Schaeffer, J.-B. Dezord, and J. Schulz-Harder, Heat pipe integrated in direct bonded copper (DBC) technology for cooling of power electronics packaging *Power Electronics, IEEE Transactions on*, vol. 21, no. 6, pp. 1541–1547, 2006.

[28] M. Groll, M. Schneider, V. Sartre, M. Chaker Zaghdoudi, and M. Lallemand, Thermal control of electronic equipment by heat pipes *Revue générale de thermique*, vol. 37, no. 5, pp. 323–352, 1998.

[29] J. Eastman, S. Choi, S. Li, W. Yu, and L. Thompson, Anomalously increased effective thermal conductivities of ethylene glycol-based nanofluids containing copper nanoparticles *Applied Physics Letters*, vol. 78, no. 6, pp. 718–720, 2001.

[30] P. Naphon, P. Assadamongkol, and T. Borirak, Experimental investigation of titanium nanofluids on the heat pipe thermal efficiency *International Communications in Heat and Mass Transfer*, vol. 35, no. 10, pp. 1316–1319, 2008.

[31] X. Y. Lu, T. C. Hua, M. J. Liu, and Y.-x. Cheng, Thermal analysis of loop heat pipe used for high-power LED *Thermochimica Acta*, vol. 493, no. 1, pp. 25–29, 2009.

[32] L. Kim, J. H. Choi, S. H. Jang, and M. W. Shin, Thermal analysis of LED array system with heat pipe *Thermochimica Acta*, vol. 455, no. 1, pp. 21–25, 2007.

[33] M. Le Berre, S. Launay, V. Sartre, and M. Lallemand, Fabrication and experimental investigation of silicon micro heat pipes for cooling electronics *Journal of Micromechanics and Microengineering*, vol. 13, no. 3, p. 436, 2003.

[34] X. P. Wu, M. Mochizuki, T. Nguyen, Y. Saito, V. Wuttijumnong, H. Ghisoiu, V. Kumthonkittikul, P. Sukkasaem, P. Nimitkiatklai, and F. Kiyooka, Low profile-high performance vapor chamber heat sinks for cooling high-density blade servers in *Semiconductor Thermal Measurement and Management Symposium, 2007. SEMI-THERM 2007. Twenty Third Annual IEEE*, pp. 174–178, IEEE, 2007.

[35] S. Tonapi, R. Fillion, F. Schattenmann, H. Cole, J. Evans, and B. Sammakia, An overview of thermal management for next generation microelectronic devices in *Advanced Semiconductor Manufacturing Conference and Workshop, 2003 IEEEI/SEMI*, pp. 250–254, IEEE, 2003.

[36] C. H. Zweben, Emerging low-cost LED thermal management materials in *Optical Science and Technology, the SPIE 49th Annual Meeting*, pp. 194–206, International Society for Optics and Photonics, 2004.

[37] A. Shakouri, Nanoscale thermal transport and microrefrigerators on a chip *Proceedings of the IEEE*, vol. 94, no. 8, pp. 1613–1638, 2006.

[38] S. Ghosh, I. Calizo, D. Teweldebrhan, E. Pokatilov, D. Nika, A. Balandin, W. Bao, F. Miao, and C. N. Lau, Extremely high thermal conductivity of graphene: Prospects for thermal management applications in nanoelectronic circuits *Applied Physics Letters*, vol. 92, p. 151911, 2008.

[39] C. J. Lasance and R. E. Simons, Advances in high-performance cooling for electronics *Electronics cooling*, vol. 11, no. 4, 2005.

[40] Y. Zhang, A. Shakouri, and G. Zeng, High-power-density spot cooling using bulk thermoelectrics *Applied physics letters*, vol. 85, no. 14, pp. 2977–2979, 2004.

[41] P. Wang and A. Bar-Cohen, On-chip hot spot cooling using silicon thermoelectric microcoolers *Journal of applied physics*, vol. 102, no. 3, pp. 034503–034503, 2007.

[42] C. K. Liu, M.-J. Dai, C.-K. Yu, and S.-L. Kuo, High efficiency silicon-based high power LED package integrated with micro-thermoelectric device in *Microsystems, Packaging, Assembly and Circuits Technology, 2007. IMPACT 2007. International*, pp. 29–33, IEEE, 2007.

[43] K. H. Do and S. P. Jang, Effect of nanofluids on the thermal performance of a flat micro heat pipe with a rectangular grooved wick *International Journal of Heat and Mass Transfer*, vol. 53, no. 9, pp. 2183–2192, 2010.

[44] jae Mo Koo, S. Im, L. Jiang, and K. E. Goodson, Integrated Microchannel Cooling for Three-Dimensional Electronic Circuit Architectures *Journal of heat transfer*, vol. 127, pp. 49–58, 2005.

[45] S. Rea and S. West, Thermal radiation from finned heat sinks *Parts, Hybrids, and Packaging, IEEE Transactions on*, vol. 12, no. 2, pp. 115–117, 1976.

[46] Y. K. Khor, Y. M. Hung, and B. K. Lim, On the role of radiation view factor in thermal performance of straight-fin heat sinks *International Communications in Heat and Mass Transfer*, vol. 37, no. 8, pp. 1087–1095, 2010.

[47] H. Ye, M. Mihailovic, C. Wong, H. van Zeijl, A. Gielen, G. Zhang, and P. Sarro, Two-phase cooling of light emitting diode for higher light output and increased efficiency *Applied Thermal Engineering*, vol. 52, pp. 353–359, 2013.

[48] P. Gravesen, J. Branebjerg, and O. S. Jensen, Microfluidics-a review *Journal of Micromechanics and Microengineering*, vol. 3, no. 4, p. 168, 1993.

[49] S. Launay, V. Sartre, and J. Bonjour, Parametric analysis of loop heat pipe operation: a literature review *International Journal of Thermal Sciences*, vol. 46, no. 7, pp. 621–636, 2007.

[50] D. Cytrynowicz, M. Hamdan, P. Medis, A. Shuja, H. T. Henderson, F. M. Gerner, and E. Golliher, MEMS loop heat pipe based on coherent porous silicon technology in *AIP Conference Proceedings*, vol. 608, p. 220, 2002.

[51] D. McDaniels and G. Peterson, Investigation of polymer based micro heat pipes for a flexible spacecraft radiator *ASME-PUBLICATIONS-HTD*, vol. 369, pp. 423–434, 2001.

[52] Y. Wang and G. Peterson, Capillary evaporation in microchanneled polymer films *Journal of thermophysics and heat transfer*, vol. 17, no. 3, pp. 354–359, 2003.

[53] C. Oshman, B. Shi, C. Li, R. Yang, Y. Lee, G. Peterson, and V. M. Bright, The development of polymer-based flat heat pipes *Microelectromechanical Systems, Journal of*, vol. 20, no. 2, pp. 410–417, 2011.

[54] N. Beratlis and M. K. Smith, Optimization of synthetic jet cooling for microelectronics applications [VCSEL array example] in *Semiconductor Thermal Measurement and Management Symposium, 2003. Ninteenth Annual IEEE*, pp. 66–73, IEEE, 2003.

[55] J. Suh, D. Cytrynowicz, F. M. Gerner, and H. T. Henderson, A MEMS bubble pump for an electronic cooling device *Journal of Micromechanics and Microengineering*, vol. 20, no. 12, p. 125025, 2010.

[56] R. Hannemann, J. Marsala, and M. Pitasi, Pumped liquid multiphase cooling *ASME paper IMECE2004-60669*, 2004.

[57] J.-H. Cheng, C.-K. Liu, Y.-L. Chao, and R.-M. Tain, Cooling performance of silicon-based thermoelectric device on high power LED in *Thermoelectrics, 2005. ICT 2005. 24th International Conference on*, pp. 53–56, IEEE, 2005.

[58] K. Takikawa and Y. Ono, "Temperature-controlled fan fluid coupling." Patent, May 28 1991. US Patent 5,018,612.

[59] J. S. Dinh and G. K. Korinsky, "Temperature dependent fan control circuit for personal computer." Patent, June 11 1996. US Patent 5,526,289.

[60] R. Zhang, S. R. Lee, D. G. Xiao, and H. Chen, LED packaging using silicon substrate with cavities for phosphor printing and copper-filled TSVs for 3D interconnection in *Electronic Components and Technology Conference (ECTC), 2011 IEEE 61st*, pp. 1616–1621, IEEE, 2011.

[61] C. Yuan, J. Wei, H. Ye, S. Koh, S. Harianto, M. van den Nieuwenhof, and G. Zhang, Polymer-based 2D/3D wafer level heterogeneous integration for SSL module in *Thermal, Mechanical and Multi-Physics Simulation and Experiments in Microelectronics and Microsystems (EuroSimE), 2012 13th International Conference on*, pp. 1–7, IEEE, 2012.

[62] W. K. Jeung, S. H. Shin, S. Y. Hong, S. M. Choi, S. Yi, Y. B. Yoon, H. J. Kim, S. J. Lee, and K. Y. Park, Silicon-based, multi-chip LED package in *Electronic Components and Technology Conference, 2007. ECTC'07. Proceedings. 57th*, pp. 722–727, IEEE, 2007.

[63] K. Bando, K. Sakano, Y. Noguchi, and Y. Shimizu, Development of high-bright and pure-white LED lamps *Journal of Light & Visual Environment*, vol. 22, pp. 2–5, 1998.

[64] M. Arik, J. Petroski, and S. Weaver, Thermal challenges in the future generation solid state lighting applications: light emitting diodes in *Thermal and Thermomechanical Phenomena in Electronic Systems, 2002. ITHERM 2002. The Eighth Intersociety Conference on*, pp. 113–120, IEEE, 2002.

[65] F.-S. Hwu, G.-J. Sheu, and J.-C. Chen, Thermal modeling and performance of LED packaging for illuminating device in *Optics & Photonics*, pp. 63371J–63371J, International Society for Optics and Photonics, 2006.

[66] A. Christensen and S. Graham, Thermal effects in packaging high power light emitting diode arrays *Applied Thermal Engineering*, vol. 29, no. 2, pp. 364–371, 2009.

[67] M. Tsai, C. Chen, and C. Kang, Thermal measurements and analyses of low-cost high-power LED packages and their modules *Microelectronics Reliability*, vol. 52, no. 5, pp. 845–854, 2012.

[68] P. G. Eliseev, P. Perlin, J. Lee, and M. Osinski, Blue temperature-induced shift and band-tail emission in InGaN-based light sources *Applied physics letters*, vol. 71, no. 5, pp. 569–571, 1997.

[69] P. Eliseev, M. Osinski, J. Lee, T. Sugahara, and S. Sakai, Band-tail model and temperature-induced blue-shift in photoluminescence spectra of In(x)Ga(1-x)N grown on sapphire *Journal*

of Electronic Materials, vol. 29, pp. 332–341, 2000.

[70] H. Ye, S. Koh, C. Yuan, and G. Zhang, Thermal analysis of phosphor in high brightness LED in *Electronic Packaging Technology and High Density Packaging (ICEPT-HDP), 2012 13th International Conference on*, pp. 1535–1539, IEEE, 2012.

[71] Y. Zhang, L. Li, X. Zhang, and Q. Xi, Temperature effects on photoluminescence of YAG: Ce3+ phosphor and performance in white light-emitting diodes *Journal of Rare Earths*, vol. 26, no. 3, pp. 446–449, 2008.

[72] S. Hui and Y. Qin, A general photo-electro-thermal theory for light emitting diode (LED) systems *Power Electronics, IEEE Transactions on*, vol. 24, no. 8, pp. 1967–1976, 2009.

[73] B.-J. Huang and C.-W. Tang, Thermal–electrical–luminous model of multi-chip polychromatic LED luminaire *Applied Thermal Engineering*, vol. 29, no. 16, pp. 3366–3373, 2009.

[74] F.-C. Wang, C.-W. Tang, and B.-J. Huang, Multivariable robust control for a red–green–blue LED lighting system *Power Electronics, IEEE Transactions on*, vol. 25, no. 2, pp. 417–428, 2010.

[75] H. Chen and S. Hui, Prediction of Correlated Color Temperature and Color Rendering Index of Phosphor-Coated White Light-Emitting Diodes *IEEE Transactions on Industrial Electronics*, vol. 61, pp. 784–797, 2014.

[76] Y. Ohno, Color rendering and luminous efficacy of white LED spectra in *Proc. of SPIE Vol*, vol. 5530, p. 89, 2004.

[77] C. Li, M. Ronnier Luo, C. Li, and G. Cui, The CRI-CAM02UCS colour rendering index *Color Research & Application*, vol. 37, no. 3, pp. 160–167, 2012.

[78] R. W. G. Hunt and M. R. Pointer, *Measuring colour.* John Wiley & Sons, 2011.

[79] C. S. McCamy, Correlated color temperature as an explicit function of chromaticity coordinates *Color Research & Application*, vol. 17, no. 2, pp. 142–144, 1992.

[80] R. Lu, Q. Hong, Z. Ge, and S.-T. Wu, Color shift reduction of a multi-domain IPS-LCD using RGB-LED backlight *Opt. Express*, vol. 14, no. 13, pp. 6243–6252, 2006.

[81] Y. Xi, J.-Q. Xi, T. Gessmann, J. Shah, J. Kim, E. Schubert, A. Fischer, M. Crawford, K. Bogart, and A. Allerman, Junction and carrier temperature measurements in deep-ultraviolet light-emitting diodes using three different methods *Applied Physics Letters*, vol. 86, no. 3, pp. 031907–031907, 2005.

[82] H. Ye, X. Chen, H. van Zeijl, A. W. Gielen, and G. Zhang, Thermal transient effect and improved junction temperature measurement method in high-voltage light-emitting diodes *IEEE Electron Device Letters*, vol. 34, pp. 1172–1174, 2013.

[83] H. Ye, A. Gielen, H. van Zeijl, R. Werkhoven, and G. Zhang, Numerical modeling of thermal performance: natural convection and radiation of solid state lighting in *Thermal, Mechanical and Multi-Physics Simulation and Experiments in Microelectronics and Microsystems (12th EuroSimE)*, pp. 1–6, IEEE, 2011.

[84] D. Peng and K. Jin, The Influence of Driving Current on Emission Spectra of GaN-Based LED in *International Conference on Electronics and Optoelectronics*, pp. 142–151, IEEE, 2011.

[85] S. Chhajed, Y. Xi, Y.-L. Li, T. Gessmann, and E. Schubert, Influence of junction temperature on chromaticity and color-rendering properties of trichromatic white-light sources based on light-emitting diodes *Journal of Applied Physics*, vol. 97, no. 5, pp. 054506–054506, 2005.

[86] Y. Gu and N. Narendran, A noncontact method for determining junction temperature of phosphor-converted white LEDs in *Optical Science and Technology, SPIE's 48th Annual Meeting*, pp. 107–114, International Society for Optics and Photonics, 2004.

[87] Y. Shuai, Y. He, N. T. Tran, and F. G. Shi, Angular CCT uniformity of phosphor converted white LEDs: Effects of phosphor materials and packaging structures *Photonics Technology Letters, IEEE*, vol. 23, no. 3, pp. 137–139, 2011.

[88] T. Tamura, T. Setomoto, and T. Taguchi, Illumination characteristics of lighting array using 10

candela-class white LEDs under AC 100V operation *Journal of Luminescence*, vol. 87, pp. 1180–1182, 2000.

[89] A. Keppens, W. Ryckaert, G. Deconinck, and P. Hanselaer, High power light-emitting diode junction temperature determination from current-voltage characteristics *Journal of Applied Physics*, vol. 104, no. 9, pp. 093104–093104, 2008.

[90] B. M. Cain, P. A. Goud, and C. Englefield, Electrical measurement of the junction temperature of an RF power transistor *Instrumentation and Measurement, IEEE Transactions on*, vol. 41, no. 5, pp. 663–665, 1992.

[91] A. Sztein, H. Ohta, J. Sonoda, A. Ramu, J. E. Bowers, S. P. DenBaars, and S. Nakamura, GaN-based integrated lateral thermoelectric device for micro-power generation *Applied physics express*, vol. 2, no. 11, pp. 111003–111003, 2009.

[92] H. Tong, J. Zhang, G. Liu, J. A. Herbsommer, G. Huang, and N. Tansu, Thermoelectric properties of lattice-matched AlInN alloy grown by metal organic chemical vapor deposition *Applied Physics Letters*, vol. 97, no. 11, pp. 112105–112105, 2010.

[93] J. Zhang, H. Tong, G. Liu, J. A. Herbsommer, G. Huang, and N. Tansu, Characterizations of Seebeck coefficients and thermoelectric figures of merit for AlInN alloys with various In-contents *Journal of Applied Physics*, vol. 109, no. 5, pp. 053706–053706, 2011.

[94] B. N. Pantha, I.-w. Feng, K. Aryal, J. Li, J.-Y. Lin, H.-X. Jiang, *et al.*, Erbium-doped AlInGaN alloys as high-temperature thermoelectric materials *Appl. Phys. Express*, vol. 4, no. 5, p. 051001, 2011.

[95] G. J. Snyder, J.-P. Fleurial, T. Caillat, R. Yang, and G. Chen, Supercooling of Peltier cooler using a current pulse *Journal of applied physics*, vol. 92, no. 3, pp. 1564–1569, 2002.

[96] T. Thonhauser, G. Mahan, L. Zikatanov, and J. Roe, Improved supercooling in transient thermoelectrics *Applied physics letters*, vol. 85, no. 15, pp. 3247–3249, 2004.

[97] A. Miner, A. Majumdar, and U. Ghoshal, Thermo-electro-mechanical refrigeration based on transient thermoelectric effects in *Thermoelectrics, 1999. Eighteenth International Conference on*, pp. 27–30, IEEE, 1999.

[98] K. Landecker and A. Findlay, Study of the fast transient behaviour of Peltier junctions *Solid-State Electronics*, vol. 3, no. 3, pp. 239–260, 1961.

[99] P.-K. Lau and T. Makino, Current–voltage characteristics of long wavelength quantum-well laser diodes *Journal of applied physics*, vol. 83, no. 3, pp. 1183–1186, 1998.

[100] L. Que, J.-S. Park, and Y. B. Gianchandani, Bent-beam electrothermal actuators-Part I: Single beam and cascaded devices *Microelectromechanical Systems, Journal of*, vol. 10, no. 2, pp. 247–254, 2001.

[101] M. T. Kim, Influence of substrates on the elastic reaction of films for the microindentation tests *Thin Solid Films*, vol. 283, no. 1, pp. 12–16, 1996.

[102] H. Tada, A. E. Kumpel, R. E. Lathrop, J. B. Slanina, P. Nieva, P. Zavracky, I. N. Miaoulis, and P. Y. Wong, Thermal expansion coefficient of polycrystalline silicon and silicon dioxide thin films at high temperatures *Journal of applied physics*, vol. 87, no. 9, pp. 4189–4193, 2000.

[103] J. Y. Rho, R. B. Ashman, and C. H. Turner, Young's modulus of trabecular and cortical bone material: ultrasonic and microtensile measurements *Journal of biomechanics*, vol. 26, no. 2, pp. 111–119, 1993.

[104] W. Zhang and K. Turner, SCREAM'03: a Single Mask Process for HIGH-Q Single Crystal Silicon MEMS in *Proc. International Mechanical Engineering Congress and Exposition*, 2004.

[105] H. Watanabe, N. Yamada, and M. Okaji, Linear thermal expansion coefficient of silicon from 293 to 1000 K *International journal of thermophysics*, vol. 25, no. 1, pp. 221–236, 2004.

[106] T. Mukai, M. Yamada, and S. ShujiNakamura, Characteristics of InGaN-based UV/blue/-green/amber/red light-emitting diodes *Japanese journal of applied physics*, vol. 38, p. 3976, 1999.

[107] Y. Huaiyu, S. Koh, H. van Zeijl, A. Gielen, and Z. Guoqi, A review of passive thermal management of LED module *Journal of Semiconductors*, vol. 32, no. 1, p. 014008, 2011.

[108] K. Yung, H. Liem, H. Choy, and W. Lun, Thermal performance of high brightness LED array package on PCB *International Communications in Heat and Mass Transfer*, vol. 37, no. 9, pp. 1266–1272, 2010.

[109] K. Zhang, G.-W. Xiao, C. K. Wong, H.-W. Gu, M. M. Yuen, P. C. Chan, and B. Xu, Study on thermal interface material with carbon nanotubes and carbon black in high-brightness LED packaging with flip-chip in *Electronic Components and Technology Conference, 2005. Proceedings. 55th*, pp. 60–65, IEEE, 2005.

[110] L. Zhang, K. E. Goodson, and T. W. Kenny, *Silicon microchannel heat sinks: theories and phenomena*. Springer, 2004.

[111] J. D. Heppner, D. C. Walther, and A. P. Pisano, The design of ARCTIC: A rotary compressor thermally insulated μcooler *Sensors and Actuators A: Physical*, vol. 134, no. 1, pp. 47–56, 2007.

[112] J.-Y. Jung, H.-S. Oh, D. K. Lee, K. B. Choi, S. K. Dong, and H.-Y. Kwak, A capillary-pumped loop (CPL) with microcone-shaped capillary structure for cooling electronic devices *Journal of Micromechanics and Microengineering*, vol. 18, no. 1, p. 017002, 2008.

[113] G. C. Birur, T. W. Sur, A. D. Paris, P. Shakkottai, A. A. Green, and S. I. Haapanen, Micro/nano spacecraft thermal control using a MEMS-based pumped liquid cooling system in *Micromachining and Microfabrication*, pp. 196–206, International Society for Optics and Photonics, 2001.

[114] J. R. Thome, Boiling in microchannels: a review of experiment and theory *International Journal of Heat and Fluid Flow*, vol. 25, no. 2, pp. 128–139, 2004.

[115] M. Mihailovic, C. Rops, J. Hao, L. Mele, J. Creemer, and P. Sarro, MEMS silicon-based micro-evaporator *Journal of Micromechanics and Microengineering*, vol. 21, no. 7, p. 075007, 2011.

[116] L. Zhang, J.-M. Koo, L. Jiang, M. Asheghi, K. E. Goodson, J. G. Santiago, and T. W. Kenny, Measurements and modeling of two-phase flow in microchannels with nearly constant heat flux boundary conditions *Microelectromechanical Systems, Journal of*, vol. 11, no. 1, pp. 12–19, 2002.

[117] M. Lee, M. Wong, and Y. Zohar, Integrated micro-heat-pipe fabrication technology *Microelectromechanical Systems, Journal of*, vol. 12, no. 2, pp. 138–146, 2003.

[118] J. Dickey and G. Peterson, Experimental and analytical investigation of a capillary pumped loop *Journal of Thermophysics and Heat Transfer*, vol. 8, no. 3, pp. 602–607, 1994.

[119] N. S. Dhillon, A. P. Pisano, C. Hogue, and M. A. Hopcroft, MLHP–A high heat flux localized cooling technology for electronic substrates in *ASME Conference Proceedings*, pp. 621–630, 2008.

[120] W. Elenbaas, Heat dissipation of parallel plates by free convection *Physica*, vol. 9, no. 1, pp. 1–28, 1942.

[121] A. Bar-Cohen and W. Rohsenow, Thermally optimum spacing of vertical, natural convection cooled, parallel plates *Journal of Heat Transfer*, vol. 106, no. 1, pp. 116–123, 1984.

[122] K. Starner and H. McManus Jr, An experimental investigation of free-convection heat transfer from rectangular-fin arrays *Journal of Heat Transfer*, vol. 85, p. 273, 1963.

[123] J. R. Welling and C. Wooldridge, Free convection heat transfer coefficients from rectangular vertical fins *Journal of heat transfer*, vol. 87, p. 439, 1965.

[124] F. Harahap and H. McManus Jr, Natural convection heat transfer from horizontal rectangular fin arrays *Journal of heat transfer*, vol. 89, p. 32, 1967.

[125] C. D. Jones and L. F. Smith, Optimum arrangement of rectangular fins on horizontal surfaces for free-convection heat transfer *Journal of heat transfer*, vol. 92, p. 6, 1970.

[126] H. Yüncü and G. Anbar, An experimental investigation on performance of rectangular fins on a horizontal base in free convection heat transfer *Heat and mass transfer*, vol. 33, no. 5-6, pp. 507–514, 1998.

[127] F. Harahap, H. Lesmana, and I. A. S. Dirgayasa, Measurements of heat dissipation from miniaturized vertical rectangular fin arrays under dominant natural convection conditions *Heat and mass transfer*, vol. 42, no. 11, pp. 1025–1036, 2006.

[128] B. Yazicioğlu and H. Yüncü, Optimum fin spacing of rectangular fins on a vertical base in free convection heat transfer *Heat and Mass Transfer*, vol. 44, no. 1, pp. 11–21, 2007.

[129] S. Baskaya, M. Sivrioglu, and M. Ozek, Parametric study of natural convection heat transfer from horizontal rectangular fin arrays *International journal of thermal sciences*, vol. 39, no. 8, pp. 797–805, 2000.

[130] M. Mobedi and H. Yüncü, A three dimensional numerical study on natural convection heat transfer from short horizontal rectangular fin array *Heat and mass transfer*, vol. 39, no. 4, pp. 267–275, 2003.

[131] H. Yalcin, S. Baskaya, and M. Sivrioglu, Numerical analysis of natural convection heat transfer from rectangular shrouded fin arrays on a horizontal surface *International Communications in Heat and Mass Transfer*, vol. 35, no. 3, pp. 299–311, 2008.

[132] L. Dialameh, M. Yaghoubi, and O. Abouali, Natural convection from an array of horizontal rectangular thick fins with short length *Applied Thermal Engineering*, vol. 28, no. 17, pp. 2371–2379, 2008.

[133] I. Tari and M. Mehrtash, Natural convection heat transfer from inclined plate-fin heat sinks *International Journal of Heat and Mass Transfer*, vol. 56, no. 1, pp. 574–593, 2013.

[134] V. Rammohan Rao and S. Venkateshan, Experimental study of free convection and radiation in horizontal fin arrays *International journal of heat and mass transfer*, vol. 39, no. 4, pp. 779–789, 1996.

[135] J. Legierski, G. de Mey, *et al.*, Measurements and simulations of transient characteristics of heat pipes *Microelectronics reliability*, vol. 46, no. 1, pp. 109–115, 2006.

[136] C. Leung and S. Probert, Heat-exchanger performance: effect of orientation *Applied energy*, vol. 33, no. 4, pp. 235–252, 1989.

[137] A. Bar-Cohen, P. Wang, and E. Rahim, Thermal management of high heat flux nanoelectronic chips *Microgravity Science and Technology*, vol. 19, no. 3-4, pp. 48–52, 2007.

[138] S. V. Garimella, A. S. Fleischer, J. Y. Murthy, A. Keshavarzi, R. Prasher, C. Patel, S. H. Bhavnani, R. Venkatasubramanian, R. Mahajan, Y. Joshi, *et al.*, Thermal challenges in next-generation electronic systems *Components and Packaging Technologies, IEEE Transactions on*, vol. 31, no. 4, pp. 801–815, 2008.

[139] G. F. Russell, "Uniform surface temperature heat pipe and method of using the same," Mar. 16 1982. US Patent 4,320,246.

[140] G.-J. Sheu, F.-S. Hwu, S.-H. Tu, W.-T. Chen, J.-Y. Chang, and J.-C. Chen, The heat dissipation performance of LED applied a MHP in *Optics & Photonics 2005*, pp. 594113–594113, International Society for Optics and Photonics, 2005.

[141] Z. Lin, S. Wang, J. Huo, Y. Hu, J. Chen, W. Zhang, and E. Lee, Heat transfer characteristics and LED heat sink application of aluminum plate oscillating heat pipes *Applied Thermal Engineering*, vol. 31, no. 14, pp. 2221–2229, 2011.

[142] J. B. Marcinichen, J. R. Thome, and B. Michel, Cooling of microprocessors with micro-evaporation: A novel two-phase cooling cycle *International Journal of Refrigeration*, vol. 33, no. 7, pp. 1264–1276, 2010.

[143] J. B. Marcinichen, J. A. Olivier, N. Lamaison, and J. R. Thome, Advances in Electronics Cooling *Heat Transfer Engineering*, vol. 34, no. 5-6, pp. 434–446, 2013.

[144] S. Mehendale, A. Jacobi, and R. Shah, Fluid flow and heat transfer at micro-and meso-scales with application to heat exchanger design *Applied Mechanics Reviews*, vol. 53, p. 175, 2000.

[145] S. G. Kandlikar, Two-phase flow patterns, pressure drop, and heat transfer during boiling in minichannel flow passages of compact evaporators *Heat Transfer Engineering*, vol. 23, no. 1,

pp. 5–23, 2002.
[146] L. Chen, Y. Tian, and T. Karayiannis, The effect of tube diameter on vertical two-phase flow regimes in small tubes *International Journal of Heat and Mass Transfer*, vol. 49, no. 21, pp. 4220–4230, 2006.
[147] A. F and S. B, *Thermal management in electronic packaging*. McGraw-Hill Inc,New York, 1989.
[148] L. Waller, An old idea may solve VHSIC cooling problem *Electronics (5 August 1985)*, pp. 19–20, 1985.
[149] A. D. Kraus and A. Bar-Cohen, Thermal analysis and control of electronic equipment *Washington, DC, Hemisphere Publishing Corp., 1983, 633 p.*, vol. 1, 1983.
[150] H. N. Chaudhry, B. R. Hughes, and S. A. Ghani, A review of heat pipe systems for heat recovery and renewable energy applications *Renewable and Sustainable Energy Reviews*, vol. 16, no. 4, pp. 2249–2259, 2012.
[151] W. Srimuang and P. Amatachaya, A review of the applications of heat pipe heat exchangers for heat recovery *Renewable and Sustainable Energy Reviews*, vol. 16, no. 6, pp. 4303–4315, 2012.
[152] M. North and C. Avedisian, Heat pipes for cooling high flux/high power semiconductor chips *Journal of Electronic Packaging*, vol. 115, p. 112, 1993.
[153] G. P. Peterson, An introduction to heat pipes. Modeling, testing, and applications *Wiley Series in Thermal Management of Microelectronic and Electronic Systems, New York*, vol. 1, 1994.
[154] X. Li, J. Wang, Q. Hu, L. Bao, H. Zhang, and C. Wang, Capillary Limit of Micro Heat Pipe with Compound Structure of a Sintered Wick on Trapezium-grooved Substrate *PRZEGLAD ELEKTROTECHNICZNY*, vol. 88, no. 9 B, pp. 141–144, 2012.
[155] S. H. Moon, G. Hwang, S. C. Ko, and Y. T. Kim, Experimental study on the thermal performance of micro-heat pipe with cross-section of polygon *Microelectronics Reliability*, vol. 44, no. 2, pp. 315–321, 2004.
[156] S.-C. Wong, K.-C. Hsieh, J.-D. Wu, and W.-L. Han, A novel vapor chamber and its performance *International Journal of Heat and Mass Transfer*, vol. 53, no. 11, pp. 2377–2384, 2010.
[157] Y. Peng, W. Liu, N. Wang, Y. Tian, and X. Chen, A novel wick structure of vapor chamber based on the fractal architecture of leaf vein *International Journal of Heat and Mass Transfer*, vol. 63, pp. 120–133, 2013.
[158] X. Ji, J. Xu, A. M. Abanda, and Q. Xue, A vapor chamber using extended condenser concept for ultra-high heat flux and large heater area *International Journal of Heat and Mass Transfer*, vol. 55, no. 17, pp. 4908–4913, 2012.
[159] P. Naphon, S. Wongwises, and S. Wiriyasart, Application of two-phase vapor chamber technique for hard disk drive cooling of PCs *International Communications in Heat and Mass Transfer*, 2012.
[160] J.-C. Wang, R.-T. Wang, T.-L. Chang, and D.-S. Hwang, Development of 30Watt high-power LEDs vapor chamber-based plate *International Journal of Heat and Mass Transfer*, vol. 53, no. 19, pp. 3990–4001, 2010.
[161] Q. Cai, B.-c. Chen, and C. Tsai, Design, development and tests of high-performance silicon vapor chamber *Journal of Micromechanics and Microengineering*, vol. 22, no. 3, p. 035009, 2012.
[162] F. J. Stenger, *Experimental feasibility study of water-filled capillary-pumped heat-transfer loops*. National Aeronautics and Space Administration, 1966.
[163] Y. F. Maydanik, Loop heat pipes *Applied Thermal Engineering*, vol. 25, no. 5, pp. 635–657, 2005.
[164] L. Meyer, S. Dasgupta, D. Shaddock, J. Tucker, R. Fillion, P. Bronecke, L. Yorinks, and P. Kraft, A silicon-carbide micro-capillary pumped loop for cooling high power devices in *Semiconductor Thermal Measurement and Management Symposium, 2003. Ninteenth Annual IEEE*, pp. 364–368, IEEE, 2003.
[165] M. Nikitkin and B. Cullimire, CPL and LHP Technologies: What are the Differences, What are the Similarities? *SAE transactions*, vol. 107, no. 1, pp. 400–408, 1998.

[166] X. B. Li, Z. Shi, S. Wang, Q. Hu, L. Bao, and H. Zhang, Analysis of structural parameters of grooved-wicksin micro heat pipes based on capillary limits *Key Engineering Materials*, vol. 499, pp. 21–26, 2012.

[167] M. Hamdan, *Loop Heat Pipe (LHP) Modeling and Development by Utilizing Coherent Porous Silicion (CPS) Wicks*. PhD thesis, University of Cincinnati, 2003.

[168] S. Launay, V. Sartre, and M. Lallemand, Experimental study on silicon micro-heat pipe arrays *Applied thermal engineering*, vol. 24, no. 2, pp. 233–243, 2004.

[169] L. Vasiliev, Micro and miniature heat pipes–Electronic component coolers *Applied Thermal Engineering*, vol. 28, no. 4, pp. 266–273, 2008.

[170] A. Mallik, G. Peterson, and M. Weichold, On the use of micro heat pipes as an integral part of semiconductor devices *Journal of Electronic Packaging*, vol. 114, p. 436, 1992.

[171] G. P. Peterson, Overview of micro heat pipe research and development *Applied Mechanics Reviews*, vol. 45, no. 12, 1992.

[172] R. J. McGlen, R. Jachuck, and S. Lin, Integrated thermal management techniques for high power electronic devices *Applied Thermal Engineering*, vol. 24, no. 8, pp. 1143–1156, 2004.

[173] V. Pastukhov, Y. F. Maidanik, C. Vershinin, and M. Korukov, Miniature loop heat pipes for electronics cooling *Applied Thermal Engineering*, vol. 23, no. 9, pp. 1125–1135, 2003.

[174] A. A. Adoni, A. Ambirajan, V. Jasvanath, D. Kumar, and P. Dutta, Theoretical Studies of Hard Filling in Loop Heat Pipes *Journal of Thermophysics and Heat Transfer*, vol. 24, no. 1, pp. 173–183, 2010.

[175] A. Ambirajan, A. A. Adoni, J. S. Vaidya, A. A. Rajendran, D. Kumar, and P. Dutta, Loop Heat Pipes: A Review of Fundamentals, Operation, and Design *Heat Transfer Engineering*, vol. 33, no. 4-5, pp. 387–405, 2012.

[176] Y. Chen, M. Groll, R. Mertz, Y. F. Maydanik, and S. Vershinin, Steady-state and transient performance of a miniature loop heat pipe *International Journal of Thermal Sciences*, vol. 45, no. 11, pp. 1084–1090, 2006.

[177] Y. F. Maydanik, S. V. Vershinin, M. A. Korukov, and J. M. Ochterbeck, Miniature loop heat pipes-a promising means for cooling electronics *Components and Packaging Technologies, IEEE Transactions on*, vol. 28, no. 2, pp. 290–296, 2005.

[178] R. Singh, A. Akbarzadeh, C. Dixon, M. Mochizuki, and R. R. Riehl, Miniature loop heat pipe with flat evaporator for cooling computer CPU *Components and Packaging Technologies, IEEE Transactions on*, vol. 30, no. 1, pp. 42–49, 2007.

[179] J. Kirshberg, K. Yerkes, D. Trebotich, and D. Liepmann, Cooling effect of a MEMS based micro capillary pumped loop for chip-level temperature control in *ASME international mechanical engineering congress & exposition, Florida*, 2000.

[180] C.-T. Wang, T.-S. Leu, and T.-M. Lai, Micro capillary pumped loop system for a cooling high power device *Experimental Thermal and Fluid Science*, vol. 32, no. 5, pp. 1090–1095, 2008.

[181] M. Whitby and N. Quirke, Fluid flow in carbon nanotubes and nanopipes *Nature Nanotechnology*, vol. 2, no. 2, pp. 87–94, 2007.

[182] H. Masuda and K. Fukuda, Ordered metal nanohole arrays made by a two-step *Science*, vol. 268, pp. 1466–1468, 1995.

[183] J. A. Weibel, S. V. Garimella, J. Y. Murthy, and D. H. Altman, Design of integrated nanostructured wicks for high-performance vapor chambers *Components, Packaging and Manufacturing Technology, IEEE Transactions on*, vol. 1, no. 6, pp. 859–867, 2011.

[184] B. J. Hinds, N. Chopra, T. Rantell, R. Andrews, V. Gavalas, and L. G. Bachas, Aligned multiwalled carbon nanotube membranes *Science*, vol. 303, no. 5654, pp. 62–65, 2004.

[185] M. Majumder, N. Chopra, R. Andrews, and B. J. Hinds, Nanoscale hydrodynamics: Enhanced flow in carbon nanotubes *Nature*, vol. 438, no. 7064, pp. 44–44, 2005.

[186] J. K. Holt, H. G. Park, Y. Wang, M. Stadermann, A. B. Artyukhin, C. P. Grigoropoulos, A. Noy, and O. Bakajin, Fast mass transport through sub-2-nanometer carbon nanotubes *Science*, vol. 312, no. 5776, pp. 1034–1037, 2006.

[187] S. Joseph and N. Aluru, Why are carbon nanotubes fast transporters of water? *Nano Letters*, vol. 8, no. 2, pp. 452–458, 2008.

[188] Q.-L. Zhang, W.-Z. Jiang, J. Liu, R.-D. Miao, and N. Sheng, Water Transport through Carbon Nanotubes with the Radial Breathing Mode *Physical Review Letters*, vol. 110, no. 25, p. 254501, 2013.

[189] S. K. Kannam, B. Todd, J. Hansen, and P. J. Daivis, How fast does water flow in carbon nanotubes? *The Journal of chemical physics*, vol. 138, p. 094701, 2013.

[190] R. Ranjan, J. Y. Murthy, and S. V. Garimella, A microscale model for thin-film evaporation in capillary wick structures *International Journal of Heat and Mass Transfer*, vol. 54, no. 1, pp. 169–179, 2011.

[191] R. Ranjan, J. Y. Murthy, and S. Garimella, Analysis of the wicking and thin-film evaporation characteristics of microstructures *Journal of Heat Transfer*, vol. 131, pp. 101001–1–11, 2009.

[192] J. Weibel, S. Kim, T. Fisher, and S. Garimella, Carbon nanotube coatings for enhanced capillary-fed boiling from porous microstructures *Nanoscale and Microscale Thermophysical Engineering*, vol. 16, no. 1, pp. 1–17, 2012.

[193] A. Melechko, T. McKnight, M. Guillorn, V. Merkulov, B. Ilic, M. Doktycz, D. Lowndes, and M. Simpson, Vertically aligned carbon nanofibers as sacrificial templates for nanofluidic structures *Applied physics letters*, vol. 82, no. 6, pp. 976–978, 2003.

[194] H. H. Bau, S. Sinha, B. Kim, and M. Riegelman, Fabrication of nanofluidic devices and the study of fluid transport through them in *Optics East*, pp. 201–213, International Society for Optics and Photonics, 2005.

[195] B. R. Flachsbart, K. Wong, J. M. Iannacone, E. N. Abante, R. L. Vlach, P. A. Rauchfuss, P. W. Bohn, J. V. Sweedler, and M. A. Shannon, Design and fabrication of a multilayered polymer microfluidic chip with nanofluidic interconnects via adhesive contact printing *Lab on a Chip*, vol. 6, no. 5, pp. 667–674, 2006.

[196] A. Han, N. F. de Rooij, and U. Staufer, Design and fabrication of nanofluidic devices by surface micromachining *Nanotechnology*, vol. 17, no. 10, p. 2498, 2006.

[197] M. Lallemand and F. Lefèvre, Micro/mini heat pipes for the cooling of electronic devices in *13th International Heat Pipe Conference, Shangai–China*, pp. 12–22, 2004.

[198] B. Babin, G. Peterson, and D. Wu, Steady-state modeling and testing of a micro heat pipe *Journal of Heat Transfer (Transactions of the ASME Series C)*, vol. 112, no. 3, 1990.

[199] D. Khrustalev and A. Faghri, Thermal analysis of a micro heat pipe *Journal of Heat transfer*, vol. 116, no. 1, pp. 189–198, 1994.

[200] G. Peterson, Modeling, fabrication, and testing of micro heat pipes: an update *Applied Mechanics Reviews*, vol. 49, p. 175, 1996.

[201] T. Cotter, Principles and prospects for micro heat pipes tech. rep., Los Alamos National Lab., NM (USA), 1984.

[202] C.-Y. Wang, M. Groll, S. Rösler, and C.-J. Tu, Porous medium model for two-phase flow in mini channels with applications to micro heat pipes *Heat Recovery Systems and CHP*, vol. 14, no. 4, pp. 377–389, 1994.

[203] M. Rahmat and P. Hubert, Two-phase simulations of micro heat pipes *Computers & Fluids*, vol. 39, no. 3, pp. 451–460, 2010.

[204] Y. Wang and G. Peterson, Analysis of wire-bonded micro heat pipe arrays *Journal of thermophysics and heat transfer*, vol. 16, no. 3, pp. 346–355, 2002.

[205] S. Launay, V. Sartre, M. B. Mantelli, K. V. de Paiva, and M. Lallemand, Investigation of a wire plate micro heat pipe array *International journal of thermal sciences*, vol. 43, no. 5, pp. 499–507,

2004.

[206] Y. Wang and G. Peterson, Optimization of micro heat pipe radiators in a radiation environment *Journal of thermophysics and heat transfer*, vol. 16, no. 4, pp. 537–546, 2002.

[207] L. Xibing, L. Xianli, S. Zhimin, J. Hui, L. XiaoZhong, W. Shigang, H. Gang, and P. Yongge, Heat Transfer Performance of Micro Heat Pipe with Trapezium-grooved Wick in *Intelligent Computation Technology and Automation (ICICTA), 2012 Fifth International Conference on*, pp. 614–618, IEEE, 2012.

[208] Y. Li, T. He, and Z. Zeng, Analysis of collapse in flattening a micro-grooved heat pipe by lateral compression *Chinese Journal of Mechanical Engineering*, vol. 25, no. 6, pp. 1210–1217, 2012.

[209] S.-W. Kang, S.-H. Tsai, and M.-H. Ko, Metallic micro heat pipe heat spreader fabrication *Applied Thermal Engineering*, vol. 24, no. 2, pp. 299–309, 2004.

[210] S.-W. Kang, S.-H. Tsai, and H.-C. Chen, Fabrication and test of radial grooved micro heat pipes *Applied Thermal Engineering*, vol. 22, no. 14, pp. 1559–1568, 2002.

[211] M. Reyes, D. Alonso, J. Arias, and A. Velazquez, Experimental and theoretical study of a vapour chamber based heat spreader for avionics applications *Applied Thermal Engineering*, vol. 37, pp. 51–59, 2012.

[212] Y. Koito, H. Imura, M. Mochizuki, Y. Saito, and S. Torii, Numerical analysis and experimental verification on thermal fluid phenomena in a vapor chamber *Applied Thermal Engineering*, vol. 26, no. 14, pp. 1669–1676, 2006.

[213] H. Hassan and S. Harmand, 3D transient model of vapour chamber: Effect of nanofluids on its performance *Applied Thermal Engineering*, 2012.

[214] S. Murer, P. Lybaert, L. Gleton, and A. Sturbois, Experimental and numerical analysis of the transient response of a miniature heat pipe *Applied thermal engineering*, vol. 25, no. 16, pp. 2566–2577, 2005.

[215] Y. M. Hung *et al.*, Effects of geometric design on thermal performance of star-groove micro-heat pipes *International Journal of Heat and Mass Transfer*, vol. 54, no. 5, pp. 1198–1209, 2011.

[216] J. Ha and G. Peterson, The heat transport capacity of micro heat pipes *Journal of heat transfer*, vol. 120, no. 4, pp. 1064–1071, 1998.

[217] V. Sartre, M. C. Zaghdoudi, and M. Lallemand, Effect of interfacial phenomena on evaporative heat transfer in micro heat pipes *International journal of thermal sciences*, vol. 39, no. 4, pp. 498–504, 2000.

[218] G. Peterson and H. Ma, Temperature response of heat transport in a micro heat pipe *Journal of heat transfer*, vol. 121, no. 2, pp. 438–445, 1999.

[219] J. Ku, Operating characteristics of loop heat pipes *SAE transactions*, vol. 108, no. 1, pp. 503–519, 1999.

[220] S. Van Oost, B. Mullender, G. Bekaert, and J. C. Legros, Secondary wick operation principle and performance mapping in LHP and FLHP evaporators in *AIP conference proceedings*, vol. 608, p. 94, 2002.

[221] T. T. Hoang and J. Ku, Heat and mass transfer in loop heat pipes in *Proceeding ASME*, ASME, 2003.

[222] P.-Y. A. Chuang, *An improved steady-state model of loop heat pipes based on experimental and theoretical analyses*. ProQuest, 2003.

[223] A. D. Hölke, *Development of silicon chemical wet etching toward the realization of an integrated thermal-electronic package*. PhD thesis, University of Cincinnati, 1999.

[224] K. Pettigrew, J. Kirshberg, K. Yerkes, D. Trebotich, and D. Liepmann, Performance of a MEMS based micro capillary pumped loop for chip-level temperature control in *Micro Electro Mechanical Systems, 2001. MEMS 2001. The 14th IEEE International Conference on*, pp. 427–430, IEEE, 2001.

[225] M. Ghajar, J. Darabi, and N. Crews Jr, A hybrid CFD-mathematical model for simulation of a MEMS loop heat pipe for electronics cooling applications *Journal of Micromechanics and Microengineering*, vol. 15, no. 2, p. 313, 2005.

[226] Z. J. Zuo, M. T. North, and K. L. Wert, High heat flux heat pipe mechanism for cooling of electronics *Components and Packaging Technologies, IEEE Transactions on*, vol. 24, no. 2, pp. 220–225, 2001.

[227] R. Savino, A. Cecere, and R. Di Paola, Surface tension-driven flow in wickless heat pipes with self-rewetting fluids *International Journal of Heat and Fluid Flow*, vol. 30, no. 2, pp. 380–388, 2009.

[228] P. Charoensawan, S. Khandekar, M. Groll, and P. Terdtoon, Closed loop pulsating heat pipes: Part A: parametric experimental investigations *Applied Thermal Engineering*, vol. 23, no. 16, pp. 2009–2020, 2003.

[229] J. Qu, H.-Y. Wu, and Q. Wang, Experimental investigation of silicon-based micro-pulsating heat pipe for cooling electronics *Nanoscale and Microscale Thermophysical Engineering*, vol. 16, no. 1, pp. 37–49, 2012.

[230] C. Sobhan, R. Rag, and G. Peterson, A review and comparative study of the investigations on micro heat pipes *International Journal of Energy Research*, vol. 31, no. 6-7, pp. 664–688, 2007.

[231] L. Vasiliev, D. Lossouarn, C. Romestant, A. Alexandre, Y. Bertin, Y. Piatsiushyk, and V. Romanenkov, Loop heat pipe for cooling of high-power electronic components *International Journal of Heat and Mass Transfer*, vol. 52, no. 1, pp. 301–308, 2009.

[232] L. Lachassagne, Y. Bertin, V. Ayel, and C. Romestant, Steady-state modeling of Capillary Pumped Loop in gravity field *International Journal of Thermal Sciences*, 2012.

[233] I. Muraoka, F. Ramos, and V. Vlassov, Experimental and theoretical investigation of a capillary pumped loop with a porous element in the condenser *International communications in heat and mass transfer*, vol. 25, no. 8, pp. 1085–1094, 1998.

[234] G. Peterson, A. Duncan, and M. Weichold, Experimental investigation of micro heat pipes fabricated in silicon wafers *Journal of Heat Transfer*, vol. 115, no. 3, pp. 751–756, 1993.

[235] B. FE, C. EG, and S. B, Construction and test of a flexible heat pipe in *Proceedings of ASME Space Systems and Thermal Technologies for the 70's1970*, 1970.

[236] R. B. Schweickart and M. M. Buchko, Flexible heat pipes for CCD cooling on the advanced camera for surveys in *Astronomical Telescopes & Instrumentation*, pp. 292–300, International Society for Optics and Photonics, 1998.

[237] C. Oshman, Q. Li, L.-A. Liew, R. Yang, V. M. Bright, and Y. Lee, Flat flexible polymer heat pipes *Journal of Micromechanics and Microengineering*, vol. 23, no. 1, p. 015001, 2013.

[238] J. Kim, S. You, and S. U. Choi, Evaporative spray cooling of plain and microporous coated surfaces *International Journal of Heat and Mass Transfer*, vol. 47, no. 14, pp. 3307–3315, 2004.

[239] J. Ha and G. Peterson, Capillary performance of evaporating flow in micro grooves: an analytical approach for very small tilt angles *Journal of heat transfer*, vol. 120, no. 2, pp. 452–457, 1998.

[240] Y. M. Hung and K.-K. Tio, Thermal Analysis of a Water-Filled Micro Heat Pipe With Phase-Change Interfacial Resistance *Journal of heat transfer*, vol. 134, no. 11, 2012.

[241] A. Mallik and G. Peterson, Steady-state investigation of vapor deposited micro heat pipe arrays *Journal of Electronic Packaging*, vol. 117, p. 75, 1995.

[242] V. H. A. Knowles K, Anodic bonding *Int Mater Rev*, vol. 51, pp. 273–311, 2006.

[243] J. Qu and H. Y. Wu, Silicon-Based Micro Pulsating Heat Pipe for Cooling Electronics *Advanced Materials Research*, vol. 403, pp. 4260–4265, 2012.

[244] J. Qu, H. Wu, and P. Cheng, Start-up, heat transfer and flow characteristics of silicon-based micro pulsating heat pipes *International Journal of Heat and Mass Transfer*, 2012.

[245] A. K. Mallik, G. Peterson, and M. H. Weichold, Fabrication of vapor-deposited micro heat pipe arrays as an integral part of semiconductor devices *Microelectromechanical Systems, Journal of*,

vol. 4, no. 3, pp. 119–131, 1995.

[246] M. S. Fluids, 2006. http://www.3m.com/market/industrial/fluids/library.

[247] C. Sperry, R. Philstrom, P. Claybaker, J. Webster, R. Cree, *et al.*, SS-1 supercomputer cooling system in *Electronic Components and Technology Conference, 1993. Proceedings., 43rd*, pp. 218–237, IEEE, 1993.

[248] A. Bar-Cohen, M. Arik, and M. Ohadi, Direct liquid cooling of high flux micro and nano electronic components *Proceedings of the IEEE*, vol. 94, no. 8, pp. 1549–1570, 2006.

[249] S. Khandekar, N. Dollinger, and M. Groll, Understanding operational regimes of closed loop pulsating heat pipes: an experimental study *Applied Thermal Engineering*, vol. 23, no. 6, pp. 707–719, 2003.

[250] L. Troniewski and R. Ulbrich, Two-phase gas-liquid flow in rectangular channels *Chemical engineering science*, vol. 39, no. 4, pp. 751–765, 1984.

[251] A. Miner and U. Ghoshal, Cooling of high-power-density microdevices using liquid metal coolants *Applied physics letters*, vol. 85, no. 3, pp. 506–508, 2004.

[252] W. Q. Liu and L. Yu, Analysis of the Evaporating Characteristics of the Grooved Micro Heat Pipe with Alkali Metals as Working Fluid *Advanced Materials Research*, vol. 516, pp. 84–87, 2012.

[253] S. U. Choi and J. Eastman, Enhancing thermal conductivity of fluids with nanoparticles tech. rep., Argonne National Lab., IL (United States), 1995.

[254] C. T. Nguyen, G. Roy, C. Gauthier, and N. Galanis, Heat transfer enhancement using Al2O3–water nanofluid for an electronic liquid cooling system *Applied Thermal Engineering*, vol. 27, no. 8, pp. 1501–1506, 2007.

[255] J. Lee and I. Mudawar, Assessment of the effectiveness of nanofluids for single-phase and two-phase heat transfer in micro-channels *International Journal of Heat and Mass Transfer*, vol. 50, no. 3, pp. 452–463, 2007.

[256] L. G. Asirvatham, R. Nimmagadda, and S. Wongwises, Heat transfer performance of screen mesh wick heat pipes using silver–water nanofluid *International Journal of Heat and Mass Transfer*, vol. 60, pp. 201–209, 2013.

[257] X. F. Yang, Z.-H. Liu, and J. Zhao, Heat transfer performance of a horizontal micro-grooved heat pipe using CuO nanofluid *Journal of Micromechanics and Microengineering*, vol. 18, no. 3, p. 035038, 2008.

[258] Z.-h. Liu, X.-f. Yang, G.-s. Wang, and G.-l. Guo, Influence of carbon nanotube suspension on the thermal performance of a miniature thermosyphon *International Journal of Heat and Mass Transfer*, vol. 53, no. 9, pp. 1914–1920, 2010.

[259] Z.-H. Liu and L. Lu, Thermal performance of axially microgrooved heat pipe using carbon nanotube suspensions *Journal of Thermophysics and Heat Transfer*, vol. 23, no. 1, pp. 170–175, 2009.

[260] S. H. Noie-Baghban and G. Majideian, Waste heat recovery using heat pipe heat exchanger (HPHE) for surgery rooms in hospitals *Applied Thermal Engineering*, vol. 20, no. 14, pp. 1271–1282, 2000.

[261] A. Faghri, Heat pipe science and technology in *Fuel and Energy Abstracts*, vol. 36, p. 285, Elsevier, 1995.

[262] P. Dunn and D. A. Reay, Heat pipes tech. rep., Pergamon Press, Ltd., New York, NY, 1978.

[263] R. Revellin and J. R. Thome, A theoretical model for the prediction of the critical heat flux in heated microchannels *International Journal of Heat and Mass Transfer*, vol. 51, no. 5, pp. 1216–1225, 2008.

[264] A. Bergles and S. Kandlikar, On the nature of critical heat flux in microchannels *Transactions of the ASME-C-Journal of Heat Transfer*, vol. 127, no. 1, pp. 101–107, 2005.

[265] L. Bai, G. Lin, H. Zhang, and D. Wen, Mathematical modeling of steady-state operation of a loop heat pipe *Applied Thermal Engineering*, vol. 29, no. 13, pp. 2643–2654, 2009.

[266] X. Zhang, X. Zhao, J. Xu, and X. Yu, Characterization of a solar photovoltaic/loop-heat-pipe heat pump water heating system *Applied Energy*, vol. 102, pp. 1229–1245, 2013.

[267] X. Chen, C. K. Wong, C. A. Yuan, and G. Zhang, Nanowire-based gas sensors *Sensors and Actuators B: Chemical*, 2012.

[268] G. Q. Zhang and A. van Roosmalen, *More than Moore: creating high value micro/nanoelectronics systems*. Springer, 2009.

[269] A. D. Kraus and A. Bar-Cohen, *Design and analysis of heat sinks*. Wiley New York, 1995.

[270] E. Yu and Y. K. Joshi, Natural convection air cooling of electronic components in partially open compact horizontal enclosures *Components and Packaging Technologies, IEEE Transactions on*, vol. 23, no. 1, pp. 14–22, 2000.

[271] V. H. Adams, D. L. Blackburn, Y. Joshi, and D. W. Berning, Issues in validating package compact thermal models for natural convection cooled electronic systems in *Semiconductor Thermal Measurement and Management Symposium, 1997. SEMI-THERM XIII., Thirteenth Annual IEEE*, pp. 10–23, IEEE, 1997.

[272] J. Standard, Integrated Circuits Thermal Test Method Environmental Conditions - Natural convection (Still Air) *JESD 51-2A*, 2008.

[273] W. H. MacAdams and W. H. McAdams, *Heat transmission*. McGraw-Hill New York, 1954.

[274] C. Cheung, B. Noska, and K. van der heide, Thermal management: Comparison of passive and active cooling effectiveness *LED Professional Review*, p. 42, 2009.

Acknowledgements

This research was carried out within the project ”Consumerizing Solid State Lighting” (CSSL), partly funded by the European Commission and AgentschapNL in the ENIAC Joint Undertaking, and under project number E63.9.10397 in the framework of the Research Program of the Materials innovation institute (M2i) (`www.m2i.nl`).

In the four years, it has been a memorable journey in this country far away from my homeland. During this period, I have met a lot of kind and wonderful people. I have learned from them about both scientific and living knowledges. Moreover, I am still remembering those nice people during my MSc period in Process and Energy Laboratory of Faculty Mechanical, Maritime and Materials Engineering for their kind support in my life.

I owe my greatest debt of gratitude to my advisors, Prof.dr. Guoqi Zhang, Dr. Alexander W.J. Gielen and Dr. Henk van Zeijl, who have given me constant help, read my manuscripts with great patience and offered me invaluable advice and informative suggestions.

I would like to express my thanks to my friends in M2i, who are always kind and patient in helping me. Giuseppe Visimberga and Iulia Degeratu help me a lot on the European Project; Gitty Bouman, Janneke Curovic and Gaby Cuss are always kind to help me to find the information and fill all the forms; and also thanks Anne-Isabelle Desmangles, Jolanda Dest, Irina Bruckner, Monica Reulink, Brigitte van Uden and etc. You all help me a lot not only for my study but also for enriching and broadening my knowledge.

As I just start my Ph.D, I have involved in the European project CSSL, where I learned knowledge, experiences and cooperation from many kind people. My thanks go to all the people I met in the project: (CTU) Jiri Jakovenko, et al.; (CEA - LITEN) Stephane Bredeau, Thomas Pietri, Marianne Consonni, Adrien Gasse, Alex Lagrange, Benjamin Pardeau, et al.; (CNM.CSIC) Xavier Perpinya, Xavier Jorda, Miquel Vellvehi, et al.; (Leitat) Jose Saez, Florencia Nava, et al.; (Aismalibar) Vicenc Muns Camp, et al.; (Wittenburg) Jan Van Opzeeland, et al.; (Plessey) John Ellis, Colin Jones, et al.; (NXP) Philippe Maugars, Pascal Talbot, Stephan Barra, et al.; (Boschman) Lingen Wang, et al.; (Philips Lighting) Marcel de Jong, Peter Bancken, Richard van Silfhout, Ernst Hermens, et al.; (TNO) Pieter Jan, Jos Kunen,

Robert Werkhoven, et al.; (University of Cambridge) Dandan Zhu, Ted Thrush, et al.; (Niko) Peter Vehent, Diederik Devenyn, et al.; (Archimede Elettronica) Magnaghi Piero, Calderara Roberto, et al.; (Legrand) Christophe Frugier, Didier Leblanc, et al.

My thanks go to all the people I met in the M2i cluster 9 meeting. We have always nice talk about each other's work which benefited me with multi discipline mind to improve my own researches. They are Prof. Jurriaan Schmitz, Dr. Ugo Lafont, Mirjam Theelen, Qingling Guan, and etc.

In TU Delft, it is unforgettable memory for me in the Clean Room. My thanks also go to all the staff there, who are always kind and patient in supporting and encouraging me to success. My thanks go to MSc. S.Milosavljevic, Dr. G.Pandraud, who trained me with your experience and patience. My thanks go to Ir. E.J.G. Goudena, Ir. A. van den Bogaard, Ir. J. van der Cingel, J. Groeneweg, J. van Hartingsveldt, R. Klerks, Ir. J.M.W. Laros, Dr. ir. H. Schellevis, Ir. T.L.M. Scholtes, L.A. Steenweg, Dr. C.C.G. Visser, W. van der Vlist, W.H.A. Wien, Dr. ir. J.van Wingerden, Ir. J.C. Wolff, Ir. M.van der Zwan and etc. And Ir. P.J.F. Swart always help me in the measurement room.

Then I would like to express my gratitude to Prof.dr. C.I.M. Beenakker, Prof.dr. P.M. Sarro, Dr. R. Ishihara who always talk to me with your encyclopedic knowledge. Meanwhile, I would like to thank M. Lagendijk-Korzeniewski, M.J.J. Roozenburg-de Bree, and Bianca Knot.

I have partly worked in TNO Eindhoven since I started my Ph.D, there I have a wonderful time with many people. Especially, I would like to thank the people in Materials for the High-tech Industry: Freddie Furrer, Paul Ngana, Monique van den Nieuwenhof, Rene Kregting, Marcel Kouters, Stephen Harianto, Eric Veninga, and etc. And I want to express my thanks to the people for sharing offices with me in TNO: Chretien Hermse, Edwin Stam, Per Ambrosiussen and Nils Erkamp.

Besides, I am appreciate to many people in Philips. I have got a lot of suggestions from thermal expert Erik Eggink when I was lost at the beginning. And I want to express my special thanks to Willem Van Driel, and Simon Kadijk in Philips Lighting. I would like to thank John Janssen in NXP Nijmegen for your professional advice for the compact model.

My sincere thanks also go to the people in TU Delft Beijing Research Center and State Key Laboratory of Solid-State Lighting in China: Cadmus Yuan, Sau Wee Koh, Bo Li, Hongyu Tang, Jia Zhao, Chenglong Zhen, Cell Wong, Stanley Leung, Chenglong Zhen and etc.

During the four years, I met my dear friends who support me in my study and life. Jiaqi Tang, Jia Wei, Xianping Chen, Rene Poelma, Zahra Kolahdouz Esfahani, Xueming Li, Thomas Moh, Vahid Mohammadi, Lin Qi, Fabio Rodriques, Chenggang Shen, Pengfei Sun, Sima Tarashioon, An Tran, Joost Meerwijk, Cinzia Silvestri, Robert Sokolovskij, Yujian Huang, Maryam Yazdan Mehr, Jin Zhang, Jing Zhang, Pan Liu, Teng Ma, Dan Farley, and etc. Without you, I cannot finish my work.

Finally and most importantly, I would like to thank my dear family: my grandparents, my uncles and aunts, my parents, my younger sister and my new family member - Jiamin who I met just after the commencement of my PhD. I am sincerely grateful to my grandparents and my mum for their love. Also, I would like to thank my dad, who is the dean of our family with his kindness and strictness. Many thanks go to my younger sister Lingyun who supporting me and giving lots of fun in my life. And I want to express my deepest appreciation to my wife Jiamin for her love, sweet smile and huge support to my study and work. And I would like to thank Jiamin's parents who accepted me and make me feel very warm in their family.

Selected publications

Journal publications

1. H. Ye, S. Koh, H.W. van Zeijl, A.W.J. Gielen, G.Q. Zhang, A Review of Passive Thermal Management of LED Module, Journal of Semiconductors, (2011) Vol.32, Issue 1, pp. 14008.1-4.

2. H. Ye, M. Mihailovic, C.K.Y. Wong, H.W. van Zeijl, A.W.J. Gielen, G.Q. Zhang, P.M. Sarro, Two-phase Cooling of Light Emitting Diode for Higher Light Output and Increased Efficiency, Applied Thermal Engineering, (2012) Vol.52, Issue 2, pp. 353-9.

3. H. Ye, X. Chen, H.W. van Zeijl, A.W.J. Gielen, G.Q. Zhang, Thermal Transient Effect and Improved Junction Temperature Measurement Method in High-voltage Light-emitting Diodes, Electron Device Letters, (2013) Vol.34, Issue 9, pp. 1172-74.

4. H. Ye, S.W. Koh, C.A. Yuan, H.W. van Zeijl, A.W.J. Gielen, S.W.R. Lee, G.Q. Zhang, Electrical-thermal-luminous-chromatic Model of Phosphor-converted White Light-Emitting Diodes, Applied Thermal Engineering, (2014) Vol.62, Issue 2, pp. 588-97.

5. H. Ye, J. Wei, H.W. van Zeijl, P.M. Sarro, G.Q. Zhang, Fabrication and Application of Temperature Triggered MEMS Switch for Active Cooling Control in Solid State Lighting System, Microelectronics Reliability, (2014) Vol.54, Issue 6-7, pp. 1338-43.

6. H. Ye, R. Sokolovskij, H.W. van Zeijl, A.W.J. Gielen, S.W.R. Lee, G.Q. Zhang, A Polymer Based Miniature Loop Heat Pipe with Silicon Substrate and Temperature Sensors for High Brightness Light-Emitting Diodes, Microelectronics Reliability, (2014) Vol.54, Issue 6-7, pp. 1355-62.

7. H. Ye, B. Li, H.Y. Tang, J. Zhao, C.A. Yuan, G.Q. Zhang, Design of Vertical Fin Arrays with Heat Pipes Used for High-power Light-Emitting Diodes, Microelectronics Reliability, In Press.

8. H. Ye, H.W. van Zeijl, A.W.J. Gielen, G.Q. Zhang, Review on the Applications of Micro/mini Heat Pipes for Thermal Management and Energy Conservation in Electronic Systems, Renewable & Sustainable Energy Reviews, under review.

Conference proceedings

1. H. Ye, A.W.J. Gielen, H.W. van Zeijl, R.J. Werkhoven, G.Q. Zhang, Numerical Modeling of Thermal Performance: Natural Convection and Radiation of Solid State Lighting, EuroSimE 2011, Linz, Austria.

2. J. Tang, H. Ye, J.B.J. Schelen, C.I.M. Beenakker, Plasma Decapsulation of Plastic IC Packages with Copper Wire Bonds for Failure Analysis, ICEPT-HDP 2011, Shanghai, China.

3. H. Ye, A.W.J. Gielen, H.W. van Zeijl, G.Q. Zhang, Thermal Analysis of HB LED Packages and Advanced Materials, ChinaSSL 2011, Guangzhou, China.

4. C.A. Yuan, J. Wei, H. Ye, S.W. Koh, S. Harianto, M. van den Nieuwenhof, G. Q. Zhang, Polymer-based 2D/3D Wafer Level Heterogeneous Integration for SSL Module, EuroSimE 2012, Lisbon, Portugal.

5. H. Ye, S.W. Koh, J. Wei, H.W. van Zeijl, G.Q. Zhang, Dynamic Thermal simulation of High-brightness LEDs with Unsteady Driver Power Output, EuroSimE 2012, Lisbon, Portugal.

6. H. Ye, S.W. Koh, C.A.Yuan, G. Q. Zhang, Thermal Analysis of Phosphor in High Brightness LED, ICEPT-HDP 2012, Guilin, China.

7. J. Wei, H. Ye, H.W. van Zeijl, P.M Sarro, G.Q. Zhang, Single-Mask Fabrication of Temperature Triggered MEMS Switch for Cooling Control in SSL System, Eurosensors XXVI 2012, Krakow, Poland.

8. H. Ye, H.W. van Zeijl, R. Sokolovskij, A.W.J. Gielen, G.Q. Zhang, Advanced LED Package with Temperature Sensors and Microfluidic cooling, ECTC 2013, Las Vegas, USA.

Curriculum Vitae

Huaiyu YE

14.06.2010 - 10.09.2014, Ph.D.
Faculty Electrical Engineering, Mathematics & Computer Science
Delft Institute of Microsystems and Nanoelectronics (Dimes), TU Delft

14.06.2010 - 14.06.2014, Researcher
Reliability and Predictability of Optoelectronic Devices, M2i
Materials for the High-tech Industry, TNO

02.11.2009 - 28.05.2010, Assistant researcher
Process & Energy Laboratory
Faculty Mechanical, Maritime & Materials Engineering, TU Delft

03.09.2007 - 30.10.2009, M.Sc.
Process & Energy Laboratory
Faculty Mechanical, Maritime & Materials Engineering, TU Delft

02.04.2007 - 29.06.2007, Assistant engineer
Caterpillar Remanufacturing Services Co., Ltd., Shanghai, China

01.09.2003 - 06.06.2007, B.Sc.
Institute of Refrigeration and Cryogenics
Mechanical & Power Engineering School, Shanghai Jiao Tong University, Shanghai, China